AER 814 AIRCRAFT DESIGN PROJECT

TEAM ALPHA

HAULER-X

Toronto Metropolitan University

Department of Aerospace Engineering
Faculty of Engineering
& Architectural Science

Semester (Term, Year)	Winter, 2023
Course Code	AER 814
Course Section	01
Course Title	Aircraft Design Project
Course Instructor	Dr. Joon Chung and Dr Zouheir Fawaz
Submission	Final Report
Submission No.	01
Submission Due Date	06/04/2023
Title	Final Report
Submission Date	06/04/2023

Submission by (Name):	Student ID (XXXX1234)	Signature
Keiny Mitchel Mugisha	XXXXX9409	K.M.M.
Mathew Manbodh	XXXXX7607	M.M.
Kaivalya Desai	XXXXX2488	K.D.
Kajethan Thalayasingam	XXXXX7069	K.T.
Shadab Sayeed	XXXXX3882	S.S.
Kaustubh Purohit	XXXXX3013	K.P.
Christian Bernardo	XXXXX4478	C.B.
Christina Al Mardini	XXXXX1990	C.A.M.
Jeffery Omorodion	XXXXX3166	J.O.
Aman Gilani	XXXXX9895	A.G.

Executive Summary

This report contains the details of Team Alpha's AER814 aircraft design project for the Winter 2023 semester. This year's capstone project involved designing a clean sheet, purpose-built, fixed-wing aircraft concept to transport Global 7500 major assemblies quickly and reliably for Bombardier Aerospace. Team Alpha was required to transport the cockpit and rear fuselage of the Global 7500 from its satellite manufacturing facility in Mirabel, Quebec to the final assembly line at Downsview, Toronto. The proposed aircraft that was designed for this mission consists of a high-mounted fixed-wing configuration with turboprop engines mounted underneath, a conventional tail, fuselage mounted landing gear, and rear loading cargo doors. The focal point of the concept entails a transitional fuselage to accommodate the payload for optimal weight and sizing of the aircraft. The optimization of the weight and sizing contributed to greater fuel efficiency, lower operating costs, and the sustainability efforts of the aircraft, while maintaining its structural integrity and performance. The designed aircraft concept conforms to all FAR part 25 regulations and meets all mission requirements and objectives.

The design procedure commenced with analyzing the mission parameters and constraints, developing requirements and objectives, and researching competitive aircrafts to develop a conceptual design. After creating three aircraft concepts with unique configurations, the final concept was chosen based on merits of the configuration in regard to the given mission. After the configuration selection, the initial sizing of the aircraft along with engine selection, airfoil selection, performance analysis, cost analysis, and the initial structures were completed for the first concept iterations. Through the progression of the project life cycle, the concept endured several design changes to meet and optimize the mission requirements. Upon arriving on a conclusive design that had been optimized for all mission requirements and objectives, the masterlines and structures were constructed using CAD and a FEA was performed on relevant components to validate the structural integrity of the design. The various software that was used to assist in the design's conception included CATIA, Solidworks, ANSYS, MATLAB, Excel, Fusion 360, XFOIL, XFLR5, and NASA's Atmospheric Calculator. Pertinent information regarding design procedures, decisions, and analyses are included in the main body of the report. All additional and

supporting information such as auxiliary schematics, tabulated data, and program codes, are included in the appendices at the end of the report.

Work Allocation

The following table outlines the main roles and responsibilities of each team member of Team Alpha with the most primary role on the left.

Table A: Work allocation

Team Member	Main Roles
Christina Al Mardini	Structures, CAD
Christian Bernardo	Interior, CAD
Kaivalya Desai	Aerodynamics, Structures
Aman Gilani	Weight & Balance, Structures, CAD
Mathew Manbodh	Chief Integrator, Interior
Keiny Mitchel Mugisha	Masterlines, Structures, CAD, Project Management
Jeffery Omorodion	Stability, Sizing, Performance, CAD
Kaustubh Purohit	Systems
Shadab Sayeed	Loads & Dynamics, Interior, Structures
Kajethan Thalayasingam	Sizing, Performance, Cost Analysis

Table of Contents

Table of Figures

List of Tables

1. Introduction

Team Alpha was tasked with designing a purpose-built fixed-wing aircraft that can transport Global 7500 major assemblies quickly and reliably from satellite manufacturing facilities to the final assembly line at Downsview. The design was to be optimized to ensure an efficient, cost-effective, and just-in-time approach to assembly line production, avoiding the build-up of costly inventory. The team's design will compete against the alternative design concepts for different missions of three other teams. The design should be efficient, low cost, and sustainable, meeting the appropriate certification requirements of the FAA's Federal Aviation Regulations. The design must consider payload handling, operational specifics, the latest technology and materials, and optimized sizing for economic and environmental concerns. Heavy emphasizes were placed on ergonomic loading and unloading, short turn-around times, and airframe life over 20 years, with a focus on ease of maintenance and repair. The use of sustainable and economically viable aircraft designs was greatly encouraged. Studies were conducted on the necessary aspects to fulfill the design task, including the distances between the facilities, airport requirements and limitations, payload capabilities and storage/transport concepts, operational specifics, and making effective use of the latest available technology and materials. The aircraft's operation shall be efficient and allow crew and ground personnel to achieve short loading and unloading times as well as ergonomic access to the payload. Environmental friendliness shall be one of the considerations for the design and operation of the aircraft.

The design procedure commenced with analyzing the mission parameters and constraints, developing requirements and objectives, and researching competitive aircrafts to develop a conceptual design. After creating three aircraft concepts with unique configurations, the final concept was chosen based on merits of the configuration in regard to the given mission. After the configuration selection, the initial sizing of the aircraft along with engine selection, airfoil selection, performance analysis, cost analysis, and the initial structures were completed for the first concept iterations. Through the progression of the project life cycle, the concept endured several design changes to meet and optimize the mission requirements. Upon arriving on a conclusive design that had been optimized for all mission requirements and objectives, the masterlines and

structures were constructed using CAD and a FEA was performed on relevant components to validate the structural integrity of the design. The following figure displays the timeline of the project life cycle in a completed Gantt chart.
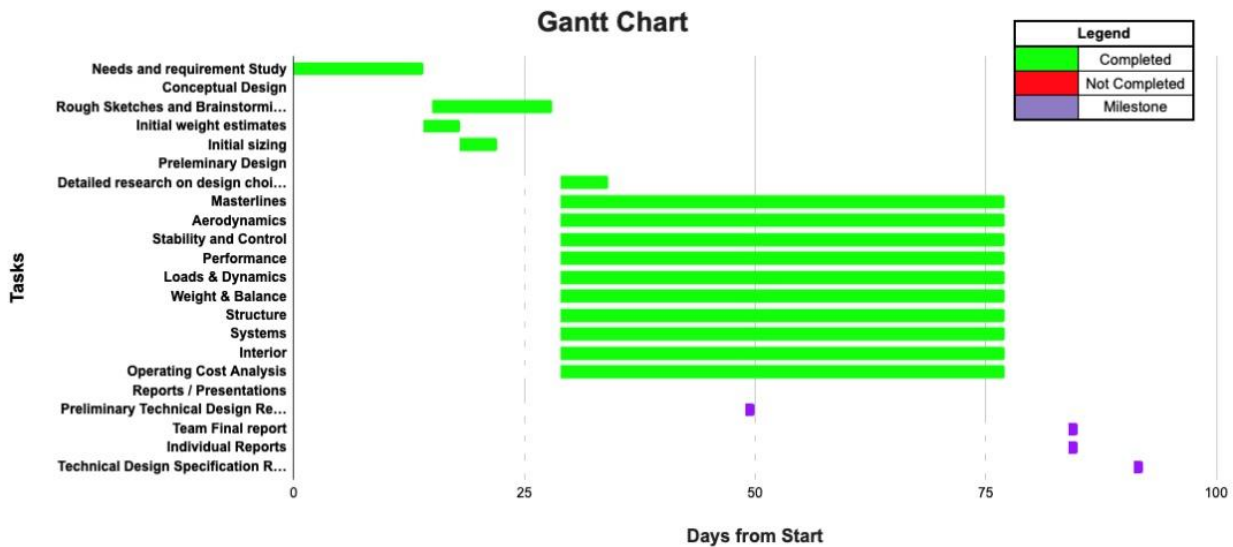
Figure 1: Project life cycle – Gantt chart

2. Requirements

After the formation of Team Alpha and the assignment of our mission statement, a comprehensive needs analysis was performed through research of the specific mission constraints and requirements. The following table outlines the requirement statements that the aircraft concept was designed around.

Table 1: Requirements definition and compliance

Statement	Actual	Compliance (Y/N)
The *Minimum Range* of the aircraft shall be *600 km.*	839 *nmi*	Y
The *Maximum Takeoff/Landing Distance* of the aircraft shall be less than *6000 ft.*	2310 *ft*	Y
The *Maximum Wingspan* of the aircraft shall be *213 ft*	113 *ft*	Y
The *Maximum Service Ceiling* of the aircraft shall be *25000 ft.*	24000 *ft*	Y
The *Minimum Cruise Altitude* of the aircraft shall be *16000 ft.*	21000 *ft*	Y
The Minimum Cruise Speed of the aircraft shall be *0.4 M.*	0.5 *M*	Y
The aircraft shall have a *Maximum Takeoff Weight* of *45000 lb.*	43497 *lb*	Y
The aircraft shall carry the *Bombardier Global 7500 Cockpit.*	Y	Y
The aircraft shall carry the *Bombardier Global 7500 Rear Fuselage.*	Y	Y
The aircraft shall have a *Maximum Load and Unload Time* of *1 hr.*	Y	Y
The aircraft shall have an *Operating Life* greater than *20 years.*	Y	Y
The aircraft shall have *lower Operation Costs* to similar aircrafts in its class.	$3402	Y
The aircraft shall have a *higher* **Fuel Efficiency** than similar aircrafts in its size class.	0.45 *lb/hp·hr* (per engine)	Y
The aircraft shall have **Powerplants** capable of utilizing at least *50% SAF blends*.	50%	Y

Team Alpha was able to successfully meet all requirements outlined through the needs analysis and project constraints. The compliance of the requirements and the values are displayed in the above table. The actual results and data are explained and verified throughout the body of the report.

3. Market Analysis

The competitor analysis was done to create a base foundation that we can work off of when designing our own aircraft. Looking into competitors sizing, weight, performance, and cost parameters will allow us to reference a margin that our values should attain to. The task at hand leaves us with a large payload size in comparison to weight. As a result, we needed to research smaller aircrafts and larger aircrafts, where the larger aircrafts can hold our payload size, but are significantly larger in terms of weight, and the smaller aircrafts cannot hold our payload size, but are similar in weight.

3.1. Configuration Analysis

For the conceptual design of the aircraft, the initial task was to conduct a round of research on current competitive options to base configuration and propulsion decisions. Current options considered for the analysis were freighters, military transporters, and specialize cargo aircrafts. For this comparison, the payload size was the main consideration since acquisition costs would be more cost effective. Boeing freight variants of the B777, B767, B747, C-17 Globemaster III and the Dreamlifter were disqualified due to lower height clearance to accommodate our specific payload. Expanding the search further, the Lockheed Martin C5 along with Airbus A350F, and Beluga ST and XL were considered. Upon detailed examination of the aircrafts, all but the Beluga XL were undersized for the designated payload. The Beluga XL has the cargo capacity and dimension to accommodate the payload. However, the range and payload capacity of the aircraft is over designed for the desired task. Looking at further options, the Antonov family of aircraft like the An-225 Mriya, An-74 and An-124 Ruslan or the Ilyushin IL-76, were also considered. Upon detailed review, these aircrafts look to be reliable options. However, due to the ongoing geopolitical events, all these options were ruled out. Several other medium transport aircraft were also considered based on range and payload weight like the An-26, Dash-8, and ATR -42 and -72. Despite these aircrafts performing well within our criteria, they did not cater to the size of the payload to be carried [1].
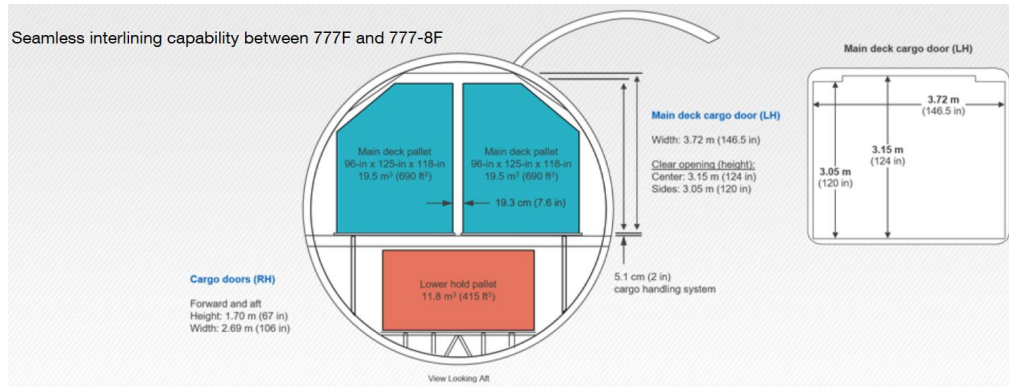
Figure 1: Cross section of the B777 cargo compartment
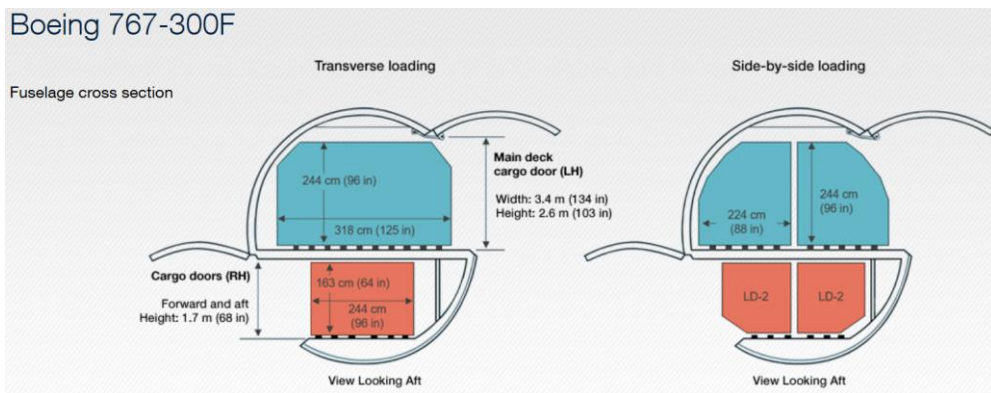
Figure 2: Cross-section of B767
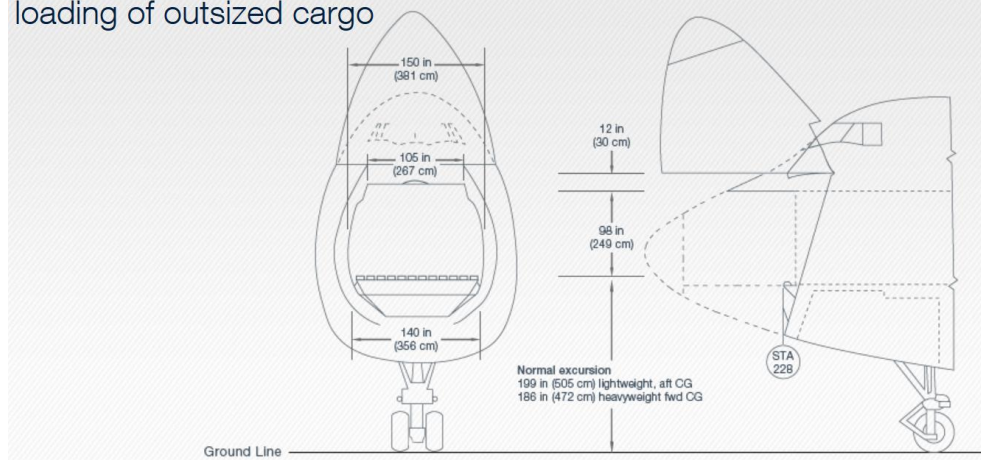
Figure 3: Cross-section of B747-8 freight cargo compartment
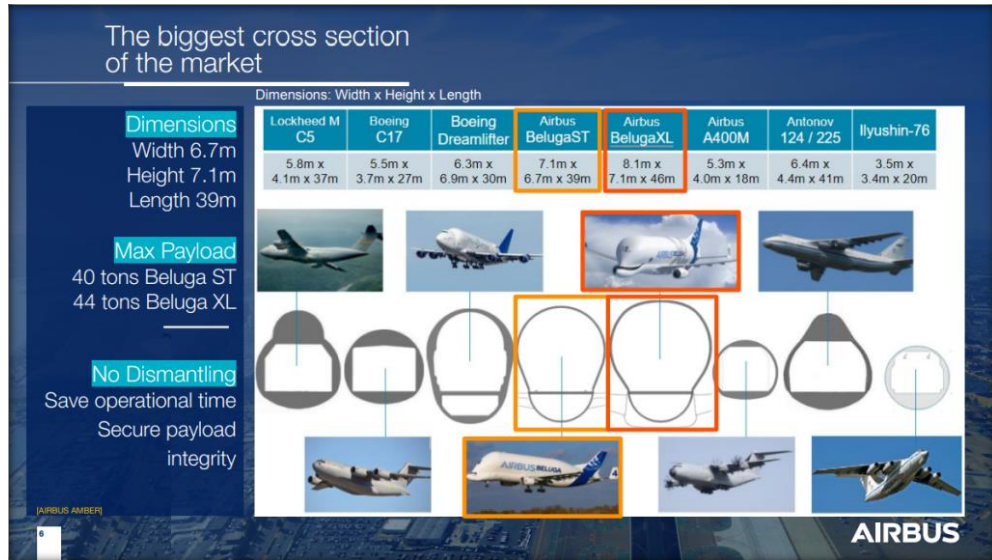
Figure 4: Cross-section of the cargo compartments of compared aircrafts

Based on the previous competitor research, only two viable alternatives were thought as replacement worthy. The first aircraft is the Airbus Beluga XL built by Airbus, which is a specialized cargo aircraft for their JIT approach for the A350 production line. The other option is the Dreamlifter from Boeing, which plays the same role as the Beluga for the 787 Dreamliner.

3.1.1 Airbus Beluga XL

The Airbus Beluga XL was launched in late 2014 as a "super transporter" for supporting the A350 production line. The BelugaXL is a larger version of the BelugaST and will be replacing the latter. Beluga's design is based on an A330 widebody aircraft with a large unpressurized nacelle to accommodate large loads. The dimensions of the loadable volume are 1842.5 x 318.9 x 295.3 *in*. This capacity is sufficient to accommodate our required loads. The payload capacity is 6929 stones, which is over designed for the payloads of the mission. This aircraft uses existing components significantly in its design like the Rolls Royce's Trent 772B engines for propulsion present on Airbus' A330. Additionally, the flight deck is integrated with the latest technologies from other programs to ensure tech lead and commonality benefits. These include, but are not limited to, fly-by-wire flight controls, LCD screens, Airport Traffic Situational Awareness (ATSA) system, and an RNP AR (Required Navigation Performance Authorization Required) to access airports with challenging surroundings. Currently, the integration of ROPS (Runway Overrun Prevention System) and automatic avoidance maneuvers with AP/FD TCAS

(Autopilot/flight Director Traffic Collision Avoidance System) facilitates improved performance. Despite the over designed cargo capacity and range of the aircraft, it comes with an existing operator, developed supply chain, training procedures, loading, and unloading procedure, and type certification from EASA airworthiness authority [2].

3.1.2 Boeing Dreamlifter

The Dreamlifter is a modified version of Boeing's 747-400 with a bulging airframe to accommodate large cargo. Rather than manufacturing new aircrafts, Boeing chose to convert existing 747s from Air China originally built in 1992. Additionally, any new aircraft that are acquired must be second-hand since the 747 production is shut down. Modifications to the rear fuselage were made to create a swinging tail to access the entire cross-sectional area of cargo bay. This modification required the removal of the APU since it is undesirable to run the required cabling through the doors. A proprietary 21-bolt locking system is also utilized for securing the doors during varying flight conditions. The removal of the APU means that the aircraft requires external supply for engine start. A specialized loader is designed for the aircraft known as the DBL from the TLD in Quebec. The wings were also modified by removing the wingtip devices to address concerns of flutter from testing, while the vertical tail was increased by 10 ft to provided additional stability. This aircraft also has a longer range at 7,800 km. A secondary cargo deck is also included and capable of carrying smaller pallets. However, the airframe size must be increased to accommodate our payload, which may come with a significant reduction in range [3].

3.1.3 Lockheed C130-Hercules

The Lockheed C130 Hercules is a transport aircraft used to carry versatile payload sizing with its large hold dimensions. It has several different applications, exceling in military and humanitarian purposes. In terms of configuration, the C130 contains 4 turboprop engines, a conventional tail, and a high wing mount. The high wing mount allows for more clearance, and bigger control surfaces for shorter runway landing and takeoff, which is an entity for its different purposes.

This aircraft was specifically chosen for analysis due to its higher margin in load capacity and sizing. However, although the payload size matches our needs, the weight of the payload and

aircraft are significantly larger. The configuration is slight favorable to our possible design, with turboprops and a high wing mount, but the considerably larger payload and aircraft weight are undesired characteristics [4].

3.1.4 ATR 72

The ATR 72 is a twin-engine turboprop, short-haul regional airliner. The purpose of this aircraft's design was to fill the niche of a relatively compact aircraft that had a large seat capacity in comparison to similarly sized aircraft. Specifically, the ATR 72 had a passenger capacity of 78 seats with additional space for cargo. This specific design was studied closely as many aspects of its configuration were favorable for the mission profile set by the project. The ATR 72's twin-engine turboprop configuration makes it an ideal hauler for short domestic flights. It's 'T-tail' design for the tail structures make it ideal for high wing engine configurations as the tail is not in the path of the engine wake. The ATR 72 was also analogous to the specific takeoff weight estimated for takeoff required for the Hauler-X design.   However certain aspects of this design were also unfavorable for the mission profile. When used specifically as a cargo aircraft the ATR 72 has slide loading bay doors located just behind the cockpit bulkhead. This style of door is not conducive to effective loading of large cargo. The aircraft itself is also not sufficiently large enough to hold the required load. Thus, the overall configuration of the engine layout and tail structures were used to inspire aspects of the Hauler-X design. While the unfavorable characteristics were used to inform how to improve the Hauler-X over the ATR 72 [5].

3.1.5 Q400 Dash 8

The Q400 Dash 8 is a twin-engine turboprop aircraft similar to the ATR 72. This aircraft has the same 'T-tail' configuration as well as high wing mounted engines; However, the aspect of this design deemed favorable was the way it mitigates noise. The Q400 Dash 8 is one of the quietest turboprop aircrafts in existence. This design characteristic very beneficial for domestic flights that may be in the path of multiple population dense areas. The unfavorable aspects to this design are also similar to the ATR 72. The aircraft itself is too small for the given payload outlined in the project. These data points were considered and incorporated during the design phase of the Hauler-X [6].

3.1.6 <u>An-26</u>

The An-26 was designed to be a Military tactical transport aircraft. The general design of this aircraft is much like the other aircraft in its size, it is a twin-engine turboprop aircraft with a conventional tail design. Due to its nature as a military aircraft the An-26 was designed to maximize its usable cargo space given its size, as well as emphasizing speed and effectiveness of loading. Because of this the An-26 does not have a dedicated space for passengers in its fuselage, instead the fuselage is only dedicated to cargo. The An-26 rear loading cargo bay configuration also helps in its ability to load cargo quicky. The aspects of this design that were favorable for the mission profile set out in the project were its rear loading door configuration as well as its general design for its cargo bay. The aspects that were not optimal for the mission profile were its conventional tail. For the Hauler-X it was deemed that the 'T-tail" configuration was the most optimal for peak performance [7].

3.2 Sizing Specification Comparison

Table 2: Competitor analysis of sizing specifications for larger aircrafts

Section	Specifications	Airbus Beluga XL	Boeing Dreamlifter	C130-Hercules
Fuselage	Length (in)	248	2822	1154
	Diameter (in)	346	330	120
Wing	Area (in^2)	560,481	838,862	195,610
	Wingspan (in)	2374	2537	1591
	Wing Loading (lb/in^2)	0.89	0.95	0.61
Cargo Hold	Length (in)	1842	2220	480
	Width (in)	318	236	123
	Height (in)	295	274	108

This table specifies the sizing dimensions for our larger aircraft competitors. Clearly, the larger aircrafts can easily hold our payload size. The wing loading however is considerably larger than

our values would need to be around, since these aircrafts are much heavier. Thus, our fuselage and wing characteristics will need to be smaller than the larger aircrafts.

Table 3: Competitor analysis of sizing specifications for smaller aircrafts

Aircraft	Sizing Specifications	ATR 72	Q400 Dash 8	An-26
Fuselage	Length (*in*)	832	1293	937
	Diameter (*in*)	100	106	91
Wing	Area (in^2)	94,550	99,216	116,219
	Wingspan (*in*)	1062	1119	1149
	Wing Loading $\left(\dfrac{lb}{in^2}\right)$	0.54	0.37	0.45
Cargo Hold	Length (*in*)	706	740	437
	Width (*in*)	89	99	86
	Height (*in*)	69	77	62

The table above shows sizing specifications for smaller competitor aircrafts. The smaller aircrafts cargo holds dimensions show that they cannot carry our payload size. This would entail that our fuselage and wing characteristics will be higher than these aircrafts.

3.3 **Performance Specification Comparison**

Table 4: Competitor analysis of performance specifications for all aircrafts

Performance Specifications	Cruise Speed(*kts*)	Cruise Altitude (*ft*)	Range (*nmi*)	Climb Rate (*ft/min*)
Airbus Beluga XL	398	35,000	2300	1200
Boeing Dreamlifter	474	43,100	4,212	1500
C130-Hercules	292	28,000	2052	2100

ATR 72	283	19685	740	1500
Q400 Dash 8	269	22,000	1101	2220
An-26	238	22000	1377	1575

The table above highlights the performances between the aircrafts chosen for comparison to the Hauler-X proposed design. Some notable takeaways from this table are that the larger aircrafts have higher cruising altitudes while the while the smaller aircrafts have greater rates of climb. The cruise speeds for the smaller aircraft are also slower than the larger ones. For the Hauler-X design the aircraft must be able to hold cargo equivalent to the larger aircraft listed above while making regional trips like the smaller aircraft. Thus, the performance values should land between the average values of the larger aircraft and the smaller ones.

3.4 <u>Weight Specification Comparison</u>

Table 5: Competitor analysis of weight specifications for all aircrafts

Aircrafts	Operating Empty Weight (OWE) (*lbs*)	Maximum Takeoff Weight (MTOW) (*lbs*)	Fuel Weight (*lbs*)	Payload Weight (*lbs*)
Airbus Beluga XL	342,845	504,444	161,599	112,436
Boeing Dreamlifter	398,000	803,001	199,150	330,690
C130-Hercules	75,562	155,000	57,000	42,000
ATR 72	20,281	39,683	11,023	16,313
Q400 Dash 8	23,111	34,500	6,952	19,290
AN-26	33,113	52,911	10,540	12,000

The table above highlights the weights of our competitors. There is a noticeable difference in the middle between the larger aircrafts and smaller aircrafts which is expected. This also shows the large margin that we must focus on, since our payload size needs to be compared to the larger aircrafts, but the weights shows that they are significantly heavier. For example, the Beluga XL can hold our payload size but the maximum payload weight is 112,436 which our aircraft will not

come close to. On the other hand, the Q400 Dash 8 cannot hold our payload size, but is within the acceptable range for our payload weight.

4. Conceptual Design

This stage of the design process dictates the overall shape and size of the aircraft. The conceptual design aims to fulfill all the design requirements and objectives derived from our customer needs and constraints.

As the payload assigned to Team Alpha was volumetrically larger compared to its weight, unconventional design was deemed viable solutions. To select a configuration, three conceptual configurations were developed to meet customer needs and requirements defined in the Introduction section. These designs maintained shorter unloading/loading procedures as the primary focus to accommodate the transport of a very large rear fuselage. The following figures contain the three conceptual designs and their various ideas used to consolidate a final conceptual design.
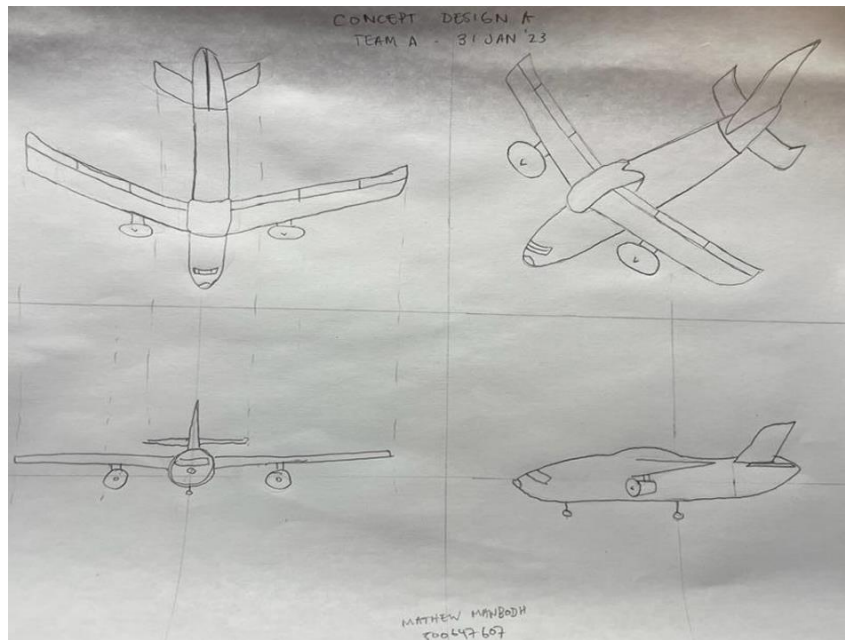
Figure 5: 3-view drawing of configuration 1
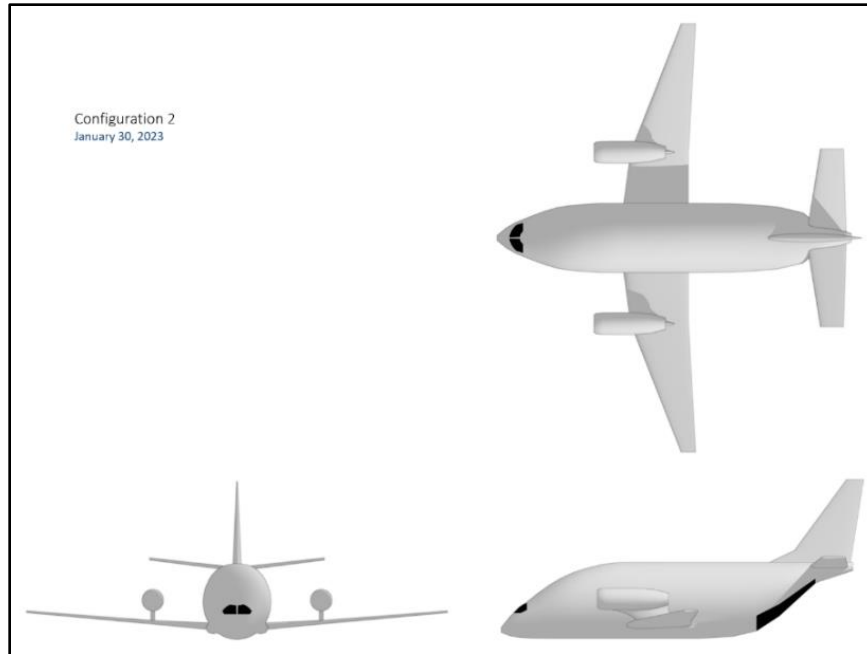
Figure 6: 3-views renders of configuration 2
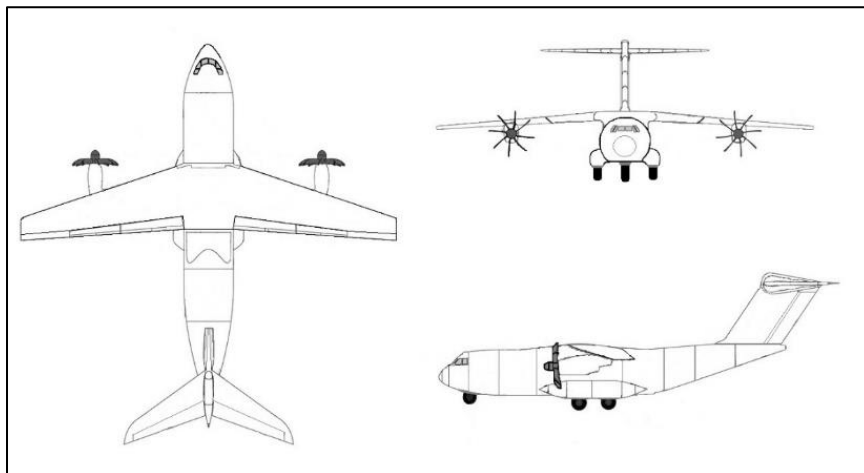
Figure 7: 3-views drawing of configuration 3

Each conceptual design explored different configurations for major aircraft components. To settle on a final configuration, a pros and cons list was developed for each design. Table 6 through Table 8 provide a list of the benefits and drawbacks of each configuration.

Table 6: Pros and cons of configuration 1

Feature	Pros	Cons
High mounted wing	- Provides significant lateral stability. - Provides ground clearance for maneuvering cargo. - Provides ground clearance to lower fuselage for un/loading procedures.	- The wing is not easily accessible by the maintenance crew. - High-wing aircraft are more likely to experience a strong buffeting effect near stall, discouraging the pilot from slowing down further. - Because of the effect of "downwash," wing-tail interference may reduce the effectiveness of the elevator.
Rear loading	- Structure does not experience additional loading due to its simplified design during flight. - A larger cargo can be loaded into the aircraft since the cargo capacity is maximized. - A higher efficiency in ground operation is achieved since the loading and unloading time is minimized.	- The entire cross-section of the fuselage is available. - Ground clearance under the tail is limited.
Conventional Tail	- High aerodynamic efficiency - Cost effective manufacturing	- Horizontal tail must be strengthened to carry the weight of the vertical stabilizer. - Needs more maintenance
Turboprop	- Highest fuel efficiency for the required range of the aircraft.	- Flies slower than other options, however, due to range constraint, the time difference is negligible.
Under-Wing Engine	- Ease of accessibility for maintenance and repairs. - Simpler fueling operations.	- Additional weight wing structure. - Extra measures need to be taken for additional ground clearance.
Fuselage Mounted Landing Gears	- Simplified landing gear structure. - Can be used to lower the fuselage for ease of loading/unloading.	- Decreased lateral balance on the ground. - Nacelles are required to stow the wheels after take-off.

Table 7: Pros and cons of configuration 2

Feature	Pros	Cons
Low Mounted Wing	- Easily accessible by ground crew- improved ground clearance. - Wider landing gear stands for improved stability during landing.	- Prevents lowering aircraft closer to ground for un/loading.
Rear Loading	- Larger cargo items can be loaded & unloaded. - Cargo can be loaded & unloaded quickly & efficiently.	- Damage to tail in explosive decompression due to door failure. - Upward slope of the aft fuselage creates low pressure zone. - Door mechanisms may facilitate a tail-heavy condition.
Conventional Tail	- Avoids shadowing of the horizontal stabilizer in stall conditions.	- May be impacted by wing downwash.
Turbofan	- Smooth & vibration-free operation - Suppressed noise levels due to a contained fan.	- High fuel consumption at low airspeeds and altitudes - Emits environmentally harmful contaminants.
Over-wing Engine Mounting	- Clear engine from ground debris	- Harder to access for maintenance. - Debris may impact the fuselage in an uncontained failure. - Engine exhaust may affect the flow over the horizontal stabilizer.
Wing Mounted Landing Gear	- Wider landing gear stance for stability on ground - Increased fuselage space for cargo	- Restricts wing fuel tank size

Table 8: Pros and cons of configuration 3

Feature	Pros	Cons
T-shape Tail	- Avoids the downwash from the wings. - Provides uninterrupted flow over the elevators, thus providing a good stall recovery attitude.	- Strengthened vertical stabilizer to carry the weight of the horizontal stabilizer.

Table 8 only contains the T-Tail as the configuration is very similar to configuration 1 with the only differences in the tail shape.

Based on the proposed aircraft configurations and their advantages, the third design configuration was selected as the final configuration for further development. The high wing configuration

allows the aircraft to be closer to the ground which improves loading and unloading. The T-tail configuration allows the tail to clear downwash from the wing.

5. Sizing

The sizing process is one of the most important stages in the design of an aircraft as it lays out the foundation for further analysis. This section will explore the various methodologies used to set initial dimensions for the fuselage, wing, tail, landing gear, and control surfaces, as well as the finalized sizing parameters. The initial sizing of our aircraft overlaps with the preliminary weight estimations made prior, as well as references made to Raymer's textbook and competitor aircraft. Through a series of adaptive iterations, optimizing performance, while meeting required constraints, we achieved parameters for our final sizing.

5.1. Initial Fuselage Geometry

The first step for initial sizing was to determine the fuselage dimensions. This was done following an equation from the Raymer textbook. Specifically for an initial estimate of the fuselage length, Raymer utilized the maximum takeoff weight with ratios, where a = 0.37 and c = 0.51 for twin turboprop aircrafts. For this case, the maximum takeoff weight is the one initially estimated as part of the Weights and Balance section.

$$\text{Fuselage Length} = a\text{MTOW}^c \tag{5.1}$$

Length = aW_0^C (ft or {m})	a	C
Sailplane—unpowered	0.86 {0.383}	0.48
Sailplane—powered	0.71 {0.316}	0.48
Homebuilt—metal/wood	3.68 {1.35}	0.23
Homebuilt—composite	3.50 {1.28}	0.23
General aviation—single engine	4.37 {1.6}	0.23
General aviation—twin engine	0.86 {0.366}	0.42
Agricultural aircraft	4.04 {1.48}	0.23
Twin turboprop	0.37 {0.169}	0.51
Flying boat	1.05 {0.439}	0.40
Jet trainer	0.79 {0.333}	0.41
Jet fighter	0.93 {0.389}	0.39
Military cargo/bomber	0.23 {0.104}	0.50
Jet transport	0.67 {0.287}	0.43

Figure 8: Fuselage ratios [8]

The initial maximum takeoff weight was determined as 39,762.74 *lbs* previously in terms of weight fractions and competitor analysis. Simply plugging this into the formula above with the assigned ratios, gave us an initial fuselage length of 984 *in*. The fuselage diameter was set as 298 *in*, which is an estimation based on payload dimensions as well as an additional 36 *in* of freeway space on each side of the payload. Moreover, the cargo floor height was established as 36 *in* as well.

5.2. **Initial Wing Geometry**

For the initial wing geometry, several different parameters were determined. This includes the wing loading, reference wing area, aspect ratio, wingspan, root, tip, and mean chords, as well as the wing taper ratio.

Initially, the wing loading, aspect ratio, taper ratio, and wing sweep are estimates for twin turboprop aircraft taken from Raymer's textbook. Hence, a wing loading of 40 lb/ft^2 an equivalent aspect ratio of 9.2, a taper ratio of 0.45, and a wing sweep angle of 4 degrees were assigned. These values with their respective table references are shown below.

Typical Takeoff W/S		
Historical Trends	**lb/ft^2**	**{kg/m^2}**
Sailplane	6	{30}
Homebuilt	11	{54}
General aviation—single engine	17	{83}
General aviation—twin engine	26	{127}
Twin turboprop	40	{195}
Jet trainer	50	{244}
Jet fighter	70	{342}
Jet transport/bomber	120	{586}

Figure 9: Wing loadings [8]

Propeller Aircraft	Equivalent Aspect Ratio
Homebuilt	6.0
General aviation—single engine	7.6
General aviation—twin engine	7.8
Agricultural aircraft	7.5
Twin turboprop	9.2
Flying boat	8.0

Figure 10: Equivalent aspect ratios [8]

Using this reference wing loading and our initial maximum takeoff weight of 39,762.74 *lbs*, the reference wing area was determined using the following equation.

$$\text{Reference Wing Area} = \frac{\text{MTOW}}{\frac{\text{W}}{\text{S}}} \qquad (5.2)$$

The wingspan was then found with respect to the reference wing area and estimated aspect ratio.

$$Wingspan = \sqrt{(Wing\ Area)(Aspect\ Ratio)} \qquad (5.3)$$

The root, tip, and aerodynamic mean chords are simply a function of the taper ratio, wing area, and wingspan.

$$Root\ Chord = \frac{2(Wing\ Area)}{Wing\ Span(1 + \lambda)} \qquad (5.4)$$

$$Tip\ Chord = \lambda(Root\ Chord) \qquad (5.5)$$

$$Mean\ Chord = \frac{2}{3}(Root\ Chord)\frac{(1 + \lambda + \lambda^2)}{(1 + \lambda)} \qquad (5.6)$$

Table 9 shows the initial wing geometry. The values highlighted yellow are estimations for a typical twin turboprop, and are used to size the wing area, wingspan, and chords. These determined values for the wing were all initial estimates based on Raymer's approach for twin turboprop aircrafts. They were continuously iterated upon to meet our aircraft needs and performance in further stages of the design.

Table 9: Initial wing sizing characteristics

Initial Wing Geometry	Determined Values
Wing Loading ($\frac{lb}{ft^2}$)	40
Aspect Ratio	9.2
Taper Ratio	0.45
Wing Sweep Angle	4°
Reference Wing Area (in^2)	143,147
Wingspan (in)	1148
Root Chord (in)	172
Tip Chord (in)	78
Mean Aerodynamic Chord (in)	131

5.3. Initial Tail Geometry

The vertical tail and horizontal tail were sized using moments arm lengths and tail coefficients. Additionally, the mean chord was applied to determine the surface areas of the vertical and horizontal tails. The moment arm length is taken as a percentage of the estimated initial fuselage length earlier. Since the engines are applied at the wing, the moment arm length was taken as 52.5% of the estimated fuselage length. In terms of the tail, since we are using a T-tail configuration, the vertical tail coefficient can be reduced by 5% based on the end plate effect. The horizontal tail coefficient can also be reduced by 5% due to clean air effect. The tail coefficient values are shown in the table below, and the values were taken for a twin turboprop [8].

	Typical Values	
	Horizontal c_{HT}	Vertical c_{VT}
Sailplane	0.50	0.02
Homebuilt	0.50	0.04
General aviation—single engine	0.70	0.04
General aviation—twin engine	0.80	0.07
Agricultural	0.50	0.04
Twin turboprop	0.90	0.08
Flying boat	0.70	0.06
Jet trainer	0.70	0.06
Jet fighter	0.40	0.07–0.12*
Military cargo/bomber	1.00	0.08
Jet transport	1.00	0.09

Figure 11: Tail coefficients [8]

The surface areas for both tails are then found using the wing area, wingspan, wing mean chord, moment arm lengths, and coefficients.

$$SVT = \frac{C_{VT}(Wing\ Area)(Wing\ Span)}{(vertical\ moment\ arm\ length)} \tag{5.7}$$

$$SHT = \frac{C_{HT}(Wing\ Area)(Wing\ Mean\ Chord)}{(horizontal\ moment\ arm\ length)} \tag{5.8}$$

The tail aspect and taper ratios were set based on a combination of suggestions made from the Raymer textbook as well as analysis of similar competitors with a T-tail configuration. Using the estimated aspect and taper ratios of the tail, the root, tip, and mean chords, as well as the spans for the tails were determined.

	Horizontal Tail		Vertical Tail	
	A	λ	A	λ
Fighter	3–4	0.2–0.4	0.6–1.4	0.2–0.4
Sailplane	6–10	0.3–0.5	1.5–2.0	0.4–0.6
Others	3–5	0.3–0.6	1.3–2.0	0.3–0.6
T-tail	–	–	0.7–1.2	0.6–1.0

Figure 12: Tail ratios [8]

Table 10: Initial tail sizing characteristics

Initial Tail Geometry	Determined Values
Vertical Tail Surface Area (in^2)	25,432
Horizontal Tail Surface Area (in^2)	32,591
Vertical Tail Aspect Ratio	2.0
Horizontal Tail Aspect Ratio	4.0
Vertical Tail Taper Ratio	0.6
Horizontal Tail Taper Ratio	0.4
Vertical Tail Root Chord (in)	126
Horizontal Tail Root Chord (in)	108
Vertical Tail Tip Chord (in)	76
Horizontal Tail Tip Chord (in)	43
Vertical Tail Height (in)	252
Horizontal Tail Span (in)	432

5.4. Initial Landing Gear Geometry

The landing gear was sized using Dr. Fawaz's AER 621: Structural Design notes. The landing gear is a crucial aspect of the sizing, as it sets the limitations to the tire selections for load applications during landing and takeoff, as well as ground clearance which can affect the tail strike angle.

To begin, specific values are assigned for the stroke and tire deflection efficiencies, tire deflection, reaction factor, and the number of main struts based on competitor analysis and historical data. Using these variables, the strut inner diameter, strut length, tire diameter, and tire width were calculated. Based on a vertical velocity (sink speed) of 10 ft/s according to FAR regulations and the previously estimated variables the stroke length is found.

$$Stroke\ Length = \frac{V_v^2}{2g\eta\lambda} - \frac{\eta_t}{\eta}S_t \qquad (5.9)$$

The stroke length is then used to calculate the strut length for the nose and landing gear.

$$Strut\ Length = 2.5(Stroke\ Length) \qquad (5.10)$$

The strut inner strut diameter is found using the load per strut, which is the landing weight over the number of struts.

$$Strut\ Inner\ Diameter = 0.0041 + 0.0025\sqrt{\frac{MTOW}{\#\ of\ Struts}} \qquad (5.11)$$

The tire diameter and tire width are functions of the maximum takeoff weight, and the load is accordingly dissipated, with the main landing gear taking 90% of the load, and the nose landing gear taking 10% of the load.

$$Tire\ Diameter = A(MTOW)^B \qquad (5.12)$$

The values for A and B were taken as 1.63 in and 0.315 in, for a transport aircraft, shown in the figure below.

Main wheel diameter or width $= AW_w^B$ (W_w =weight on wheel)

W_w in Kg	Diameter (cm)		Width (cm)	
	A	B	A	B
General Aviation	5.1	0.349	2.3	0.312
Business twin	8.3	0.251	3.5	0.216
Transport/bomber	5.3	0.315	0.39	0.480
Jet fighter/trainer	5.1	0.302	0.36	0.467
W_w in lbs	Diameter (in.)		Width (in.)	
General Aviation	1.51	0.349	0.7150	0.312
Business twin	2.69	0.251	1.1700	0.216
Transport/bomber	1.63	0.315	0.1043	0.480
Jet fighter/trainer	1.59	0.302	0.0980	0.467

Figure 13: Coefficients for landing gear sizing [9]

Table 11: Initial main landing gear dimensions

Variable	Initial Main Landing Gear Geometry
Strut Inner Diameter (in)	4.3
Strut Length (in)	10.7
Tire Diameter (in)	45.8
Tire Width (in)	16.8

Table 12: Initial nose landing gear dimensions

Variable	Initial Nose Landing Gear Geometry
Strut Inner Diameter (in)	4.3
Strut Length (in)	10.7
Tire Diameter (in)	34.8
Tire Width (in)	20.8

After completing the landing gear sizing, the tire size and type needed to be chosen. This was analyzed by comparing the computed tire diameters and widths with the table values shown below.

Size	Speed mph	Max load, lb	Press psi	Max width, in	Max diam, in	Rolling radius	Wheel diam	Number of plies
				Type III				
5.00-4	120	1,200	55	5.05	13.25	5.2	4.0	6
5.00-4	120	2,200	95	5.05	13.25	5.2	4.0	12
7.00-8	120	2,400	46	7.30	20.85	8.3	8.0	6
8.50-10	120	3,250	41	9.05	26.30	10.4	10.0	6
8.50-10	120	4,400	55	8.70	25.65	10.2	10.0	8
9.50-16	160	9,250	90	9.70	33.35	13.9	16.0	10
12.50-16	160	12,800	75	12.75	38.45	15.6	16.0	12
20.00-20	174kt	46,500	125	20.10	56.00	22.1	20.0	26
				Type VII				
16 × 4.4	210	1,100	55	4.45	16.00	6.9	8.0	4
18 × 4.4	174kt	2,100	100	4.45	17.90	7.9	10.0	6
18 × 4.4	217kt	4,350	225	4.45	17.90	7.9	10.0	12
24 × 5.5	174kt	11,500	355	5.75	24.15	10.6	14.0	16
30 × 7.7	230	16,500	270	7.85	29.40	12.7	16.0	18
36 × 11	217kt	26,000	235	11.50	35.10	14.7	16.0	24
40 × 14	174kt	33,500	200	14.00	39.80	16.5	16.0	28
46 × 16	225	48,000	245	16.00	45.25	19.0	20.0	32
50 × 18	225	41,770	155	17.50	49.50	20.4	20.0	26
				Three-Part Name				
18 × 4.25-10	210	2,300	100	4.70	18.25	7.9	10.0	6
21 × 7.25-10	210	5,150	135	7.20	21.25	9.0	10.0	10
28 × 9.00-12	156kt	16,650	235	8.85	27.60	11.6	12.0	22
37 × 14.0-14	225	25,000	160	14.0	37.0	15.1	14.0	24
47 × 18-18	195kt	43,700	175	17.9	46.9	19.2	18.0	30
52 × 20.5-23	235	63,700	195	20.5	52.0	21.3	23.0	30

Figure 14: Tire characteristics

Based on the chart above, the tire size chosen for the main landing gear and nose landing gear are 36 x 11 Type VII and 7.00-8 Type III, respectively. This size withstands the max applied load per tire, while also fitting into the dimensional constraints.

5.5. <u>Initial Control Surface Geometry</u>

To produce initial dimensions for the control surfaces, the location of the rear and the required space for actuators and mechanisms was considered. Considering the rear spar spanning along the 70% chord line of the wing, the control hinge for the control surfaces situated on the wing was place along the 75% chord location. This allowed for space between the spar and the control hinge to house the necessary actuators. Historical trends were then applied to estimate the spanwise size of these control surfaces. The same process was initiated to compute the desired sizes for the other control surfaces not situated on the wing. These surfaces were placed in such a way that allowed the control hinge to reside along the 75% chord line of their relevant stabilizers, with full span (or height) being employed – a common occurrence in present-day aircraft.
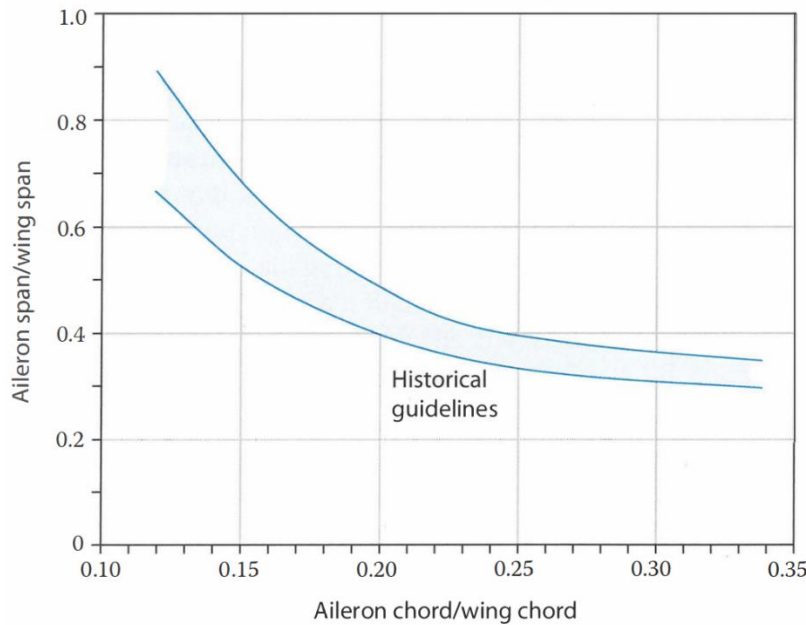
Figure 15: Control surface chord ratios

Table 13: Initial control surface dimensions

Initial Control Surface Geometry	Span (in)	Chord (in)	Area (in²)
Aileron	114	13	78
Rudder	228	26	197
Elevator	343	32	315

5.6. Initial Sizing Problems
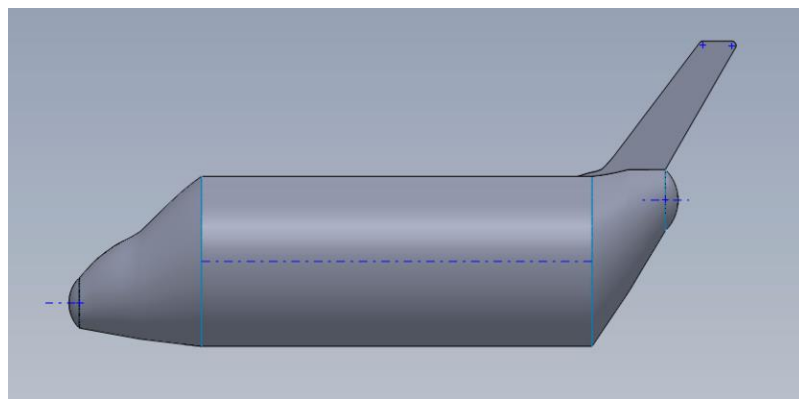
Figure 16: Initial sizing I
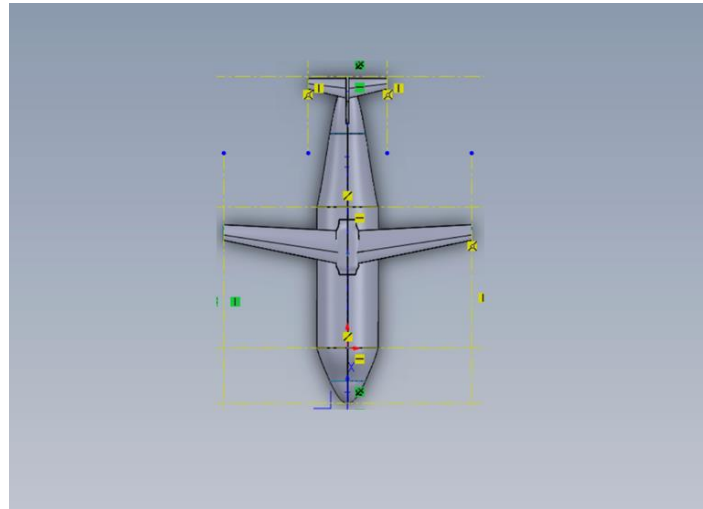
Figure 17: Initial sizing II

The figures above show the first two iterations of our aircraft with its initial sizing. After completing the initial sizing with the dimensions shown in the sections above, it was noted that the wing and tail were not proportionate with the fuselage diameter required to carry the payload. This was mainly due to the initial estimates favouring weight, rather than the physical volume required to carry the load. The payload and structure are relatively light, resembling the weight characteristics of the ATR 72. However, the actual size of the payload required a fuselage that is significantly larger than aircraft of comparable mass. This resulted in the fuselage appearing significantly larger compared to the rest of the components – which themselves appear more appropriately sized for a regional turboprop aircraft, rather than a large-component transport aircraft. As a result, putting this into consideration and operating under the advice that the fuselage cross-section should be optimized to fit the geometry of the payload, an elliptical fuselage shape was proposed to better house the height of the tail being carried in the aircraft. This design choice was carried into the final design of the aircraft, which features a circular section where the cockpit payload sits, and an elliptical section where the rear-fuselage payload sits. The two cross sections gradually converge, optimizing the space for the payload.

5.7. <u>Final Sizing</u>

The final sizing was achieved through numerous different iterations, ultimately leading to the aircraft size that was optimal, while maintaining excellent performance. The gradual changes eventually led to our final sized aircraft, with the parameters shown in the tables below.

Table 14: Final fuselage dimensions

Fuselage Geometry	Final Sized Values
Length (in)	1260
Diameter (in)	168
Cargo Floor Height (in)	34.8

Our fuselage length increased from 984 in to 11260 in, our diameter decreased from 298 in to 168 in, and our cargo floor height decrease from 36 in to 34.8 in. This was a result of minimizing the fuselage as much as possible while also comfortably fitting the payload. This fuselage length was increased for loading purposes as well as making space for actuators and mechanisms for the rear door.

Table 15: Final wing dimensions

Wing Geometry	Final Sized Values
Wing Loading (lb/ft^2)	34.115
Wing Area (in^2)	183,600
Wingspan (in)	1356
Aspect Ratio	9.552
Sweep Angle	9.5°
Root Chord (in)	187
Tip Chord (in)	84
Mean Chord (in)	142
Taper Ratio	0.45

The wing characteristics had major changes to the wing loading which was reduced from 40 lb/ft^2 to 34.115 lb/ft^2, the wing area which increased from 143,146 in^2 to 183,600 in^2, and the wingspan which was increased from 1148 in to 1356 in. The aspect ratio and chords slightly increased, while the taper ratio remained constant at 0.45. The change in wing geometry is proportional to the fuselage, while also accommodating our control surfaces and performance needs.

Table 16: Final tail dimensions

Tail Geometry	Final Sized Values
Vertical Tail Surface Area (in^2)	28,326
Horizontal Tail Surface Area (in^2)	30,989
Vertical Tail Aspect Ratio	1.200
Horizontal Tail Aspect Ratio	4.000
Vertical Tail Taper Ratio	0.686
Horizontal Tail Taper Ratio	0.533
Vertical Tail Root Chord (in)	168
Horizontal Tail Root Chord (in)	108
Vertical Tail Tip Chord (in)	116
Horizontal Tail Tip Chord (in)	58
Vertical Tail Height (in)	200
Horizontal Tail Span (in)	432

The tail had a significant change from initial sizing to the finalized sizing. The adjusted tail sizing is needed for optimal stability. The change in sizing also adds space for the control surfaces, in which our initial tail size was not big enough for.

Table 17: Final landing gear dimensions

Landing Gear Geometry	Final Sized Main Landing Gear Values	Final Sized Nose Landing Gear Values
Strut Inner Diameter (in)	4.5	4.5
Strut Length (in)	41.1	41.1
Tire Diameter (in)	33.5	20.8
Tire Width (in)	10.4	5.1

From the initial estimates for the landing gear, it was noted that our tire diameter was larger than required, and our strut length was significantly small. After adjusting these values, the final landing gear dimensions are more reasonable and comparable to competitors. The control surfaces dimensions were confirmed through XFLR.

Table 18: Final control surface dimensions

Final Control Surface Geometry	Span (in)	Mid Chord (in)
Aileron	169	26
Rudder	200	36
Flaps	338	38
Elevator	432	20

Table 19: Final fuel tank dimensions

Final Fuel Tank Geometry	Final Sized Values
Span (in)	72
Root Chord (in)	90
Tip Chord (in)	4
Height (in)	18

Total Tank Volume Per Wing (in³)	115430

Although not mentioned in our initial sizing, the fuel tank was sized accordingly to within the structures while holding our required fuel. Initially, the required fuel was underestimated, resulting in a much smaller fuel tank. After adjusting the fuel from 2500lbs to 5000lbs, we obtained these fuel tank dimensions.

Please refer to Appendix B for different views of our final aircraft sized.

6. Masterlines

This section covers the design process of the aircraft masterlines. The masterlines had many iterations as the aircraft's cross-section changed multiple times in the conceptual and preliminary design phases. This section is divided into 4 sections: the cockpit, fuselage, wing, and empennage.

6.1. Fuselage

The fuselage was the first section that was designed. As mentioned in the Initial Sizing section of this report, the initial fuselage was based on statistical formulas and payload size requirements. With the re-orientation of the payload and cargo bay sizing a smaller fuselage height characterized the following fuselage iteration. A defining feature was the change from a circular cross-section to an elliptical cross-section. Changing the cross-section reduced the mass of the aircraft by using less material and optimized the aircraft to fit the V-stab attached to the rear fuselage payload. Figure 18 shows the isometric and front view of the third fuselage iteration.
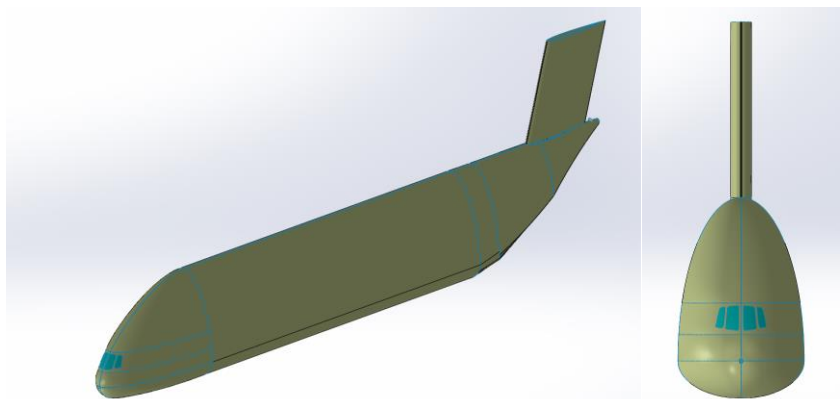
Figure 18: Elliptical fuselage cross-section (left: isometric view, right: front view)

The fuselage was designed to fit the load and provide adequate space for the crew to walk in the carbo bay and for the additional systems to be included. The major drawback of non-circular cross-sections is the need for additional structures to pressurize the aircraft. The cruise altitude was reduced to 21000 ft, and the cargo bay and rear fuselage were chosen to be unpressurized and only the cockpit was pressurized to reduce the fuselage size further and optimizing the cockpit section for pressurization.

The 4th and 5th (final) iterations changed the front section of the fuselage to be circular, starting from the cockpit to optimize for pressurization, and the rear section transitioned into an ellipse to allow the rear fuselage cockpit to fit. The comparison of these iterations to the 3rd iteration are shown in Figure 19 and Figure 20.
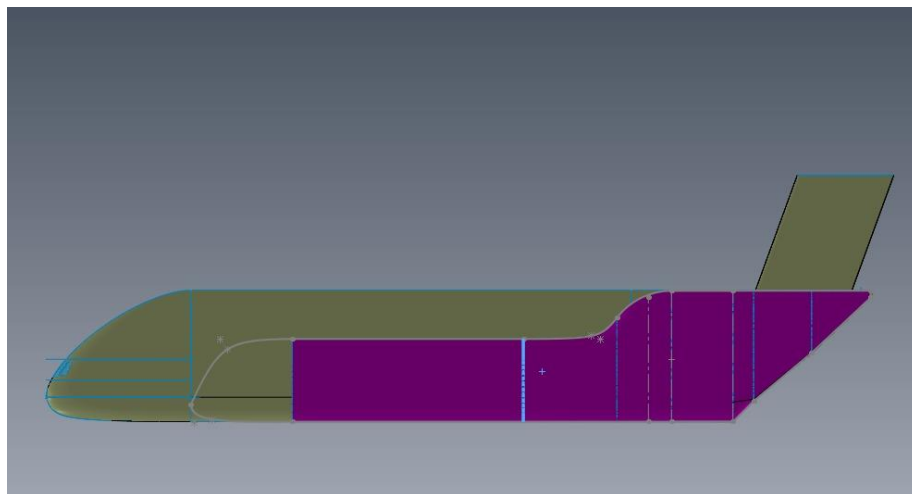
Figure 19: Comparison between 3rd fuselage iteration and 4th fuselage iteration
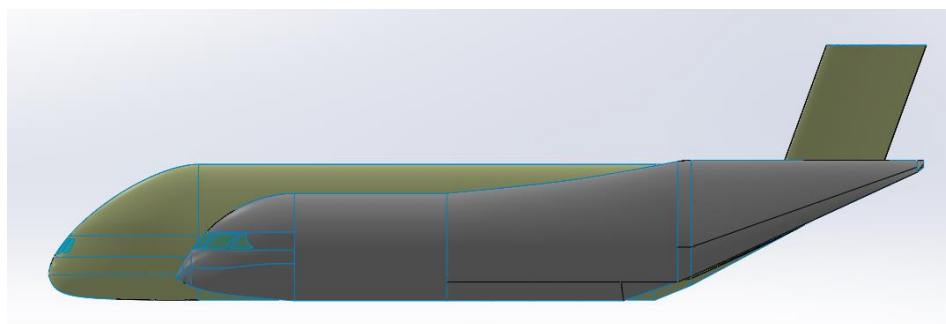
Figure 20: Comparison between 3rd fuselage iteration and final fuselage iteration

The final iteration focused on reducing the ramp angle and the abrupt change in the fuselage cross-section. The ramp was at 44° angle in the 4th iteration which is not favourable for aircrafts as it

increases the pressure drag of the aircraft. The transition was changed to be more gradual to reduce the stress concentration, and the ramp angle was reduced to 24.7°.
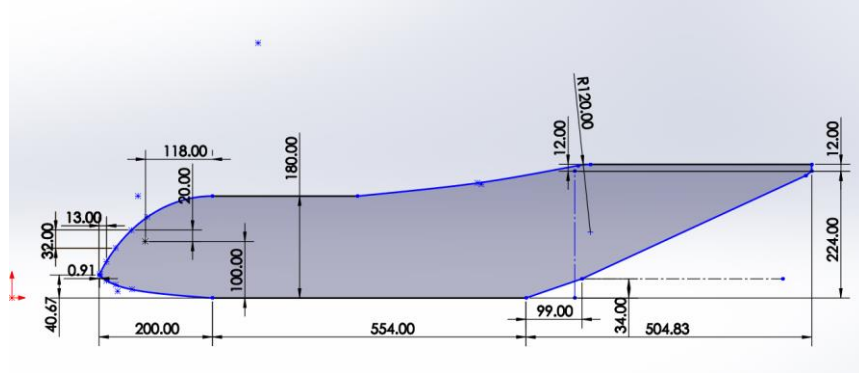
Figure 21: Final fuselage contour

Figure 21 shows the final contour of the aircraft with a smaller tail angle and a gradual transition from circular to elliptical. The cockpit length was slightly increased to improve the aesthetic shape of the cockpit. The cockpit was inspired by the B787 and A350, which have a more modern look.

6.2. Cockpit

The cockpit design was performed after the fuselage cross-section was finalized. The cockpit was required to house two pilots and two additional crew members for loading and unloading operations. To accommodate all the system and crew, the cockpit was initially designed to be 14.8 *ft* long but was increased by 2 *ft* to improve the aesthetics of the cockpit. To simplify the design process and reduce file sizes, only one half of the cockpit was drawn and mirrored at the end.

The cockpit design's first step was establishing the pilot's ERP or eye reference point. The ERP allows to determine the size and shape of the windows. The basic datums are shown in Figure 21 and Figure 22. The ERP is 100 *in* from the fuselage waterline, 118 *in* from the cockpit bulkhead fuselage station and 24 *in* from the aircraft's center axis. In Figure 22, the ERP is represented by a green sphere.
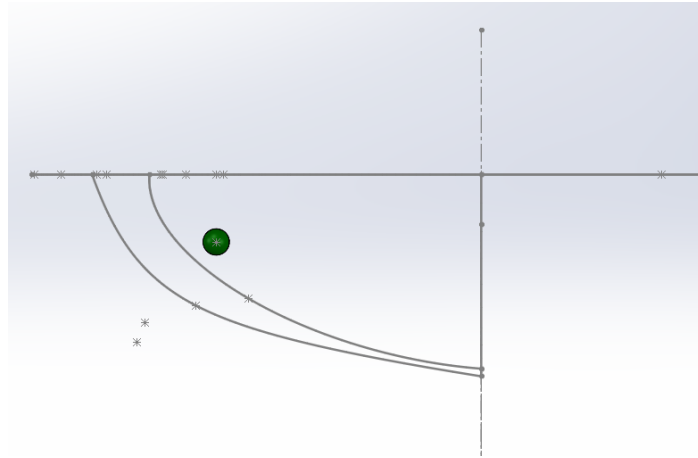
Figure 22: Upper and lower conic curves, and pilot ERP

The upper and lower conic curves drive the overall shape of the aircraft window. The upper and lower conic were adjusted manually until the created window contained the pilot vision pattern outline in Figure 23.
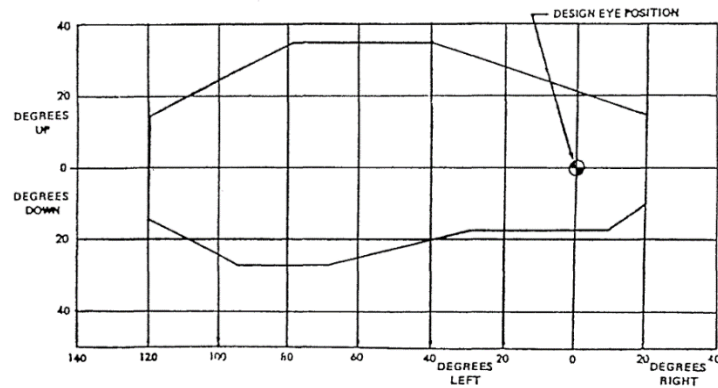
Figure 23: FAA pilot vision pattern advisory [10]

The FAA pilot vision advisory is not a requirement but a guide to show that an aircraft cockpit allows a pilot to safely perform any maneuvers within the operating limits of the aircraft. The pilot should be able to see 35 degrees up and down, 20 degrees to the opposite side of his seat and 120 degrees on his side. For example, the captain should be able to see 120 degrees to his left, 35 degrees up and down, and 20 degrees to his right.
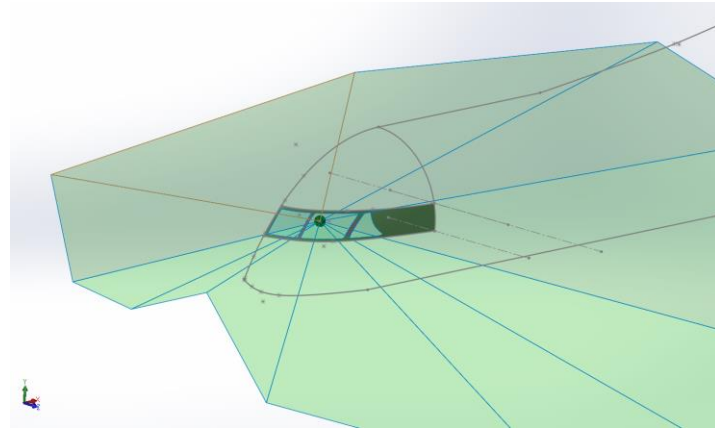
Figure 24: Pilot vision pattern overlayed to cockpit masterlines

As seen in Figure 24, the pilot vision pattern fits within the area encompassed by the windows of the final cockpit design.

The MHB spline was created to guide the cockpit surfaces. This line greatly impacted the overall cockpit shape and aesthetics; a comparison between the cockpit design with and without the MHB line is shown later in this section.
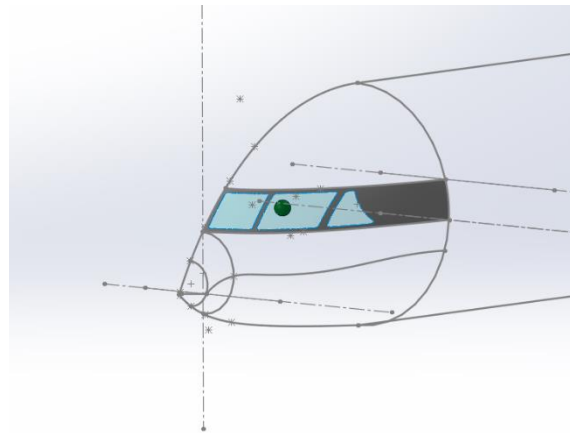
Figure 25: MHB line and additional guide lines for cockpit surfacing

In Figure 25, the MHB line is the spline below the lower conic curve of the cockpit. The spline starts at the beginning of the cockpit and ends at the intersection of the nose and the axis of symmetry of the aircraft. The MHB spline was adjusted until an aesthetically pleasing shape and sufficient space for structures and other systems were reached.
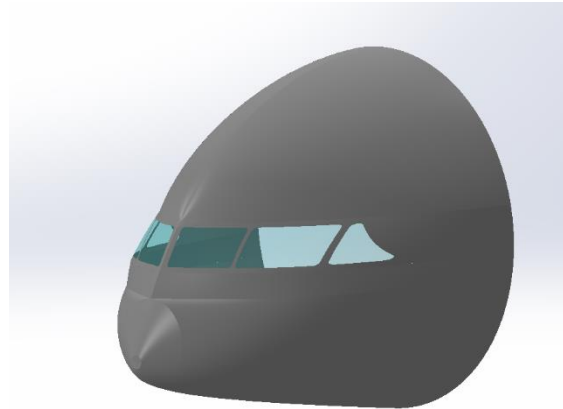
Figure 26: PDR cockpit masterlines

The cockpit pictured in Figure 26 contains the cockpit masterlines presented in the PDR. The problem in this cockpit was that curves were not tangent. Non-tangent curves reduce the aircraft's aerodynamic performance and make the cockpit structures heavier as more frames would be required to accommodate the larger changes in curvature.
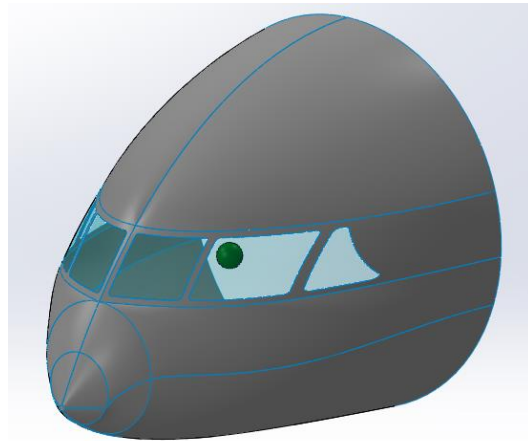
Figure 27: Revised final cockpit masterlines

Figure 27 shows the final cockpit masterlines. This cockpit is the culmination of multiple iterations to achieve a cockpit with enough space to house crew and systems while remaining aerodynamic and aesthetically pleasing.

6.3. Wing

The initial wing design was based on initial sizing calculations. The initial sizing calculations were validated through a performance analysis, aerodynamic analysis, and stability analysis. The NACA 643418 airfoil for its low drag at cruise speed, lowering the fuel burn rate. The wing CAD model was then created using the airfoil and the wing geometry and dimensions stipulated in initial sizing section.
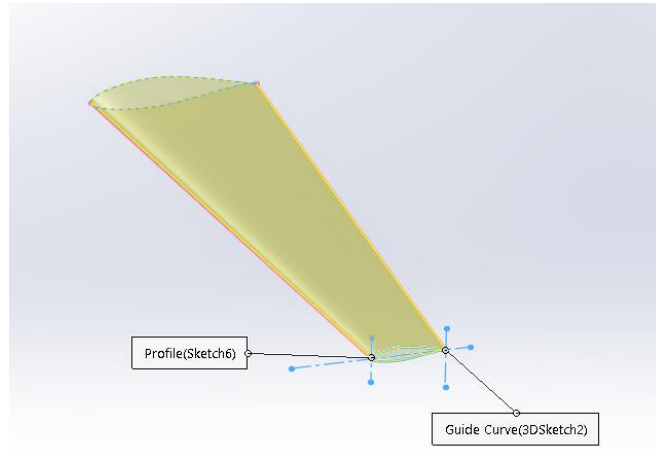
Figure 28: Wing airfoil planform sketch
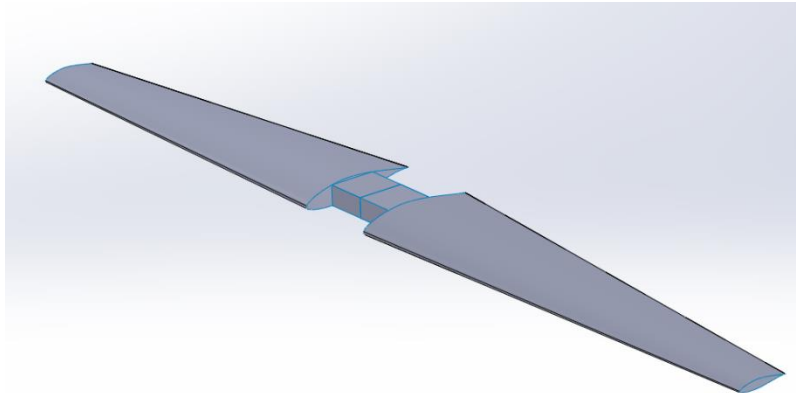
Figure 29: Final wing masterlines

A noticeable feature of the wing is a straight trailing edge. The missing section of the wing at the center is the wing fairing which is described in a following section.

6.4. <u>Horizontal Stabilizer</u>

Similarly to the wing, the airfoil chosen was the NACA 0015 because it is a symmetric airfoil that minimizes the aircraft's pitch up moment. An inverted camber airfoil was tested but produced a larger trim angle range that is not in line with most certified aircrafts.
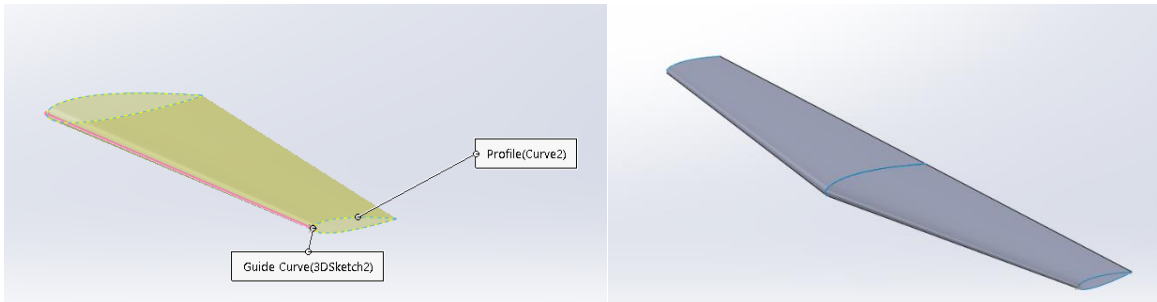
Figure 30: Horizontal stabilizer masterlines (left: airfoil planform sketch, right: final H-stab)

6.5. <u>Vertical Stabilizer</u>

The vertical stabilizer modelling had the same process as the wing and vertical stabilizer; hence, details about the procedure can be skipped. The vertical stabilizer has the same airfoil as the horizontal stabilizer but is not reflected about the body axis of the aircraft.
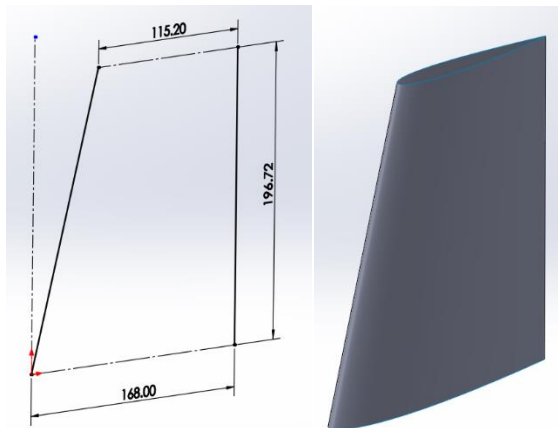
Figure 31: Vertical stabilizer masterlines (left: airfoil planform sketch, right: final v-stab)

6.6. Engine

The engine consisted of 2 main sections, the nacelle and the propeller. Prior to the design of the nacelle, the engine for the Hauler-X was chosen to be the Pratt & Whitney PW127XT based on performance and comparative estimates. This engine is specifically design for use in ATR-72 aircraft, and as such it was determined that the best choice in nacelle design would be to replicate that of the ATR-72 nacelle, not only because of its capability of being specially designed for that aircraft, but also to keep the necessary geometry such as the ram air intake and exhaust that would be needed for the Hauler-X's systems and performance. This nacelle is nearly symmetrical and consists of multiple panels assembled together. The rear section of the nacelle is slightly modified to allow for room for the exhaust port located at the back of the engine.
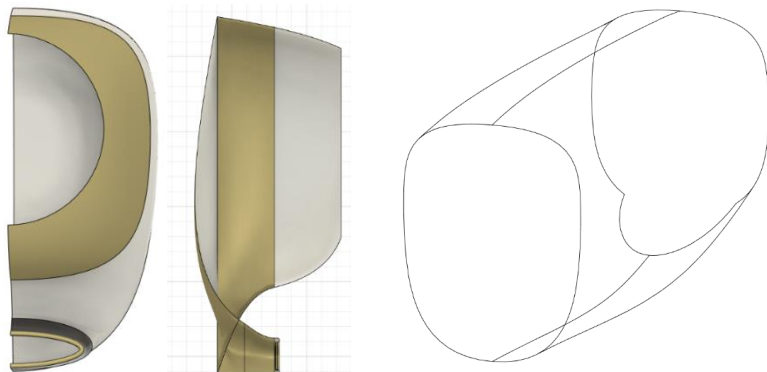
Figure 32: Aft nacelle front view (left), aft nacelle side view (center) and isometric nacelle lines (right)

The propeller was also designed and modified based on the PW127-XT engine, which has a total of 6 blades per engine. A singular blade was made using splines and replicated 5 more times to create the required number of sections. Preliminary research also allowed for the determination of the blade diameter, equalling 13.17 *ft*.
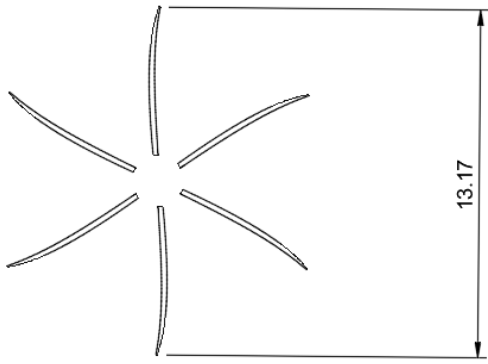
Figure 33: Dimensioned propeller blades
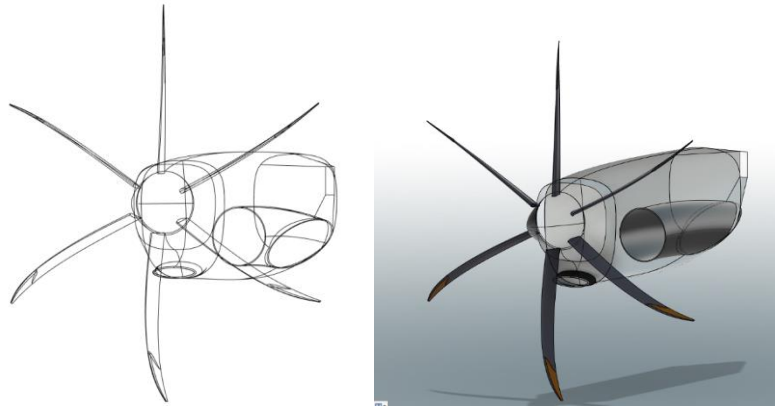
Figure 34: Engine with only lines and complete diagram with superimposed lines

6.7. Wing Fairing

The masterlines for the wing fairing was completed based on the wing sizing, wing placement and airfoil selection. The wing fairing structure encompasses the integration of the wing structure with the fuselage- frame structure. Figure 35 illustrates the sketch for the final iteration of the designed wing fairing. The shape of the fairing was reconstructed a couple of times in order to make it more aerodynamic and less draggy while maintaining its physical functionality. A combination of sketches and splines made on the top plane and the right plane were used to CAD the desired shape of the wing fairing. These sketches where then lofted in sections and trimmed with each other.
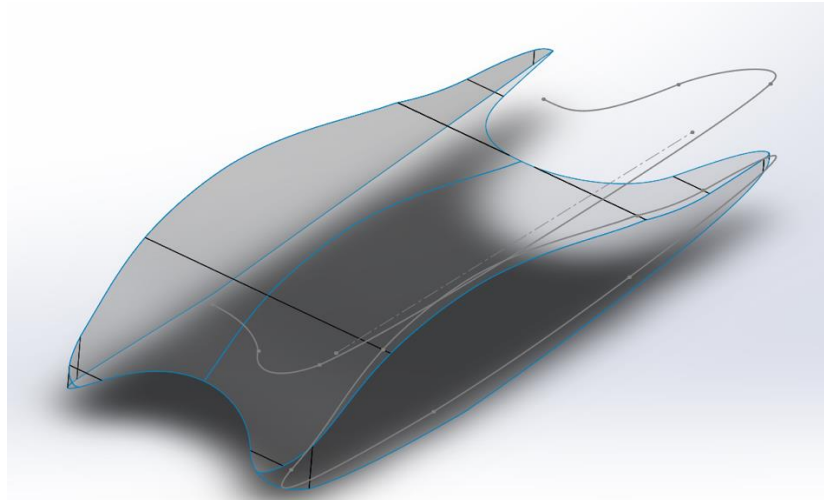
Figure 35: Wing fairing sketch.

6.8. Landing Gear Fairing

The masterlines for the belly fairing was completed using a similar approach to that of the wing fairing. The belly fairing was completed based on the MLG sizing, location, and retraction mechanism. The belly fairing design consists of six parallel sketches placed strategically and in alignment with the fuselage frames. Figure 36 illustrates the designed belly fairing for the aircraft masterlines. The front and back curved sketches for the fairing were adapted from the fuselage masterlines. This was done so that the fairing tapers in front and at the back to follow the fuselage bottom surface. The fairing was formed by surface lofting these sketches using specific guide curves such that the shape is aerodynamic, less draggy while delivering optimal functionality.
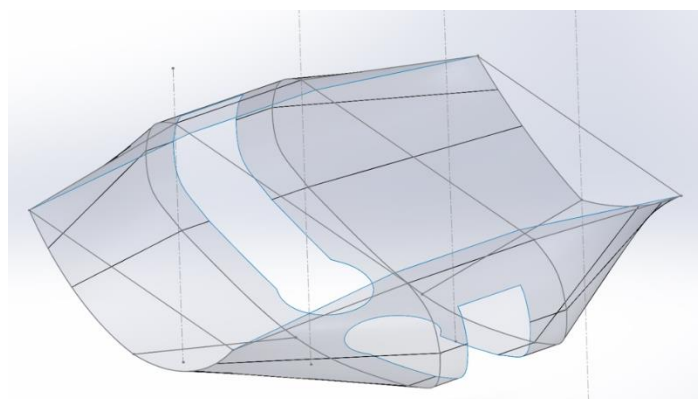
Figure 36: Main landing gear fairing.

7. Loads and Dynamics

During take-off, flight, and landing, an aircraft will experience static and dynamic loads. Calculating these loads is a crucial step in the design process. These parameters dictate the performance of an aircraft in terms of speed and structural rigidity. A flight envelope was constructed via MATLAB applications for the Hauler – X using input parameters which are provided in the table below.

Table 20: Loads and dynamics input parameters

Input	Value
Aspect Ratio	9.55
Wing Area (ft^2)	1275
Wingspan (ft)	113
Mean Chord (ft)	11.83
MTOW (lbs)	43497
Cruise Altitude (ft)	21000
Positive Load Factor	2.5
Negative Load Factor	-1
Sweep Angle @ Take-Off ($°$)	8.62
Lift Curve Slope ($/°$)	0.1
Air Density @ 21000 ft ($slugs/ft^3$)	0.001227
Air Density @ Sea Level ($slugs/ft^3$)	0.002378
Cruise Speed (V_c) (kts)	331
Stall Speed (V_b) (kts)	128
C_{Lmin}	0.2
C_{Lmax}	1.7

The following is the flight envelope for our aircraft which plots the V-n diagram between gust lines. The key regions are highlighted using iPad sketch tools, and the key points of airspeed are also marked within the diagram.
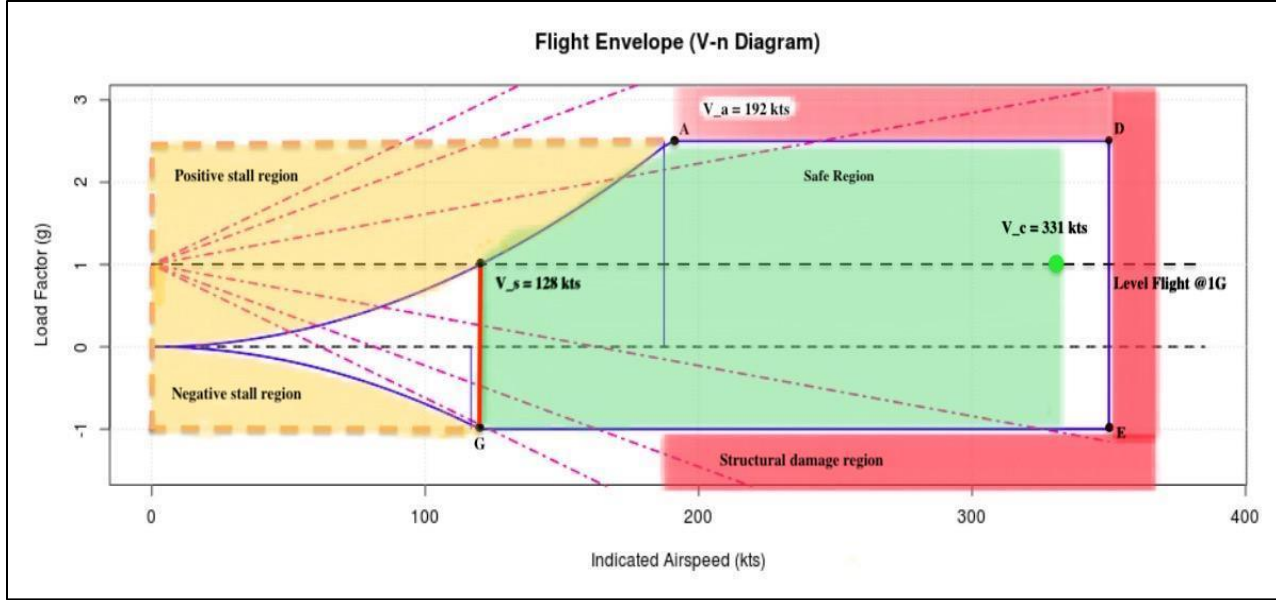
Figure 37: Hauler-X flight envelope

The indicated regions consist of the red, yellow and green transparent shading. The yellow area represents the stalling region, which is for both positive and negative load factor of 1. Next, we have the safe area engulfed in green which spans horizontally from stall speed to the cruise speed. Beyond that point would be the caution range. Extending to a zone further than the dive speed would result in structural damage which is highlighted in red. Flying the aircraft at that condition would cause wear and tear beyond what can be considered negligible. Prolonged flying at those or worse conditions will ultimately lead to structural failure. The gust lines for dive speed (outer) and cruise speed (inner) are derived from the lift curve slope value. The resultant outputs were a maneuvering speed (V_a) of 192 knots and dive speed (V_d) of 355 knots.

8. Aerodynamics

The first step in conducting a successful aerodynamic analysis for the preliminary design is to select an efficient airfoil for the wing and tail. The initial sizing of the wing and tail was obtained from the sizing team, and this, along with Mach number, is necessary to determine the Reynolds

42

numbers enveloping the wing. While the Mach number of 0.5 was derived from the expected flight envelope, the Reynolds number was calculated using NASA's Calculator. [11]

$$Re = \frac{V*L}{\mu} \tag{8.1}$$

Using Standard atmospheric conditions at 21,000ft and at Mach 0.5, produced Reynolds numbers for both the tip and root chord. Either represented the limitation of the Reynolds numbers experienced by the wing.

Table 21: Range of Reynolds No's experienced on the wing

	Chord Length (*ft*)	Reynolds No.
Root Chord	15.57	5,887,886
Tip Chord	7.007	2,659,737

Once the range was calculated, airfoil selection process was based on the handbook for airfoil selection utilized, in particular the figure representing below. [12]
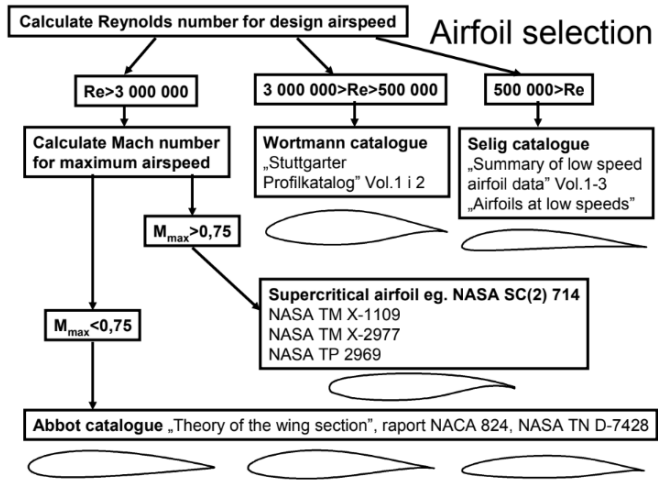
Figure 38: Airfoil selection matrix

This approach narrowed down the airfoil selection to the "Theory of wing Section". However, it did not provide a definitive solution. Therefore, using a University of Illinois Urbana-Champaign database of used airfoils, a list of airfoils was compiled of similarly weigh aircrafts as a guide [13]. The results are represented in a tabulated form. Additionally, Airbus' research on its high-lift wing

for its heavy-lift aircrafts was also utilized for shortlisting airfoils that preliminary analysis will be conducted on [14].

Table 22: Airfoils of similar aircrafts

Aircraft	Wing Root Airfoil	Wing Tip Airfoil
Dash 8-100	DHC 18%	DHC 13%
AN-26	TsAGI S-5-18	TsAGI S-3-13
FOKKER F27 Friendship	NACA 64-421	NACA 64-415
ATR 42 CARGO	RA 1843 (NACA 43018 mod)	RA 1343 (NACA 43013 mod)
ATR 72 CARGO	RA 1843 (NACA 43018 mod)	RA 1343 (NACA 43013 mod)
BAE HS 748	NACA 23018	NACA 4412
CONVAIR CV-580	NACA 63A120	NACA 63A415
C-130J Hercules	NACA 63A318	NACA 63A412

From the previous two analysis, it was clear that most aircrafts were utilizing a supercritical airfoil for both root and tip. A total of five airfoil types were chosen for analysis using XFLR5. A complete guide from YouTube was followed to complete the analysis several times **Error! Reference source not found.**. Airfoils chosen were NACA 4418, 0012, 0015, 64015, and 64 (3)-418. The first step I took to was to import the respective DAT file to XFLR5 for XFOIL Direct Analysis. The DAT file was acquired for another UIUC data with files for all airfoils [15]. A DAT file contains the coordinates of the airfoil. A batch analysis with varying Reynolds numbers to capture the maximum range. From the analysis of airfoils NACA 4418, 64015, and 643418, it was concluded that these airfoils are best suited for the wing while NACA 0012 and 0015 are suited for the tail. Comparing the analysis of NACA 0012 and 0015, the C_L vs α and C_D vs. α are the main parameters for design selection. Both graphs for the two airfoils looks very similar therefore NACA 0015 was chosen specifically considering the space required for structure.
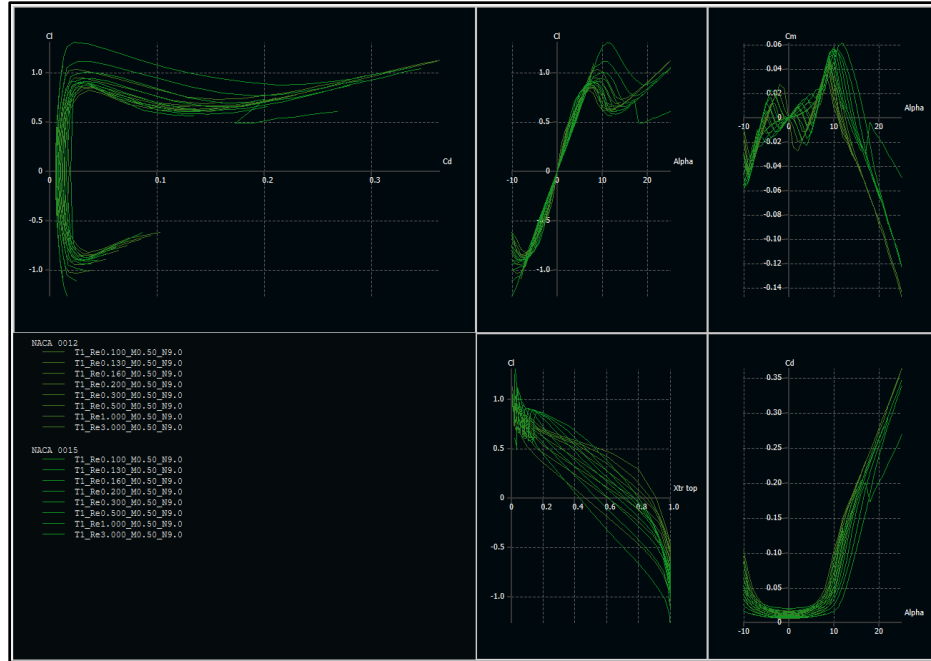
Figure 39: Results of direct XFOIL analysis on NACA 0012 and 0015
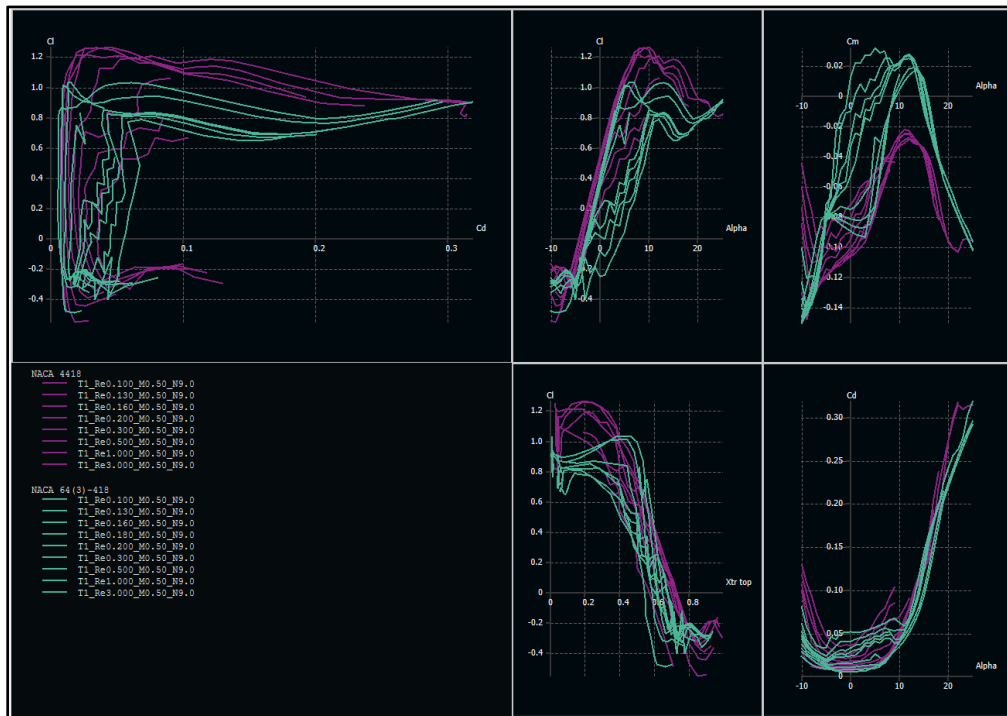
Figure 40: Results of direct XFOIL analysis on NACA 4418 and 64(3)-418
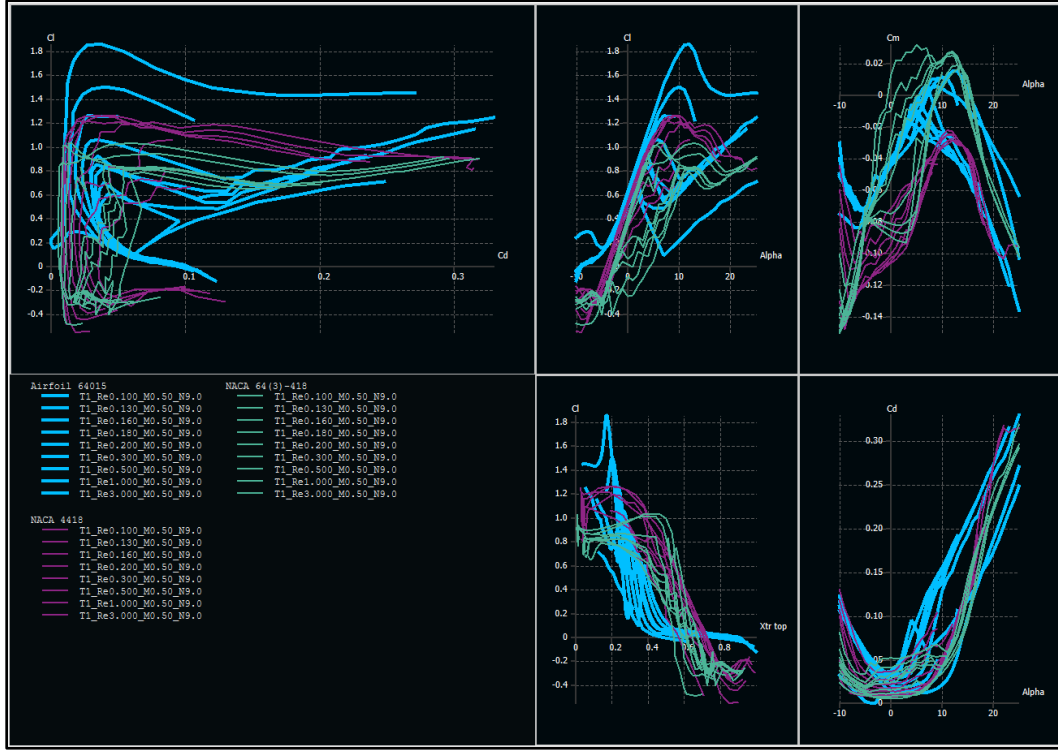
Figure 41: Results of direct XFOIL analysis on NACA 4418, 64015 and 64(3)-418

Following the analysis on the airfoils, the airfoils for the wing is analyzed as a wing and plane design with only wing. This produces C_D and C_L spanwise for a range of -10-to-25-degree angle of attack. The atmospheric conditions set for the analysis corresponds to the cruise altitude. Additionally, the fixed speed, wing only analysis is run on the three airfoils. The results concluded that the NACA 643418 produce sufficient lift for the given planform and correspondingly, the drag coefficient is least. Comparatively, NACA 4418 and 64015 have similar lift coefficients but higher drag coefficients.
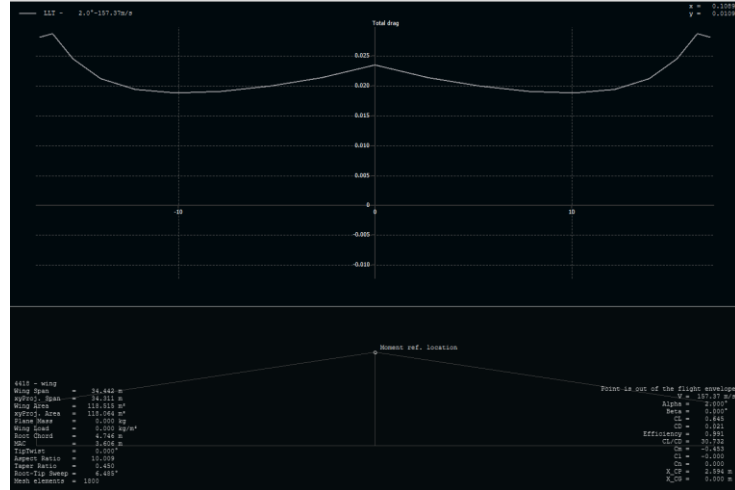
Figure 42: Spanwise total drag coefficient for NACA 4418
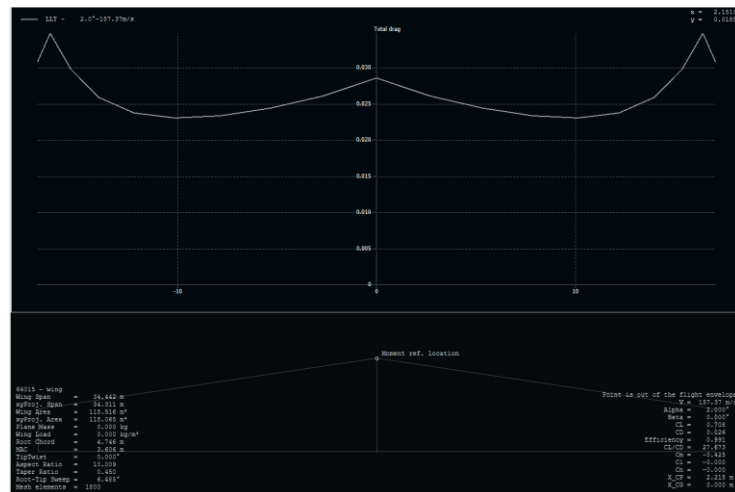
Figure 43: Spanwise total drag coefficient for NACA 64-015
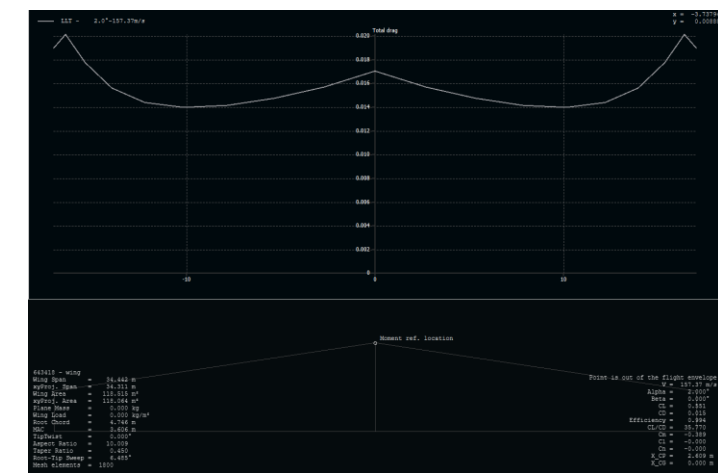
Figure 44: Spanwise total drag coefficient for NACA 64(3) - 418
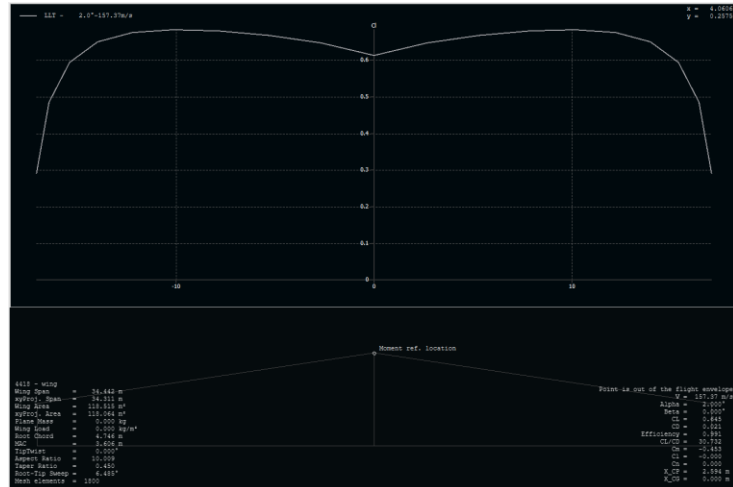
Figure 45: Spanwise total lift coefficient for NACA 4418
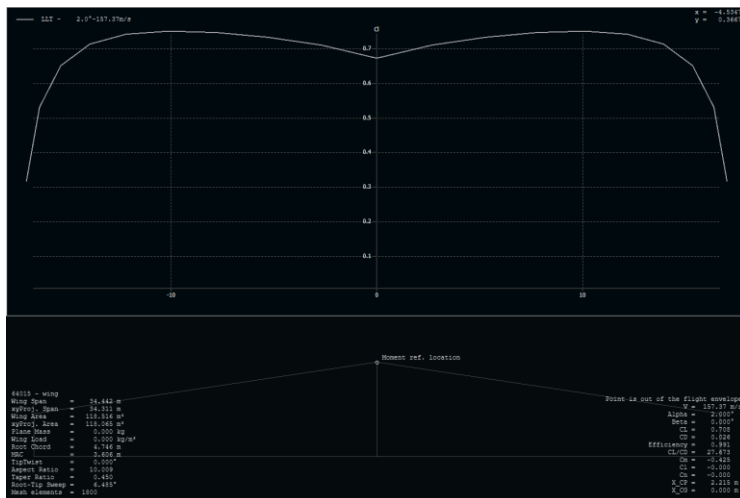
Figure 46: Spanwise total lift coefficient for NACA 64015
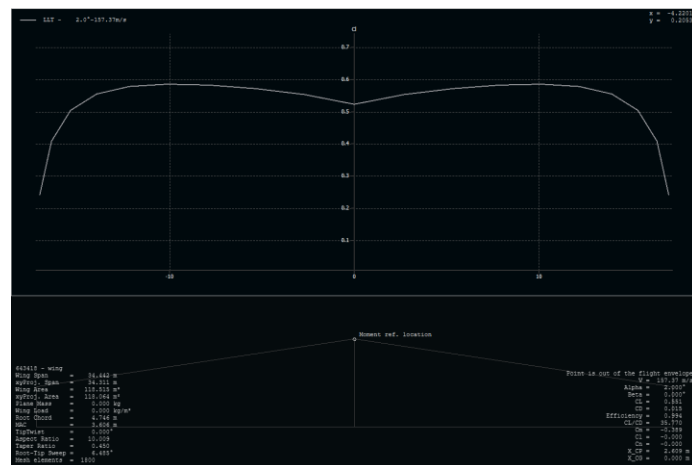
Figure 47: Spanwise total lift coefficient for NACA 64(3)-418

Based on these results, NACA 64(3)-418 is the selected airfoil for the wing. Additionally, NACA's original report of NACA 64(3)-418 affirms the results of the XFOIL Direct Analysis and the wing design analysis. Additionally, the NACA 64(3)-418 also allows for delayed onset of separation point and therefore reduces the area affect by turbulent flow. This is a significant reason is reduced drag. Additionally, the wing presents excellent low speed characteristics with simple high-lift devices. Therefore, the wing is designed with only flaps and the need for slots, slats, and spoilers are mitigated. As a next step, the design of the tail was integrated with NACA 0015 airfoil with the correct dimensions. The analysis type was changed to Horseshoe Vortex (no sideslip). The result of the Analysis is shown in figures below.
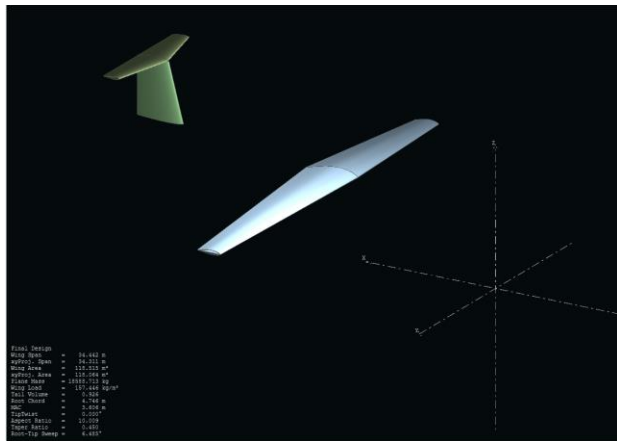
Figure 48: Final configuration with selected airfoils
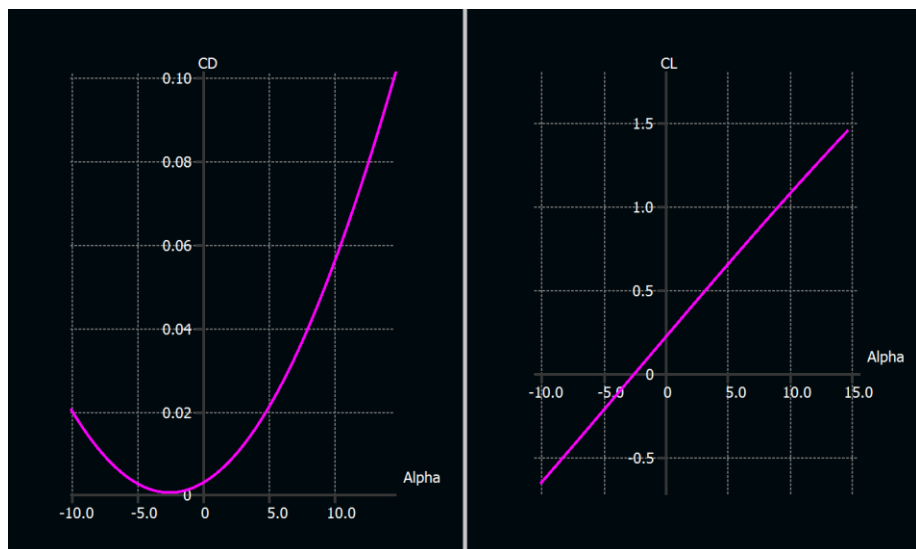
Figure 49: Lift and drag versus angle of attack

Since the drag calculated from the XFLR5 analysis only contains induced drag, parasitic drag was calculated using estimate component drag equations from Raymer's textbook. The estimates included all components, leakages, and perturbations (including lights, sensors, antennas, and antennas), and miscellaneous included upsweep and base drag from the "base", which is the rearward-facing flat area or the loading door. This is due to the sharp angle causing the wake to collapse on itself. Additionally, the flat plate analysis was conducted for cruise conditions without including landing and takeoff conditions, since landing and T/O experience varying angles of attack and fight speeds. The tail calculations are divided into horizontal and vertical components to accurately include interference drags from the fuselage connection and the component connection. The coefficient of friction calculations for the wing since a feature of the chosen supercritical airfoil is to delay separation point. For this reason, the flow was assumed to be laminar. Additionally, the tail was also assumed to be laminar, while the nacelle for the engines and the fairing was assumed to experience turbulent flow. Neither of these cases were considered for fuselage, instead the length of the fuselage guarantees transition therefore both flows are considered. The formulas listed below were utilized for the indicated component.

$$(C_D)_{min} = \frac{\Sigma\left(C_{f_c}FF_cQ_cS_{wet_c}\right)}{S_{ref}} + C_{D_{misc.}} + C_{D_{L\&P}} \tag{8.2}$$

The drag coefficient of each component was calculated based on Reynolds number and flow condition.

Laminar: $C_{f_c} = \frac{1.33}{\sqrt{Re}}$ 　　　Turbulent: $C_{f_c} = \frac{0.074}{\sqrt[5]{Re}}$ 　　　Combined: $C_{f_c} = \frac{0.074}{\sqrt[5]{Re}} - \frac{1742}{Re}$

Different formulas for form factor were utilized based on flight condition and location.

Wing, and Tail: $FF = \left[1 + \frac{0.6}{(^x/_c)_m}\left(\frac{t}{c}\right) + 100\left(\frac{t}{c}\right)^4\right][1.34M^{0.18}(\cos(\Lambda_m))^{0.28}]$

Fuselage and Fairing: $FF = 0.9 + \frac{5}{f^{1.5}} + \frac{f}{400}$

Engines: $FF = 1 + \frac{0.35}{f}$

　　　Where: $f = \frac{l}{d} = \frac{l}{\sqrt{\left(\frac{4}{\pi}\right)*A_{max}}}$

The interference drag, Q, was also included in the calculation to account for intersecting components, and boundary-layer thickness. The Q factors were selected based on the aircraft geometry and shape. The selection is tabulated below. Additionally, the wetted areas of each

component and the reference area of the wing are mentioned in the final 3-D view drawing in appendix A.

Table 23: Component wise interference drag, Q

Component	Interference Drag, Q
Nacelle, and Fairing	1.5
High Wing	1.0
Fuselage	1.0
T-Tail	1.08

The miscellaneous drag contains two major components. The first is the upsweep drag that is caused by the sharp upsweep at the aft. Fuselage. The second is the base drag that it caused by the rearward-facing flat area. This causes wake to collapse on itself increasing drag. The formulas below are utilized.

Upsweep: $C_D = \frac{3.83 * u^{2.5} * A_{max}}{S_{ref}}$

Base Drag: $C_D = \frac{[0.139 + 0.419(M - 0.161)^2] * A_{base}}{S_{ref}}$

Last, but not the least, the leakage and protuberance drag was based on the industry standard for propeller aircraft of 5-10%. Due to the complex nature of the fuselage shape, 10% for this drag was assumed. The total drag calculated is 0.05 with parasitic and induced added.

9. Material Selection

The appropriate selection of materials in structural design for aircraft components is critical to their cost efficiency and ability to withstand typical loads, considering factors such as strength, weight, durability, and adherence to industry standards and regulations.

Aluminum is a commonly used material in aircrafts due to its high strength-to-weight ratio, reasonable cost, abundance, ductility, and resistance to corrosion [16]. Aluminum alloy 7075-T6 was chosen for the entire fuselage and wing due to its lightweight properties and durability in withstanding stress [16]. Aluminum alloy 2024-T3 was chosen as aircraft skin due to its high

strength-to-weight ratio and excellent fatigue resistance. It is also easily formable and has excellent corrosion resistance [17].

The manufacture of landing gears involves the use of different materials, such as aluminum, steel, and titanium. Yielding is the main cause of failure in landing gears, making yield strength the most crucial property. Titanium boasts the highest yield strength, followed by steel and aluminum. Nonetheless, weight is also a significant factor, which is determined by a material's density and specific weight [18]. Specific strength, the ratio of yield strength to density, indicates the amount of material required to support a particular load. A lower specific strength necessitates more material to support a load. The titanium alloy has the highest specific strength, offering the best strength-to-weight ratio [18].

Laminated glass is a type of glazing material commonly utilized in the manufacturing of cockpit windshields, composed of two layers of glass that are joined together by a layer of plastic film [19]. Laminated glass for cockpit windshields provides improved safety, durability, clarity, and UV protection by holding together when shattered, resisting breakage or cracking, withstanding harsh weather and high speeds, enhancing visibility, and blocking harmful UV rays [19]. Table 24 represents the materials chosen for each component. Appendix A contains information on the mechanical and physical properties of the chosen materials.

Table 24: Material selection per component

Components	Material
Aircraft	
Spar/Ribs/Stiffeners/Frames	Al 7075-T6
Bulkheads/ Floor Support Structure	
Skin	Al 2024-T3
Landing Gear	Ti-6AL-4V

Windshield	Laminated Glass

10. Structures

This section details the technical specifications and design considerations for the primary structural components of the aircraft, encompassing the fuselage, cockpit, wing, empennage, landing gear, engine pylon, and cargo door.

10.1. <u>Fuselage</u>

The design of the fuselage was completed by complying to the masterlines created which outlined the fuselage transition to accommodate the payload. Figure 50 shows a final render of the fuselage structure with the appropriate number of frames, stringers, and floor support structure.
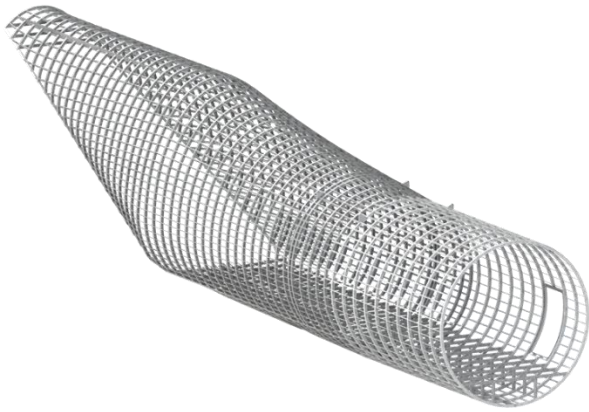
Figure 50: Fuselage structure CAD

10.1.1 <u>Structural Idealization</u>

Structural idealization assumes that direct stress is constant across the cross section of a stringer [20]. This assumption was valid as the cross-sectional area of a stringer is small compared to the cross-sectional area of the fuselage. The stringers were reduced to Boom areas that only carry direct stress. Additionally, the fuselage skin is usually very thin, between 0.11 to 0.14 in [21]. Hence, the skin panels can be approximated as thin panels that only carry shear stress.

It is important to determine the loads and forces acting on the fuselage. The loading configuration was developed from the payload spacing.
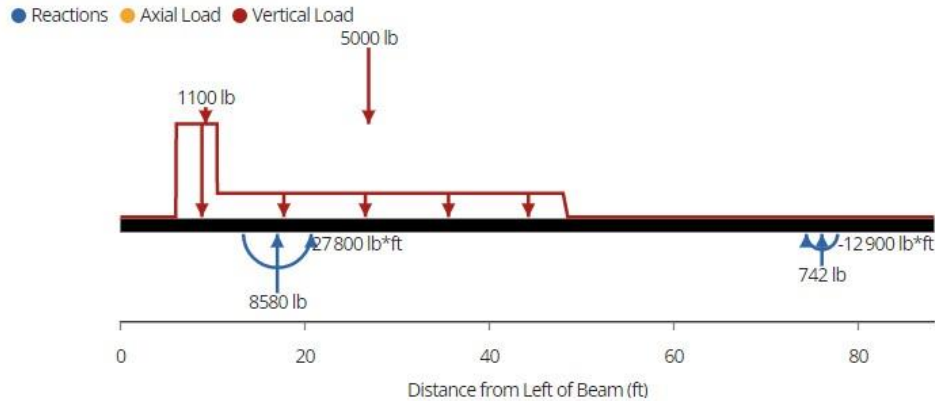
Figure 51: Loading configuration

The cockpit payload was placed forward *3ft* from the rear cockpit bulkhead and the rear fuselage payload right behind it. The loading configuration included point loads for the payloads at their respective CG locations provided by the Bombardier team. The distributed loads represent the weight of the two jigs used to carry the payloads. The fixed boundary conditions were placed at the wing and empennage aerodynamic centers. The fixed boundary condition was placed at those two locations because, during flight, the lift produced by the wing and empennage opposes the aircraft's weight.

The loading configuration resulted in the shear and moment diagrams in Figure .
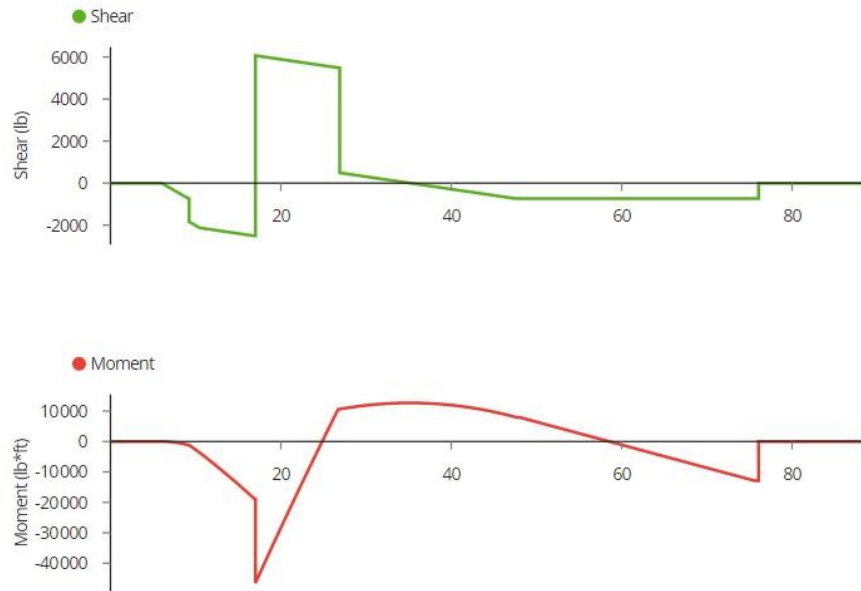
Figure 52: Fuselage shear and moment diagram

The fuselage experiences a maximum moment of 559,200 *lb.in* about the lateral axis and a maximum shear force of 6000 *lb*.

The boom areas must be found from the stiffener areas and idealized skin panels. The following formula was used to find the boom areas.

$$B_i = A_{stiffener} + \frac{t_d b}{6}\left(2 + \frac{\sigma_{i+1}}{\sigma_i}\right) + \frac{t_d b}{6}\left(2 + \frac{\sigma_{i-1}}{\sigma_i}\right) \tag{10.1}$$

Where $A_{stiffner}$ is the area of the stiffeners, σ_i is the vertical distance from the neutral axis to boom n, σ_{i-1} is the vertical distance from the neutral axis to the previous boom and σ_{i+1} is the vertical distance from the neutral axis to the following boom. The boom areas were then used to find the moments of inertia about the aircraft's lateral axis.

$$I_{yy} = \sum_{i=1}^{n} B_i \, \sigma_i{}^2 \tag{10.2}$$

Where σ_i is the vertical distance from the centroid to boom i. Finally, the direct stress in each boom was calculated using equation 3.

$$\sigma_z = \frac{\sigma_i * M_y}{I_{xx}} \tag{10.3}$$

Where M_y is the moment about the lateral axis. With the equations and loads determined, a MATLAB code was written to make the iteration between stringer sizes and areas easier. The MATLAB code can be found in the Appendix A section. The number of stringers, stringer area and skin thickness were iterated multiple times to reduce weight while still fulfilling tensile strength and skin panel buckling requirements.

10.1.2 Panel Buckling

To verify that the calculated area and number of stringers were sufficient, it was necessary to check that the skin panels did not fail before the stingers. Skin panel buckling depends on the thickness and width of the panels, and the critical buckling stress for the skin panel is given by equation 4.

$$\sigma_{cr} = \frac{k\pi^2 E}{12(1-v^2)}\left(\frac{t}{b}\right)^2 \tag{10.4}$$

Where k is the buckling coefficient, E is the elastic modulus of the stringer material, t is the thickness of the skin panels, b is the spacing between stringers, and v is the poison ratio. The

buckling coefficient depends on the frame spacing to stringer spacing ratio. The buckling coefficient can be found using the selection chart in Figure 53.
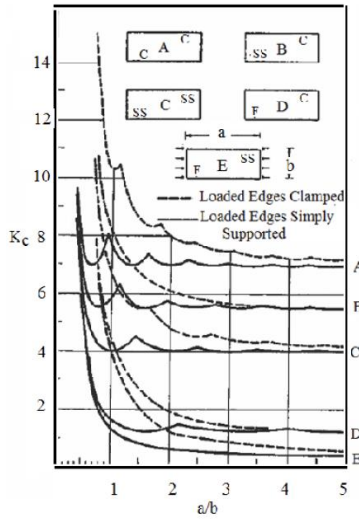
Figure 53: Buckling coefficient selection chart

As mentioned in the masterlines section, a major feature of Hauler-X is the transition from a circular cross-sectional area to an elliptical cross-sectional area. The described analysis process was performed for both cross-sections. Table   summarizes both fuselage cross-sections' final stringer characteristics and frame spacing.

As mentioned in the masterlines section, a major feature of Hauler-X is the transition from a circular cross-sectional area to an elliptical cross-sectional area. The described analysis process was performed for both cross-sections. Table   summarizes both fuselage cross-sections' final stringer characteristics and frame spacing.

Table 25: Final fuselage idealization results

Circular cross-section	
Number of stringers	60
Frame spacing	24 in
Stringer area	0.298 in^2
Stringer spacing	9.42 in
Stringer critical stress	691 Psi
Maximum direct stress	354 Psi

Elliptical cross-section	
Number of stringers	79
Frame spacing	18 in
Stringer area	0.298 in^2
Maximum stringer pacing	13.7 in
Stringer critical stress	348
Maximum direct stress	202 Psi

It is important to note that the spacing between stringers is not equal for the elliptical cross-section. The spacing is not equal because the curvature of the ellipse is not constant, and half-cosine spacing was used to increase the number of stringers in regions of tighter curvature. For this reason, a second code was developed to try and reduce the difference between the closest stringer spacing and the maximum stringer spacing as much as possible. The MATLAB code can be found in the Appendix B section.
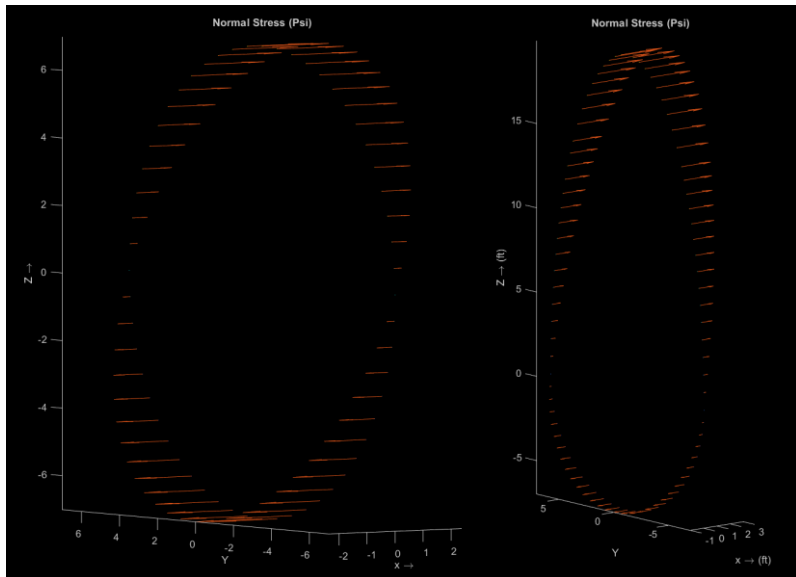
Figure 54: Stress distribution (left: circular cross-section, right: elliptical cross-section)

Figure 54 shows the stress distribution across the cross sections. As expected for the circular cross-section on the left, the normal stresses are the same about the lateral axis. For the elliptical section, the highest stress was at the furthest point away from the floor, the top of the fuselage.

10.1.3 Shear Flow

An additional failure mode examined is failure due to shear. Shear flow analysis is performed by applying a shear force away from the cross-section centroid. The constant shear flow is calculated using this shear force that creates a torque about the centroid or shear center. The total shear flow is then calculated by superimposing the constant shear with the shear flow in each panel. For our fuselage, a maximum shear force of 6000 lb was used, as determined in Figure 52.

Table 26: Shear flow results

Circular cross-section	
Aluminium 2024 shear strength	48 000 Psi
Maximum shear flow	48.1 lb/in
Elliptical cross-section	
Aluminium 2024 shear strength	48 000 Psi
Maximum shear flow	63.7 lb/in

As seen in Table , the maximum shear flow is much lower than the material's shear strength which makes us up the panels. Therefore, the current structural configuration will not fail due to shear.

10.1.4 Stringers

The Z cross-section was chosen for our design for its greater moment of inertia that improves rigidity and increases resistance to bending [22]. Additionally, Z-stringers are easy to manufacture, making them cost-effective [22]. Figure 55 shows the dimensions of the designed stringer.
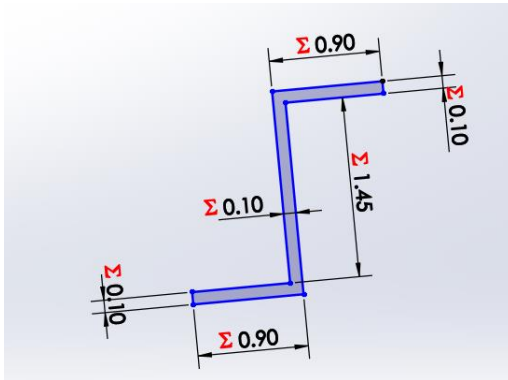
Figure 55: Fuselage and cockpit stringers cross-section

10.1.5 Frames

Frames are major structural components that prevent the skin from buckling when the fuselage experiences bending loads. The I-beam cross-section was selected for Hauler-X because it weighs less than solid beams and is almost as stiff and strong. The following I-beams were developed for our aircraft using following an ATR 42 testing document as a reference [23].
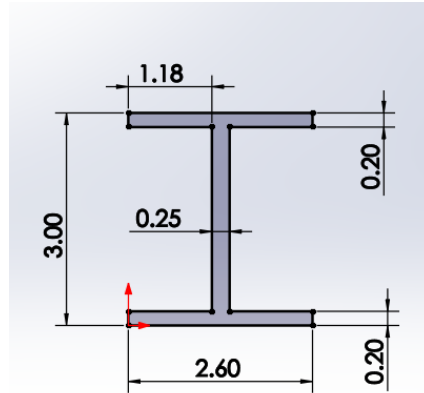
Figure 56: Fuselage frame cross-section
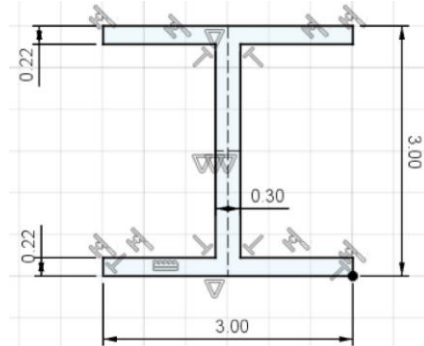
Figure 57: Fuselage frame cross-section for wingbox mounting frames

Figure 56 contains the cross-section of all the frames on the aircraft except for the frames attached to the center wingbox. As shown in Figure 57, the frames that the wingbox attaches to are slightly thicker and wider than the other frames. This design choice was made to accommodate the larger loads expected on these frames due to the transfer of loads from the wing front and rear spars onto the frame.

10.1.6 Floor Support Structure

The floor support structures consist of two components, vertical and horizontal beams. The horizontal beams were placed where frames were present to make manufacturing easier. Similarly, the vertical frames were placed at frame locations and 24 *in* away from the axis of symmetry of the aircraft. The horizontal beams have the same cross-section as the frames, and the vertical beams have a slightly thicker web.
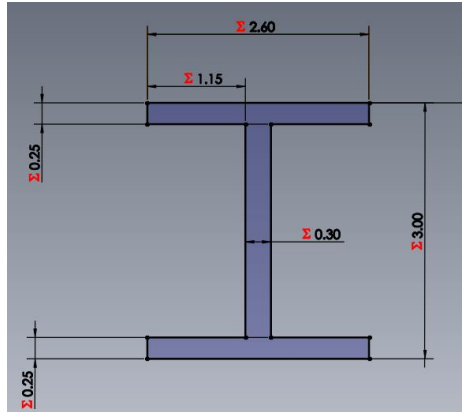
Figure 58: Vertical floor beam cross-section

Figure 59 shows a render of the final floor structure with the vertical beams and horizontal beam at every frame.
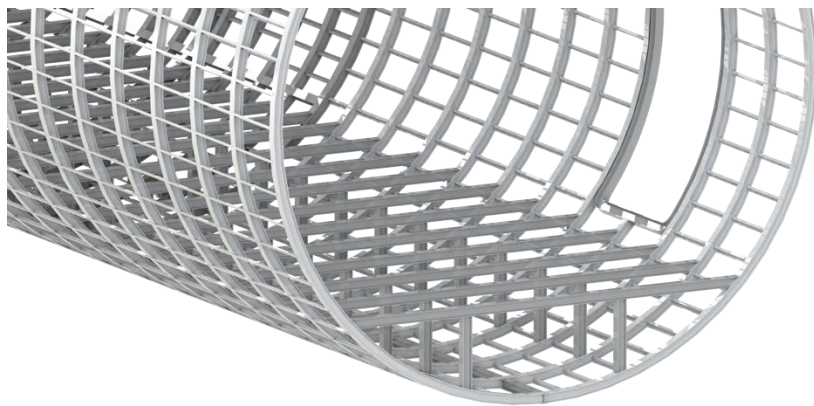
Figure 59: Floor support structure CAD

To validate the cross-section, performing FEA specifically for the vertical floor beams is required to avoid column buckling. A load of 6,900 *lb* was applied on the beam's upper surface, which is in contact with the cargo floor. Examining Figure 59, the load factor was found to be 3.38, above the required safety factor of 1.5. Hence, the designed cross-section does not buckle.

Model name: Cockpit Structures
Study name: Vertical Floor Buckling(-Default-)
Plot type: Buckling Amplitude1
Mode Shape : 1 Load Factor = 3.3814
Deformation scale: 16.6609

AMPRES

4.423e-03

3.981e-03

3.538e-03

3.096e-03

2.654e-03

2.212e-03

1.769e-03

1.327e-03

8.846e-04

4.423e-04

0.000e+00
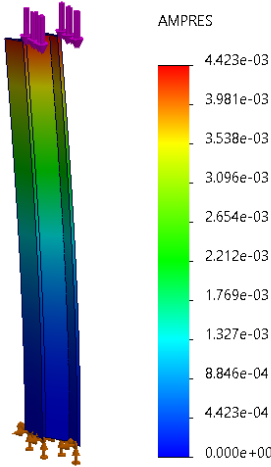
Figure 60: Vertical beams eigenvalue column buckling analysis results

The axis on the right of the beam in Figure 60 represents the displacement of the beam in mm.

10.2.   Cockpit

Figure 61 shows a rendering of the final cockpit structure. The cockpit is made up of 9 frames that are spaced 19 *in* apart with the same cross-section as the main fuselage.
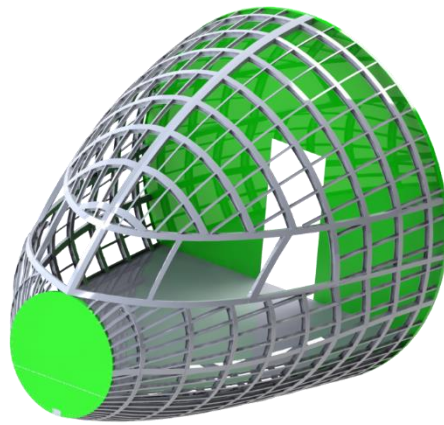
Figure 61: Final cockpit structures

Additional frames were added along the axis of symmetry of the aircraft on the top and bottom surfaces to increase the structural rigidity of the cockpit. A not-so-noticeable detail in renders is

the slight change in curvature of the cockpit surface below the windows. To support this change in curvature, two more frames were added on the sides of the cockpit where the curvature changes. More frames vertical and conical frames were added at the window edges to strengthen the window section.

The cockpit has a pressure bulkhead in the front ahead of the nose to accommodate space for the radome that houses aircraft weather and antenna systems. An additional one is placed at the end of the cockpit section right before the cargo bay. These are the only pressure bulkheads required as the aircraft does not cruise at a high altitude, and the cargo bay is unpressurized.

10.2.1 Windshield Impact Analysis

To ensure the continued airworthiness of an aircraft following a bird or foreign material strike, it is imperative to conduct a comprehensive analysis of the damage sustained. A simulated bird strike on the primary windshield serves as an effective means of evaluating the impact and determining the necessary corrective measures. The standards for the impact of a single bird with a large aircraft airframe, are outlined in CFR Part 25-571 [24]. The regulation necessitates the aircraft's ability to safely continue flight and land after colliding with a bird weighing 4lb, at cruise speed and sea level [24]. The analysis consisted of a sphere with a diameter of 3 *in* and constructed of structural steel, traveling at a velocity of 375 *ft/s*. The windshield used in the simulation was 2 inches thick and fixed on the edges and faces that are in contact with the airframe to accurately reflect its placement within the cockpit structure. Employing ANSYS explicit dynamics enabled the analysis of the outcome of a hypothetical bird strike on the windshield, is shown in Figure 62 and Figure 63.
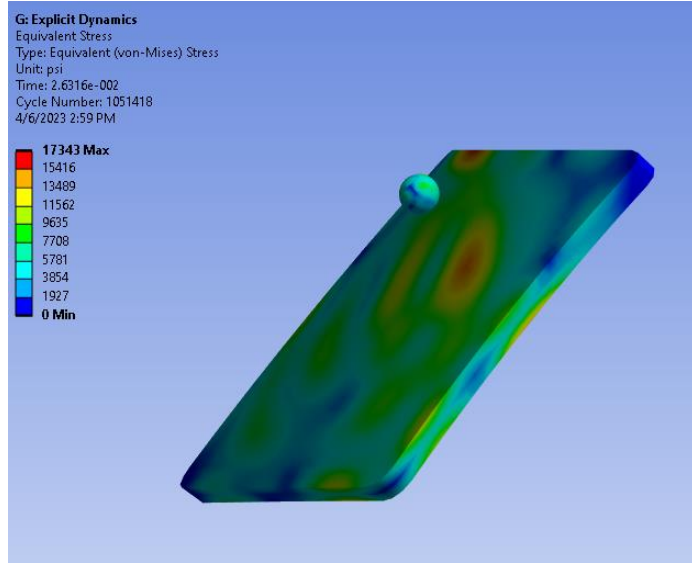
Figure 62: Event simulation of bird strike on windshield Von-Mises stress
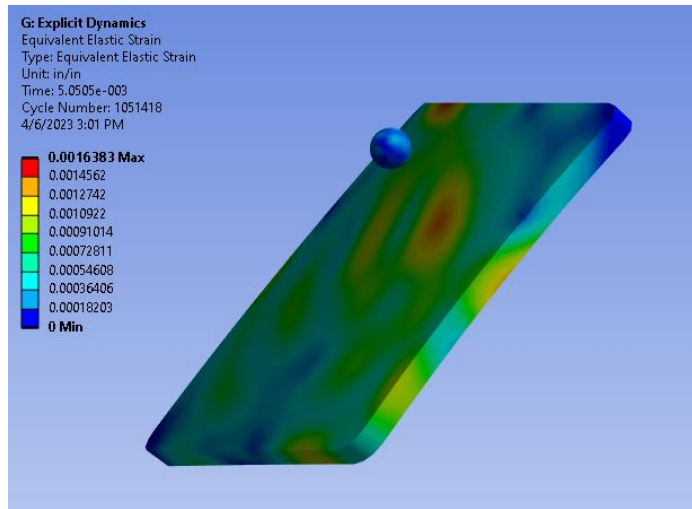
Figure 63: Event simulation of bird strike on windshield elastic strain

The maximum stress obtained was post-impact was 17343 *psi* and the maximum elastic strain obtained 0.0016 inches. The tensile strength of laminated glass is roughly 29 *ksi* [25]. Based on the FEA results, it was observed that the windshield exhibited no signs of penetration and thus demonstrated its capacity to withstand a direct impact from a bird strike with a velocity of 375 *ft/s* and a weight of 4 *lbs*.

10.3. <u>Wing</u>

The wing is a crucial component of an aircraft design of paramount importance to ensure the safety and structural strength of the airframe. Similarly, to the fuselage, the wingbox can be divided into booms that are responsible for bearing direct stresses and thin skin panels that are only required to withstand shear stresses.
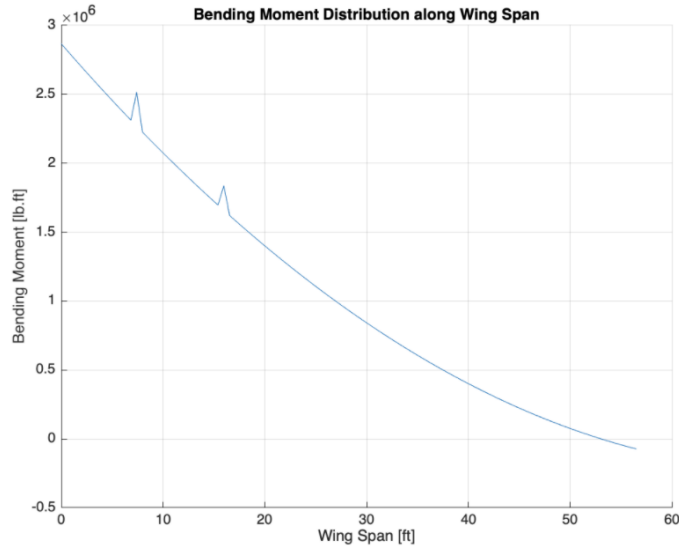
Figure 64: Bending moment distribution along the span

The loads acting of the wing are the lift produced by the aircraft, engine weight and fuel weight. The lift was approximated using Schrenk's approximation and the engine approximated as a point load and the fuel distributed over the size of the fuel tank. Figure 64 shows the obtained moment distribution over the span.

Table 27: Wingbox idealization

Wingbox Idealisation	
Maximum direct stress (*ksi*)	69.7
Material allowable stress (*ksi*)	83.0
Skin panel critical stress (*ksi*)	74.4
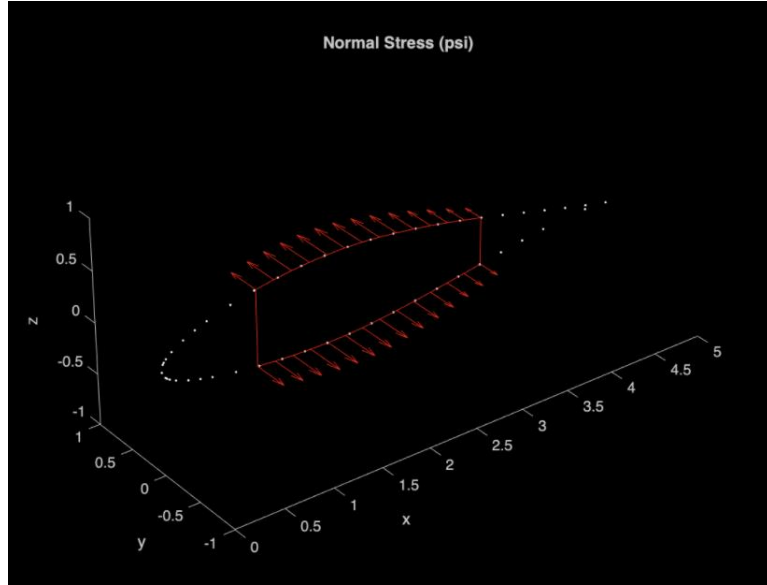
Figure 65: Stress distribution across the root

These results are for a final stringer spacing of 7 *in* at the root and 14 stringers on each upper and lower wing surfaces. The results in Table   confirm that the spacing used is adequate as the maximum direct stress and skin panel critical stress are lower than the material allowable stress. Figure 65 provides a visual representation of the direct stress acting on the root wingbox section. A MATLAB code was written to iterate stringer sizes and areas and can be found in Appendix C.

10.3.1   Component Sizing

The wing structure is composed of several distinct components that are integrated together. The three primary constituents of the wing structure are spars, ribs, and stringers. The present section provides a description of the sizing of these constituents.

Spars

Spars are a critical aspect of any wing design, providing structural support and strength along the span of the wing. Spars are responsible for carrying the loads due to lift distribution and transferring them to the rest of the wing structure.

The front spar was placed at 20% of the chord, aft of the leading edge, while the rear spar was placed 70% of the chord, from the leading edge. The final spar placement considered the size of

the flaps and aileron, wing fuel tank volume, and geometric cross-sectional properties of the wing box.

The final spar cross section is shown in Figure 66. The spar cross-section was validated through a Finite Element Analysis discussed in the next section. Like other sections of the aircraft, the spar cross-section was iterated over time to meet structural requirements while remaining lightweight.
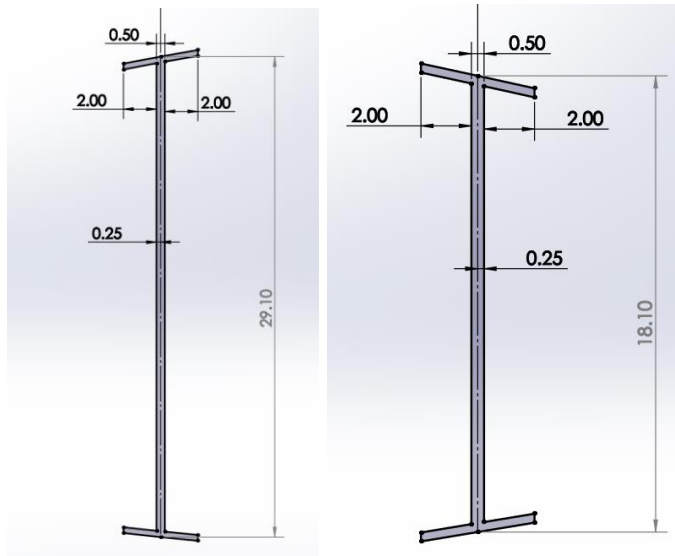
Figure 66: Front (left) and rear (right) spar dimensions at the root

Ribs

Ribs are a crucial part of the wing structure, serving as a link between the wing stringers and spars. Each wing rib is designed to conform to the airfoil shape of the wing, which as a result contributes to the aircraft's aerodynamic performance. In addition, ribs help transfer loads and distribute shear forces, which aids in resisting the torsion caused by lift.

The spacing of the ribs was determined by examining other transport aircrafts. The spacing between ribs was selected to be 24 with additional ribs incorporated in the wing box at a 12 *in* spacing. To maintain structural rigidity, the rib thickness was chosen to be 0.2 *in*. Figure 67 provides a visual representation of the designed wing rib.

Figure 67: Wing root rib CAD model

A crucial aspect of rib design was to include cutouts on the nose and center rib, which allow for equipment and fuel pipes to pass through while reducing weight. It should also be noted that rib sizing varies along the span due to wing tapering.

Stringers

The stringers, in addition to the spars, are crucial elements of the wing box and run parallel to the wing structure. They serve the purpose of defining the wing's shape and transferring load and stress from the skin to the underlying structures.

The stringer was designed with a Z cross-section because of they provide a greater moment of inertia which makes stringers more rigid and better withstand bending loads [22]. Additionally, the Z-shape is easy to manufacture and install while also being a cost-effective solution [22]. From the wingbox idealization the stringer area was calculated to be 0.310 in^2. Figure 68 shows the cross-section of the stringers which reflect the calculated stringer area.
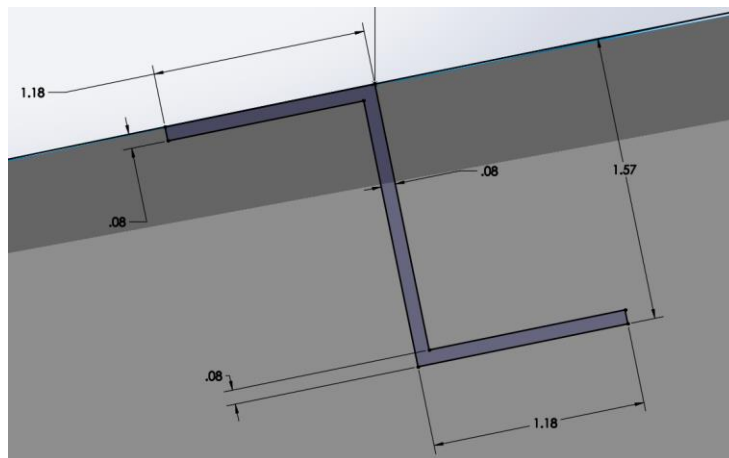
Figure 68: Stringer cross-section

The spacing at the root, or the base of the wing, is 7 *in*, while the spacing at the tip is 3 *in*. In total, there are 24 stringers present. The thickness of each stringer is 0.08 *in*.

10.3.2 FEA Results

To validate the design of the wing an FEA analysis was performed. The wing was fixed at its root and the forces related to the moment stipulated in Figure 69 were applied to the front and rear spar. 70% of the load was applied to the front spar as it closer to the aerodynamic center. Additionally, stringers were omitted in this analysis to avoid running into errors related to meshing and available computer memory. The wing skin and torsion were also ignored to simplify the analysis.
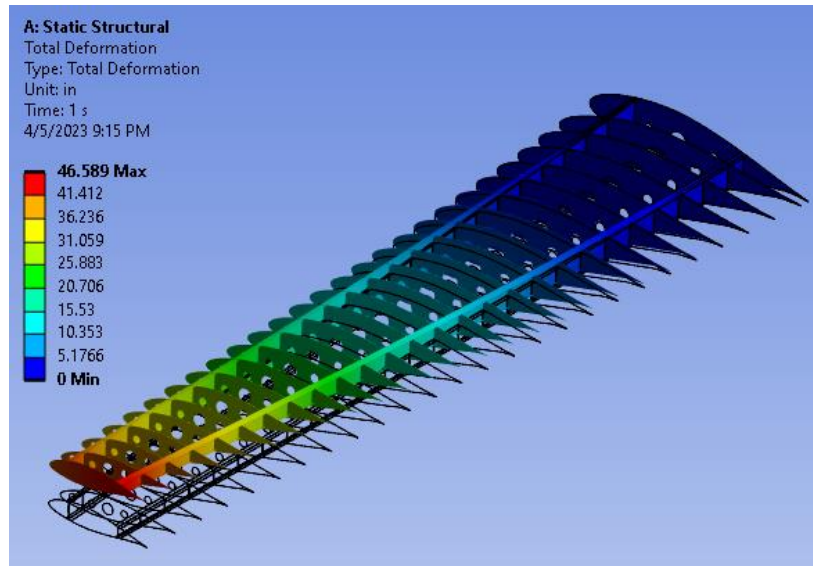
Figure 69: Wing total deformation
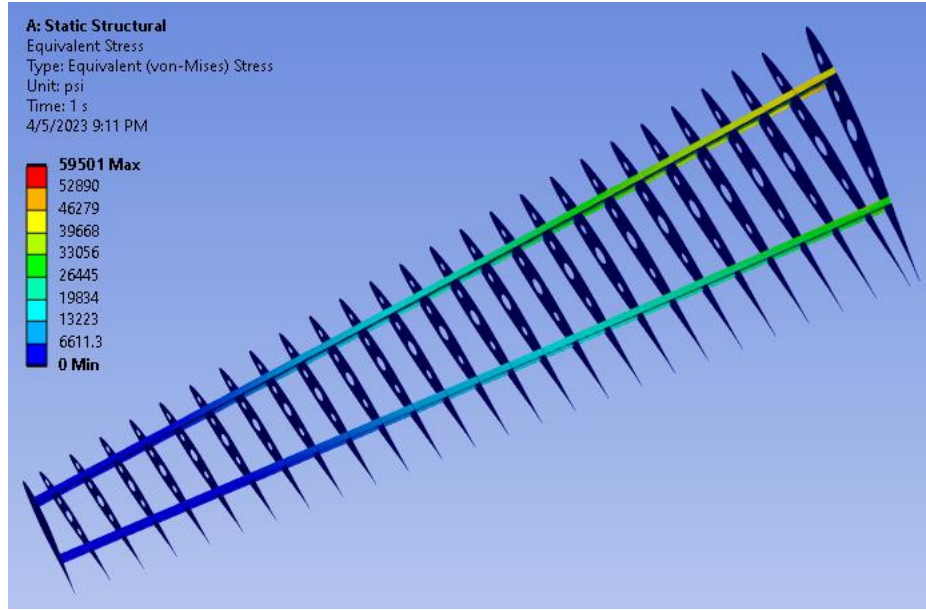
Figure 70: Wing Von-Mises stress

The results presented in Figure 69 and Figure 70 show a total deflection of the wing of 47 *in* and a maximum stress of 59.5 *ksi*. The maximum stress is below the material limit of 78 *ksi* with a safety factor of 1.3. The total deflection of the wing is fairly high, but airplane wings do bend during flight as they are not completely rigid, and the analysis modelled the wing as a cantilever beam.

10.3.3 Wing Mounts

Mounts were installed on the fuselage frames to connect the wings to the fuselage, with the capability to withstand the shear load exerted by the wings. The mounts are connected to both the trailing and leading-edge spars.

The wing is mounted to the fuselage using eight shear lugs or bolts connect to the front and rear spars. Mounting in shear makes manufacturing easier as less fasteners must be installed. Figure 71 contains the final wing mount structure including how it attaches to the center wingbox and integrated fuselage frames.
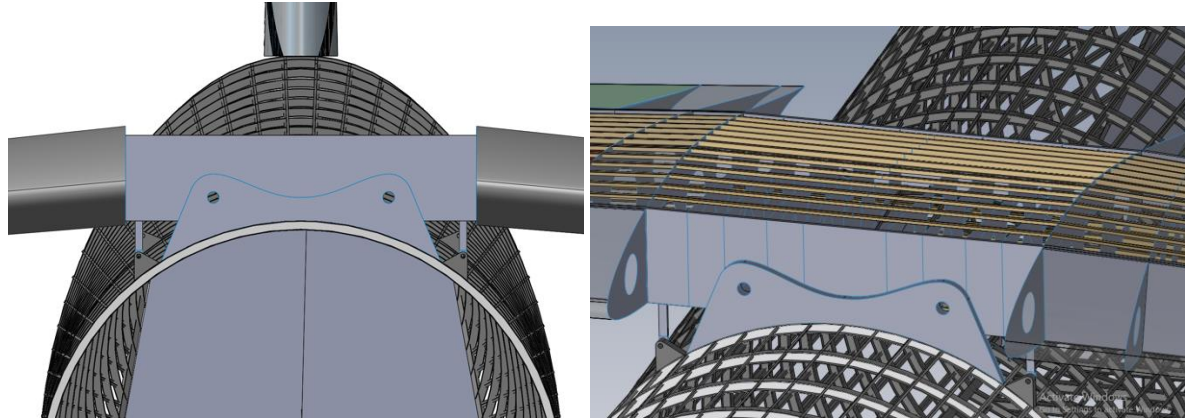
Figure 71: Wing mount structure

10.3.4 Final Wing Structure

This final wing section consolidates all the design parameters that were selected the wing structure. Table 28 and Table 29 contain the wing's geometry and the spacings of its structural elements and Figure 72 shows a final render of the wing structure with the appropriate fuel tank.

Table 28: Final wing geometry

	Geometry
Reference Wing Area (S) (in^2)	183456
Wingspan (b) (in)	1347
Root Chord (c_{root}) (in)	187
Tip Chord (c_{tip}) (in)	84
Mean Chord (in)	142

Table 29: Final wing structural element specifications

Components	Location	Value
Front Spar	Root - 20% Chord	37 *in* from LE
	Tip - 20% Chord	17 *in* from LE
Rear Spar	Root - 70% Chord	131 *in* from LE
	Tip - 70% Chord	59 *in* from LE

Ribs	Spacing	24 *in*
	Number	29
Stiffeners	Root spacing	7 *in*
	Tip spacing	3 *in*
	Number	28
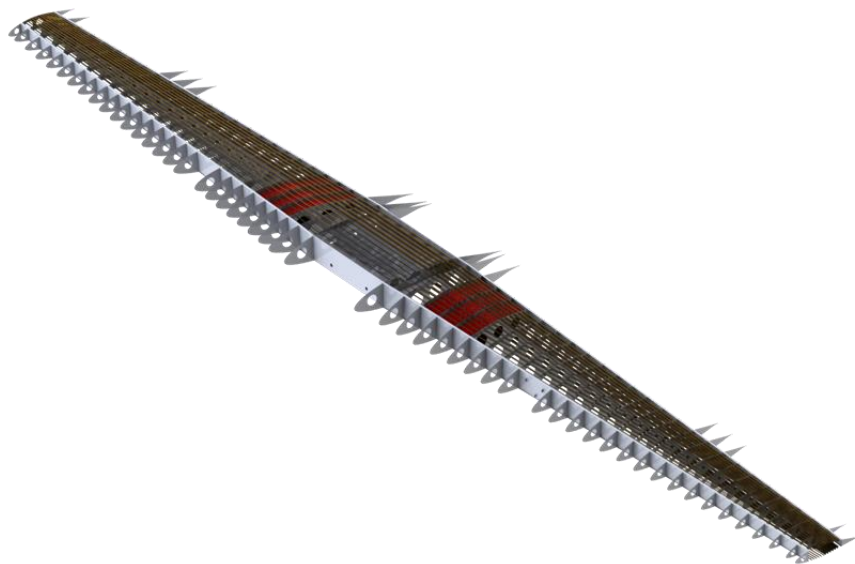
Figure 72: Final wing structure rendering

10.4. Empennage

The empennage structure was developed similarly to the wing, using dimensions for the wing spars, stringers, and ribs as references. Using this information, the front and rear spars were positioned at 20% chord and 70% chord, respectively, to align with the fuselage primary member and provide ample space for the elevator and rudder. The structural arrangement of the empennage can be seen in Figure 73.
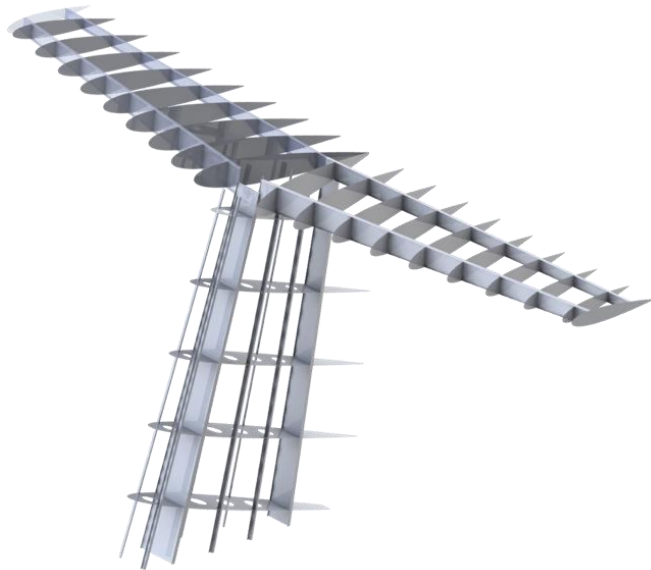
Figure 73: Empennage structural render

10.4.1 Vertical Stabilizer

The vertical stabilizer is an essential component of an aircraft's tail section that provides directional stability and control during flight. The spars are located at 20% and 70% of the chord length from the leading edge, while the ribs are spaced 24 *in* apart and 8 stiffeners are evenly spaced around the center cell of the rib. The connection of the vertical stabilizer to the horizontal stabilizer is made at the top of the spars, while the connection to the fuselage is made at the bottom of the spars.

10.4.2 Vertical Stabilizer FEA Results

Finite element analysis is carried out on vertical stabilizers to assess their structural integrity and performance under different load situations. A force of 13,488 *lbf* was applied as the side force generated by the rudder at maximum deflection. The load distribution was approximated to be non-uniform, with 70% of the load being carried by the front spar, while the rear spar carried the remaining 30%. The total deformation and equivalent stress of the vertical stabilizer structure was analyzed and measured in *in* and *psi*, respectively.
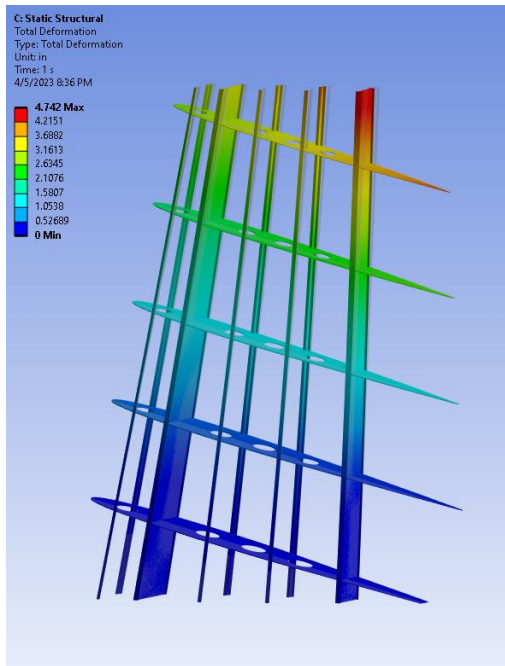
Figure 74: Vertical stabilizer total deformation
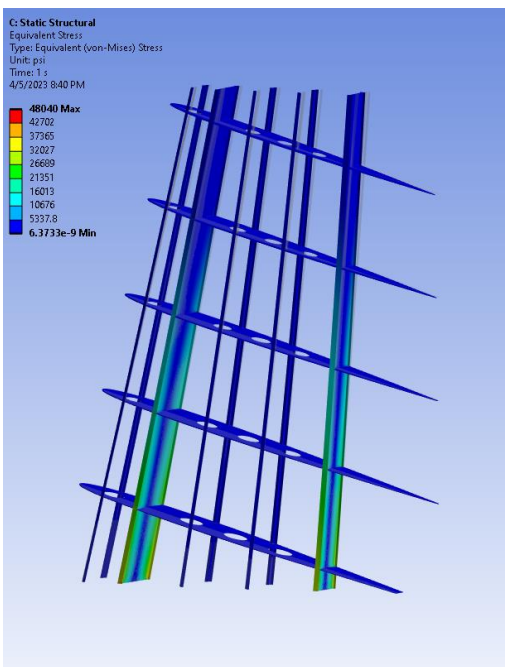
Figure 75: Vertical stabilizer Von-Mises stress

Based on Figure 74 and Figure 75, it was observed that the maximum stress recorded in the horizontal stabilizer was 58 *ksi*, which is lower than the yield strength of the material used.

Additionally, the maximum deformation measured was 4.74 *in*, which is deemed to be within acceptable limits.

10.4.3 Horizontal Stabilizer

The horizontal stabilizer is an integral component of an aircraft's tail section that plays a vital role in maintaining the aircraft's pitch stability and control. The structure of a typical horizontal stabilizer includes spars and ribs. The spars are located at 20% and 70% of the chord length from the leading edge, while the ribs are spaced 24 inches apart. The spars serve as the primary load-bearing members of the structure and provide support to the ribs. The ribs help to maintain the shape and integrity of the horizontal stabilizer and provide a surface for the attachment of the control surfaces such as the elevators.

10.4.4 Horizontal Stabilizer FEA Results

A total lift force of 12,281 *lbf* was applied on the vertical stabiliser. This force was calculating the amount of force the horizontal stabilizer produces at maximum elevator deflection. Similarly, to the wing, the front spar is closer to the aerodynamic center so 70% of the load was applied to the front spar and the remaining 30% on the rear spar. However, the load was not uniformly distributed between the front and rear spars of the horizontal stabilizer, with 70% of the load being carried by the front spar and the remaining 30% by the rear spar. The total deformation and equivalent stress of the horizontal stabilizer structure measured was analyzed and expressed in inches and psi, respectively.
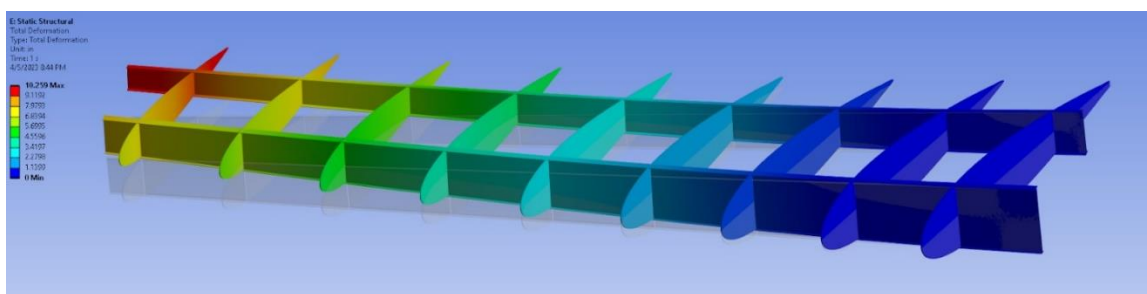
Figure 76: Horizontal stabilizer total deformation
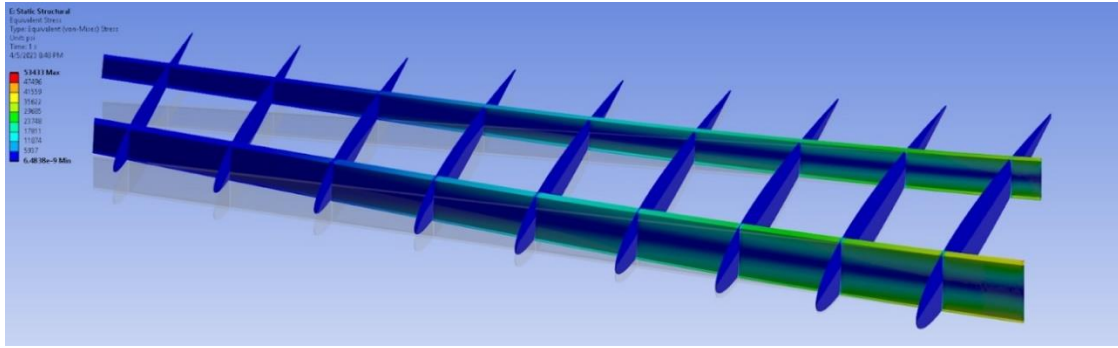
Figure 77: Horizontal stabilizer Von-Mises stress

Referring to Figure 76 and Figure 77, the maximum stress was 53433 *psi*, which is lower than the material's yield strength. As well as the maximum deformation was 10.26 *in*, which is within an acceptable range.

10.5. **Landing Gear**

The landing gear must be designed to withstand the forces of impact during landings, support the weight of the aircraft, and provide stability on the ground. Throughout the design process, the landing gear has undergone multiple iterations, with reference to existing designs mechanism and newly developed. This section will provide a detailed explanation of both the main landing gear and nose landing gear.

10.5.1 Main Landing Gear

The design of the landing gear was described in the sizing section; therefore, this section will only discuss the validation of the calculated dimensions. The challenging task in performing an FEA on the landing gear is to simulate the dynamic nature of the landing gear. For the analysis a static scenario was followed, where all the weight of the aircraft is on the landing gears. The landing gear must be able to withstand the maximum weight of the aircraft without failure. The maximum landing weight assumed in the design process was 90% of the maximum takeoff weight. The main landing gear is responsible for carrying 90% of the aircraft's weight, which means that each strut must take on 45% of the load. In a dynamic analysis scenario, such as during an impact with the landing, the landing gear design must also consider the dynamic forces generated during the landing. Figure 78 depicts the main landing gear in both the retracted and extended positions.

Figure 78: Main landing gear in retracted (left) and extended positions (right)

10.5.2 MLG FEA Results

As stated previously the load applied on the main landing gear was 45% of the maximum takeoff weight which was calculated to be 19,783 *lbf*. This load was applied on the bottom of the tires while the top of the strut was fixed to simulate the reaction force from the tarmac.
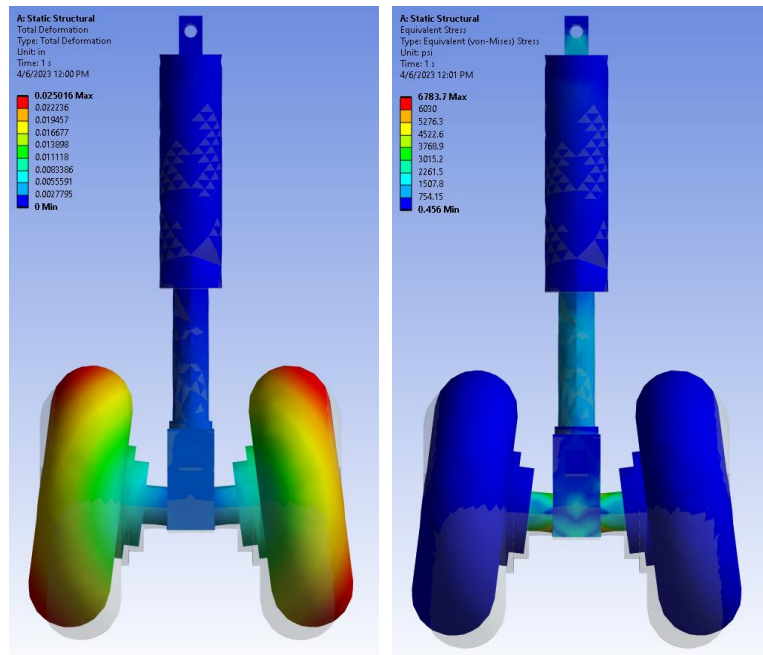
Figure 79: Main landing gear total deformation (left) and Von-Mises stress (right)

Figure 79 contains the results of the FEA for the main landing gear and depict how the strut and strut fittings distribute stress under a load and withstand deformation. The maximum deformation was determined to be 0.025 *in*, which is not a significant amount. The maximum stress was 6,784 *psi*, which is lower than the yield strength of Ti-6AL-4V.

10.5.3 Nose Landing Gear

The structure of the nose landing gear consists of a single strut with a wheel at the bottom, which is attached to the cockpit of the aircraft. The nose landing gear, which is responsible for supporting approximately 10% of the aircraft's weight, has been designed with specific specifications to withstand braking and static forces, and to ensure the aircraft remains balanced during landing. Figure 80 displays the nose landing gear in both the retracted and extended positions.

Figure 80: Nose landing gear in extended (left) and retracted (right) positions.

10.5.4 NLG FEA Results
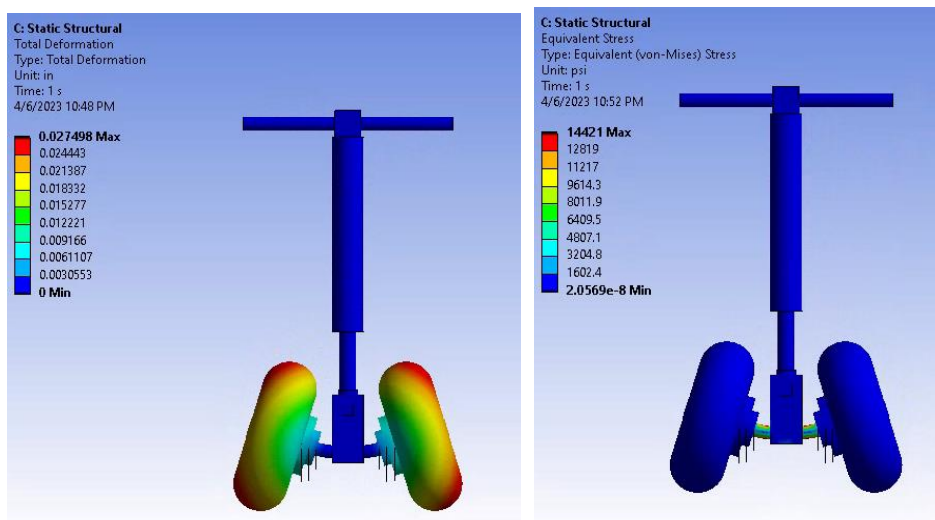
Figure 81: Main landing gear total deformation (left) and Von-Mises stress (right)
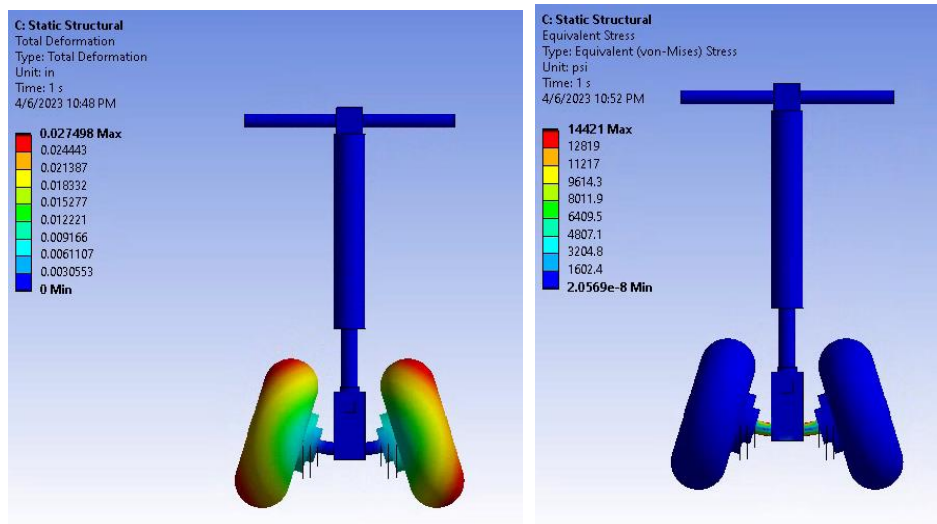
Figure 81 above represents the FEA results for the nose landing gear under 10% of the maximum takeoff weight which was determined 4400 lbf. Similarly, to the main landing gear this force was applied to the bottom of the tires while the struts were fixed. The results of this analysis were that the maximum deformation was 0.026 inches while the maximum stress was 5257 psi. This maximum stress value was found to be below the yield strength of Ti-6AL-4V.

10.6.   Engine Structure

The engine is mounted of the wing using a simple truss structure. The truss structure houses the PW127XT turboprop engine. The truss structure resists axial loads from the engine thrust transferred through engine hard points.
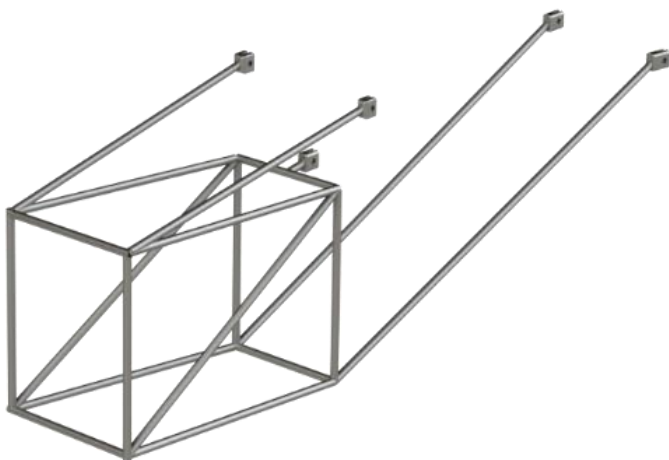
Figure 82: Engine structure

The engine is secured onto the wing using shear lugs on the front and rear spars. There are three shear lugs on the front spar and an additional two lugs on the rear spar. Figure 83 shows the integration of the engine structure to the wing and engine.
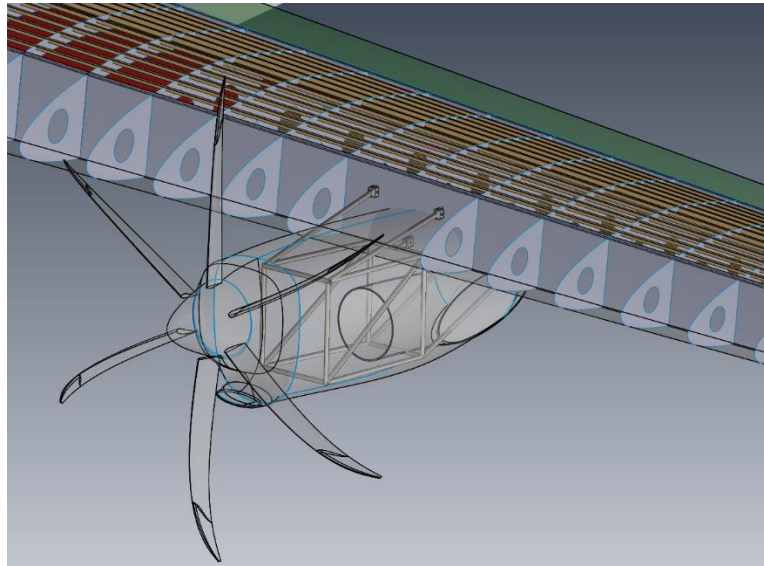
Figure 83: Integrated engine structure

As seen in Figure 83, the rib right in front on the engine was cut to allow the third hard point to be placed on the front spar.

10.7.   Cargo Door

The cargo door is an essential part of the aircraft. It should be able to withstand the weight of the payload, jigs and any operational personnel. To validate the design of the door an FEA was performed to simulate a worse case loading scenario. The door was fixed at the hard points used for actuators and the pogo sticks. The worst-case scenario is an event where the MTOW is applied of the surface of the door. Hence, a pressure force of 10,000 *lb* was applied on the upper surface of the bottom door.
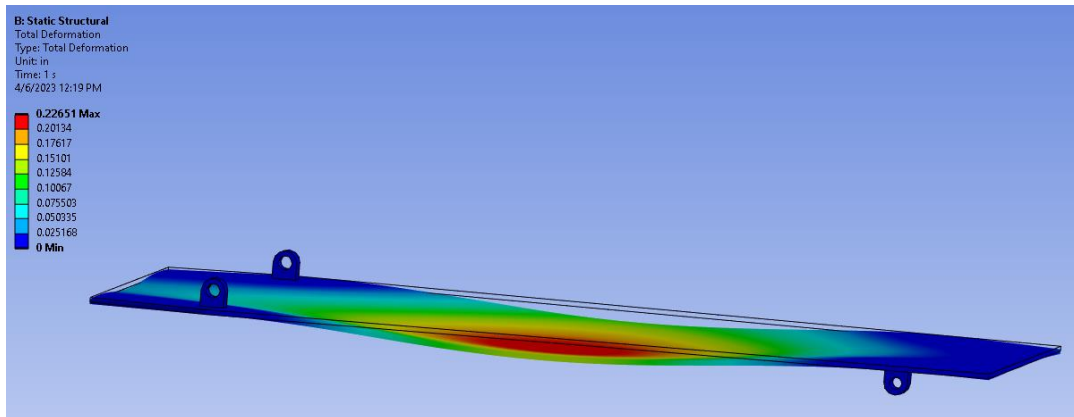
Figure 84: Cargo door total deformation
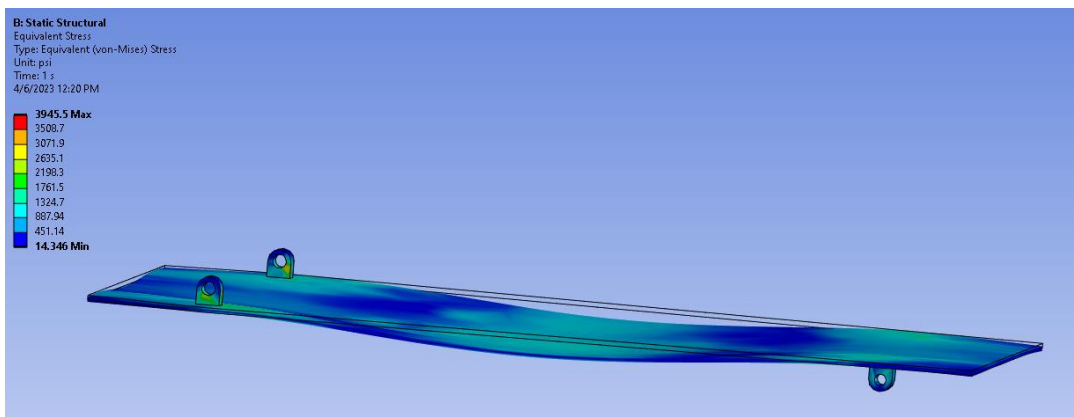
Figure 85: Cargo door Von-Mises stress

Figure 84 and Figure 85 represent the displacement and stress on the cargo door under the pressure due to the maximum payload weight.

11. Interior

The interior of the Hauler – X aircraft consists of numerous components to ensure that the payload undergoes safe loading, stays secure throughout the entire flight, and can be unloaded easily and efficiently after landing. Thorough research has been collectively conducted to comprehend the various methods which could be implemented to meet the mission objective. First the required spacing was assessed, then the bay's size was calculated as a rectangular parallelepiped. Next, support structures to hold the payload in place were designed, which included support jigs, locks, rollers, and rails.

11.1 Jig Formation

Jigs for the cockpit and rear fuselage of the Global 7500 were initially designed separately to ensure that each section of the jig could support the respective payload. This was verified through a structural analysis in ANSYS. The following figure shows an isometric view of the cockpit jig.
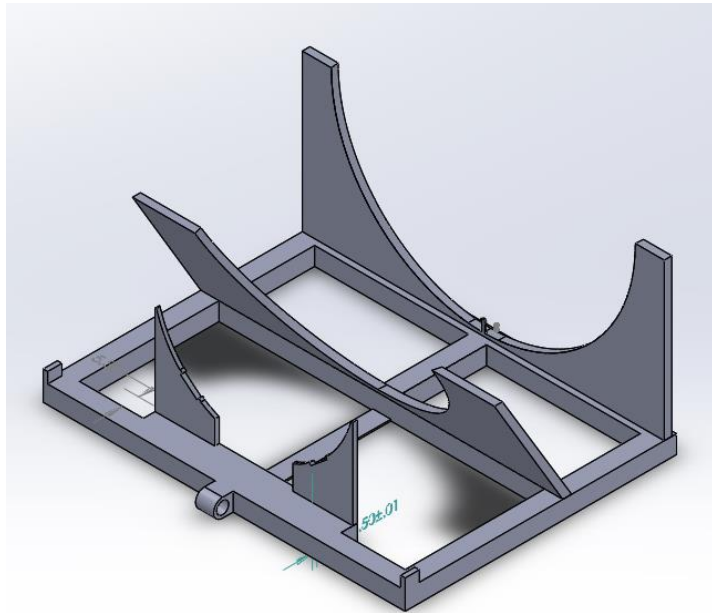
Figure 86: Cockpit jig assembled

The jig consists of a base with a winch attachment point, a front, rear, and middle support that rest along the hardpoints of the Global 7500's cockpit. At the semi-circular supports will be tie to

further support the payload in conjugation with the hardpoints. The tie down areas are shown by the purple sections on the payload. The cockpit is constrained in the horizontal direction through the front support, which is displayed in the following figure.
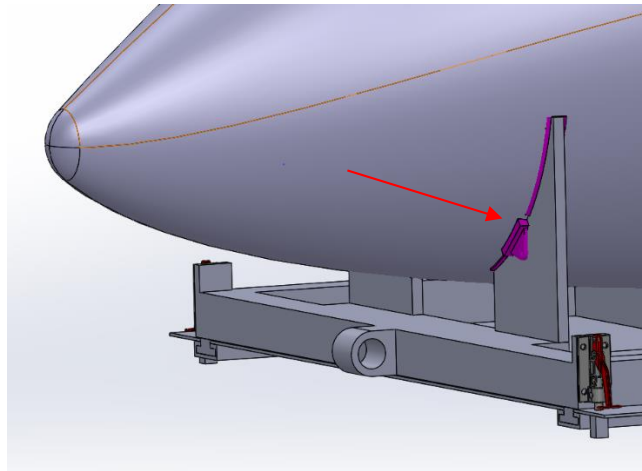
Figure 87: Front tiedown support of the cockpit jig

The rear fuselage jig was similarly designed with front middle and rear supports along the hardpoints of the Global 7500's rear fuselage. The rear fuselage jigs will also be supported with tie down over the semi-circular support sections similarly to the cockpit jig. The tie down areas for the rear fuselage are highlighted in purple. Engine mount supports were incorporated as well as a front support to secure the rear fuselage in the horizontal direction. The rear fuselage jig and the horizontal supports are displayed in the following figures.
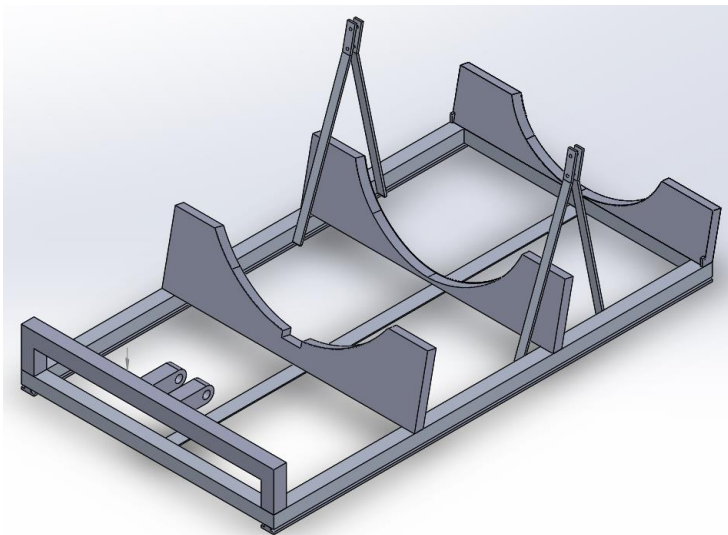
Figure 88: Rear fuselage assembled jig
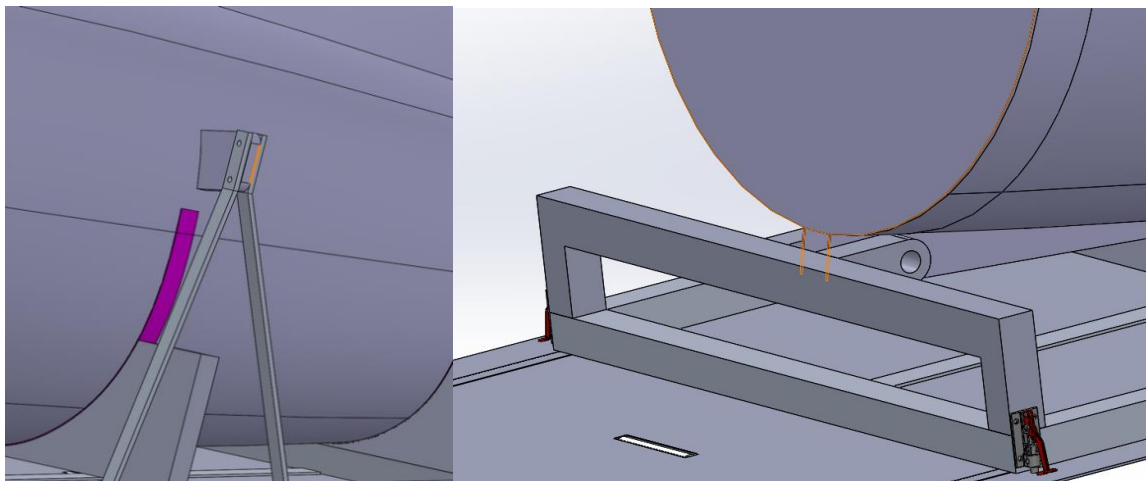
Figure 89: Front and engine mount support on the rear fuselage jig

The following figures display the cockpit and rear fuselage of the Global 7500 loaded onto their respective jigs.
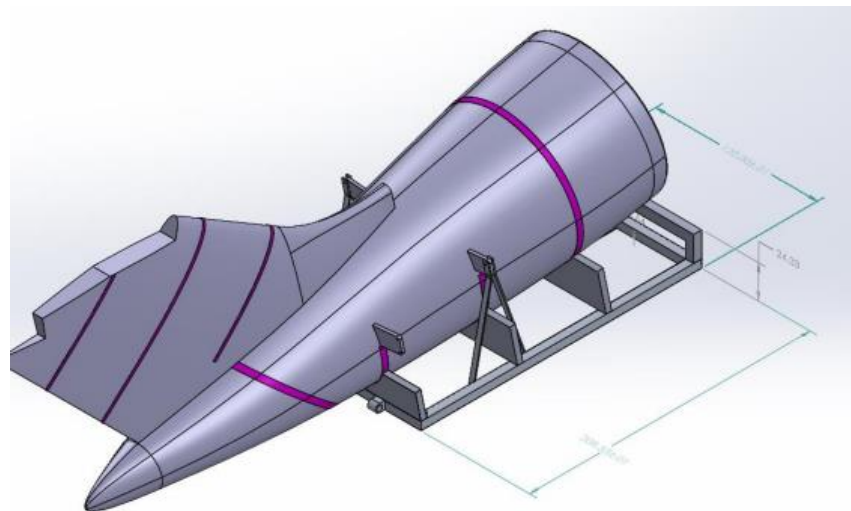
Figure 90: Assembled rear fuselage payload on corresponding jig
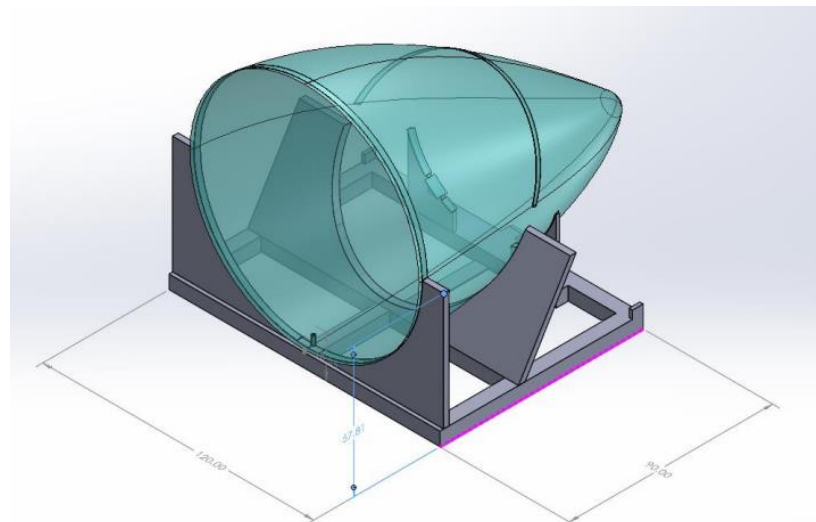
Figure 91: Assembled cockpit payload on corresponding jig

The above figures further display each jigs front, middle, and rear supports along the hardpoints of the Global 7500 assembly parts.

11.2 Payload Securing Components

Several interior parts were designed in Solidworks for the loading and unloading procedure of the payload, including rollers and locks. The following figure displays the assembled roller that will be used within the floor of the cargo bay.
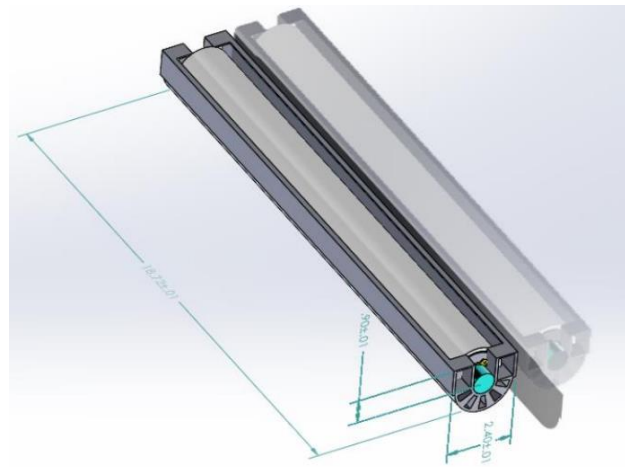
Figure 92: Assembled roller

The roller displayed in the above figure consists of the holder for the roller, the inner pipe shaft (blue), the pipe shaft (white), and ring (yellow), to keep them aligned. Rollers were chosen to be used inside the floor of the cargo bay over having a jig design with wheels to minimize the height of the payload within the cargo bay. Using rollers helped to optimize the sizing of the plane for greater fuel efficiency and lower operating costs. Placing the assembled rollers on the floor with each end pointing towards the rails, in an equidistant manner allows for a smooth loading/offloading. Like most of the interior components, besides the pipe shaft, the roller would be composed of Al 7075-T6. The pipe shaft was chosen to be composed of stainless steel since it would be the point of contact for the payload and is most commonly used for that purpose.

Similarly, cantilever locks were incorporated into the full assembly of the payload within the cargo bay in order to fully secure the jigs in the horizontal direction. The cantilever lock is displayed in the following figure.
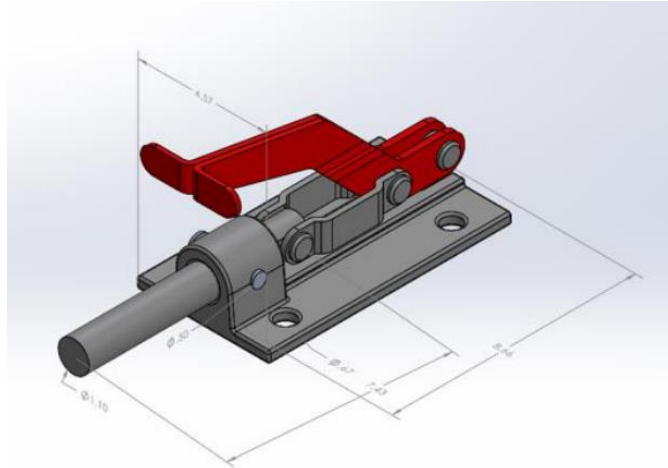
Figure 93: Cantilever lock

A cantilever lock was chosen for the design concept as it operates linearly and requires no external mechanism to operate. In order to have a strong and robust linkage, no hydraulic or electronic system were required. A pin going through the lock itself prevents it from unlocking. The lever cannot be pulled upwards until that exact pin is displaced. The payload requires 6 of these locks to be fully secure as we planned, with 2 of them being on the engine mount section and the other 4 would be at each corner of the combined jig structure. The flight crew on board could easily activate and disengage the locks. Another advantage of this type of locking mechanism is that it is visibly noticeable when it is locked or unlocked. This lock would be composed of the same Al 7075-T6, as most of the other metal components for the interior.

Lastly, a winch was required for the payload structure to be pulled into the interior during rear loading. We researched existing models and found an abundance of useful winch designs. Based on our interior sizing, the winch model shown in the figure below was selected to be implemented as it is capable of pulling over 50000 *lbs*.
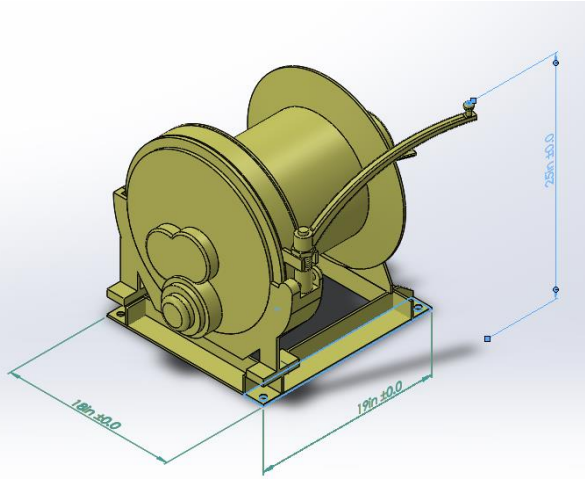
Figure 94: Winch used for moving the payload

It's noteworthy that the same winch is placed on the other end, i.e., on top of the loading truck. This is displayed in figures included in the next section which outlines the procedure for loading and offloading.

Appendix B can be referred to for all other designs for the interior such individual jig components and their respective dimensions. The following figure shows the full assembly of the payload within the Hauler – X interior including the jigs, floor, rollers and locks.
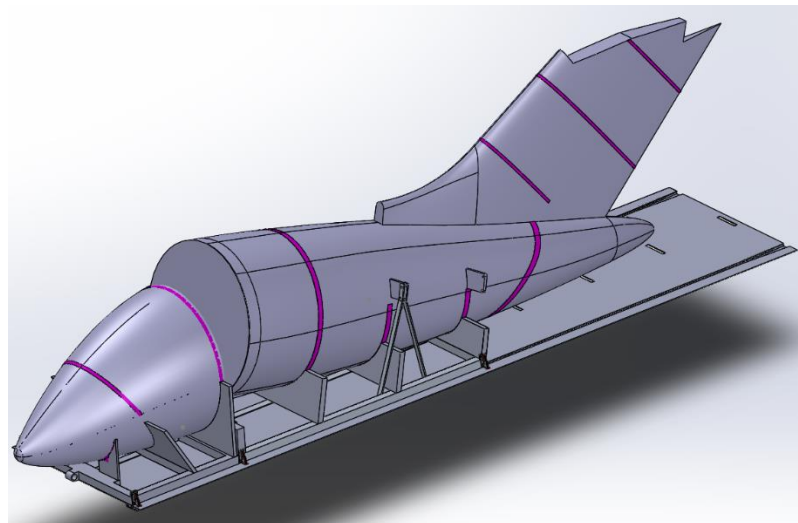
Figure 95: Fully assembled payload with all supporting components

11.3 <u>Loading and Unloading Procedure</u>

The chosen method to transfer the payload onto the aircraft is from the rear. This option was selected to optimize the loading/unloading time taken. The rear door opening mechanism was hence designed accordingly to accommodate the payload with adequate clearances. The specifications and placements of the actuators play a vital role in this procedure. The rear door has 3 parts. The two symmetrical parts on the top open outward on their respective sides while the bottom section opens downward to the ground. However, for the loading and unloading process, the bottom section lies parallel to the ground sitting on top of the truck that shall carry the components. This is done with the aid of 2 pogo sticks supporting the door from falling out completely and to prevent any chance of the aircraft tipping over during loading. An example of same level loading is shown below:

Figure 96: TLD-DBL-100 truck loading cargo onto a Dreamlifter [26]

Lift platforms carried by trucks of such category are capable of carrying over 40,000 *lbs* of load which is well above our maximum payload of 10,000 *lbs*. The platform is typically 1458 inches long and 885 inches wide. Our assembled payload is well within this range (600x120 sq. ft maximum) which is why selecting this lift is justified. The entire process for the cargo loading of the Hauler - X is outlined below chronologically, step by step. Screenshots of CAD for each phase were used to help visualize the full process. The procedure begins with the assembled payload on

an airport loading truck. A simple CAD model of the supposed loading truck was used to demonstrate what this would look like and can be seen in the following figure.
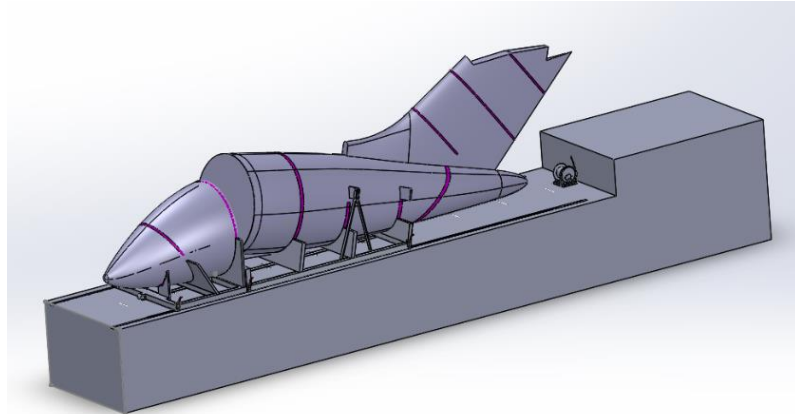
Figure 97: Assembled payload on a temporary model of the loading truck

The loading truck is to make its way to the rear of the plane to align itself with the rear cargo door. As this is happening, the rear cargo doors should be opened and pogo sticks should be attached. The following figures demonstrates the process of the rear door opening.
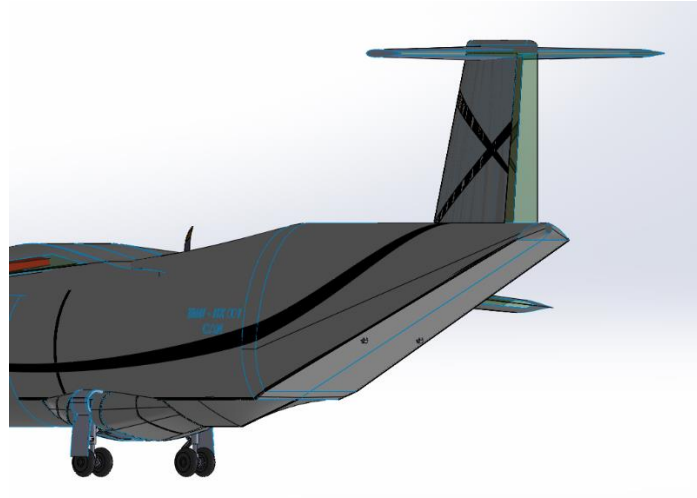
Figure 98: Closed cargo doors
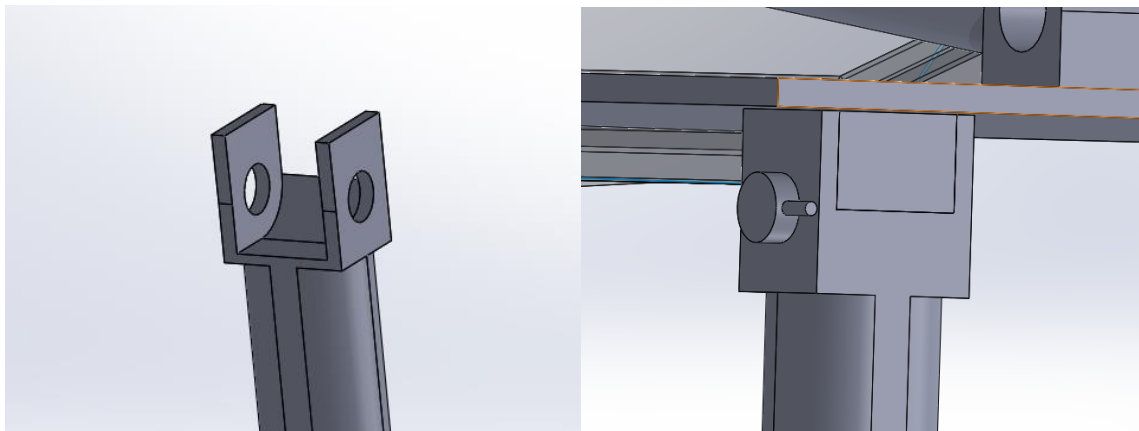
Figure 99: Pogo stick

Figure 100: Cargo doors open with pogo sticks attached

Figure 99 displays how the pogo stick attaches to the rear door through a pin connection. Once the rear door is open, the truck should be aligned to the aircraft as shown in the following figures.
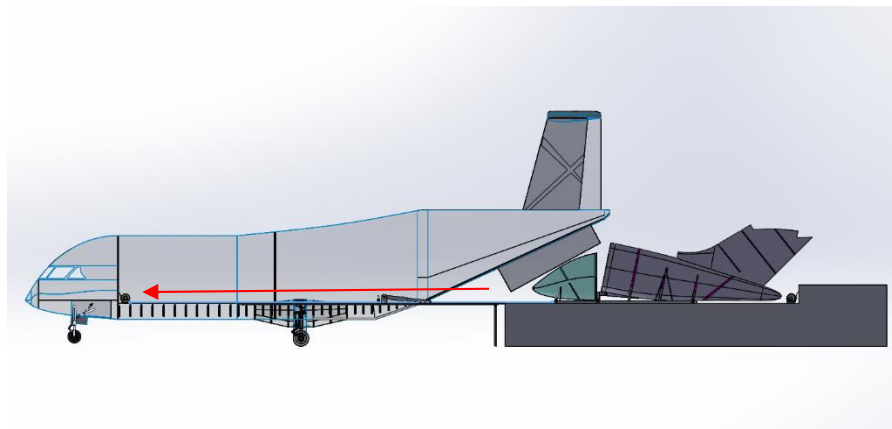
Figure 101: Truck aligning with the Hauler-X for loading
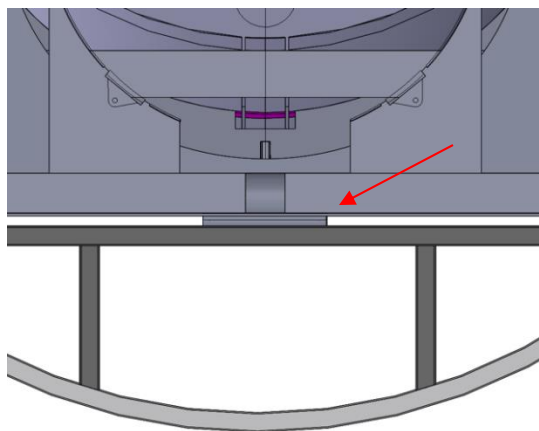
Figure 102: Jig on top of the rollers
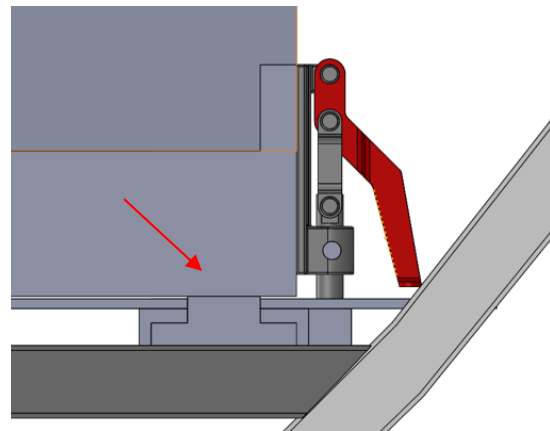
Figure 103: T-rails fitting into the cargo floor

Figure 101 demonstrates the location of the loading truck in reference to the Hauler-X's extended rear doors, with the arrow signifying the intended direction that the winch at the back of the bay will pull in the payload. Figure 102 outlines the connection of the jig base to the rollers in the cargo floor where Figure 102 shows how the T-rails should align and fit into the floor. Furthermore the following figures display the winch attachment points at the front of the jig, along with further demonstrations of the winch loading process.
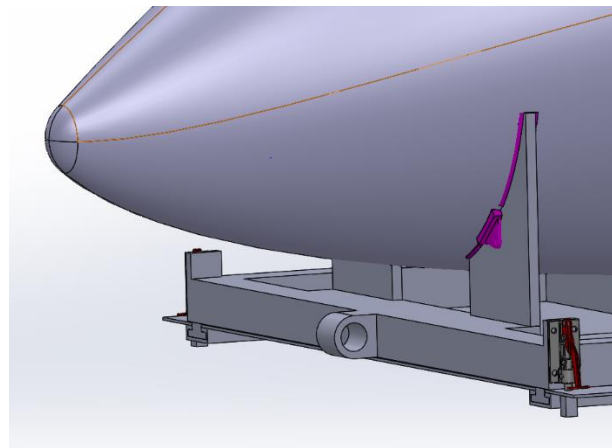
Figure 104: Winch attachment point on the cockpit jig
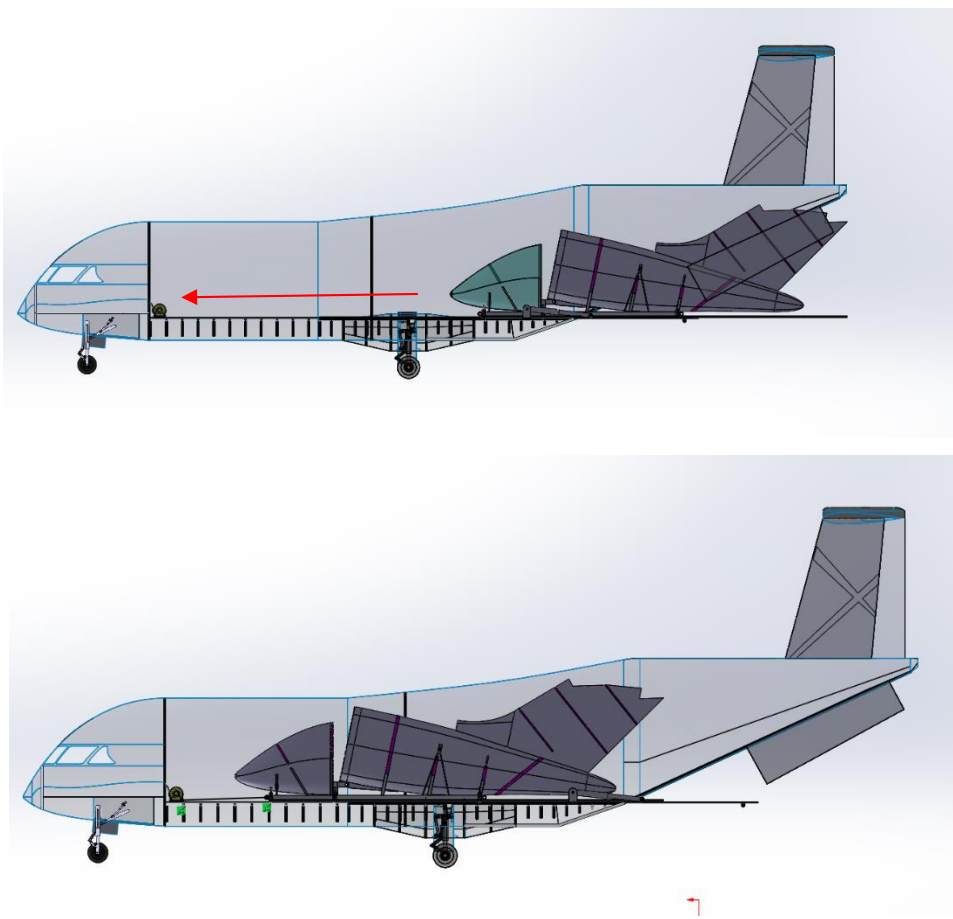
Figure 105: Payload being pulled into the cargo bay by the winch

Figure 105 displays the progression of the winch loading process. Once the payload has been entirely loaded into the cargo bay, the crew members are to lock the jig in the horizontal direction

using 6 cantilever locks. 4 locks are placed in each corner and 2 more are on either side of the engine mount connection points of the jig. The locks open and engaged position is shown in the following figures.
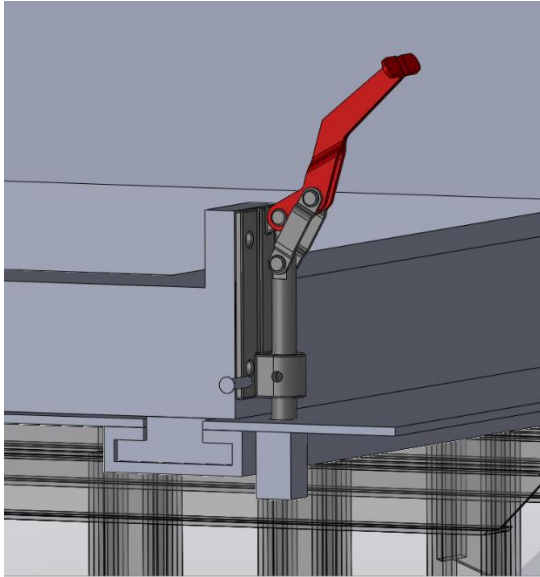
Figure 106: Payload lock in open position
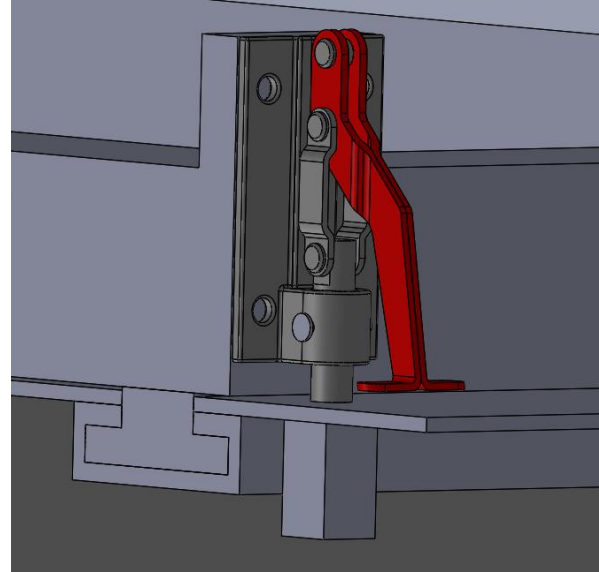
Figure 107: Payload lock in locked position

Once the locks are engaged, the rear doors are to be closed. The unloading procedure is the same as the loading procedure in reverse. Once the payload arrives at the desired location, a loading truck should line itself up with the rear of the aircraft. The rear doors should then be opened, locks disengaged, and the winch attached to the winch attachment points found at the back of the jig. The rear winch attachments points are shown in the following figure.
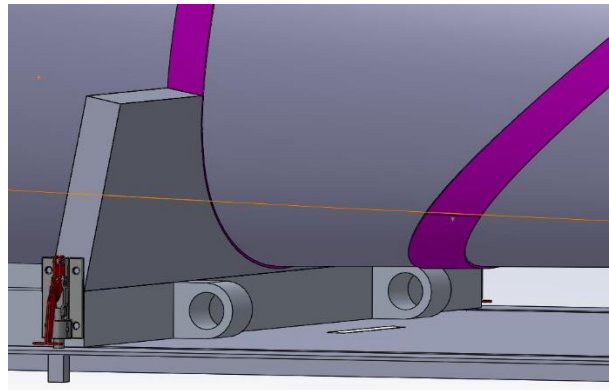
Figure 108: Winch attachment points on the rear fuselage jig

11.4 Structural Analysis of Jig Components

FEA structural analyses were performed on key supporting structures and components regarding the payload support and loading assembly including the jigs, locks, and pogo sticks. It was observed that minimal deformation and equivalent stresses occurs in every relevant supporting structure and component which is responsible for accommodating the payload and its loading/unloading procedure. This validates the structural integrity of the design and contributes to the requirement compliance of safely transporting the payloads. The following figures show the deformation and stresses of each analyzed component.
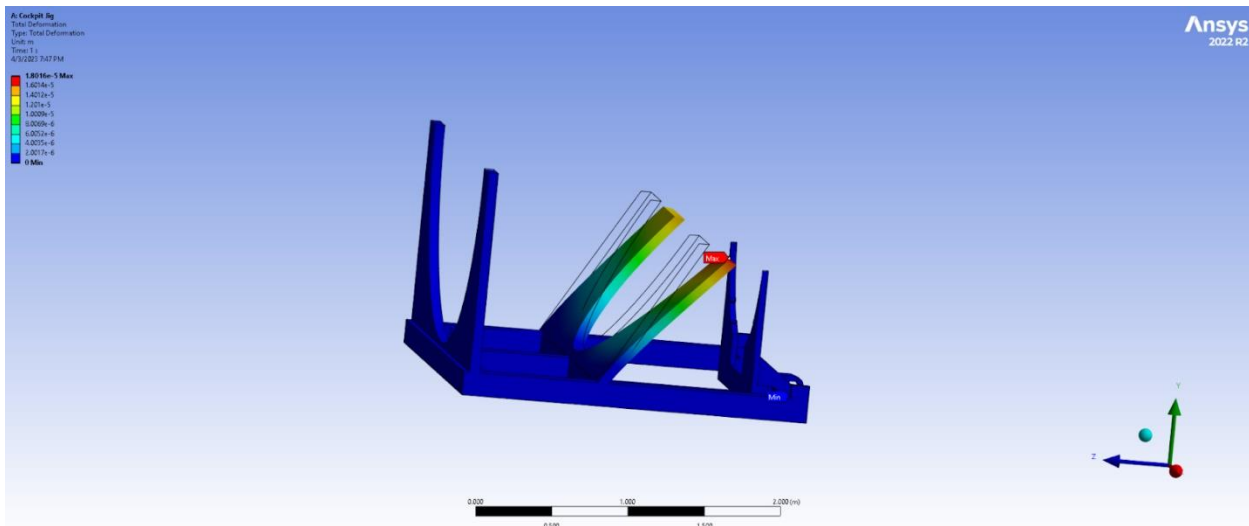
Figure 109: Total deformation of the cockpit jig

The figure above depicts the total deformation of the cockpit jig under loading with level flight conditions. As shown the maximum deformation of the jig due to the weight of the payload was 0.007 *in* which occurs at the middle support. This demonstrates that the proposed jig design is sufficiently strong for the payload it is required to carry. Similarly, equivalent stresses of the cockpit jig are displayed in the following figure.
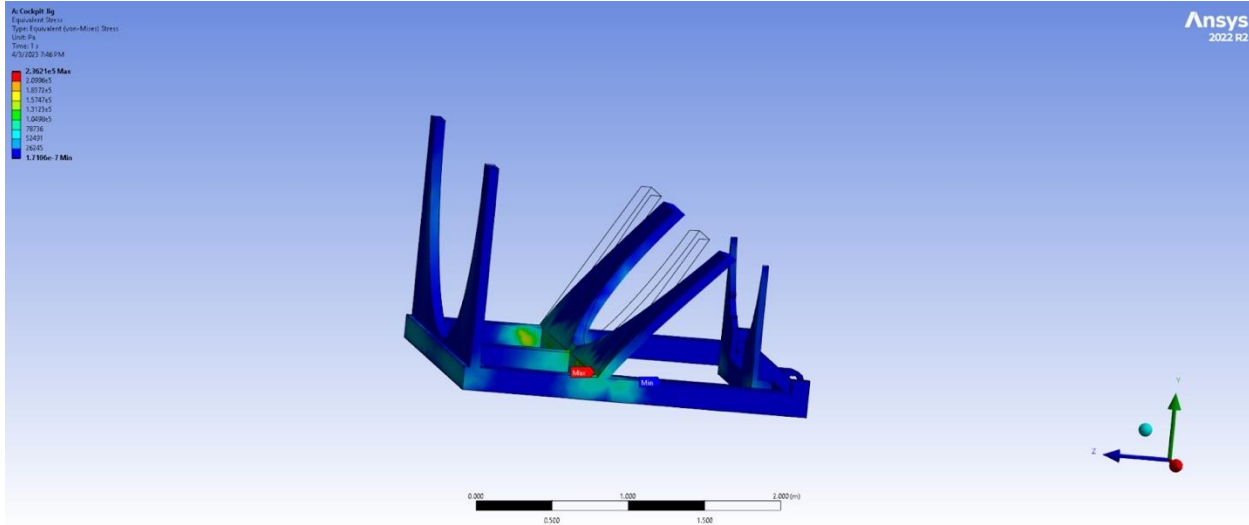
Figure 110: Equivalent (von-Mises) stress of the cockpit jig

The following figure displays the total deformation of the rear fuselage jig.
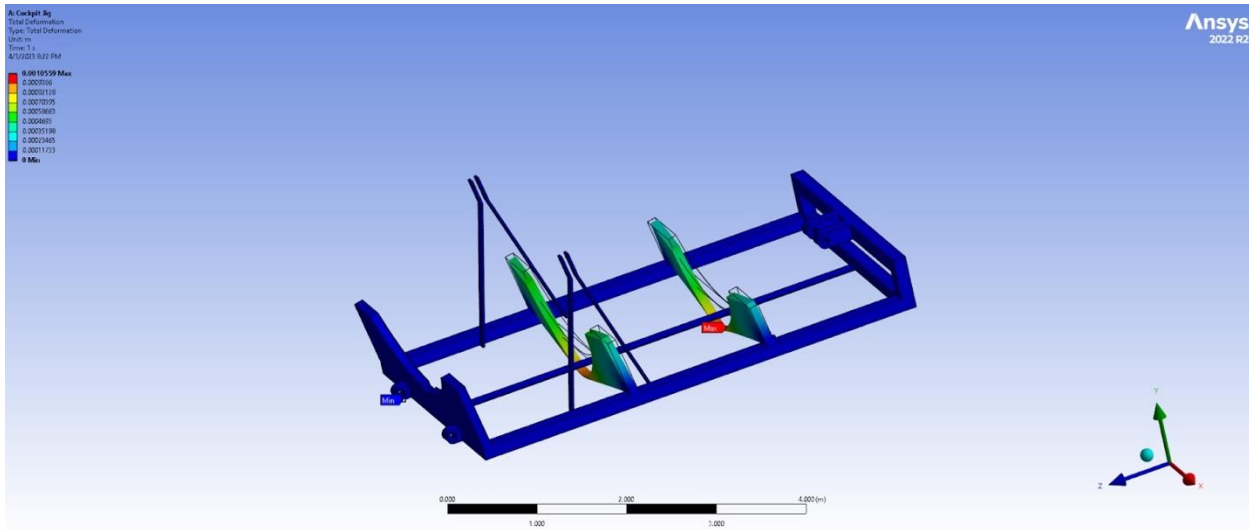
Figure 111: Total deformation of the rear fuselage jig

The maximum deformation of the rear fuselage jig occurs in the middle support with a value of 0.04 *in*. Similar to the proposed cockpit jig design, the rear fuselage jig is exceedingly strong for its intended purpose. Furthermore, the equivalent stresses of the rear fuselage jig are displayed in the following figure.
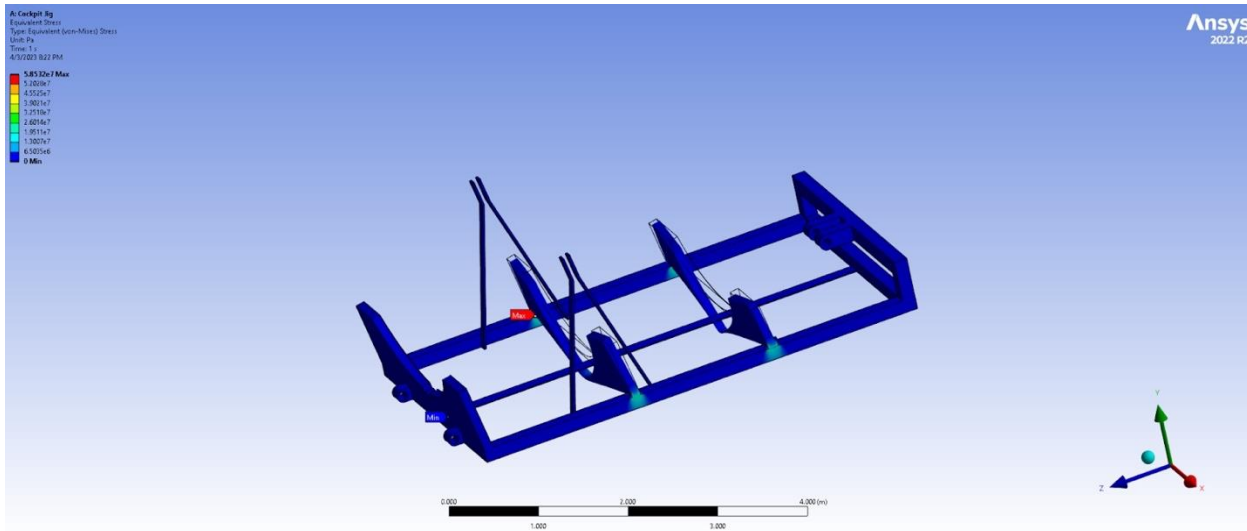
Figure 112: Equivalent (von-Mises) stress of the rear fuselage jig

The figure below displays the deformation on the pogo stick supports as the payload is being loaded onto the rear cargo bay doors.
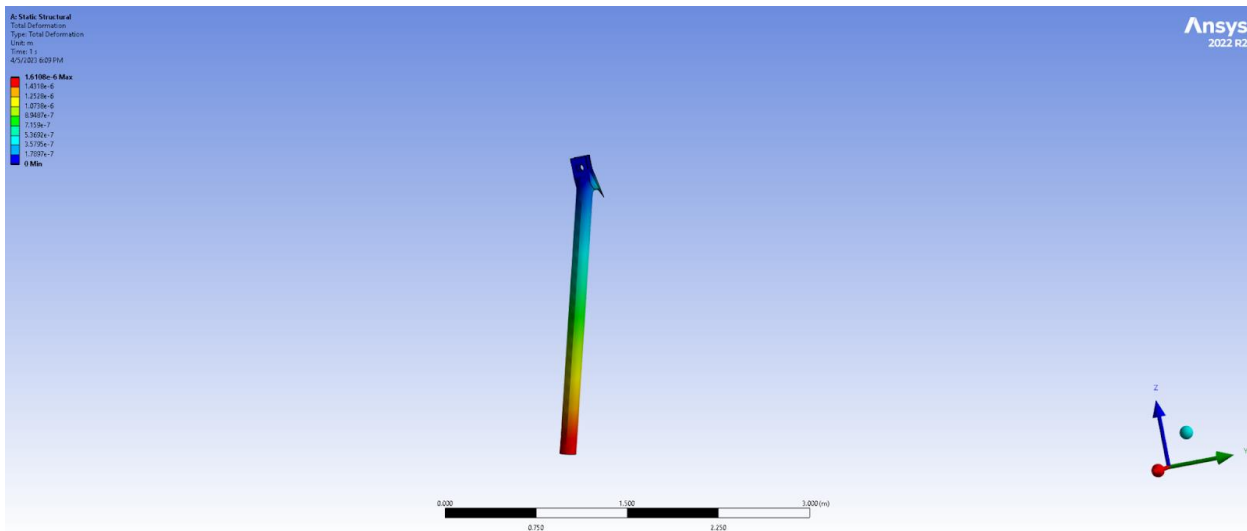
Figure 113: Total deformation of the pogo stick

From the FEA analysis conducted on the component, the maximum deformation was shown to be 0.00006 inches. This shows that the pogo sticks are exceptionally strong for their given application. Furthermore, equivalent stresses of the pogo stick is displayed in the figure below.
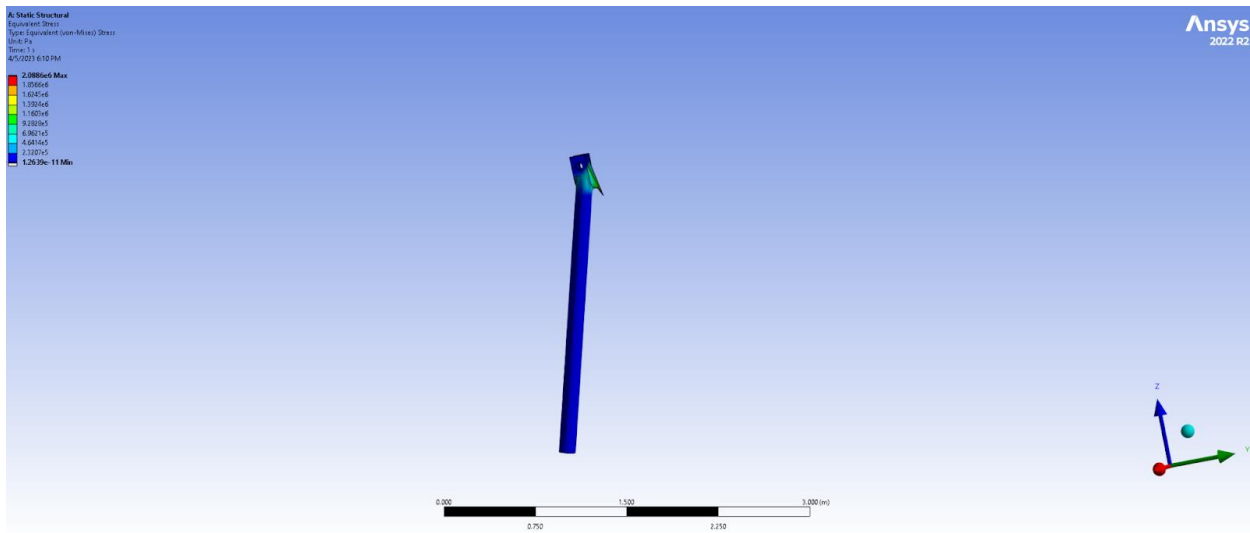
Figure 114: Equivalent (von-Mises) stress of the pogo stick

11.5 <u>Layout of Passenger Accommodation</u>
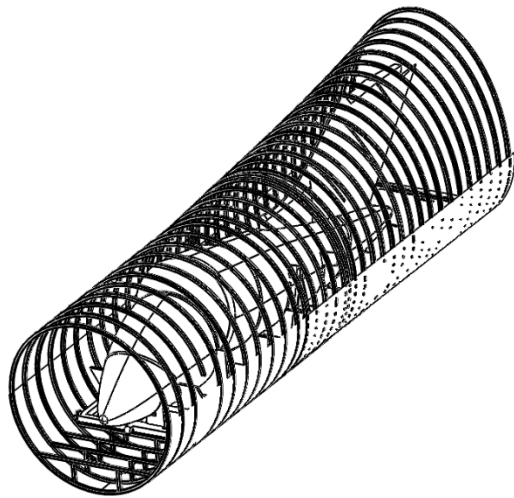
Figure 115: LOPA - Isometric view of the cargo bay

The image above depicts the LOPA of the cargo bay from an isometric view when the payload is in it fully locked configuration. In this configuration the interaction between the male rail fitting of the jigs and the female fittings in the floor, securing the payload to the floor can be seen. Also shown in this image is the structures beneath the floor which provide the support and structural integrity required to hold the cargo. Finally, the frames encompassing the circular cross-sections

as well as the transition can be shown. These provide the rigidity for the fuselages as well as a place for stringers and other support structures to be mounted.
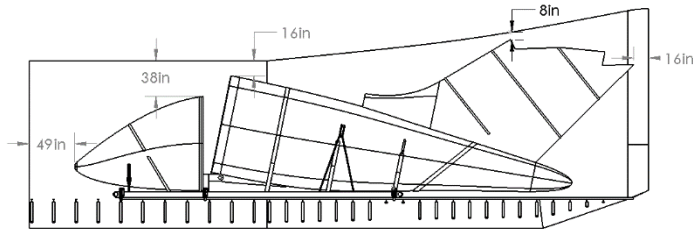
Figure 116 : LOPA - Sideview of the payload

The image above shows the LOPA of the cargo bay from the side view. The all of the clearances between the cargo and ceiling as well as the rear door and bulkhead have been dimensions. The notable clearance is between the nose of the cockpit payload section and the bulkhead at 49 inches. This is enough to have sufficient clearance according to far regulations. This clearance is shown further in the LOPA top view
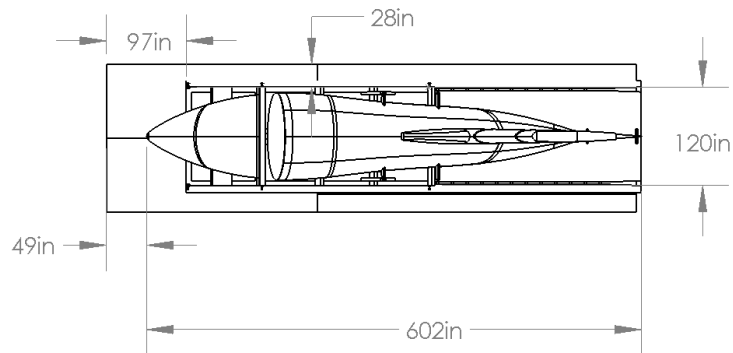
Figure 117: LOPA - Top view of the payload

The illustration above represents the LOPA from the top view of the cargo when fully loaded with the payload. As with the side view the clearances between the payload the interior structure is dimensioned. In this image the space between the cockpit payload and the bulkhead are more clearly represented.

98
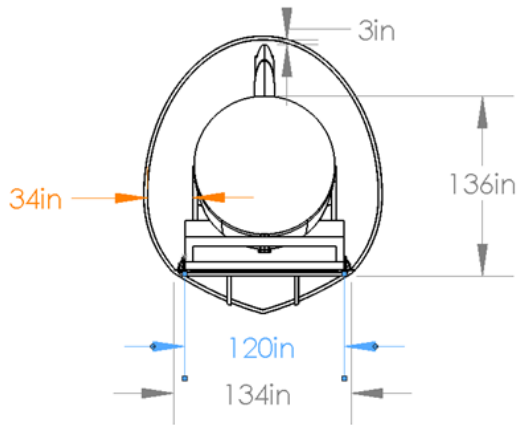
Figure 118: LOPA - Cross-section for the transitional section for the fuse

The figure above represents the cross-section view of the transition section of the fuselage which houses the rear fuselage section of the payload. The width between the payload and the interior wall, the width of the payload and the floor, the clearance of the payloads vertical tail, and the height of the payload from the floor are dimensioned. The space allocated for crew traversal is the width between the wall and the payload at 34 *in*. Although this area tapers down it is enough room for the crew to reach and engage the jig locks comfortably.
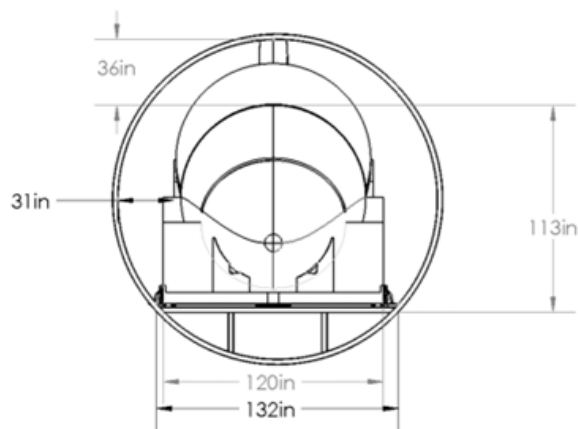
Figure 119: LOPA for the cross-section of the circular section of the fuselage

The image above shows the cross-sectional view of the circular part of the fuselage which encompasses the cockpit jig and its payload. As with the transitional section the dimensions for the width between the cargo and interior wall, the clearance of the payload, payload height, as well

as the payload and floor width are dimensioned. The space for the crew traversal did diminish slightly as due to the design of the cockpit jig's support as well as the circular cross-section. However, at 31 *in* there is still a comfortable amount of space for the crew to move.

11.6 Emergency Door

The one and only door specifically designed for crew members to directly access the interior was placed on the left side of the circular section of the fuselage. This door is placed 48 *in* behind the start of the fuselage section starting point or the end of the cockpit section. It's been fitted perfectly between 2 structural frames. The Type-B door according to the Federal Aviation Administration was selected which is a floor level exit not less than 32 *in* wide, 72 *in* high and corner radii not more than 6 *in*. The figure below shows how the designed door satisfies all of these geometric requirements.
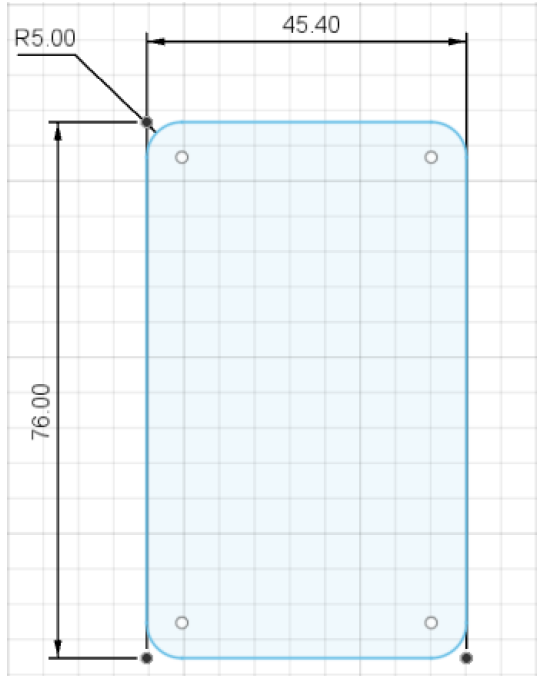
Figure 120: Redesigned entrance door

It's noteworthy that the curvature of the door is with respect to the radius of the circular section of the fuselage which was 90 *in*. An aircraft with this door type is allowed to have 75 passengers. Since the Hauler-X will only be flying crew members, this door meets the mission needs by quite a substantial margin.

11.7 <u>Risk Management</u>

A qualitative failure mode and effects analysis was conducted during conceptual design phase. The RPN (Risk Priority number) was calculated which is a score for how high of a risk the respective failure mode results in. It is a product of the score's severity, occurrence and detection. It was decided to prioritize risks that are more obvious to recognize. Taking that into consideration, our riskiest mode of failure would be the detachment of the payload leading to weight imbalance. This could affect more than the mission objective since an unsafe flight would put the crew members' lives at risk. It's noteworthy that the structural failure of the layout for jigs came at a close 2nd place. This further emphasizes on the focus in eliminating errors on any of the calculations made in that regard. Appendix A can be referred to for the FMEA chart used for an accurate comprehension of the causes and effects.

The design process of the jigs and interior as a whole has had several iterations to mitigate errors in load and sizing calculations. Before operation, it would be the maintenance crew's responsibility to minimize all areas of risk. Fortunately, the most likely modes of failures are the easiest to detect. Preventative measures taken against such situations would include:

- Revised calculations on jig designs, weight, and FEA.
- Ensuring the locks are in place and fully locked before flight.
- Adequate spacing is maintained between the jigs.
- Winch and tie down tools having no looseness.
- APU is checked well in advance before loading.

12. Weight and Balance

The weight and balance analysis are an essential process of aircraft design, operation, and maintenance. To maintain safe and effective operation, an aircraft's weight and balance must be within the calculated parameters. The total weight of an aircraft includes the weight of the airframe (manufacturers empty weight), fuel, crew/passengers, baggage, and cargo. The distribution of weight along an aircraft's longitudinal, lateral, and vertical axes is referred to as its balance. The weight and balance analysis are an important part of aircraft safety, performance, compliance, and maintenance. It contributes to the safe and optimal operation of an aircraft, lowering the risk of

accidents and mishaps. Throughout the course of this project, this analysis was divided into three stages.

12.1. Initial Weights Estimation Methodology

The first stage of this analysis, also called preliminary weight estimation was the extensive market research for aircraft in similar category in terms of performance, payload weight and range. The operating empty weight (OWE), maximum takeoff weight (MTOW), fuel weight, and payload weight for such aircrafts were analysed using mass fractions. Specifically, the ratios of OWE vs. MTOW and fuel weight vs. MTOW were calculated. Following this, the Raymer's methodology for initial weight estimation was utilized to calculate the design aircraft's MTOW and OWE. This statistical methodology is suitable for the conceptual design process because it ensures a more reliable and accurate estimation rather than making an educated guess. The approach is also data driven as this analysis investigates various historic data for trends, relationships, and patterns. Table 30 tabulates the results of this preliminary analysis as it highlights the aircrafts utilized, along with their MTOW, OWE, and mass fractions.

Table 30: Initial weight estimation and mass fractions

Aircrafts	Operating Empty Weight (OWE) (*lbs*)	Maximum Takeoff Weight (MTOW) (*lbs*)	Fuel Weight (*lbs*)	OWE/ MTOW	Fuel Weight/ MTOW
Dash 8-100	23,111	34,500	6,952	0.67	0.202
AN-26	33,113	52,911	10,540	0.626	0.198
Fokker 27	27,964	45,000	11,308	0.621	0.251
ATR 42	22,680	37,257	11,023	0.609	0.296
ATR 72	20,281	39,683	11,023	0.511	0.278
BAE HS 748	25,671	46,500	11,200	0.552	0.241
CONVAIR CV-580	30,275	55000	10,000	0.55	0.182
Design Aircraft	**19,898**	**36,629**	**6000**	**0.54**	**0.162**

For this analysis, the equations developed in section "6.2 Initial Weight Analysis Methods" [27] were used to calculate the MTOW and OWE for the design aircraft. The payload weight in this process is a design requirement (10,000 lbs) and the fuel weight is obtained from the aircraft performance calculations presented in section 14. The MTOW was calculated to be 36,629 lbs. the OWE was calculated to be 19,898 lbs. The aircraft is designed to accommodate a maximum of four crew members in the cockpit. Considering an average weight of 200 lbs per person, the total crew weight is 800 lbs. Table 31 tabulates the payload and crew weight along with their C.G. locations. The C.G. location is presented in X, Y, and Z positions relative to the datum (100 inches to the waterline and 12 inches to the fuselage line).

Table 31: Crew, payload, and jigs weight distribution and c.g. location

Aircraft Component	Component Weight (*lbs*)	X (*in*)	% MAC	Y (*in*)	Z (*in*)
Crew Weight Total	800	21.8		0	16.8
FWD Jigs	1,719	34.2		0	12.6
FWD Payload	1,100	34.7		0	12.9
AFT Jigs	2,183	53.7		0	12.1
AFT Payload	5,000	53.7		0	12.9
Zero Fuel Weight (ZFW)	38,996	49.3	12	0	17.5

12.2. <u>Detailed, Component Wise Weight Estimation</u>

The second stage of the weights and balance analysis is the detailed and component wise analysis of all aircraft structures and systems. This analysis incorporates utilizing of Raymer's equations developed in section "6.4 Statistical Weights Estimation Methods" [27]. Upon completing the first iteration of the weights analysis to obtain the MTOW and OWE, this section focuses on the methodology utilized to calculate the structural and systemic weights of the aircraft. Specifically, these include fuselage, wing, empennage (vertical tail and horizontal tail), MLG, and NLG structural weight. The systemic weights include flight control system, hydraulic system, avionics and electrical system, air conditioning and anti-icing, and furnishings.

Using the calculated MTOW and OWE from the first design stage and utilizing the calculated aircraft sizing parameters (presented in section 5) and aircraft performance characteristics

(presented in section 14) Raymer's formulas were applied to calculate the structural weight of each of the above-mentioned system and aircraft structure. The aircraft sizing parameters and performance characteristics include AR, TR, Sweep, S, load factor, airspeed, dynamic pressure etc. The calculated weights are tabulated in Table 32. This table also highlights the overall structural weight of the aircraft. The MTOW from the second iteration of the weights and balance analysis is calculated to be 41,480 lbs. At this point, it is worth noting that the MTOW as increased by 13.5%. This significant increase was expected at the beginning as the analysis considers historic data of reference aircrafts and statical methodology to calculate component weights for the design aircraft.

Table 32: Detailed, component wise weight estimation

Component-Wise Weight	Value (*lbs*)	Systems Weight	Value (*lbs*)
Engines (X2)	2,120	Fuel	2,500
Main Landing Gear (Wheels, Tires, Breaks)	731	Flight Control System	3,179
Nose Landing Gear (Wheels, Tires, Breaks)	178.51	Hydraulics System	397
Wing (Structure)	4,805	Avionics	93
Fuselage (structure)	11,663	Electrical System	692
Horizontal Tail (Structure)	1,079	Air Conditioning and Anti-icing	322
Vertical Tail (Structure)	668	Furnishing	2,249
Total (Structures)	21,246	**Total (Systems)**	9,434
Total Weight (Structures + Systems + Crew + Payload)			**41,480**

12.3.   Final Weight and C.G. Analysis

The final stage of the weights and balance analysis is the calculation of the C.G. location for each component. Table lists the weights for every component and their respective C.G. location in terms of X, Y, and Z. These dimensions are presented relative to the datum as a reference. Along with this, the weight group totals are also tabulated in the table. Following this, the C.G. location for each weight group total was calculated in % MAC. Utilizing the MAC of 141.84 *in* and LEMAC of 547 *in*. The LEMAC location is presented using the datum as a reference.

Table 33: Final weights and c.g. analysis

Component Name	Weight (lbs.)	C.G. Location (ft)			% MAC
		x	y	z	
Wing	4,805	53	0	21	
Fuselage	11,663	57	0	17	
Vertical Stabilizer	669	102	0	35	
Horizontal Stabilizer	1,079	104	0	44	
Engines (Left)	1,060	46	-22	18	
Engines (Right)	1,060	46	22	18	
Landing Gear (Nose)	178	18	0	6	
Landing Gear (Main)	731	52	0	6	56.31
Flight Control Group Total	2,891	20	0	17	
Hydraulic Group Total	397	40	0	15	
Electrical Group Total	692	30	0	15	
Furnishing Group Total	2,249	20	0	17	
Air Conditioning and Anti-icing	322	40	0	15	
Avionics Group Total	100	30	0	15	
Manufacturer's Empty Weight	27,899	50	0	19	34.93
Engine Oil Total	50	51	0	18	
Unusable Fuel Total	45	50	0	22	
True Empty Weight	27,994	50	0	19	34.95
Operating Items Group Total	1,000	20	0	17	
Operating Empty Weight	28,994	49	0	19	26.16
FWD JIG	1,719	32	0	12	
FWD Payload	1,100	32	0	13	
AFT JIG	2,183	51	0	12	
AFT Payload	5,000	51	0	13	
Zero Fuel Weight	38,996	48	0	17	20.33
Fuel to MTOW	4,500	50	0	22	

Maximum Takeoff Weight	43,496	48	0	18	22.05
Fuel to MRW	500	50	0	22	
Maximum Ramp Weight	43,996	48	0	18	22.22

From the above table, the manufacturer's empty weight is calculated to be 27,900 *lbs*. The manufacturer's empty weight includes all the aircraft structural and systemic weights as calculated during the second stage of the analysis process. The true empty weight of the aircraft includes the engine oil weight and the unusable fuel weight. The unusable fuel weight for the design aircraft was estimated to be 1% of the total fuel to MTOW weight. The true empty weight was calculated to be 27,995 *lbs*.

In reality, the aircraft cannot be in flight without the operating items on board. For the designed aircraft the operating items group total weight was estimated to be 1000 *lbs*. The operating items group total weight incorporates the weight of the crew and other miscellaneous operating items. As mentioned previously, the crew includes of 4 persons with and average weight of 200 *lbs*. Following this, the OWE was calculated to be 28,995 *lbs*. Comparing the OWE calculated during the first stage, the final OWE increased by approximately 45%. This significant increase was expected because the first iteration uses reference aircrafts for the weight's estimations, whereas the final iteration is more specific to the structure, sizing, and performance of the designed aircraft.

The zero-fuel weight (ZFW) for the aircraft includes the payloads and the jigs designed to carry the payloads. For the given combined payload weight of 6,100 *lbs* as the design constrain, the designed jigs for the payloads weigh approximately 3,900 *lbs*. The ZFW is calculated to be 38,996 lbs. Following this, adding the fuel to MTOW of approximately 4,500 *lbs*, the MTOW was calculated as 43,496 *lbs*. Adding the fuel to maximum ramp weight (MRW) of approximately 500 lbs, the MRW is calculated to be 43996 *lbs*. The fuel to MRW includes for activities such as engine start-up and taxing. The C.G. location for the total weight groups is illustrated as % MAC in Figure . The graph also illustrates the C.G. travel, neutral point, and C.G. limits for the designed aircraft. The C.G. travel is an important factor as it determines aircraft safety and performance. As evident in the figure, the C.G. location of the aircraft lies in between the travel limits as the trend for the

C.G. travels forward. The neutral point lies far AFT of the AF C.G. limit. This is a good design practice for the aircraft to have static longitudinal stability at all phases of the flight envelope.
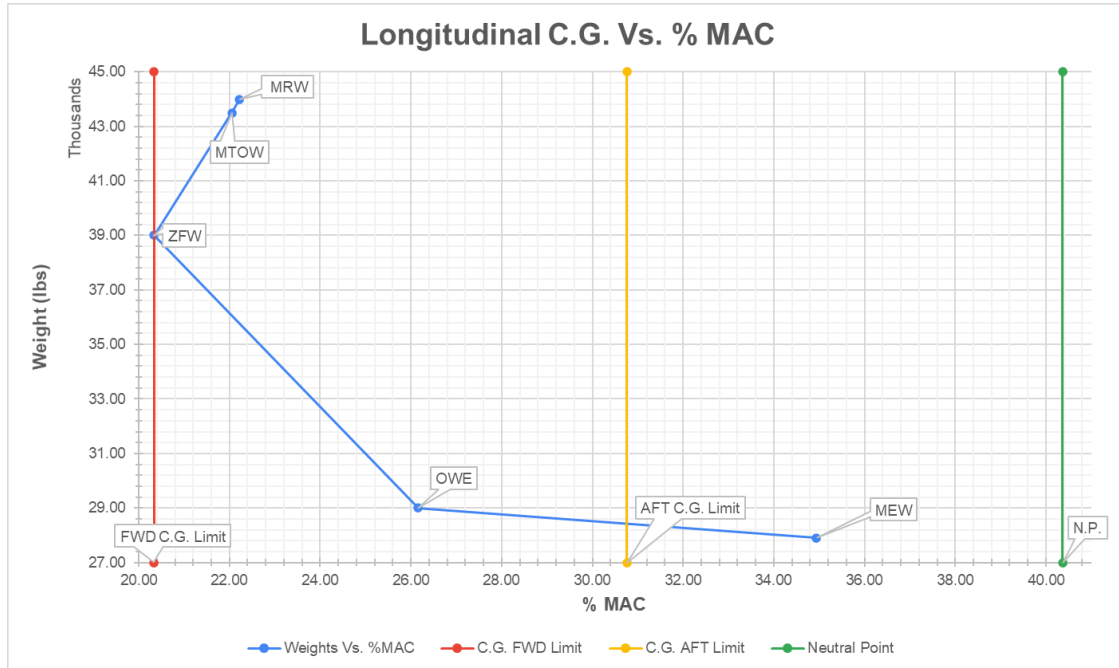
Figure 121: Longitudinal c.g. vs. % MAC.

12.4.   Tip Over Analysis and MLG Positioning

The extension of the weights and balance analysis incorporates the positioning of the Main and Nose Landing Gear systems. The aircraft balance and static stability is determined by the fulcrum location based on the C.G. and landing gear's location calculations. The position of the MLG is determined by utilizing the above presented MRW in the final weight estimation Table. It is considered that the MLG is carrying 90 % of the total MRW whereas the NLG is carrying the rest (10 %) of the total MRW. Therefore, considering the C.G. AFT and FWD limits shown in Figure , the MLG was positioned at 652.8 *in* from the datum as a reference. The location for the MLG is 56.3 *in* % MAC. The NLG is positioned at 240 *in* from the datum as reference.

In addition to the positioning of the landing gears, it was important to analyze whether the aircraft would tip over during loading and unloading procedures. This is a significant analysis for aircraft's safety as it ensures that the aircraft's C.G. during the loading and unloading procedure does not travel beyond the prescribed C.G. limits. This analysis utilizes the aircraft's final MTOW, OWE,

weight of the real load and jig, and the C.G. location for these group weight totals. Table 34 tabulates the parameters utilized for this analysis.

Table 34: Tip-over analysis results.

Parameter	Value
MTOW	43,497 *lbs*
OWE	28,994 *lbs*
Rear Payload	7,183 *lbs*
OWE + Rear Payload	36,177 *lbs*
C.G. with Rear Load	30 % MAC
FWD and AFT C.G. Limit	20.33 % - 30.76 % MAC
Aircraft's Stability Margin	5.4 % MAC

As it is evident from the table, the C.G. location of the aircraft with the rear payload on the main door is well within the C.G. limits of the aircraft OWE. Therefore, the aircraft is balanced and wont tip-over during the process. Further, the calculated neutral point is located further aft of the rear C.G. limit. Therefore, the aircraft showcases better stability and fewer possibility of tipping.

13.Stability and Control

Once the wing and tail geometry was settled upon, stability analysis commenced at that very moment. The design took an iterative approach which referred to the results of preliminary static and dynamic stability calculations to verify if the design targets were being met. To make iteration easier, XFLR 5 was used heavily throughout the design process, which is a tool that employs the two-dimensional flow solving methods of XFOIL with interpolation across the wingspan. This tool approximates viscous flow around a three-dimensional wing by splitting the wing into a collection of two-dimensional airfoils and applying the same boundary layer equations used in the likes of XFOIL, with interpolation in between [28]. For the purpose of simplicity, and after continued difficulty producing native viscous results, a parasitic drag coefficient was assumed and then applied to the analysis. Based on the findings by Snorri Gudmundsson, a value of $C_{D_o} = 0.03$ is sufficient for this class of aircraft, as referred to from the chart below [27].

Class	C_{Dmin}	C_{DTO}	C_{LTO}	Comment
Amphibious	0.040–0.055	0.050–0.065	≈ 0.7	Assumes flaps in T-O position.
Agricultural	0.035–0.045	0.045–0.055	≈ 0.7	Assumes flaps in T-O position.
Biplane	0.045–0.050	0.045–0.050	≈ 0.4	Assumes no flaps.
GA trainer	0.030–0.035	0.040–0.045	≈ 0.7	Assumes flaps in T-O position.
GA high-performance single	0.025–0.027	0.035–0.037	≈ 0.7	Assumes flaps in T-O position.
GA typical single, fixed gear	0.028–0.035	0.038–0.045	≈ 0.7	Assumes flaps in T-O position.
Turboprop commuter	0.025–0.035	0.035–0.045	≈ 0.8	Assumes flaps in T-O position.
Turboprop military trainer	0.022–0.027	0.032–0.037	≈ 0.7	Assumes flaps in T-O position.
Turbofan business jet	0.020–0.025	0.030–0.035	≈ 0.8	Assumes flaps in T-O position.
Modern passenger jetliner	0.020–0.028	0.030–0.038	≈ 0.8	Assumes flaps in T-O position.
1960s–70s passenger jetliner	0.022–0.027	0.032–0.037	≈ 0.6	Assumes flaps in T-O position.
World War II bomber	0.035–0.045	0.045–0.055	≈ 0.7	Assumes flaps in T-O position.
World War II fighter	0.020–0.025	0.030–0.035	≈ 0.5	Assumes flaps in T-O position.

Figure **122**: Lift and drag characteristics for common aircraft configurations [27].

With the iterations being handled in software, it became possible to build a framework with the various geometries serving as the input. Analyses could be pre-defined for each critical scenario – takeoff, cruise, and landing, in this case – and then ran upon the iterative geometries without the need to re-define and re-reference for every design change. The only task that was required between design changes was the definition of the wing and tail geometry. The analyses themselves could also be changed with updated information on the desired takeoff and landing characteristics, of which the reference speed serves critical importance.

XFLR5 also allows one to specify point masses on the aircraft model. This became extremely useful, as the center-of-gravity analysis conducted prior had already established masses and locations for each relevant component, allowing for verification of the estimated center of gravity value.

13.1.   Static Stability and Margin

One of the first things that had to be computed was the static margin. An aircraft is said to be statically stable if its static margin is positive. This means that, after an initial disturbance, the aircraft will tend to correct itself and re-establish a stable orientation. To compute this value, one must first know the variance of the lift and moment coefficients in terms of the angle of attack.

These values were obtained for each iteration by defining an analysis which considered the desired cruise condition of 21,000 ft (approximately 6,000 m) at Mach 0.5 (approximately 160 m/s at 0°C). These values were set as constants, while a sequence of angles of attack were then applied on the aircraft model. For each angle of attack, a resultant lift, induced drag, and moment value were returned from the analysis. This allowed one to see the relation between the lift and moment coefficients relative to the angle of attack, and thus, determine values for the lift curve slope, $C_{L\,\alpha}$ and moment curve slope, $C_{m\,\alpha}$. An (inviscid) lift-to-drag ratio and drag polar could also be constructed, as done below.
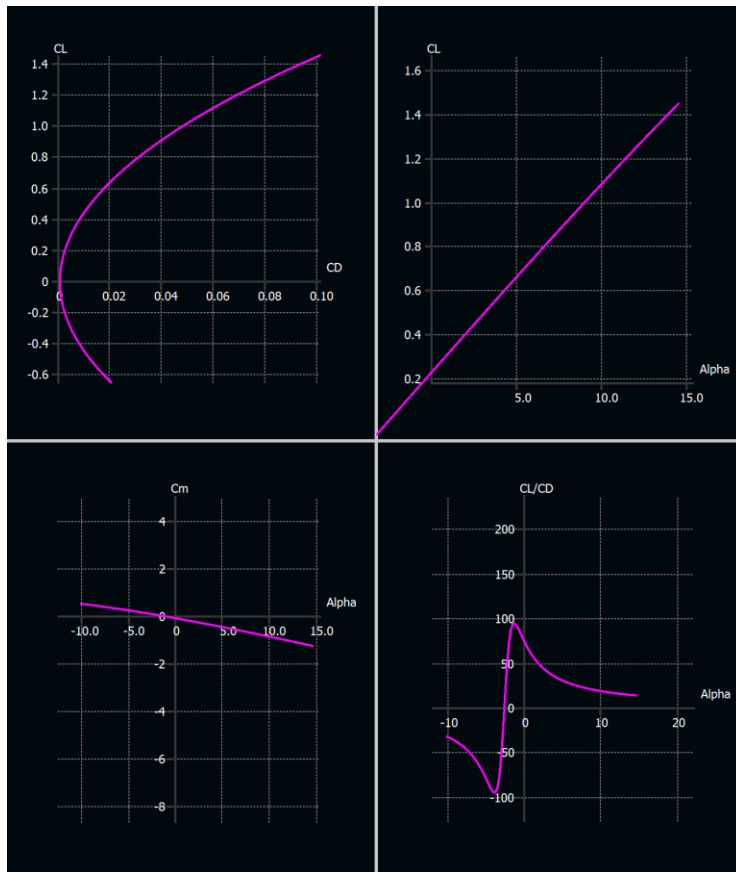
Figure 123: Various polars returned by a single stability analysis in XFLR 5

From the above polars, one can compute the lift and moment curve slope by comparing two data points on the respective graphs. This was done with the data points that coincided with an angle of attack of -5° and +5°. Using this, preliminary values of $C_{L\,\alpha} = 5.634$ and $C_{m\,\alpha} = -3.627$ were established. The remaining variable required for computing the static margin, is the location of the center of gravity normalized to the mean chord length of the wing. This was computed by Aman

during the detailed CG analysis phase, having a value of $h = 0.3163$, or approximately 31.6% of the mean chord length.

The static margin of an aircraft is, by definition, the distance between an aircraft's neutral point, h_n, and its center of gravity, h. Establishing this value is extremely important, as it can be used for determining an acceptable CG travel for the aircraft. If the center of gravity aligns with the aircraft's neutral point, it becomes extremely difficult to control the aircraft, as there exists no inertial moment arm to counter rotational motion. Mathematically, the lift and moment curve slopes are related to each other by the static margin, K_n – similar to the way that forces and moments are related to each other by the moment arm. In essence, the static margin is analogous to the aircraft's moment arm. Its relation to $C_{L\alpha}$ and $C_{m\alpha}$ is defined as followed.

$$C_{m\alpha} = C_{L\alpha}(h - h_n) = -C_{L\alpha}K_n$$

Given the values of $C_{L\alpha}$ and $C_{m\alpha}$ from the constant-speed analysis, a static margin of $K_n = 0.0544$, or 5.4% of the mean aerodynamic chord (or 0.64 feet) can be computed. From this value, one can easily compute the neutral point by acknowledging the definition of static margin stated earlier, yielding a value of $h_n = 0.3707$, or 37% of the mean aerodynamic chord. Daniel P. Raymer states that typical transport aircraft have static margins that reside in the 5% to 10% range [8], thus verifying that the aircraft has a reasonable amount of positive static stability. Slight revisions of the wing geometry under the advice of the structural team saw an increase in static margin to 8% mean aerodynamic chord, as evaluated in the cruise condition.

One of the questions proposed by the Bombardier team in response to the preliminary design review presentation concerned the choice of a straight trailing edge in the design. In response to this, additional analysis was done on a revised wing with a more conventional wing sweep. This was achieved by translating the wing tips by 4 feet towards the nose, thus reducing the leading-edge sweep to approximately 4°, which is more in line with the velocity-based historical trends observed by Raymer.
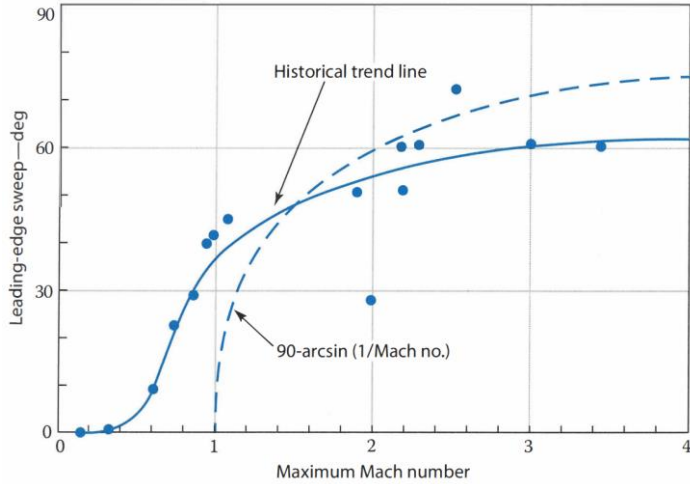
Figure **124**: Historical variance of sweep with maximum Mach number [8].

Upon conducting the analysis in the cruise condition, it was revealed that the modified wing exhibited a reduction in the magnitude of its moment curve slope, $C_{m\,\alpha}$, while providing negligible effects on lift production – and hence, $C_{L\,\alpha}$. This resulted in a loss of static margin by as much as 1% of the mean aerodynamic chord length. This value deviated from the expected value range defined by Raymer and was thus discarded. The analysis served as a means of validating the choice to continue with the straight trailing edge wing design.
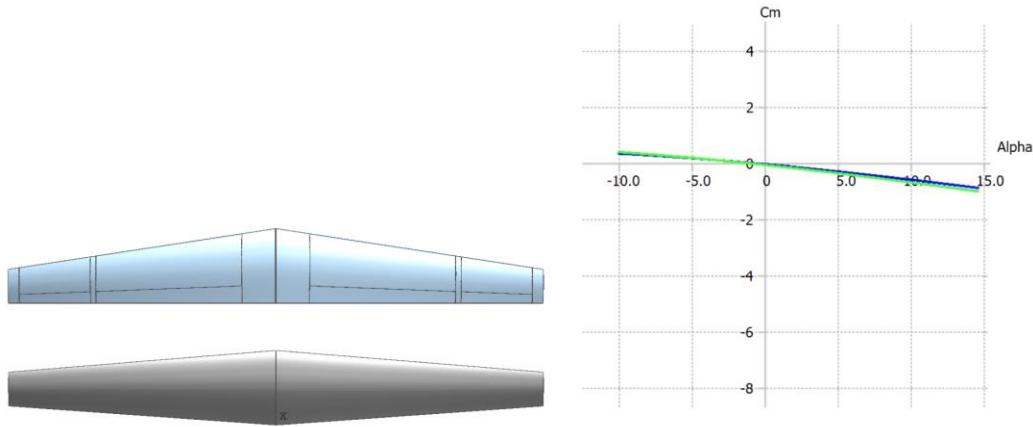
Figure 125: C_m differences between the original (green) and candidate (blue) wings.

13.2. <u>High Lift Devices</u>

During periods of low speed, such as during takeoff and landing, high-lift devices are typically employed to compensate for the loss of lift while traveling at such speeds. It is therefore imperative to determine the wing devices required to produce this extra lift, and to have them properly size to meet lift requirements. Referring to the findings by Snorri Gudmundsson (in Figure), and applying additional factors of safety for the takeoff and landing configurations, a target was established for the lift coefficient values during takeoff and landing: $C_{L\,TO} = 1.20$ and $C_{L\,LAND} = 1.34$ respectively.

The process was started with an assumed takeoff and landing configuration consisting of trailing-edge flaps only. With an aft spar placement of 70% chord within the wing, an initial flap hinge position of 75% chord was chosen to give additional space for actuators and mechanisms. From this point, the spanwise length of the flap was varied, and the constant speed analysis was conducted again with the target takeoff and landing speed of 127.7 *kts*. A default flap deflection of 15° was chosen throughout these analyses.
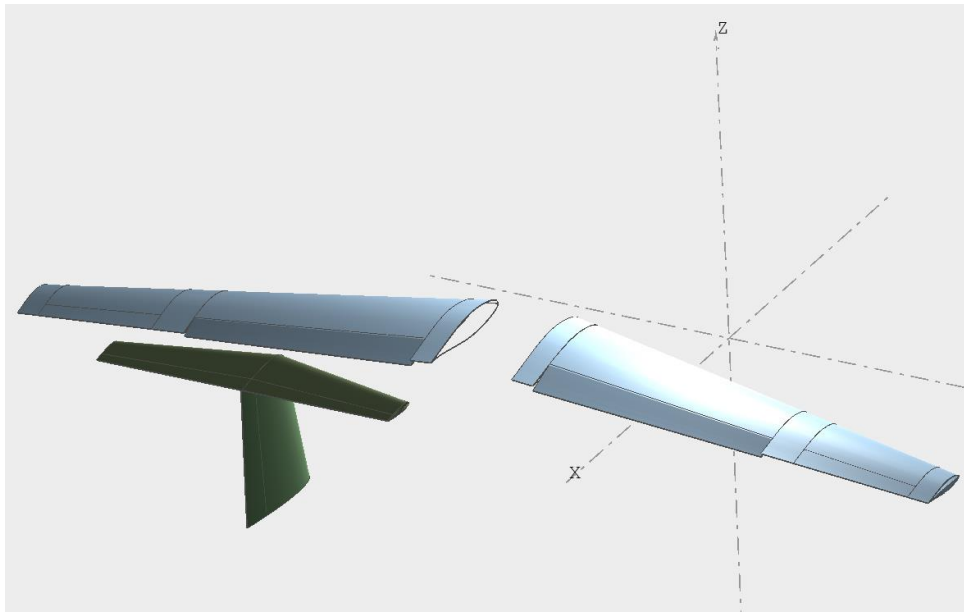
Figure 126: Wing and tail geometry in XFLR with flaps deflected.

Results from the analysis show that plain flaps alone were sufficient in generating the targeted lift coefficient. Further refinement of the spanwise size of the flap with feedback from the structures team resulted in the final flap size being solidified. For a given half of the wing, the flap surface

begins at 7.6 *ft* along the trailing edge from the aircraft's centerline and ends at 35.8 *ft* along the trailing edge from the aircraft's centerline. The flap is hinged along the 75% chord line. To achieve the predefined targets for $C_{L\,TO}$ and $C_{L\,LAND}$, a flap deflection of 10° is required for takeoff, and 20° is required for landing. At these deflections, the aircraft can comfortably hold an angle of attack of 8° in the takeoff configuration and 5° in the landing configuration (both without trim considerations) while maintaining the required speed.
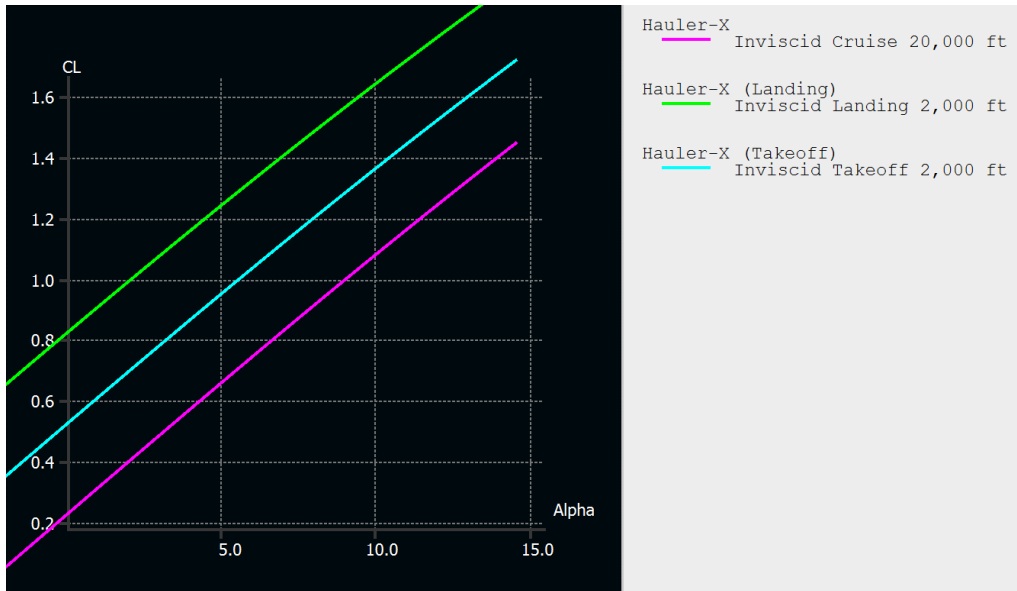
Figure 127: Lift characteristics in the takeoff and landing configurations.

The fact that plain flaps alone could achieve the defined targets also aligned with the findings from Daniel P. Raymer. Based on his research, it is suggested that plain flaps alone are sufficient in generating the maximum expected lift coefficient of 1.8, based on the sweep of the chosen wing.
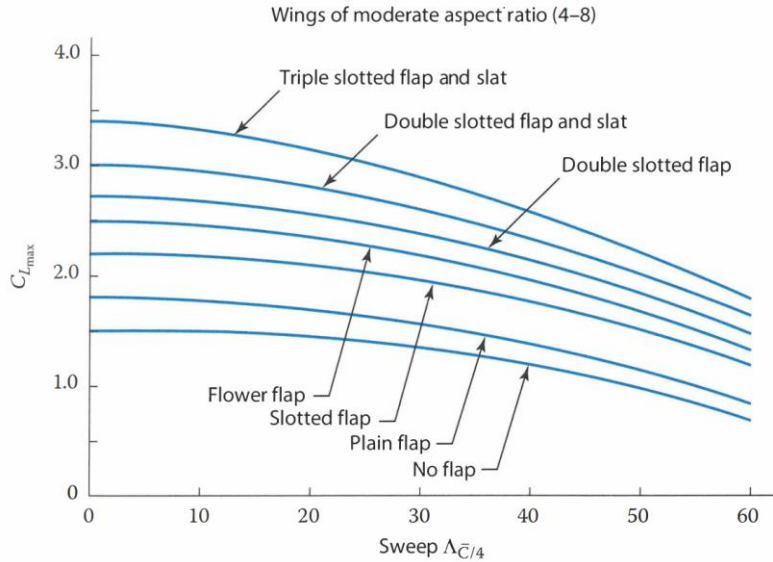
Figure 128: High-lift devices used to achieve desired $C_{L\,max}$ values [8]

13.3.   Stabilizer Trim

As part of easing the load on the pilot, it is necessary to provide a method of trimming the aircraft for certain speeds. Doing so relieves the constant pressure required on the control column to keep the aircraft's pitching moment at 0. Considering the design of our aircraft, a conventional method of trimming was first explored, in which the aircraft would negate its moment by tilting the entire horizontal stabilizer up or down. With inputs from Kaivalya, two airfoils were to be tested as candidates for the horizontal stabilizer: a standard symmetric NACA 0015 airfoil, and one with an inverted camber.

The stability analysis commenced by first defining a range of angles for the stabilizer to reside. The speed of the free stream and angle of attack were then varied until the aircraft enters a trimmed condition, where the moment is 0. To capture all possible horizontal stabilizer angles in which the aircraft could enter said condition, a range of 15° leading-edge-down to 5° leading-edge-up was chosen with an angular delta of 0.25° between each computation, with the aircraft being forced to trim at said angles. This was repeated for all configurations (including the takeoff and landing configuration) for the two different airfoils.

After running the analyses, we found that the inverted-camber horizontal stabilizer required a less aggressive angle to trim during low speeds, bottoming out at approximately 12° leading-edge-down. This was expected, given that its camber allowed for negative lift to be produced even at low angular settings. However, when it came to analysing the cruise performance, it was found that a large leading-edge-up angle of 5° was required to keep the aircraft in the trimmed condition at Mach 0.5. This was not desired, since this resulted in a larger amount of drag during the cruise phase – which is the phase hat dominates the flight. Overall, a larger range of horizontal stabilizer deflection was required to keep the aircraft in the trimmed condition throughout the different phases of flight.

The analyses done on the symmetric horizontal stabilizer yielded results that were more conventional and within expected values. It was found that the aircraft could trim to a stick-free condition within a few knots of the stall speed (83 *kts*) with a horizontal stabilizer deflection of 15° leading-edge-down while in the takeoff configuration. It was also found that the aircraft could maintain the trim condition during cruise with a horizontal tail deflection of 0.5° leading-edge-up, which suggests a significant improvement on the drag produced by the tail, relative to the inverted-camber airfoil. This was achieved while maintaining an angle of attack of 0.46° nose down. The range of trim also fell into a more conventional range, requiring 15° leading-edge-down to 2° leading-edge-up. Due to these reasons, the inverted-camber airfoil was dropped in favour of the symmetric NACA 0015 horizontal stabilizer.
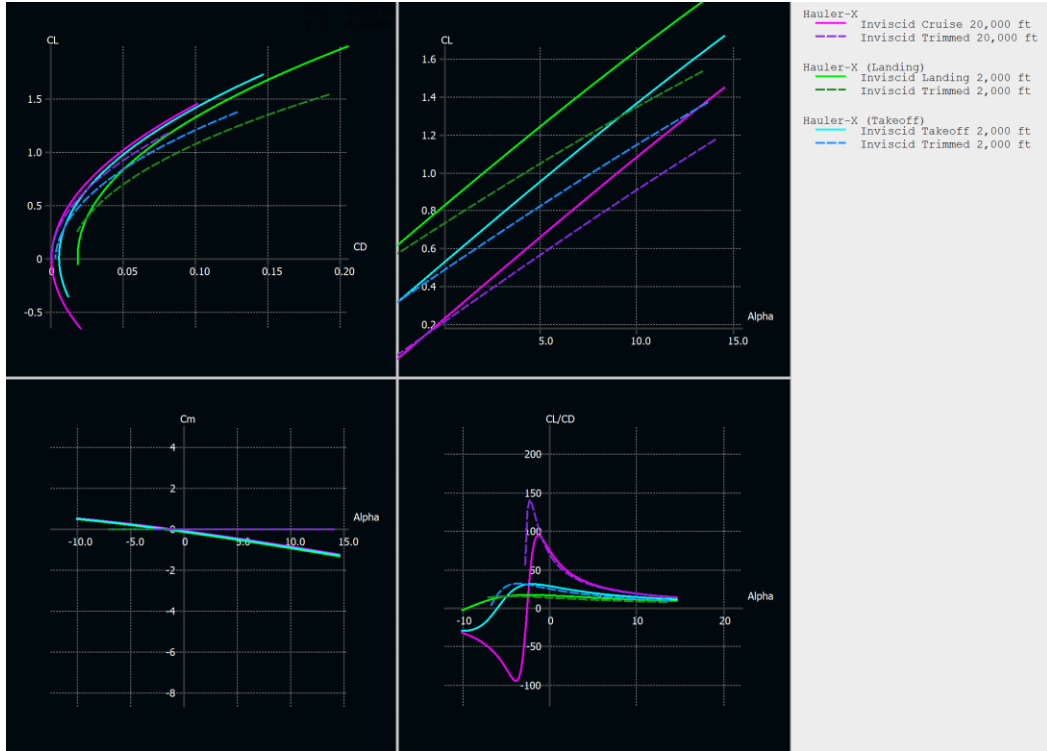
Figure 129: Lift-induced polars for the different configurations with trim.

13.4. **Dynamic Stability and Derivatives**

As part of the stability analysis defined above, XFLR 5 also allows one to extract stability derivatives and view the response to pitch, yaw, and roll disturbances. Capturing stability derivatives is important, as they help provide a sense of authority for the various control surfaces and help identify potential degrees of freedom where stability may be reinforced. This process was also used to size the elevators attached to the horizontal stabilizer. For an initial value, the sizing guidelines employed for the flaps were replicated, in that the control hinge resided along the 75% chord position of the horizontal stabilizer. The elevator was assumed to run along the entire span of the stabilizer.
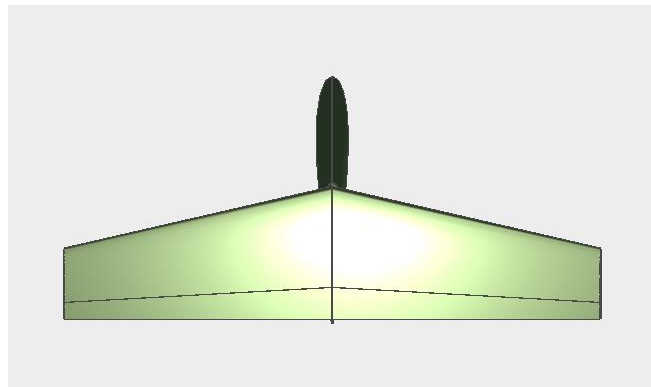
Figure 130: Horizontal stabilizer with appropriately sized elevators.

To determine the stability derivatives, the analysis was run again in the cruise configuration with a trim of -0.5°, at 20,000 *ft* with a speed of Mach 0.5. Control derivatives for both the trimmable horizontal stabilizer and the elevator control surfaces were then established by re-running the analysis over a sequence of stabilizer trim and elevator deflection angles. The resultant stability derivatives obtained from the analysis are listed in Table .

Table 35: Stability and longitudinal control derivatives evaluated at cruise.

Longitudinal Stability Derivative	Value	Lateral Stability Derivative	Value
C_{X_u}	-0.00446	C_{Y_β}	-0.49455
C_{L_u}	0.00005	C_{l_β}	-0.00493
C_{m_u}	0.00000	C_{n_β}	0.23934
C_{X_α}	0.09279	C_{Y_p}	0.07678
C_{L_α}	5.01219	C_{l_p}	-0.74969
C_{m_α}	-3.98759	C_{n_p}	0.01739
C_{X_q}	0.08182	C_{Y_r}	0.48702
C_{L_q}	13.31518	C_{l_r}	0.16537
C_{m_q}	-41.73173	C_{n_r}	-0.25404
H-Stabilizer Control Derivative	**Value**	**Elevator Control Derivative**	**Value**
$C_{X_{\delta_{Stab}}}$	0.00576	$C_{X_{\delta_e}}$	0.00375
$C_{Z_{\delta_{Stab}}}$	-0.91024	$C_{Z_{\delta_e}}$	0.56074
$C_{m_{\delta_{Stab}}}$	-4.12855	$C_{m_{\delta_e}}$	-2.62998

From these stability derivatives, the eigenvalues associated with the various stability modes can then be computed natively within XFLR. Knowing these eigenvalues becomes extremely important, as they are indicators of the type of motion undertaken during the phugoid and short period longitudinal modes, and the roll-stability, spiral, and Dutch-roll lateral modes. Said eigenvalues are listen in the table below.

Table 36: Eigenvalues for dynamic aircraft modes evaluated at cruise

Longitudinal Stability Mode	Eigenvalue(s)	Amplitude Double/Half Time	Damped Frequency
Phugoid	-0.00045 ± 0.07702i	1540 *s*	0.012 *Hz*
Short Period	-2.26752 ± 4.92795i	0.306 *s*	0.784 *Hz*
Lateral Stability Mode	**Eigenvalue(s)**	**Amplitude Double/Half Time**	**Damped Frequency**
Roll-Stability	-8.80403	0.078 *s*	N/A
Spiral	0.00592	117.1 *s*	N/A
Dutch-Roll	-0.65068 ± 3.29735i	1.065 *s*	0.525 *Hz*

Based on the eigenvalues computed above, one can note that the aircraft remains dynamically stable across all possible stability modes, excluding the spiral mode, which is inherently divergent. As long as the real portion of the eigenvalue remains negative, the aircraft will reach a steady state within the given mode. Knowing the unstable nature of the spiral mode, the operator of the aircraft must avoid entering a spiral situation. However, as can be seen by the relatively longer doubling time of the spiral amplitude, the pilot is given a larger margin to correct the situation if a spiral is induced.

13.5. <u>Control Authority and Derivatives</u>

Understanding the controllability of the aircraft at different phases of flight is imperative for verifying its airworthiness. To validate the selected control surface sizing for the ailerons and rudder, additional stability analyses were conducted to simulate the full range of control surface deflection, to a maximum magnitude of 30° in either direction. These analyses were evaluated while the aircraft was in its landing configuration with flaps deployed, at the desired landing speed of 127.7 *kts*. The distribution of force can be plotted across the spans of the control surfaces, as done in the figures below.
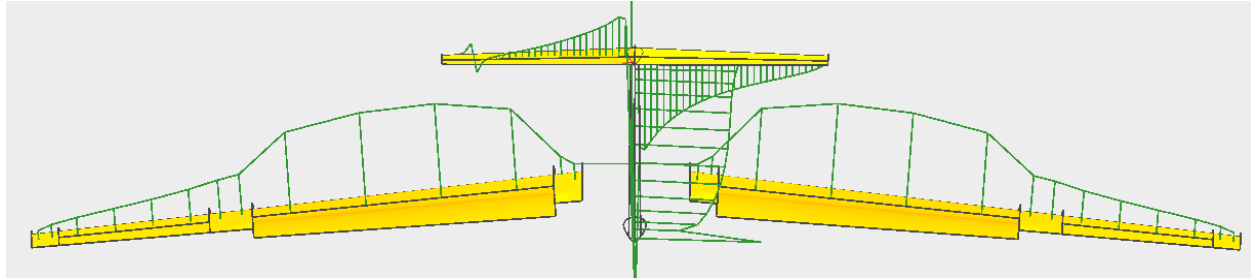
Figure 131: Aerodynamic forces at maximum rudder deflection evaluated at landing.
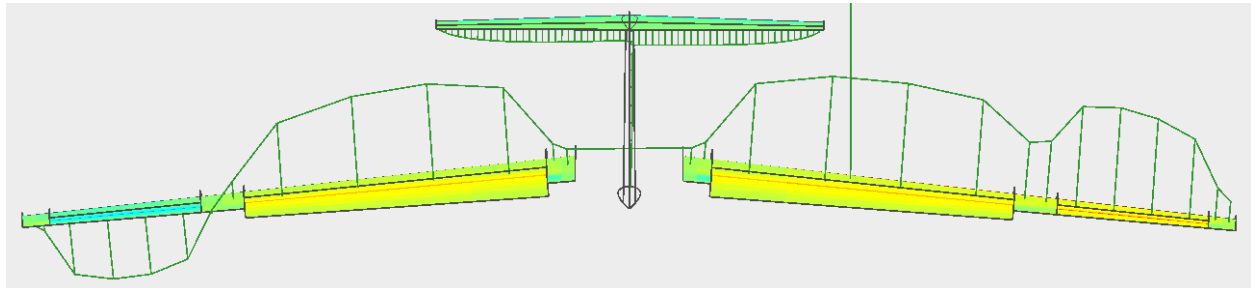
Figure 132: Aerodynamic forces at maximum aileron deflection evaluated at landing.

The aerodynamic forces being generated by the control surfaces for each given angle of deflection were noted, allowing one to compute the control derivatives on the lateral axis. These derivatives are a good measure of the control authority during the landing phase, assuming that the speed of the aircraft remains at a considerable margin above the stall speed. The values of these derivatives are given in the table below.

Table 37: Lateral control derivatives evaluated at cruise.

Aileron Control Derivative	Value	Rudder Control Derivative	Value
$C_{Y_{\delta_a}}$	0.04776	$C_{Y_{\delta_r}}$	-0.31362
$C_{l_{\delta_a}}$	-0.18787	$C_{l_{\delta_r}}$	0.05828
$C_{n_{\delta_a}}$	0.00505	$C_{n_{\delta_r}}$	-0.15277

According to the Federal Aviation Regulations, Part 25, section 223, an airworthy aircraft must be able to maintain its control in a 20-*kts* crosswind component during the takeoff and landing phases. To verify that this requirement was being met, the simulations were conducted once more with a sideslip angle that would result from a 20-*kts* wind component on the lateral axis. Given that the rudder serves the purpose of maintaining coordinated flight, the rudder deflection angle was varied until the aircraft stabilized at the desired landing speed.
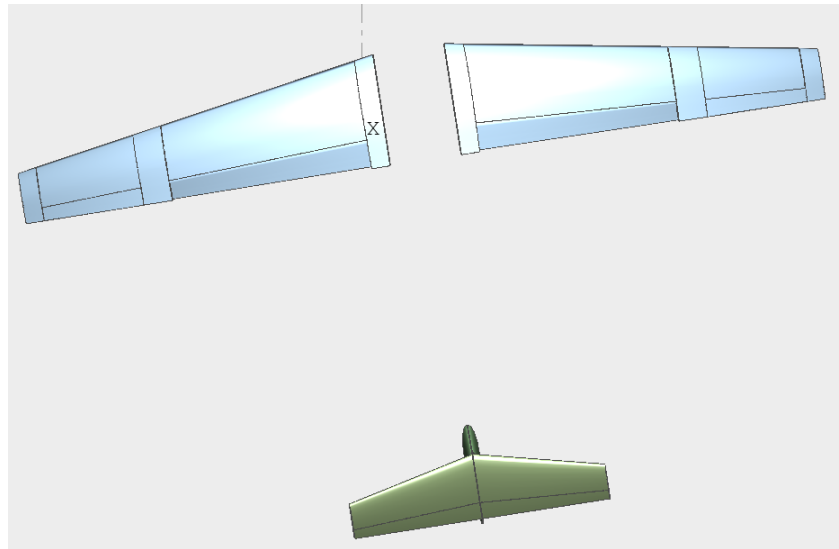
Figure 133: Aircraft in a 20-knot crosswind.

Based on the analysis, a rudder deflection of 2° was required to keep the aircraft in coordinated flight with a 20-*kts* lateral velocity component. This fall well within the operational range of the rudder, thus satisfying the requirement.

14. Performance

The design approach took a mixture of empirical data, historical trends, and mathematical computations to estimate the various performance metrics. Given that the ATR 72 uses the same engines as the ones chosen for the aircraft, many of the engine-related parameters can be estimated from pre-established values from said aircraft. Other, more critical parameters, such as the takeoff length, range, and stall speed, required manual computations using established equations.

14.1. <u>Engine Selection</u>

For the initial performance analysis, calculations were conducted using the PW150A engine present on Bombardier's Q400 aircraft. This was done as a means to provide familiarity to the customer, given that their own aircraft used the same engine. However, after running preliminary computations on the power-to-weight ratio and comparing said value to those of similarly massed aircraft, it was determined that the PW150A may produce an excessive amount of power greater than that required for the mission. Because of this, the PW127XT was opted for instead. This engine produces a significantly smaller amount of power (2750 shaft horsepower compared to the 5000-shaft horsepower of the 150A), but does so with a smaller amount of fuel per unit of power. For simplicity, a 6-blade propeller was also chosen, with a diameter of 13.17 feet, which slots in between the diameters of the propellers used on the ATR 72 and Q400 aircraft. The engine choice was later verified with computations for takeoff length and range, as done in the following sections.

14.2. <u>Range</u>

An iterative process was undertaken in which the range was computed for a given fuel load, starting at 2,500 *lbs*. As mentioned prior, and acknowledging the relatively short trip, a fuel load of 5,000 *lbs* was deemed acceptable for the aircraft after iterations. Based on similar weight fractions from the ATR 72 aircraft, 900 *lbs* of fuel has been reserved for ground operations and loiter in the air, leaving an expendable fuel amount of 4,100 *lbs*. Knowing this, along with the aircraft's maximum takeoff weight of 43,496 pounds, the PW127XT's power-specific fuel consumption of 0.45 *lb/hp·hr* (per engine) [29], and an assumed lift-to-drag ratio of 13, one can use Breguet's range equation to compute the cruise range of the aircraft, as given in the equation below.

$$R = \frac{V_{cruise} \left(\frac{L}{D}\right)}{SFC} \ln \left(\frac{MTOW}{MTOW - W_{fuel\ expend}}\right) \qquad (14.1)$$

14.3. Stall and Takeoff Speeds

With the data obtained via the stability analyses conducted in XFLR, a maximum lift coefficient for the aircraft was noted for the takeoff condition (with appropriate trim). This value was used to compute the stall speed of the aircraft with takeoff flaps and trim set, which was approximately 83 *kts*. Knowing the stall speed, a rotation speed could then be computed. According to the recommendations outlined by the FAR Part 25 regulations, the takeoff speed was computed by multiplying the stall speed by 1.23 [30], plus an additional safety margin, resulting in the present value of 128 *kts*.

14.4. Takeoff Performance

One of the most important parameters as part of analysing the performance of an aircraft is its ability to takeoff and land within an expected runway length. For an aircraft to fly, it must first leave the ground, and must also return to the ground after its flight. The limiting factor for the takeoff and landing performance is the runway length at Downsview airport, given that it remains the shortest between the two airports. With a runway length of approximately 7,000 *ft* and knowing that the touchdown markers of the runway are placed 1,000 *ft* from the threshold, a design target of 6,000 *ft* was established for takeoff and landing runs.

Takeoff ground roll was computed by first calculating the acceleration of the aircraft. It is known that a force is the product of its mass and acceleration. Therefore, by knowing the thrust being produced, and the forces that act against said thrust (such as drag and ground friction), the net force acting in the direction of the ground roll can be computed. This is commonly referred to as the excess thrust, which can be used to compute the acceleration of the aircraft knowing its mass. To cover the most critical scenario, the analysis took place while considering the aircraft's maximum takeoff weight. Acknowledging the significant sources of drag and friction against the thrust available, the acceleration of the aircraft can be computed as followed.

$$a = \frac{T - D - F}{W/g} = g\left(\left(\frac{T}{W} - \mu_g\right) - \frac{(C_D - \mu_g C_L)qS}{W}\right) \tag{14.2}$$

- Where μ_g is the coefficient of kinetic friction: 0.025 for asphalt.

For simplicity, this analysis was done under the assumption that the aircraft produced a consistent amount of thrust during its takeoff run. Of course, this is an ideal case, and does not match the real thrust characteristics of a turboprop-powered aircraft. To compensate, and to also match real-world takeoff procedures, a derating factor of 88% was applied to the thrust, given that pilots rarely use 100% of the thrust available during this phase unless absolutely required. The (static) thrust available from a turboprop engine can be estimated using an empirical calculation defined by Daniel P. Raymer, onto which the derating factor can be applied afterwards [8]. This equation is given below, which resulted in a takeoff thrust of 5980 *lbs* available per engine.

$$T_{av} = 5.75 \, BHP \left(\frac{\sigma N_e D_p^2}{BHP}\right)^{\frac{1}{3}} \tag{14.3}$$

- Where σ is the density ratio at the airport's altitude (approximately 0.982 at Downsview), N_e is the number of engines (2 in this case), and D_p is the diameter of the propeller disk (which is 13.17 *ft*).
- The PW127XT produced a maximum of 2750 brake horsepower (BHP) [29].

With a known thrust, weight, and drag, the acceleration of the aircraft can be computed at different points of time during the takeoff run. The acceleration can be applied for a short period of time, after which the computation can be ran again to apply the resultant acceleration for another short period of time. This can easily be repeated until the applied acceleration results in the aircraft reaching its takeoff speed. For this analysis, the acceleration was applied for the equivalent time it would take for the aircraft to gain 1 *kts* of airspeed. This process was repeated until the aircraft reach its rotation speed of 127.7 *kts*. Knowing that the lift and drag – and hence, the acceleration – at any given moment is a function of velocity, one can compute the ground distance covered by evaluating the integral of the velocity over said acceleration (V/a – a value of time) in terms of the computed velocity.

Once the aircraft reaches its rotation speed, it them begins to lift its nose into the air. As per Federal Aviation Regulations, the aircraft must be able to clear 50 *ft* above the ground level before it is considered "airborne". This can also be captured in the analysis by assuming that the aircraft follows a circular path during the rotation, with the motion occurring about a fictional point right above the aircraft at the start of its rotation. A rotation rate of 5° per second (to a maximum of 10° nose up) was assumed to compute the tangential acceleration along said circular path, and the distance covered during said acceleration was found. With the datapoints computed via MATLAB script, a graph was constructed to provide a clearer picture of the takeoff roll process, shown below.
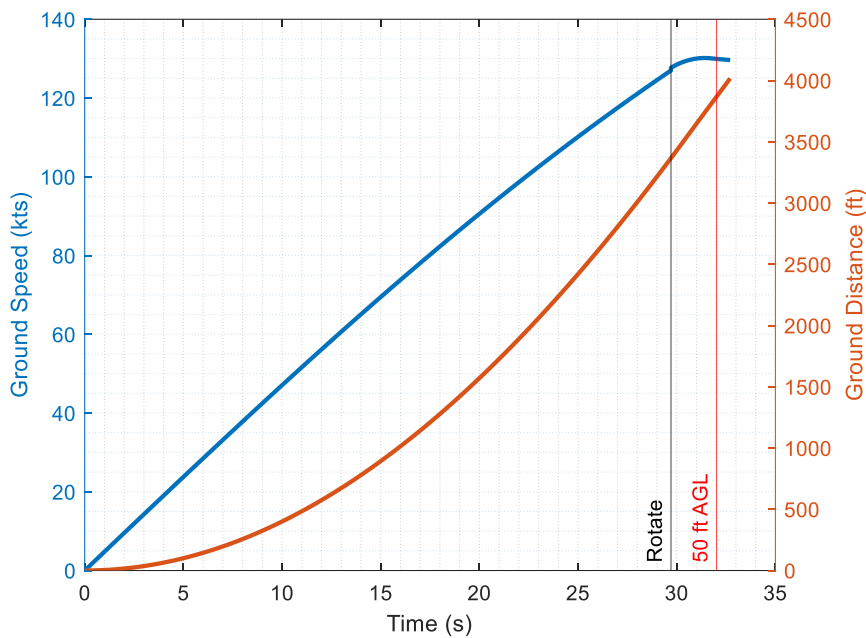
Figure 134: Takeoff roll evaluation and results.

Using the method described above, a total ground distance of 3,868 *ft* is required for the aircraft to become airborne, covered over a period of roughly 32 seconds. The process was repeated with potential head and tail winds in consideration; the results of which are shown in the table below. As expected, the required ground distance is shortened while taking off in a head wing, and lengthened while taking off in a tail wind.

Table 38: Takeoff distance required with wind considerations.

Head Wind Velocity	Required Ground Distance	Ground Roll Time
+ 20 kt	3656 ft	30.7 s
+ 10 kt	3752 ft	31.3 s
0	3868 ft	32.0 s
- 10 kt	4010 ft	33.0 s
- 20 kt	4187 ft	34.1 s

14.4.1 Tail Strike Angle

A factor to consider during takeoff and landing is the tail strike angle. When the angle is steep during takeoff or landing, the tail can possible strike the ground. This is tested for landing and takeoff in XFLR. The maximum angle at takeoff is 19.63° before the tail will strike the ground, and our required rotation angle for takeoff is 8°. Since our required angle for takeoff is within the maximum margin, we can avoid tail strike. During landing, our rotational angle is 6.25°, also passing within the maximum margin. Although tail strike angle is avoided based on our trim setting and speed parameters, tail strike can still occur through pilot errors and wind effects.

14.5. Balanced Field Length

According to the Federal Aviation Regulations, Part 25, section 113, an aircraft must be able to become airborne within an appropriate distance computed for an engine-out scenario, or within 115% the distance required with all engines running – which ever value is the greatest [30]. Daniel P. Raymer provides equations and reference charts for estimating a takeoff length. The values from said charts can be used to compare against the real value computed in the acceleration analysis outlined above. Raymer's method involves computing a takeoff parameter and referencing a historical chart, like the one pictured in the figure below.
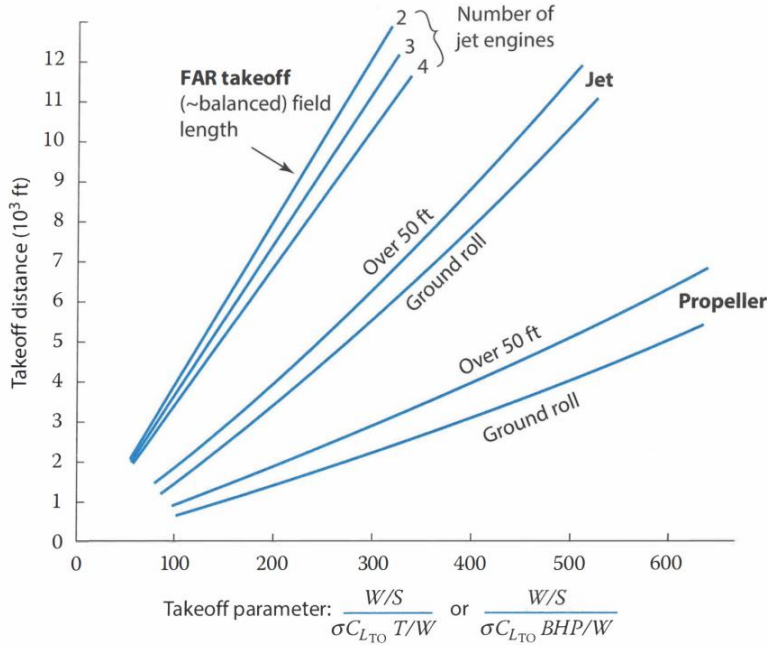
Figure 135: Reference chart for takeoff performance based on historical trends [8]

Both the value retrieved from the chart, and the value computed via acceleration were multiplied by the 115% specified by the FAR Part 25 regulations. With the acceleration-derived takeoff length being higher, its post-multiplied value of 4487 *ft* was solidified as the true takeoff field length.

14.6.   Landing Distance

For one to compute the landing distance of an aircraft accurately, many parameters are required that may not be available during the design phase of an aircraft. Important values such as the energy limits of the selected braking system cannot possibly be known before the design and selection of such components. It is therefore sufficient to estimate the landing distance based on empirical computations. Daniel P. Raymer provides an equation to compute the approximate landing distance of an aircraft, which is given below. Conducting the calculation yielded a value of approximately 3100 *ft*.

$$S_{land} = 80 \left(\frac{W}{S}\right) \left(\frac{1}{\sigma C_{L\,max}}\right) + 1000 \; ft \qquad (14.4)$$

14.7. <u>Final Performance Parameters</u>

Table 39: Final performance parameters

General Assigned Variables	
Maximum Lift Coefficient (XFLR)	1.46
Landing Lift Coefficient	1.34
Density Ratio (Downsview/Sea Level)	0.98
Power to Weight Ratio	0.101
Lift to Drag Ratio	13
Cruise Speed (*ft/s*)	526.37
Applied Takeoff Power (%)	88
Engine Specifications	
Maximum Engine Power (*SHP*)	2750
Specific Fuel Consumption (*lb/hp·hr*)	0.45
Propeller Diameter	13.167
Propeller Efficiency	0.8
# of Propeller Blades	6

The table above shows the parameters that were used in determining the performance values. The maximum lift coefficient was computed through XFLR, which is a more accurate estimation in comparison to historical data. The applied takeoff power can vary accordingly to the pilot and the situation, but 88% takeoff power was arbitrarily applied with the assumption that it is constant. The engine specifications are obtained from the Pratt and Whitney brochures for the PW127XT engine. The table below highlights the performance values for our final design.

Table 40: Aircraft performance specifications

Specification	Value
Maximum Takeoff Weight (*lbs*)	43496
Maximum Fuel Weight (*lbs*)	5000
Reserve Fuel Weight (*lbs*)	900
Static Thrust Available (/engine) (*lbs*)	5978
Range (*nmi*)	753
Cruise Altitude (*ft*)	21000
Service Ceiling (*ft*)	25000
Stall Speed (Takeoff Config) (*kts*)	83
Takeoff and Landing Speed (*kts*)	128
Recommended Climb Speed (*kts*)	187
Rate of Climb (*ft/min*)	2026
Ground Roll Distance (*ft*)	3366.2
Engine Out Obstacle Clearance (*ft*)	4448.71
Takeoff Field Length (FAR 25) (*ft*)	4487
Landing Distance (*ft*)	3072

14.8.   Constraint Analysis

One question that came up as part of the preliminary design review presentation was related to the computed wing loading of 34 *lbs/ft²*, which sits at nearly half of that exhibited in aircraft of similar weight [29]. It was argued that this value may seem to be on the lower side of the spectrum. Internally, this was to be expected, given that the aircraft's design required a relatively larger fuselage (and hence, proportionally larger wing) for its maximum takeoff weight. However, to verify that this wing loading was indeed sufficient, a full constraint analysis was conducted. The various condition-specific power-to-weight requirements – such as those for takeoff, cruise, and constant turn – were computed for a series of different wing loading values, based on the

performance figures that were previously calculated. It was found that the aircraft was indeed meeting its requirements even with its relatively smaller wing loading.
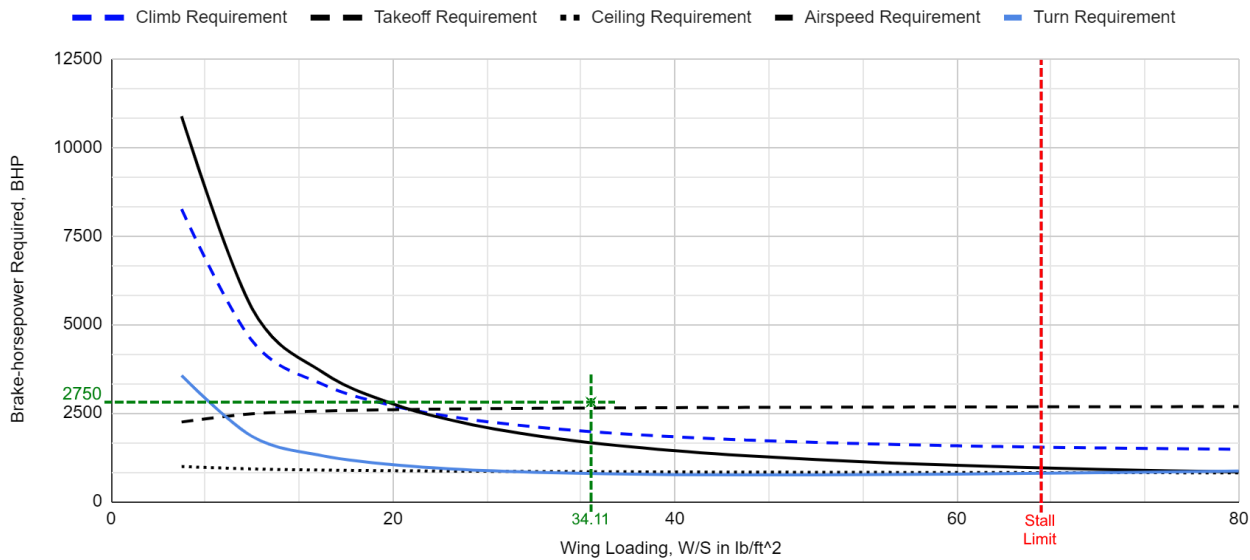
Figure 136: Full constraint analysis of Hauler-X

14.9.   **Mission Profile**

A full mission profile for a typical flight was constructed to serve as a means of verifying the various performance estimates. For a typical flight, the airborne portion of the mission can be separated into three major segments: takeoff/climb, cruise, and approach/landing. The first and last segments themselves can be broken up into separate legs when factoring additional flight time due to loitering. The time and distance flown for each leg is critical for mission planning and scheduling, and a detailed mission profile can provide a visual sense of the flight path.

To simulate the aircraft in its climb, it has been assumed that the aircraft uses all its excess power to execute a steady, non-accelerated climb at the suggested climb speed. Knowing this, the rate of climb can be computed for any flight condition, at any altitude. With the drag characteristics defined in the previous sections, the power required to overcome said drag – and thus, the excess power – computed as followed.

$$RoC = \frac{P_{ex}}{W} = \frac{P_{av} - DV}{W} \qquad (14.5)$$

The computed rate of climb can be applied for a small interval of height, and the calculation can then be repeated. This allows one to construct the profile of the aircraft's climb out of small altitude steps, with an assumed constant rate of climb during each step. The horizontal distance covered, and the flight time for each altitude step can then be obtained via trigonometric relations between the rate of climb and the previously-mention suggested climb speed. To account for loitering due to air traffic, the climb is stopped for 2 minutes once the aircraft reaches 10,000 *ft*. The aircraft then resumes its climb with a speed of 200 *kts*.

For the descent portion of the mission, a constant rate of descent is assumed which coincides with a flight speed of 250 *kts* and the design lift-to-drag ratio of 13. With these given values, the rate of descent can be computed via the equation below. The same process defined for the climb phase is repeated for the descent phase. To simulate additional loitering time due to traffic movements and potential go-around procedures, the aircraft is held for 15 minutes once the aircraft descends through 6,000 feet. The aircraft then continues its descent to the runway at the suggested landing speed.

$$L/D \approx \frac{V_{fwd}}{V_{down}} = \frac{V}{RoD}, \qquad therefore, \qquad RoD = \frac{V}{L/D} \qquad (14.6)$$

The distance and time of the cruise segment can be computed knowing the parameters of the climb and descent segments of the flight. The cruise portion accounts for the remainder of the flight, so with the desired cruise speed of Mach 0.5 and the flight distance of approximately 350 *nmi* (which considers an additional 50 *nmi* for loiter and go-arounds), one can easily compute the distance and time covered during this phase through simple subtraction.

With the distances and flight times of all airborne mission segments known, the results can be plotted in sequence to form the entire flight mission profile. The results of this as done in MATLAB can be found in the figure below. As a result of conducting the mission profile analysis, an established flight time of 84 minutes is necessary to cover the 350 *nmi* flight.

Figure 137: Mission profile

The fuel required for the trip can also be acquired by analysing the generated mission profile. For each segment of the mission, i, the required fuel is simply the product of power-specific fuel consumption, C_i, the engine power, P_i, and the time of the segment in hours, t_i. This value must be multiplied by 2 to account for the number of engines in operations.

$$W_{fuel\ burn} = 2 \sum_{i=1}^{n} C_i P_i t_i$$

It is assumed that the aircraft operates at its rated power for the climb and cruise legs. For the descend phase, it is also assumed that the aircraft powers down to 25% of the rated value while bleeding altitude and powers up to 50% of the rated value while loitering. Considering these values, one can compute a fuel burn of 2,823 *lbs* for the given mission. When factoring power reductions for the cruise segment, this value can be even lower, allowing the aircraft to fly to and from the destination airport without refueling. This can result in significantly lower times on the ground during the loading and unloading phases.

15.Systems

The Hauler-X aircraft has a variety of systems needed to achieve the set mission requirements, most importantly of which is the ability to transport the assigned payload from Downsview, ON to Mirabel, QC. These range from the systems necessary to control the aircraft such as the fly-by-wire controls and hydraulics to critical life support systems for the crew. As the main goal of this flight was to transport a payload with no need for life-support systems, certain parts of traditional aircraft systems such as cabin air conditioning and pressurization were neglected due to there being no passengers besides the pilots and a maximum supporting flight crew of two, all of whom would be situated in the cockpit for the duration of the flight. As the goal is to provide innovation in areas related to payload delivery and structural design, systems will largely be adapted from aircraft of similar build to ensure reliability, interoperability, affordability, and procurement availability, and where required, introduce original elements that are otherwise not included in the chosen systems.

Key factors that were made when determining which types of aircraft fit our requirements and flight profile for each system group included the redundancy of the system in the case of hydraulic or electrical failure, as well as its compatibility with the Hauler-X aircraft design, namely its turboprop classification. As a result, the ATR family of aircraft, namely the ATR-42/ATR-72 models were heavily referenced, as system interoperability between the two aircraft structures and systems closely fits those of the requirements. Another aircraft that systems were adapted from was the Airbus family of aircraft, largely due to the similarities in cockpit design as well as its robust suite of avionics architecture in comparison to other aircraft that were evaluated. While emphasis was placed on turboprop aircraft such as the ATR-72, the Airbus aircraft were also explored as potential sources of system implementation, provided they had no conflict with the Hauler-X aircraft, due to the different nature of turboprop versus turbofan engines.

15.1. Layout

15.1.1 System Views

Figure 138 and Figure 139 provides a brief overview of the systems and their approximate locations in the Hauler-X aircraft in both a top and side view configuration. For specific CG locations of the systems, refer to the weights and balance section. The following sections will then

explain each system in depth, as well as including the referenced aircraft and system architecture diagrams, whether original or adapted where necessary.
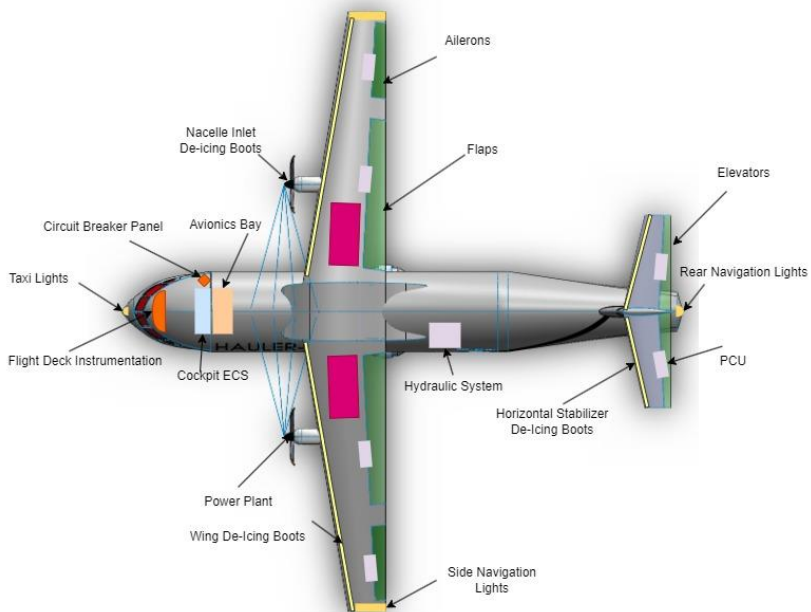
Figure 138: Location of systems within Hauler-X (top view)
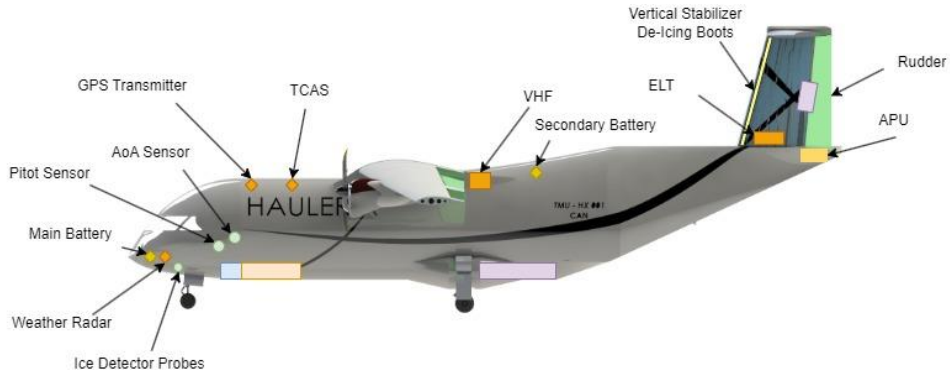
Figure 139: Location of systems within Hauler-X (side view)

15.1.2 Cockpit Views

An important aspect in the construction of this aircraft was to create a cockpit in which the pilots would be able to familiarize themselves with the layout based on previous experience flying other aircraft, and for it to contain all the necessary displays and equipment to allow for a safe and effective flight. As mentioned in the master lines section, the cockpit's shape was largely inspired by the A350's design, and as such the cockpit design remains largely unchanged from this plane, with certain elements also being taken from the A320. Certain features such as a lavatory, crew

rest area, and other amenities that would be expected in a long-haul flight are eliminated due to the short flight time in which this plane is expected to operate. However, due to the difference in engine types between the Hauler-X and the A350, certain changes in the panels for each system were introduced with the majority of the newly adapted systems coming from the ATR-72 due to the similarities it shares with the Hauler-X as a turboprop-driven aircraft.
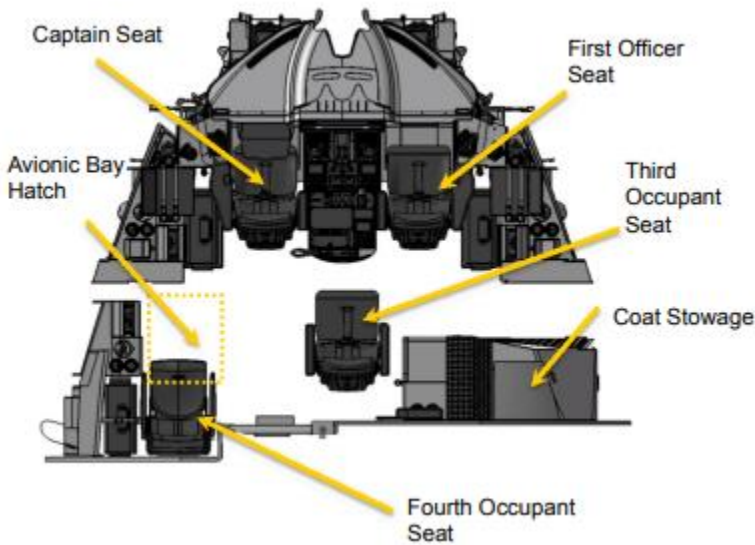
Figure 140: Adapted overhead cockpit view of A350 used in Hauler-X [31]

The Hauler-X will consist of a captain's seat, an F/O seat, and two additional seats for occupants, which are likely to be crew members present to assist with the loading/unloading procedure of the payload. Each seat will have adjustable armrests, headrests, and a reclining backrest with lumbar adjustment. These seats can be adjusted electrically or mechanically as a backup.

The following views are adapted from the A350, and due to their similarities in sizing and instrumentation, will also be considered as an accurate representation of the cockpit interiors for the Hauler-X. Figure 141, Figure 142, Figure 143, and Figure 144 show the captain's view facing frontwards, the LH captain view, the RH aft view, and the LH aft view respectively. These images are also labelled to provide a clearer concept of the layout of accommodations present within the aircraft, the design of which is to be a near-similar representation of the

Hauler-X aircraft.
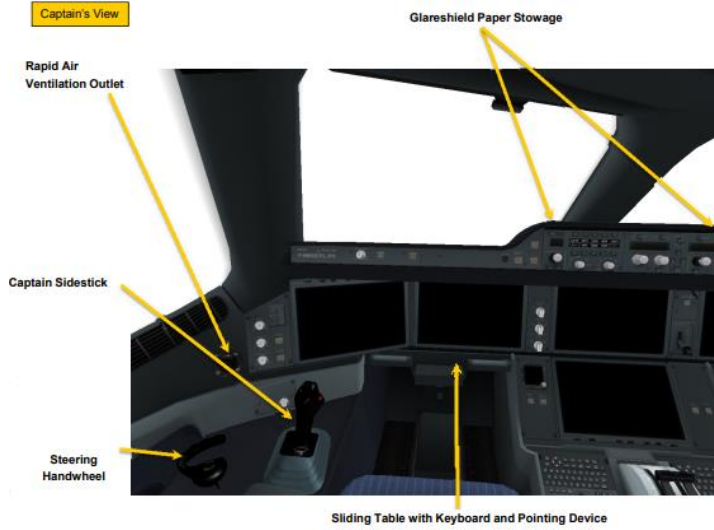
Figure 141: Captain's Front Facing View of Cockpit Interior [31]: Captain's front facing view of cockpit interior
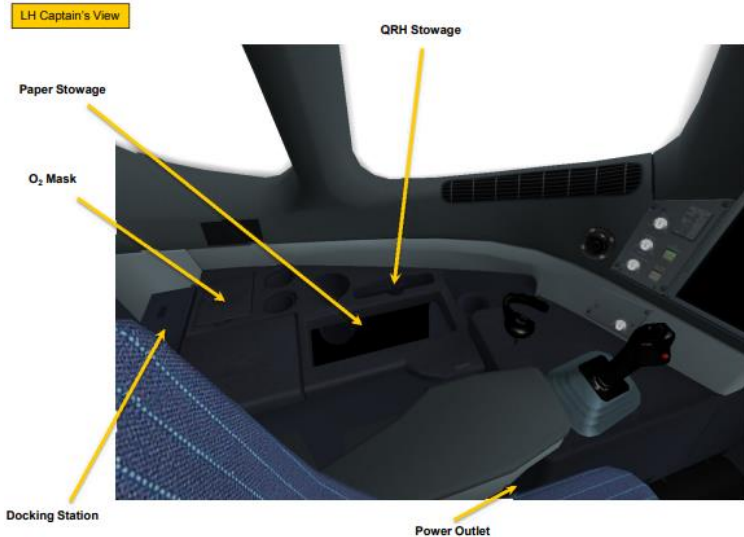
Figure 142: Captain's LH view of Cockpit Interior [31]cockpit interior
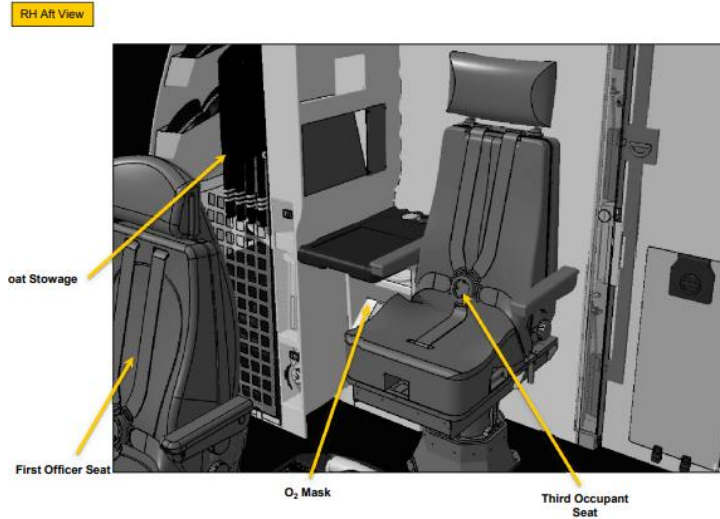
Figure 143: Right Hand Aft View of Cockpit Interior [31]: Right hand aft view of cockpit interior
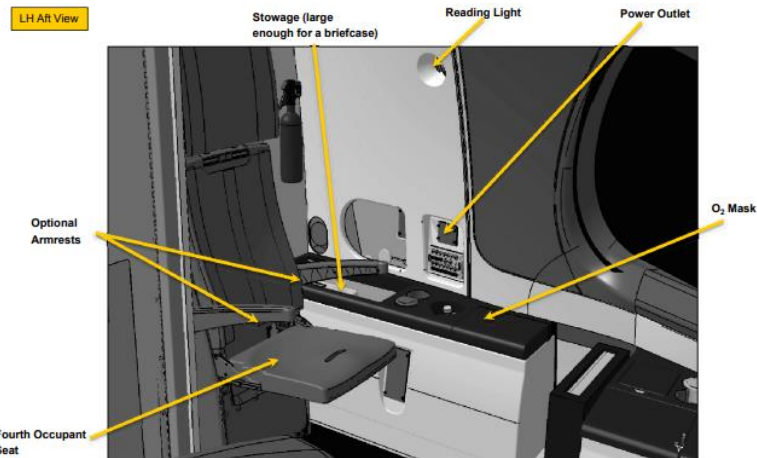
Figure 144: Left Hand Aft View of Cockpit Interior [31]: Left hand aft view of cockpit interior

15.1.3 Flight Deck and Instrumentation

For the avionics of the Hauler-X aircraft, the necessary systems are largely adapted from the Airbus A320, A350 and the ATR-72 models of aircraft, as has been the case for most of the system groups. The reasoning for this is due in large part to the similarities found between the ATR-72 and the Hauler-X, for its systems, resulting from its classification as a turboprop engine aircraft. As such, the hydraulics, air-dependent systems, and others will include the corresponding ATR-72 avionics

panels and will be used as reference charts if necessary. The A350 has been chosen as an aircraft of reference due to its robust and reliable architecture, as well as its relative modernity when compared to other comparable aircraft included in the competitor analysis section. As such, the flight deck and general layout of the avionics will largely be adapted from the A320, and where necessary use figures from relevant manuals. The following sections will showcase the various systems and their corresponding instrumentation panels, as well as other key aspects including communications, navigation, and the autopilot mode.

The main philosophy behind the layout of the cockpit panels was to arrange them according to the frequency in which they were to be used, as well as being ergonomic and easy to reach between the crew members. For the overhead panels, the "lights out" philosophy is applied, in which warning lights corresponding to the present situation are the only ones that are kept illuminated, and the rest are kept dark. Hauler-X also has the following external light types: navigation, landing, taxi, takeoff, beacon, and strobe lights.

 The cockpit consists of the following flight deck elements, an overhead panel, a main instrument panel, pedestal, glareshield, as well as sidesticks. Figure 145 shows the adapted layout of the A350 main instrumentation panel that will also be used in the Hauler-X cockpit, with Figure 146 and Figure 147 showing the pedestal and overhead panel configurations respectively.
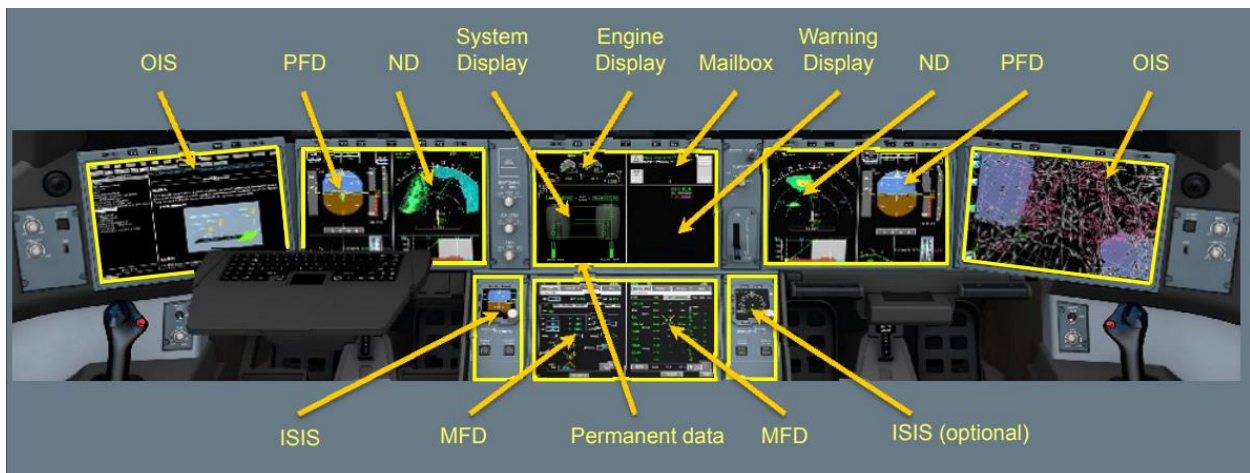
Figure 145: Main Instrumentation Panel [31]: Main instrumentation panel
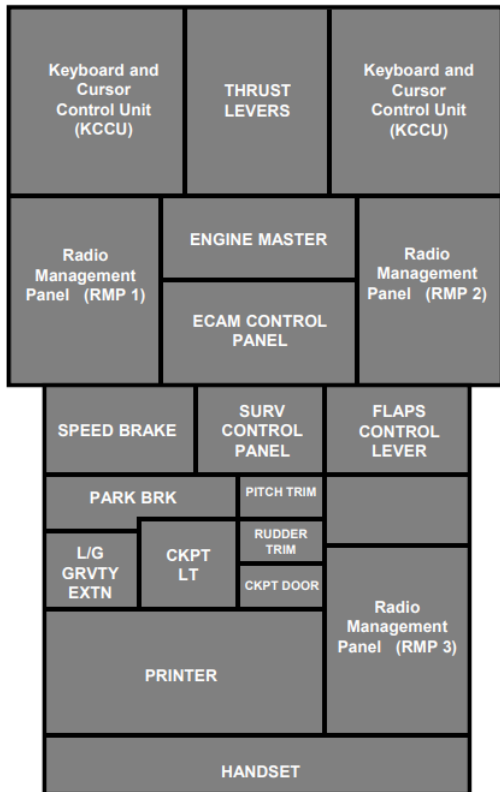
Figure 146: Pedestal Configuration

[31]configuration
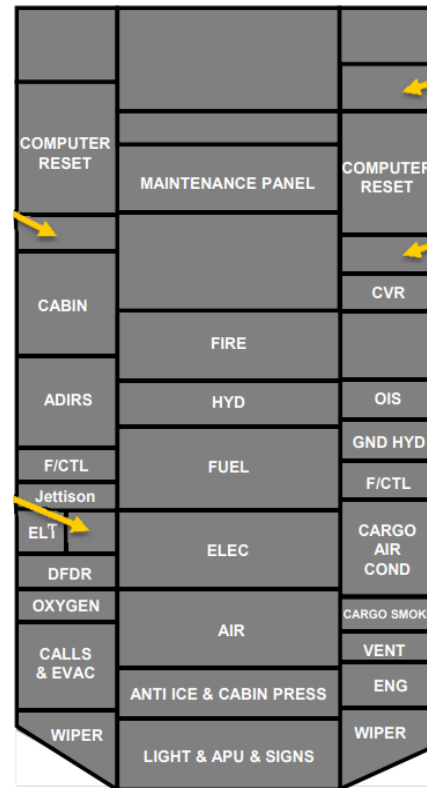
Figure 147: Overhead Panel Configuration

[31]: Overhead panel configuration

The Hauler-X will use sidesticks, which are installed on both forward later consoles located on either side of the cockpit for the captain and first officer use. The sidestick is one of the main control mechanisms for operation of the control surfaces. Aside from its primary use of controlling the aircraft's behaviour, it also includes a radio communication trigger and a take-over button for autopilot disconnection and subsequent priority take-over, as represented in
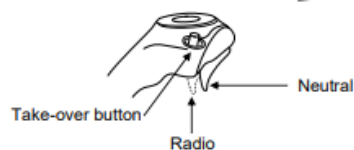
Figure 148. Both sidesticks are coupled electronically to deal with simultaneous inputs and other sources of conflict.
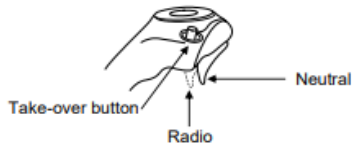
Figure 148: Sidestick anatomy

15.2. **Air Dependant Systems**

15.2.1 Pneumatics

In the Hauler-X aircraft, the pneumatic system is to provide high pressure air to the following systems: air conditioning, de-icing, pressurization, and ventilation systems. For each engine, there exists a Bleed Monitoring Computer (BMC), which monitors the pneumatic system. The connection between the BMC and the pneumatic system is partially redundant, such that a failure in one BMC will allow the other BMC to take over its responsibilities. Sensors in the vicinity of the hot air ducts detect leakage and if detected, automatically shut down the affected area [32].

Engine bleed air is tapped at two compressor ports known as the Intermediate Pressure (IP) port and the High Pressure (HP) port. The HP port only provides air when the IP pressure is insufficient. The system automatically controls the delivery of air from the HP port from its respective HP valve, which is electrically controlled and pneumatically operated [32]. Figure 149 shows the schematic of the pneumatic system located in the aircraft. When high pressure air is detected, the air cycles through the high-pressure line to the required locations, with the bleed valve interrupting a recycling of the air back into the LP port. An electrically controlled, pneumatically operated cross valve connects both the left and right lines of the pneumatic system, which is used to operate both air packs on the ground or if one engine is shut down. The two non-return valves located below the cross valve on the system diagram are included to direct air from the engine into its respective pack during flight when the cross valve is closed. In the event of a singular functioning pack, the flight level is to be limited to 20000 *ft* as a single pack cannot provide pressurization above this level.

Temperature sensors are also fitted across the system to warn the pilots in the event of an overheat. Additionally, for the HP system to operate without being automatically shut down, the temperature must be less than 270 °C. Additionally, if this temperature loop senses the bleed air to be greater than 153 °C, the corresponding pneumatic line valves are closed off for the rest of the flight [32].
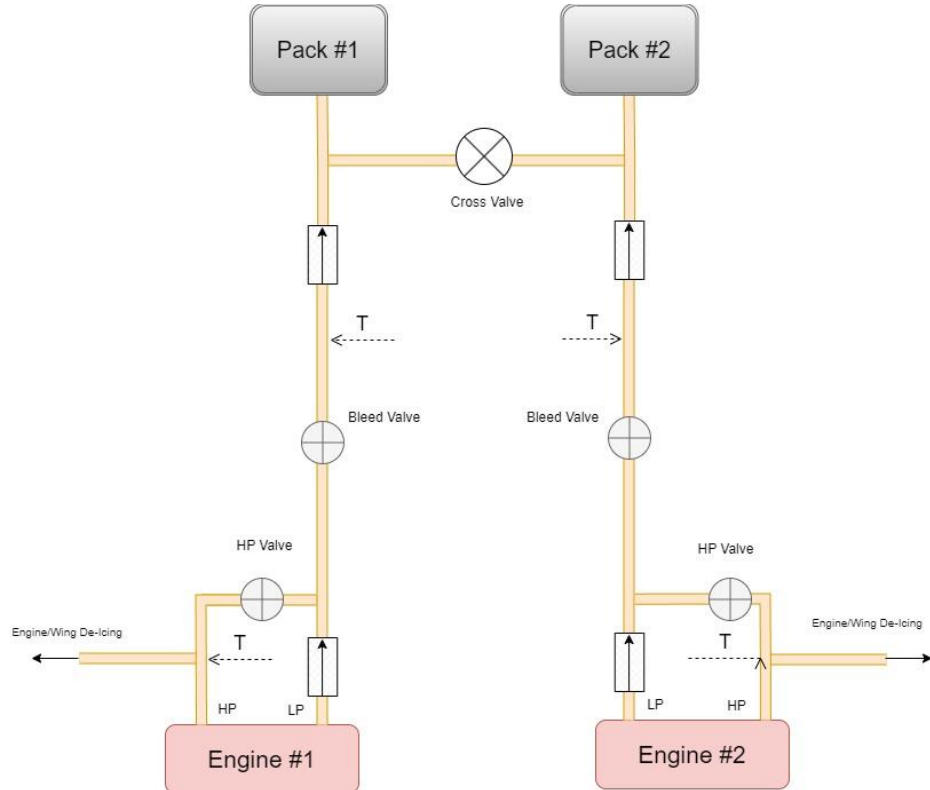
Figure 149: Hauler-X pneumatics system
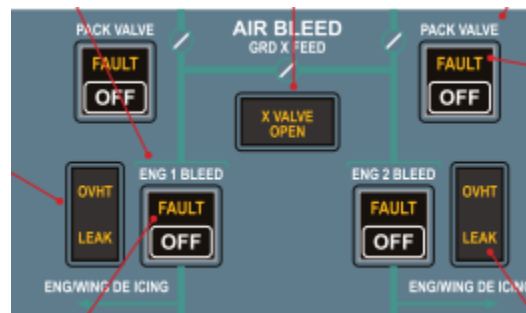
Figure 150: Adapted air bleed panel for pneumatic system [33]

15.2.2 <u>Air Conditioning</u>

The air conditioning system is configured solely for the cockpit in the Hauler-X and is provided to keep the cockpit to the required temperature, humidity, pressure, and level of comfort that is to be expected by the crew of the aircraft. Figure 151 shows an adapted schematic of the Hauler-X's air conditioning system as appropriated from the ATR-72. The main reason why this aircraft was chosen as a reference point was its similarities between the pneumatic systems of both aircraft, which is ultimately the source of the air used in the AC system. Thus, the interoperability between both is likely to be expected, and can be used as an effective reference.

The system is controlled by 2 dual lane air conditioning system controllers which provide appropriate inputs to the pack flow control valves, the packs, and the various regulating valves. If one lane is to fail, the system has protections which allow the backup lane to take over all its duties. The pack flow control valves are used to regulate the flow of warm pre-conditioned air, which were originally derived from the pneumatic system. They are all pneumatically operated, electrically controlled, and spring-loaded to the open/closed positions when required. Fault protections within the system ensure that valves will automatically close when a pack overheats, with the option to also manually close [32].

Each pack consists of an air cycle machine and a ram air duct for the heat exchangers. The air cycle machine turbine also drives a fan that pushes cool air over the exchangers and is regulated by modulating the ram air intake. This cooling process is only operable by ram air when IAS>150 *kts* to avoid ingestion of foreign objects. In the event of a failure within the system, the packs can still work under reduced flow solely by using the heat exchanger. The cooled air from the packs is then processed into the mixer where it is mixed with recirculated cockpit air. The pilots have the option to set temperature requirements by means of a Zone Control Computer, which operates the trim valves and provides data inputs to the pack controllers [33].
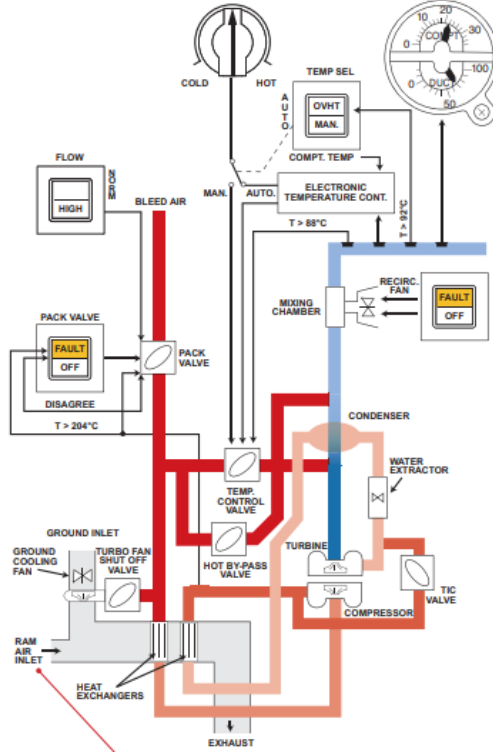
Figure 151: Adapted Hauler-X air conditioning schematic [33]

15.2.3 Avionics Ventilation

Ventilation for the avionics in the Hauler-X is done by the Avionics Equipment Ventilation Computer (AEVC). Adapted from the Airbus family of aircraft, specifically the A320, this system consists of three main configurations, which are automatically selected by the AEVC depending on the skin temperature [32]:
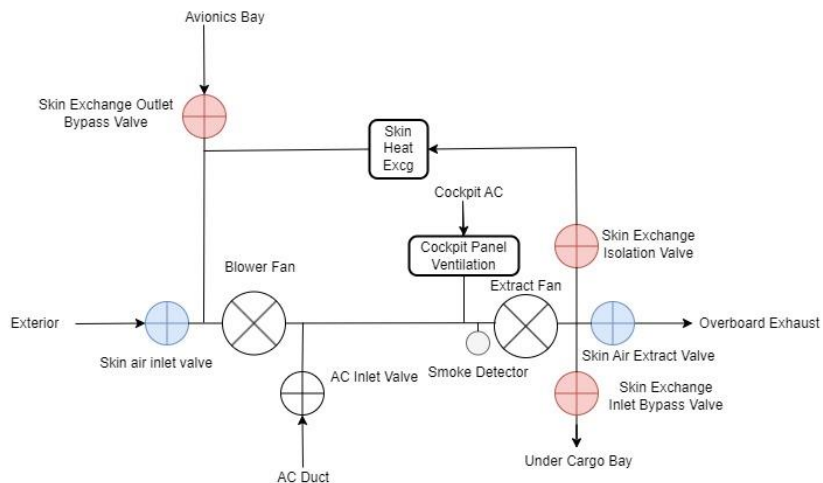
Figure 152: Hauler-X avionics ventilation schematic

- Closed-Circuit: Used when the skin temperature is low, the skin exchange outlet bypass, isolation valves, and inlet bypass represented in red in Figure 152 are opened and all other valves are closed. This leads to the air being drawn from the avionics bay exhausted below the cargo bay floor, with a return loop in place via the skin heat exchanger.
- Intermediate: Used when skin temperature is high. Similar operation to the closed-circuit, however the skin air extract valve is partially open to allow for air to go overboard.
- Open-Circuit: Used during ground operations with a high skin temperature. In this mode, the blue valves as shown in the ventilation diagram are opened, which results in air from outside the aircraft to be moved across the avionics equipment for cooling purposes, after which it is exhausted externally.
- Cooling of the cockpit panels is done by drawing air-conditioned air from the cockpit over the panels.

15.2.4 Pressurization

Pressurization control is provided by an outflow valve and two safety valves, to prevent both over-pressurization (>8.6 psi), and under-pressurization (>1 psi below ambient). Pressure is controlled by the amount of cabin air discharged out of the plane. This profile was adapted from the ATR-72 aircraft; however, the flight profile characteristics have been modified to suit the Hauler-X's flight pattern.

Table 41: Automatic pressurization control operates in 6 modes

Mode	Description
Ground (GN)	• Prior to take off/55 seconds after landing • At touchdown any residual cabin pressure is released at a cabin vertical speed of 550 *fpm* • Cabin Altitude = Aircraft Altitude, up to 3500 *ft*

Takeoff (TO)	• Aircraft is pre-pressurised to a difference of 0.1 *psi* at a rate of 400 *fpm*.
Climb (CL)	• Cabin altitude is a function of actual rate of climb.
Cruise (CR)	• The higher value between cabin altitude at level-off (typically 8000 *ft*) or landing field elevation is maintained.
Descent (DE)	• Cabin rate of descent is maintained so that cabin pressure equals landing field pressure, with a maximum R.O.D. of 500 *fpm*.
Landing (LD)	• Cabin pressure set to take-off altitude + 0.1 *psi*.
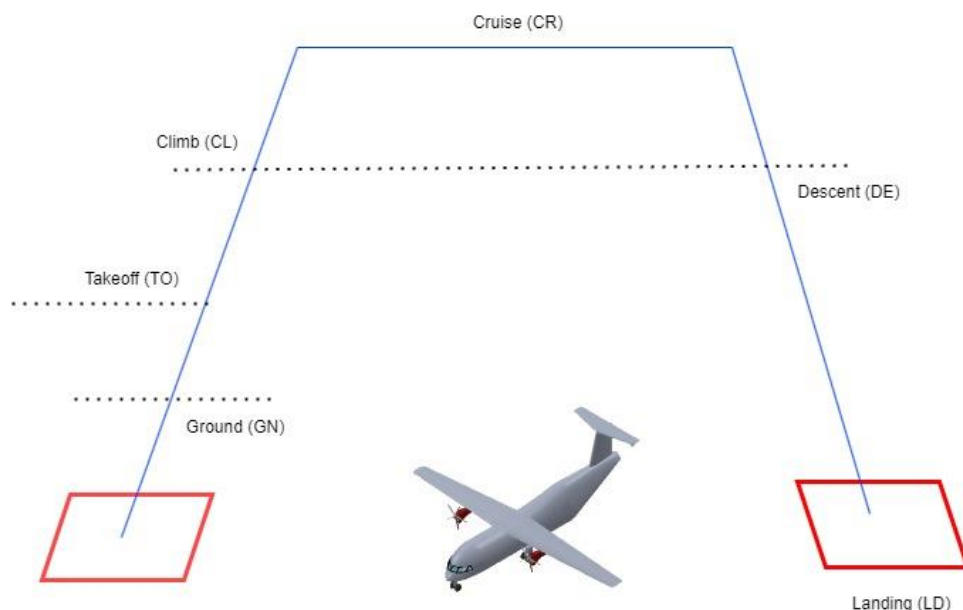
Figure 153: Hauler-X pressurization modes

15.3. <u>**Environmental Hazard Protection**</u>

15.3.1 <u>Fire</u>

In the Hauler-X, each engine has an identical fire detection system, consisting of 2 parallel detection loops monitored by a fire detection unit (FDU). A level 1 ECAM warning is produced if one detection loop is tripped, with the loss of both loops triggering a level 2 ECAM warning indicating loss of fire detection capability on that engine. If both loops break within 5 seconds, a fire warning is triggered. In the cockpit, the pilot has the capability to shut off all pneumatic, pack, hydraulic, and fuel valves to prevent any further damage to the systems of the aircraft.

A similar setup is in place for the cargo bay section, with smoke detectors in place within these loops. An SDCU (Smoke Detection Control Unit) receives positive indications detailing that smoke is present from the detectors and forwards it to the FWC which will then display appropriate warnings for the pilots. If smoke is to be detected here, both the inlet and exhaust valves in the cargo bay are to be automatically closed. A single fire bottle is also present for use in extinguishing efforts, and when deployed by the pilot, is completely emptied out into the section(s) of the cargo bay that are affected. Other fire protection measures include the installation of a smoke detector in the air extraction duct for the avionics.
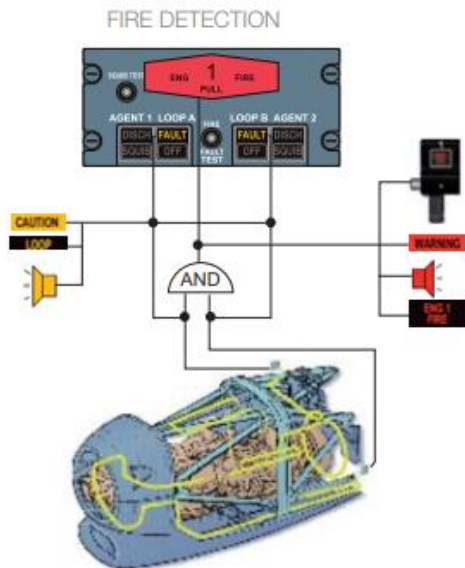
Figure 154: Adapted fire detection loop

15.3.2 <u>Ice/Rain</u>

For protection against ice and rain, the engine air intakes are anti iced using an independent air bleed from the HP compressor. For each engine, hot air is routed via an electrically controlled, pneumatically operated engine anti-ice valve to the intake. In addition to the engine intake, the cockpit windshield, pitot heads, static ports, AOA probes and TAT probes are also electrically heated. All probes are controlled by a Probe Heat Computer (PHC) which provides automatic regulation should a hot air leak be detected, in which case the wing anti-ice valve on the affected side automatically closes. In cases of moderate to heavy rain only, rain repellent can also be applied to the windshield to provide better visibility. Each front windshield also has an electric wiper that can be used up to speeds of up to 230 *kts*. Figure 155 provides a schematic which details the various surfaces that are protected against these ice and rain conditions as adapted from the ATR-72, with surfaces either being pneumatically or electrically operated.
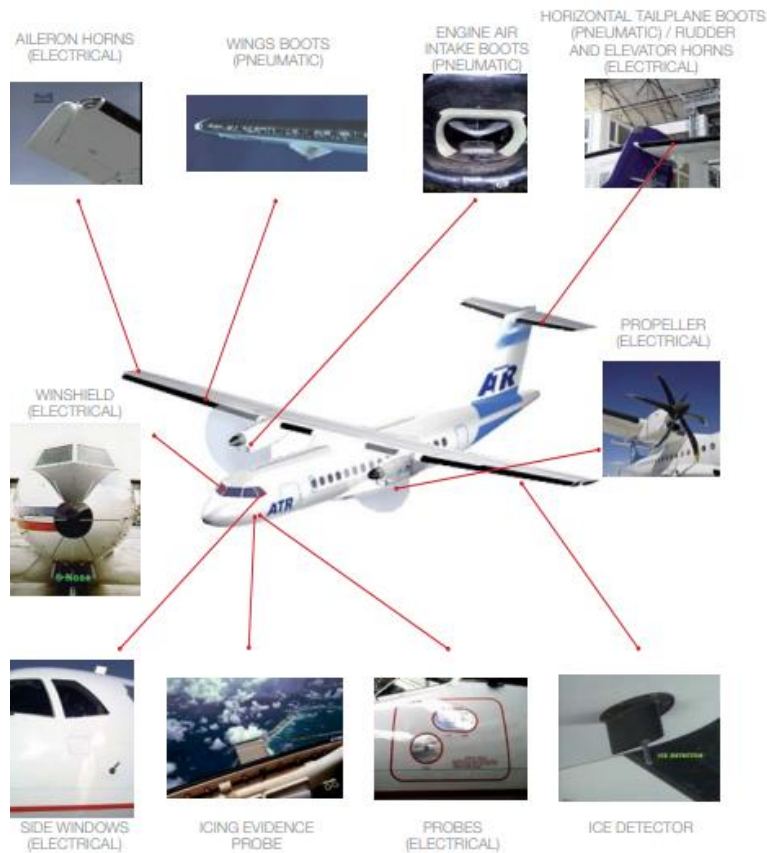
Figure 155: Adapted schematic of heated surfaces of ATR-72

15.3.3 Flight Control

When adapting the flight controls for the Hauler-X, the Airbus A320 was chosen as the main source of inspiration. This is mainly due to the hydraulic actuation of its control surfaces via fly-by-wire technology as opposed to the over-reliance on mechanical inputs as found on the ATR-72 and comparable turboprop aircraft, as well as the addition of the Electrical Flight Control System (EFCS). The EFCS provides safety improvements in stall, windshear, overstress, and overspeed conditions in comparison to other flight control systems. Several economical aspects are also present with the inclusion of the EFCS, namely weight saving measures due to the elimination of major sections dedicated to mechanical mechanisms such as pulleys/bell-crank levers. As observed on the A320, maintenance, training, and production costs were all decreased when this system was implemented, as well as improvements in flight handling and overall comfort, and similar projections are to be expected when the system is adapted to Hauler-X.

The flight controls on the Hauler-X can be separated between the primary flight controls (ailerons, elevators, and rudder) and the lift augmentation devices (flaps). Control is achieved through these conventional surfaces, in which explanations behind the inclusion of certain devices can be found in section 10 of the report. All these surfaces are hydraulically actuated, with the devices responsible for roll and pitch control being electrically controlled, and the trim stabilizers and rudders having mechanical backups and being electrically insured.

A multitude of flight control computers take the input from the sidestick, after which it is analyzed to ensure the validity of the input and outputted to the control surfaces. These include: Two ELACs (Elevator Aileron Computer), responsible for commands of the ailerons, elevator and stabilizer under normal conditions, two SECs (Spoiler Elevator Computer) which are devoted to standby elevator and stabilizer control, two FACs (Flight Augmentation Computer) which assists in achieving rudder control, and two SFCCs (Slats Flaps Control Computer) which are used to control the flaps.
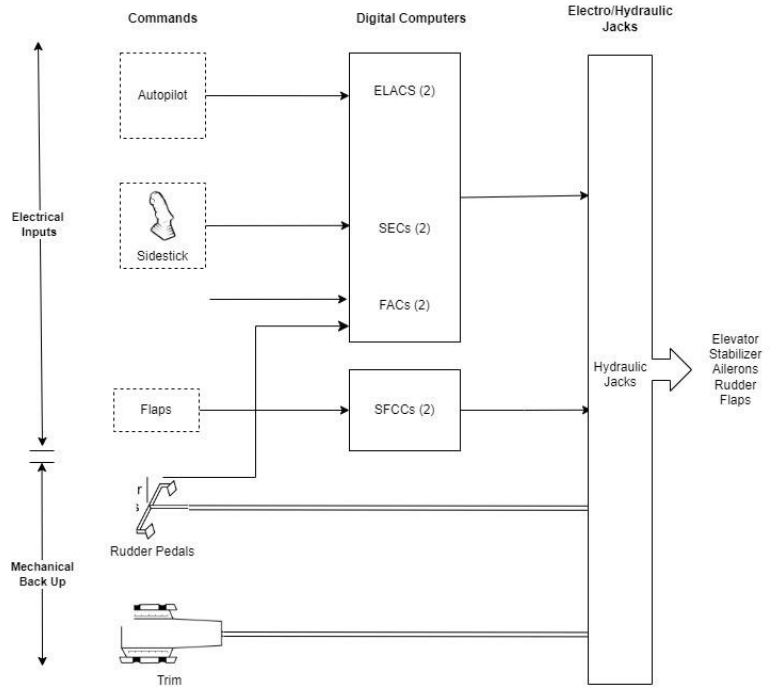
Figure 156: Hauler-X EFCS system architecture

As previously mentioned, the fly-by-wire control method has been implemented for use within the Hauler-X aircraft. This method was chosen due to the superior flight control characteristics such as improved handling and stability, as well as improved safety in overspeed, stall and wind shear protections as opposed to classic flight controls where there is a direct proportional relationship between the pilot stick input and the control surface position. This can lead to an increasingly complex system within the aircraft, not to mention the various airworthiness and aircraft performance requirements that would need to be met as opposed to fly-by-wire controls, where an artificial feel is applied between the pilot stick input and control surface position when attempting to modulate the surfaces.

As this system is adapted from the A300 family of aircraft, several tests that were performed by their test pilots also showcase the reliability of a sidestick-FBW combination over conventional controls. Figure 157 shows the performance comparison of these two methods under various angles, rates, and acceleration transitions, in which the following results can be gathered:

- Parameters related to fuel burn showed significantly better values with the sidestick, thus improving fuel economy by eliminating unnecessary control surface inputs and increased rear CG limits.
- Pilot control inputs were reduced by 50%+, this system thus allows for lower workloads and more time for the pilot to focus on dealing with emergencies instead of controlling the plane.
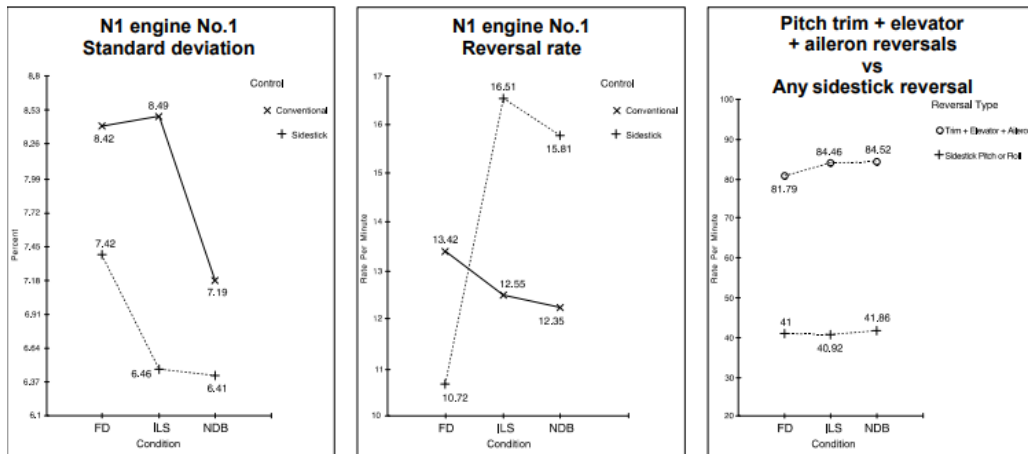
Figure 157: Performance comparison graphs of FBW vs conventional controls

Another important way in which pilots gather information necessary to perform their duties is using pitot tubes and other similar probes. The Hauler-X will have 4 pitot tubes, 2 located on either side of the nose on the underside of the fuselage facing forward and 2 located on either side of the tail. The pitot tubes located on either side of the nose are independent systems for each pilot, and the two on the tail located at the base are used for elevator feel and centering unit when transmitting to the sidestick in the cockpit. The reasoning behind this placement can be attributed to there being less distortion caused by the aircrafts structure in these areas, so the points closest to the body in which the 'cleanest' air can be found shall serve as locations for the pitot tubes. FAR laws 23.1325 and 23.1326 supports these statements, stating that where duplicate airspeed indicators are needed, respective pitot tubes must be far enough apart to avoid damage.

15.4.   <u>Electrical</u>

The electrical system architecture within the Hauler-X aircraft is largely adapted from the ATR-72 aircraft, due to the identical use of the PW127-XT engine as well as its overall configuration similarities such as having battery backups for the hydraulic auxiliary pump in identical locations. Due to these similarities, the ATR-72's electrical system architecture will be used when discussing the various configurations of the Hauler-X's electrical system as a point of reference where appropriate.

The electrical system within the Hauler-X consists of 3 different kinds of current: Direct Current (DC), Constant Frequency Alternating Current (AC), and Variable Frequency Alternating Current (ACW). Figure 158 shows the different conversion methods of AC/DC that the Hauler-X uses.
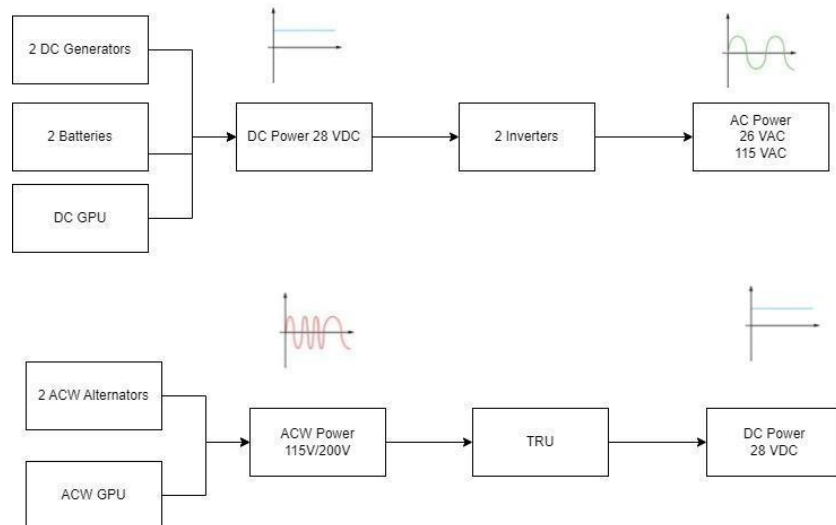
Figure 158: Original design schematic of electrical power conversion for Hauler-X
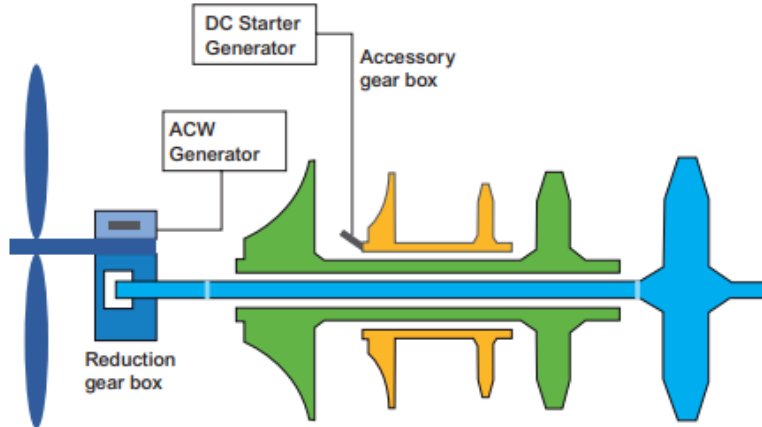
Figure 159 details a DC Starter Generator which is driven by the HP spool through the Accessory Gear Box. When operating 0 to 45% NH, it is in starter mode, and above 65% NH it is in generator mode, referring to the way in which power is to be supplied. The ACW Generator is driven by the Reduction Gear Box (RGB) to which it is connected to and is available when NP (propeller speed) > 66%, When below this value, ACW frequency is not supplied, which sets the engine in hotel mode.
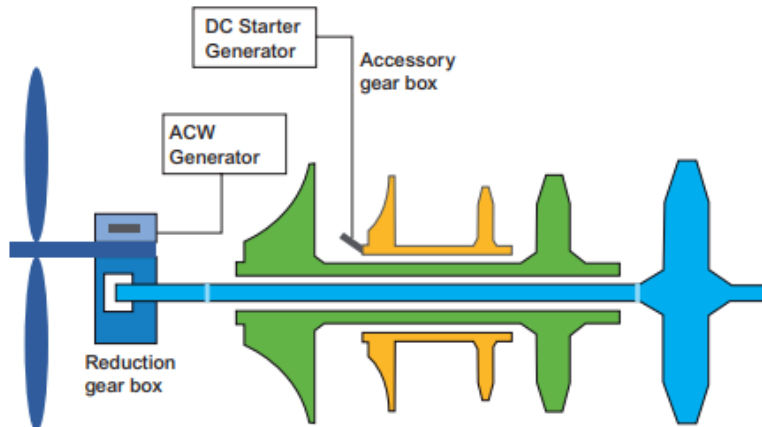
Figure 159: Adapted schematic of engine turbine

Figure 160 below details the system's electrical features when in nominal operation. In this scenario, the bus tie contactor which connects both systems and is responsible for supplying power to the other bus pathway in the event of a failure is opened, and each generator is to supply its own

busses. In the event of a dual generator loss, the TRU which is connected to the ACW Bus 2 will supply and energize the various emergency and standby buses.
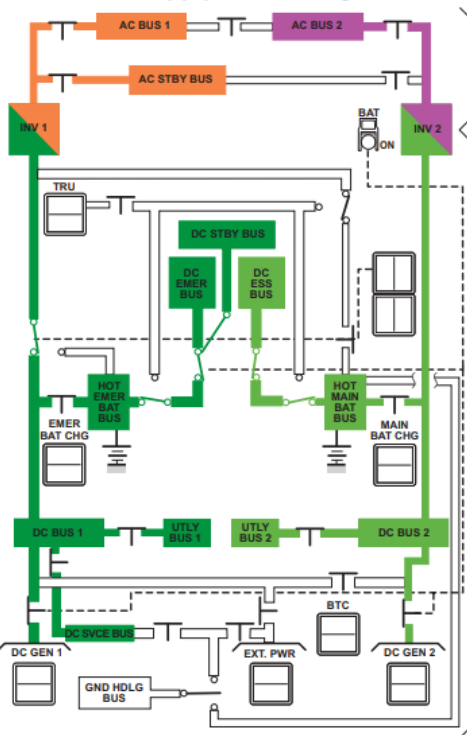
Figure 160: Adapted electrical schematic with both generators online

Figure 161 below shows a close up of the ACW schematic and its corresponding cockpit panel under normal operating conditions and maximum propeller speed. In this scenario, ACW Gen 1 and ACW Gen 2 supply ACW Bus 1 and ACW Bus 2 respectively, with ACW Bus 2 also connecting to the TRU, which supplies the TRU in case of emergencies.
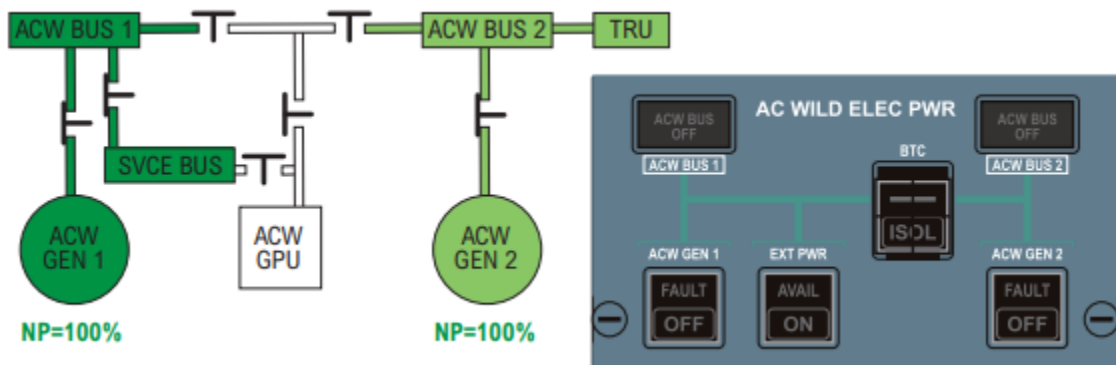
Figure 161: Adapted ACW schematic at nominal operation with accompanying cockpit panel

15.5. **Hydraulics**

The hydraulic system within Hauler-X will have all its functions contained across 2 separate lines, which will share a common tank separated by a partition. This is done to prevent the leak in one line from emptying out the other line's fluid in case of a line break. For the following explanations, the hydraulic lines will be referenced as represented in the hydraulic system diagram picture in Figure 162 by their respective colours. The responsibilities of each of the two main lines, as well as the emergency line is also shown below:
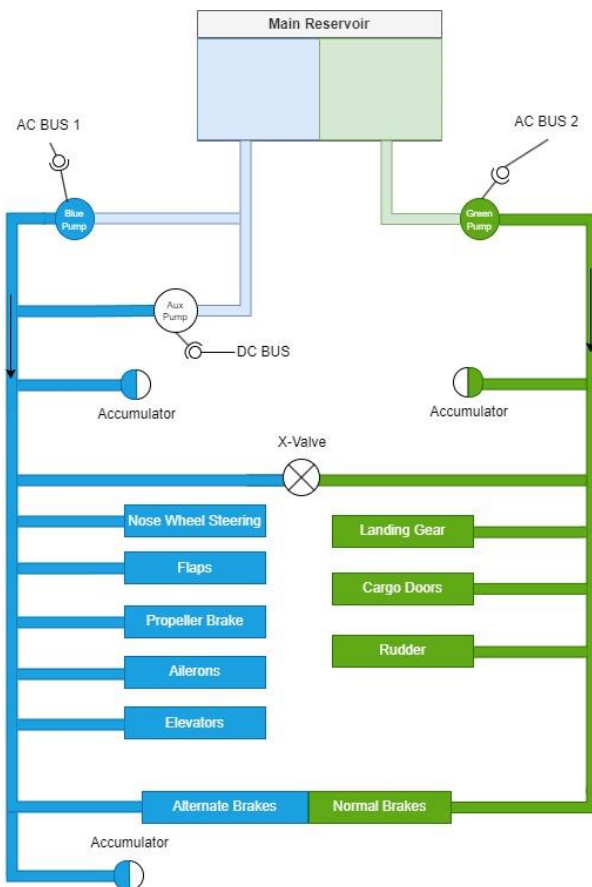
Figure 162: Hauler-X hydraulics system

Table 42: Hydraulic system redundancies

Blue	Green
• Nose Wheel Steering • Propeller Brake • Flaps • Ailerons • Elevators • Emergency/Parking Brake	• Normal Brakes • Landing Gear • Cargo Doors • Rudder

To prevent cavitation, the reservoirs will be pressurized by bleed air. Starting with the two main pumps, indicated on the system diagram as blue and green pumps respectively, these pressurize the fluid to 3000 psi, which run continuously when the engines are powered up, otherwise the fluid will return to the tank. Both pumps are powered by AC wild frequency buses, with the blue and green lines being powered by AC Bus 1 and AC Bus 2 respectively. In the event of a failure in one of the lines where the fluid pressure or flow is insufficient in providing for the aircraft's systems, a cross bleed valve has been installed to allow for one main pump to provide hydraulic support to the other line. This is a reversible process, with the blue line able to pressurize the green line and vice versa. An auxiliary pump powered by DC frequency, or the battery bus is also fitted to the blue line for operation of the system when the pump is not powered, such as during ground operations. Also fitted within the system are various accumulators that are filled with nitrogen. These accumulators are tasked with preventing shock loads and damage to hydraulic lines by acting as an absorber.

The blue line provides the actuation of the nose wheel steering and both flaps on the aircraft, with all hydraulically actuated flight control surfaces being actuated with a PCU. Also connected to the blue line is the propeller brake, which is attached to the propeller gearbox on engine 2. When engaged, this will halt the propeller operation, allowing the engine to supply electrical power and air conditioning. Also connected to this line is the emergency/parking brakes, and a secondary accumulator which stores enough pressure to allow for six applications of the emergency brake, which allows for the possibility of landing in the event of hydraulic failure mid-flight. The green

line has fewer complex responsibilities, overseeing the landing gear, normal brakes, as well as the cargo doors.

Certain operating specifications are also provided for the hydraulic system, namely for suboptimal fluid levels, overheat, pressure, and auxiliary pump conditions. These will show up on the hydraulic power panel in the flight deck in the form of warnings should these conditions be met.

Overheat	• Fluid drain if temp > 121°C (250°F)
Low Pressure	• Pressure less than 1500 psi, indicated for both lines
Fluid Levels	• Total Fluid Volume: 9.6 L • Operating Volume: 9.3 L • Minimum Filling 8.5 L • Low Level/Alert: 2.5 L
Aux Pump	Automatic trigger conditions: • One engine must be running • Blue system pressure < 1500 psi • Propeller brake is disengaged • Landing gear engaged

The design methodology behind the hydraulics of the Hauler-X was to consider the other system groups that it is responsible for actuating and ensuring that the most effective and reliable method is chosen, before other factors such as weight and complexity are considered. More depth regarding the flight control surfaces will be provided in section 12.3. When selecting aircraft to adapt hydraulics from, a blend of the ATR-72 and Airbus A320 were considered, the former's overall architecture including the two lines joined by a common tank separated by a partition proved useful in justifying weight savings, and the exclusion of variables such as auxiliary power can be justified due to the short nature of the Hauler-X's intended flight path. The ATR-72 however lacked hydraulic actuation via fly-by-wire in its design, and it was imperative to eliminate traditional bell-crank mechanisms for flight controls, hence the decision to adapt the Airbus A320's architecture regarding the hydraulic actuation. Original modifications were also made, such as the inclusion of the cargo doors. With these checks and adaptive measures in place, this design can be considered reliable in accordance with FAR regulations, specifically FAR 25.1435. Figure 163 shows the

corresponding hydraulic panel to be adapted from the ATR-72 and used in the Hauler-X aircraft:
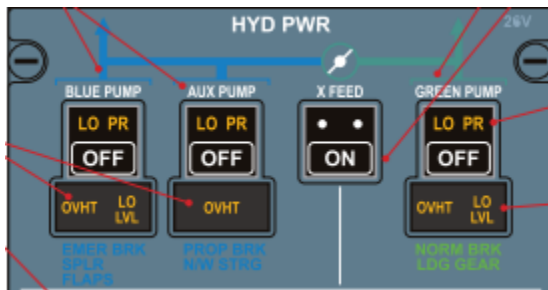
Figure 163: Hydraulic panel

15.6. Engine

15.6.1 Power Plant

The Hauler-X is fitted with two Pratt & Whitney PW127XT engines, each of which is fitted with a 6-bladed propeller. This engine is a direct upgrade of the PW127 engine found within the ATR-72 and is more fuel efficient in addition to being less costly when it comes to operating and maintenance cost. The performance calculations conducted earlier in earlier analysis led to the choice of fitting this engine to the Hauler-X as it was the most suitable for the mission profile at hand. This is a free turbine engine consisting of 3 concentric spool shafts; an HP spool composed of the HP turbine and HP compressor, an LP spool composed of the LP turbine and LP compressor, and a power shaft which consists of 2 power turbines which drive the propeller through the reduction gear box (RGB).

Figure 164 shows a cut-out schematic of the PW127 engine variety, which is nearly identical to the PW127XT engine being used, as there are no major structural changes:
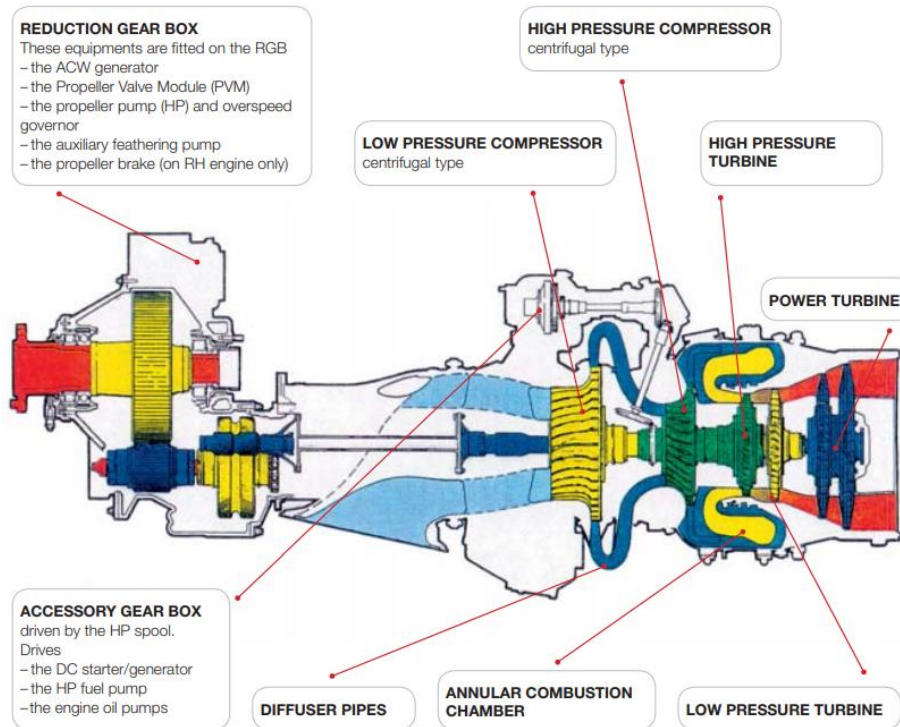
Figure 164: PW127 engine schematic

15.6.2 Fuel

The Hauler-X's fuel is stored in 2 tanks, one in each section of the wing. The aircraft has two main methods of refueling, with a gravity cap located near the leading edge of the left wing to assist in gravity assisted refuelling, as well as a refueling point located at the junction near the fuselage and the right-side wing's trailing edge.

The following schematics showcase a normal cycle of the engine and the cross-feed operation in the event of a failure of an ATR-72 aircraft, which is what the fuel system in the Hauler-X is adapted from Figure 165 detailing the nominal fuel procedure goes as follows:

1. Engine is started after which the flow from the return line of the HMU opens the motive flow valve to supply the engine feed pump

2. Engine Feed Pump begins to operate by consuming fuel located in the feeder tank and simultaneously supplies the feeder jet pump

3. Once the engine feed pump outlet pressure reaches the target value of 8.5 psi, any operations by the electrical pump are stopped and the pump is de-energized after 30s, as in normal operation the engine is only supplied by the engine feed pump.

The electrical pump is only energized in the following scenarios:
- If a cross feed operation is initiated
- Engine feed pump outlet pressure < 5 psi
- Low Fuel Levels in tanks

In the case of the cross-feed procedure, the cross-feed valve is opened to supply the engine from the opposite tank if the fuel line to which it is connected to is in an inoperable state. In the case of an engine fire, the corresponding fire handle is pulled for the jeopardized engine, which leads to the closure of the LP shutoff valve.
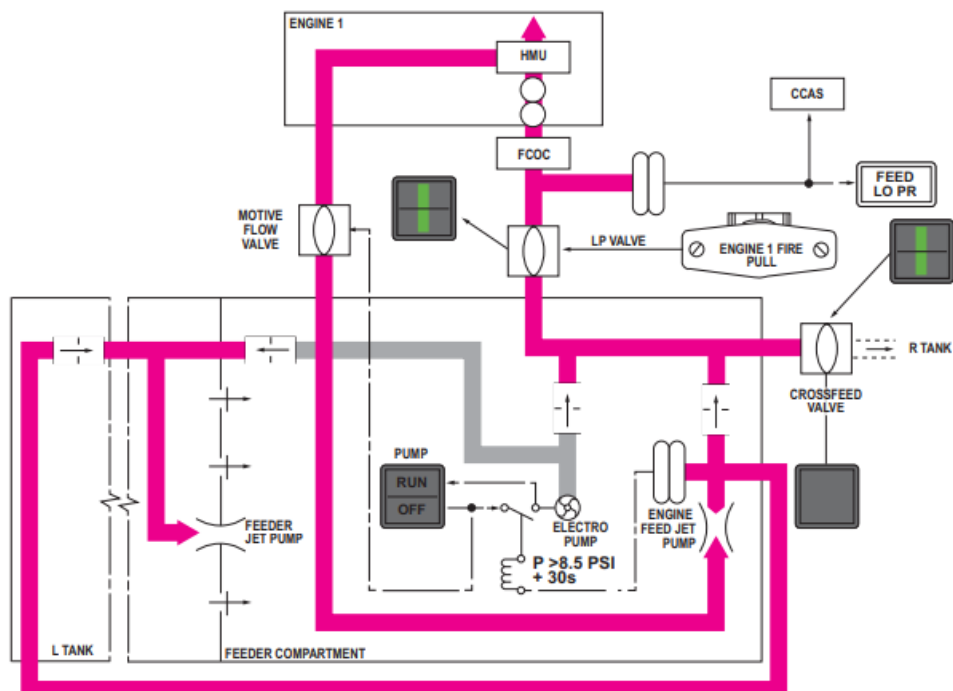
Figure 165: Adapted fuel system under nominal operation
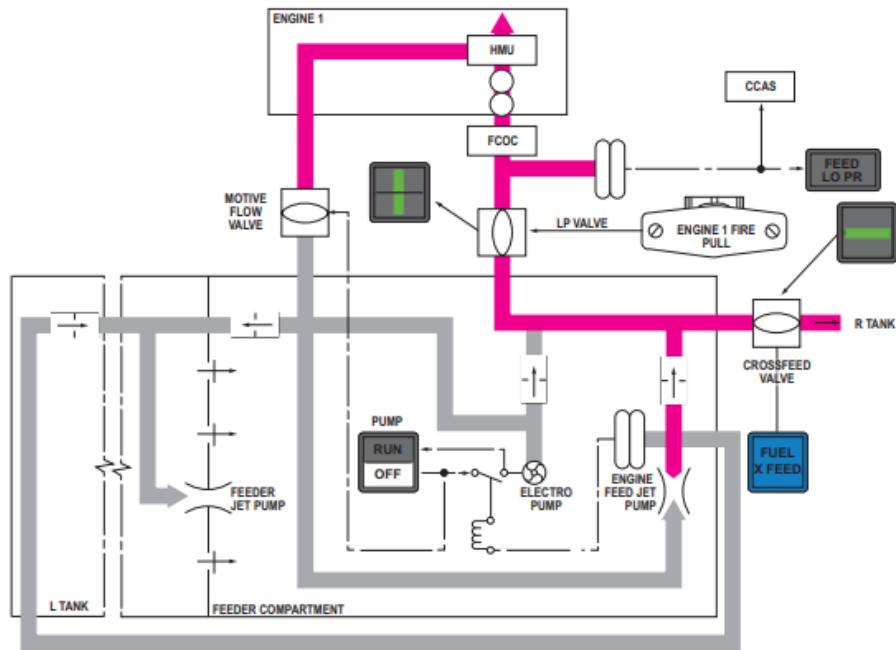
Figure 166: Adapted schematic of cross-feed fuel supply operation

16.Sustainability

Bombardier's commitment to sustainability is reflected in its approach to environmental challenges. The company recognizes the need to promote greater environmental responsibility, and to invest in the development and diffusion of environmentally friendly technologies. As part of its continuous innovation, Bombardier is working to minimize the environmental impacts of its products, services, and operations. One of the fundamental ways Bombardier is addressing environmental concerns is by continually improving the environmental performance of its manufacturing, servicing activities, and products across its value chain. The company has set ambitious goals to reduce carbon emissions, energy consumption, and waste generation, demonstrating its commitment to sustainability [34].

The proposed Hauler-X concept was designed with the focus on furthering Bombardier's sustainability initiative and fit in seamlessly with the rest of the company's fleet of aircrafts. A transitional fuselage was designed to optimize the weight and sizing of the aircraft for the specific payload, maximizing the fuel efficiency for the given mission. Similarly, due to the short range of the mission, PW127XT turboprop engines were selected for our aircraft configuration as they provide adequate performance while being lighter and more fuel efficient than engines used on aircrafts of similar sizing. The two turboprops allow the Hauler-X to complete the mission with 900 *lbs* of fuel for ground operations and loiter in the air, leaving an expendable fuel amount of 4100 *lbs,* while boasting a power-specific fuel consumption of 0.45 lb/hp·hr (per engine). Furthermore, the PW127XT supports the consumption of 50% SAF blends with expectations of reaching 100% by 2025, in line with Bombardier Aerospace standards.

Additionally, the use of existing systems has allowed us to reduce the energy required during the manufacturing process. This reduction in energy consumption not only reduces costs but also contributes to Bombardier's sustainability initiative by minimizing the Hauler-X's carbon footprint. By utilizing existing systems, the design is also able to take advantage of proven technologies and established supply chains. This allows for faster and more efficient production, ultimately reducing costs and allowing for a quicker time to market. Similarly, a concerted effort was made to incorporate materials that are both sustainable and ethically sourced. Specifically, the

design made use of structural steel, Ti-6AL-4V titanium, and Al 7075-T6 and Al 2024-T3 aluminum, which are widely recognized as being among the most environmentally friendly materials available. These materials are highly recyclable, which reduces waste and promotes greater environmental responsibility. Additionally, by sourcing these materials from reputable suppliers that adhere to strict ethical and social responsibility policies, the proposed concept aims to support a more sustainable supply chain. To ensure that the materials to be used in our aircraft are ethically sourced, it is imperative to work closely with suppliers to establish clear standards for responsible sourcing. This includes a focus on fair labor practices, responsible environmental stewardship, and adherence to strict ethical and social responsibility policies.

The aircraft design aims to comply with Bombardier's commitment to environmental sustainability by prioritizing the use of environmentally friendly materials and processes. In line with Bombardier's focus on Environmental Product Declarations (EPDs), our design seeks to provide a transparent and comprehensive assessment of the environmental impacts of our aircraft. By embracing the principles of EPDs and continually striving to reduce the environmental impacts of our products, we are proud to contribute to the leadership that Bombardier has shown in the aviation industry in terms of environmental sustainability. Overall, Bombardier's sustainability goals are centered around respecting the environment and investing in the development and diffusion of environmentally friendly technologies. The Hauler-X's design focus aimed to be in line with Bombardier's continuous innovation and improvement, as well as its commitment to reducing carbon emissions, energy consumption, and waste generation. The design pushes to be a leader in sustainable practices within the aviation industry.

17. Cost Analysis

The costs related to the aircraft production and operation are crucial in separating ourselves from the competitors, and being a more viable option for buyers. A key aspect of this project was to have lower operating costs. In addition to that, we have explored the possible purchasing price as well as development costs to really pinpoint our position on the market as an aircraft hoping to lead future transport.

17.1. Purchasing Price

The purchasing price can be found using a few equations, although they are very rough estimates. It is hard to predict the exact purchasing price of an aircraft unless real life applications are applied and testing can be done. To get a first rough estimate, the cost per pound of modern aircraft material is researched. After adjusting for inflation, a rough estimate can be the product of our empty weight and cost per pound of material [8].

$$Purchasing\ Price = (Empty\ Weight)(Cost\ of\ Material\ per\ Pound) \qquad (17.1)$$

Another method shown in the Raymer textbook that was applied to obtain the purchasing price, simply outputs the cost as a function of the empty weight.

$$Purchasing\ Price = \$6{,}375{,}310.69 + 550(Empty\ Weight) \qquad (17.2)$$

Finally, the last approach was to take research-based parameters of empty weight and purchasing price of close competitors, and creating a line of best fit. The empty weight of our aircraft is simply plugged in to output the purchasing price. The line of best fit is shown in the graph below, yielding a line of best fit equation, which is almost exactly the same as the equation provided in the Raymer textbook [8].

$$Purchasing\ Price = \$6{,}380{,}000 + 550(Empty\ Weight) \qquad (17.3)$$
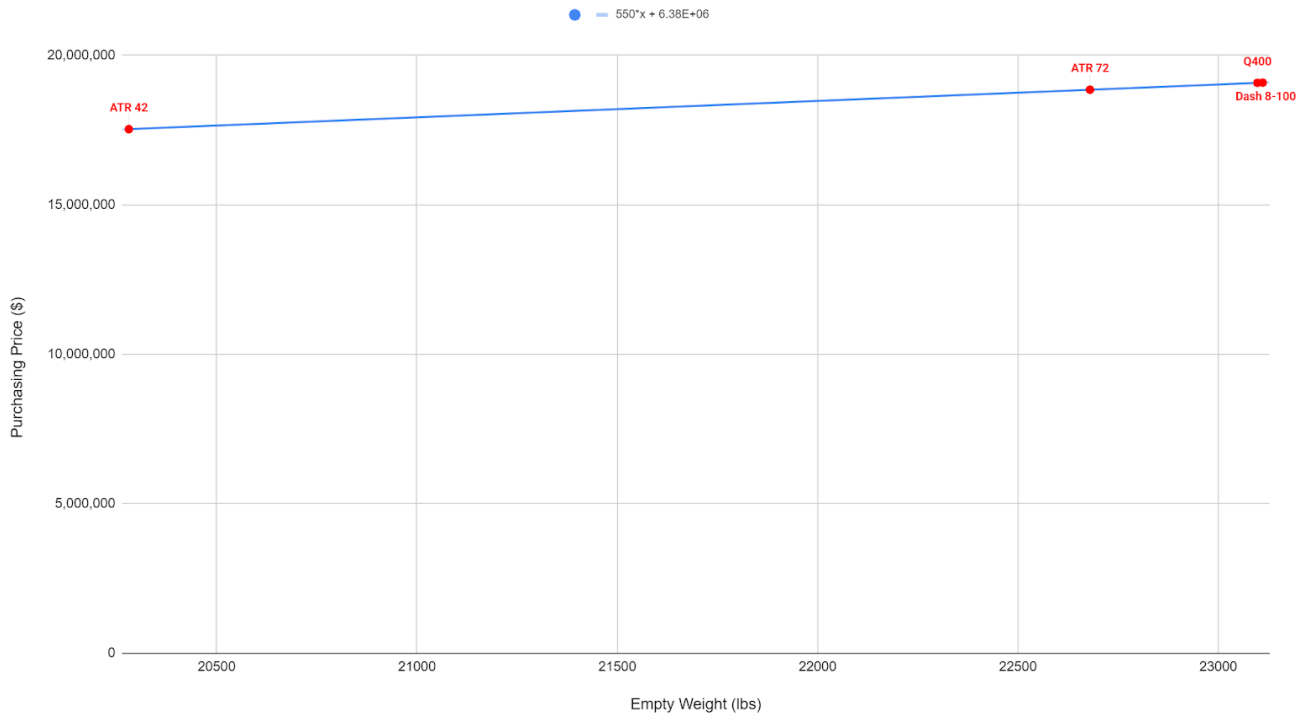
Figure 167: Line of best fit for purchasing price

After applying the Hauler-X's empty weight of 28,994lbs, the three methods of purchasing prices are shown in the table below. As a result of the three approaches, we can approximate our purchasing price to range from $22,000,000 to $29,000,000. However, considering that our closest competitors are in the lower range of this, our purchasing price would likely be around $22,000,000.

Table 43: Purchasing prices of Hauler-X

Method	Purchasing Price ($)
Material Per Pound Method	$29,362,067.85
Raymer Equation	$22,322,010.69
Line of Best Fit Approach	$22,326,700

17.2. Development Costs

The development cost emphasizes the cost that would go into producing the aircraft from scratch, and would consist of costs allocated to development support, flight testing, manufacturing materials, and engine production. The costs as well as the engineering, manufacturing, tooling, and quality control hours are found using equations in the Raymer textbook, which applies the empty weight (W_e), max cruise velocity (V), production quantity (Q), FTA (# of tests), engine maximum temperature (T_{max}), maximum Mach number (M_{max}), and inlet temperature (T_{inlet}). The values for R input in the development costs are simply the labour wrap rates for that specific production stage [8].

$$Engineering\ Hours(H_e) = 4.86W_e^{0.777}V^{0.894}Q^{0.163} \tag{17.4}$$

$$Tooling\ Hours(H_t) = 5.99W_e^{0.777}V^{0.696}Q^{0.263} \tag{17.5}$$

$$Manufacturing\ Hours(H_m) = 7.37W_e^{0.82}V^{0.484}Q^{0.641} \tag{17.6}$$

$$Quality\ Control\ Hours(H_q) = 0.076(Manufacturing\ Hours) \tag{17.7}$$

$$Development\ Support\ Cost(C_d) = 91.3W_e^{0.630}V^{1.3} \tag{17.8}$$

$$Flight\ Test\ Cost(C_f) = 2498W_e^{0.325}V^{0.822}FTA^{1.21} \tag{17.9}$$

$$Manufacturing\ Materials\ Cost(C_m) = 22.1W_e^{0.921}V^{0.621}Q^{0.799} \tag{17.10}$$

$$Engine\ Production\ Cost(C_e)$$
$$= 3112(0.043T_{max} + 243.25M_{max} + 0.969T_{inlet} - 2228 \tag{17.11}$$

$$RDTE + Flyaway\ Cost(Development) = H_eR_e + H_tR_t + H_qR_q + H_mR_m + C_d + C_f + C_m + C_eN_e + C_{avionics} \tag{17.12}$$

Using the listed formulas, the total hours and total development cost can be calculated. However, in a real-world application, there is a learning curve, in which the more quantities that are

produced, the lower the development costs and hours will be. This is a result of understanding the process of developing the aircraft, where more efficient methods can be applied to speed up the process as well as lower the costs [8].

$$Learning\ Curve = \ Hours\left(\frac{1}{Production\ Quantity}\right)^{x-1} where\ 2^x = 2\left(\frac{Learning\ Curve}{100}\right) \quad (17.13)$$

The equation above can be applied according to the percent of learning curve as well the number of aircraft produced. Typically, for transport aircraft, an 80% learning curve is set.

Table 44: Production hours per production quantity

Production Quantity	Engineering Hours	Manufacturing Hours	Tooling Hours	Quality Control Hours
1	3,860,907	1,376,145	697,703	53,025
50	810,381	288,844	146,443	11,129
100	170,094	60,626	30,737	2336

Table 45: Production costs per production quantity

Production Quantity	Development and Support Cost	Flight Test Cost	Manufacturing Materials Cost	Engine Production Cost	**Development Cost**
1	$203,895,577	$162,963	$13,934,979	$812685	$1,088,285,797
50	-	-	-	-	$402,736,958
100	-	-	-	-	$258,844,379

The tables above show the learning curve of 80% being applied. It is evident that as the production quantity increases, the required number of hours as well as the total development costs decrease significantly. At the current moment, to develop our aircraft, it will cost around $1 billion.
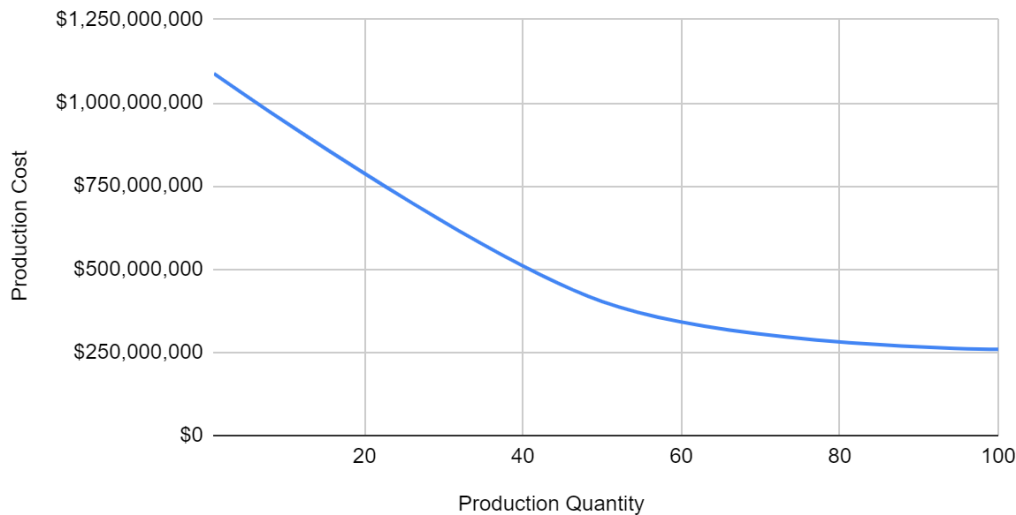
Figure 168: Learning curve

The graph above indicates the learning curve being applied, with the production cost significantly decreasing as production is ramped up. Eventually, the development cost will plateau as the room for improvement will be minimized.
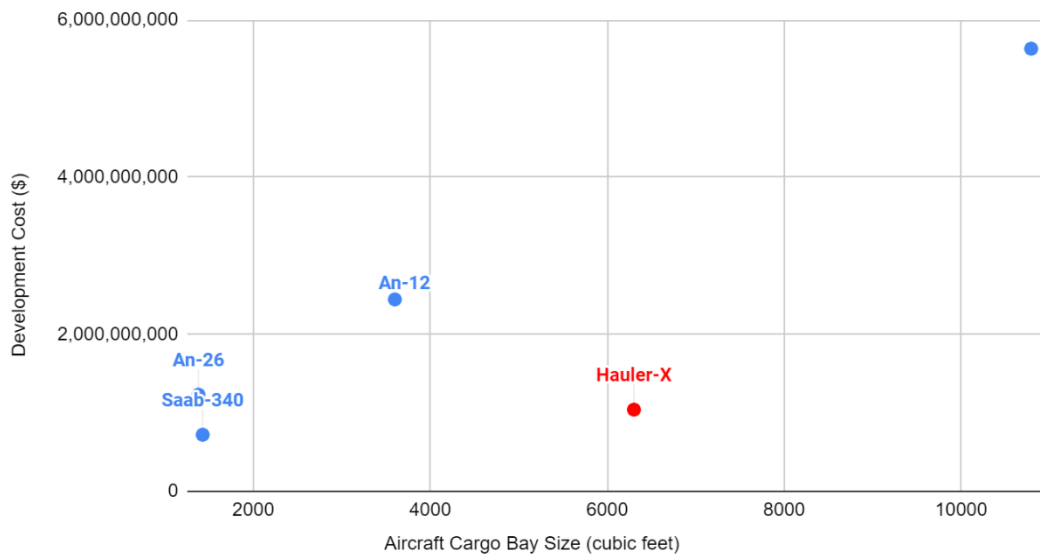
Figure 169: Development cost analysis with respect to cargo bay size

The development cost was assessed with respect to competitors of similar cargo bay size. Based on the graph, it is evident that even with a large cargo bay size than closest competitors, our development cost remains at a lower cost than most.

17.3. **Operating Costs**

The main aspect of cost analysis and a key requirement for this project is operating costs. The indirect and direct operating costs were assessed, which include fuel and oil, crew salary, maintenance, landing fees, insurance and depreciation. Moreover, the operating costs were determined per flight as well as per year. The costs per year is based on the number of flight hours per year which is estimated considering the amount of Global 7500 jets Bombardier produces per year.

17.3.1 Fuel and Oil

In terms of the fuel, the cost was determined by first determining the fuel characteristics. In order to know the fuel cost, the amount of fuel burned needs to be calculated. This is done by taking into account our flight distance, flight duration, cruise velocity, and the fuel mass. The fuel burned is simply the fuel volume divided by the trip distance. This can then be adjusted for the fuel burned per flight, dividing the fuel volume by the trip duration. The total fuel cost can then be found by multiplying the fuel burned by the cost of the fuel. In respect to oil costs, taking Raymer's suggestions, the oil cost is 5% of the fuel cost.

Table 46: Fuel and oil costs

Cost Designation	Cost/Flight ($)	Cost/Year ($)
Fuel	2340	187,221
Oil	117	9361

17.3.2 <u>Crew Salary</u>

The crew salary was analyzed for a 2-man crew and a 3-man crew. The crew salary can only be made as an estimate, because the exact flight maintenance requirements and hours towards that cannot be determined without experiencing the project scope at hand. However, a block time can be estimated, and assigned to the total maintenance time, where the crew salary can be allocated accordingly to that. The block time is the total time including taxiing, ground hold, mission flight, airborne holding, ATC communication, and gate waiting times. Since our flight trip is significantly smaller, our block time will also be small. Based on our block time, the crew salary can be approximated for that specific block time. The crew salary for a 2-man crew and 3-man crew were found using Raymer's equations [8].

$$2 - man\ Crew\ Cost\ =\ 70.4 \left(\frac{V_c W_o}{10^5}\right)^{0.3} + 168.8 \tag{17.14}$$

$$3 - man\ Crew\ Cost\ =\ 94.5 \left(\frac{V_c W_o}{10^5}\right)^{0.3} + 237.2 \tag{17.15}$$

Table 47: Crew salary

Cost Designation	Cost/Flight ($)	Cost/Year ($)
2-man Crew	475	38,069
3-man Crew	649	51,950

17.3.3 <u>Maintenance</u>

The maintenance expenses take into consideration the maintenance man hours, labour wrap rates, engine and aircraft costs, as well as materials and supplies. The maintenance aspect of the operating costs is where we can really optimize for a lower total cost. This is because our aircraft has lower flight time per year compared to competitors, and we also use the PW127-xt engine known for its sustainability, which reduces the total maintenance costs.

The maintenance man hours per flight hour for typical transport aircraft is 5 hours. Considering that our aircraft requires less maintenance as a product of its lower flight time, the maintenance man hours per flight hour was adjusted to 4. Another transport aircraft, the C-9, has a maintenance man hours per flight hour of 12. The C-9 is significantly larger, and is for military purposes, requiring a lot more maintenance. The maintenance labour cost is then determined by multiplying the maintenance man hours by the pay rate. This was adjusted per year, based on the maintenance man hours per year. The materials, parts, and supplies cost are found using the aircraft cost, engine cost, and number of engines. Typically, the higher the aircraft cost, the more components that may need maintenance. Similarly, a higher engine cost will contain more elements that may need to be checked. The following equations were used to determine these parameters, where C_a is the aircraft cost, C_e is the engine cost, and N_e is the number of engines [8].

$$Material\ Cost\ Per\ Flight\ Hour = 3.3\left(\frac{C_a}{10^6}\right) + 14.2 + \left[58\left(\frac{C_e}{10^6}\right) - 26.1\right]N_e \qquad (17.16)$$

$$Maintenance\ Labour\ Cost = (Maintenance\ Man\ Hours)(Labour\ Rate) \qquad (17.17)$$

Table 48: Maintenance expenses

Cost Designation	Cost/Flight ($)	Cost/Year ($)
Maintenance Labour	180	14,400
Materials and Supplies	253	20,296

17.3.4 Landing Fees

The landing fees are typically set based on the aircraft maximum weight. Since the specific landing fee per weight for the Downsview airport couldn't be found, the landing fees were assessed at Billy Bishop airport nearby. At Billy Bishop, the landing fee is $9.73 per 1000 kg. By referencing this, the landing fees for our aircraft are $191.97 per flight and $15,357.60 per year [35].

17.3.5 Insurance

The insurance fees are allotted to liability and serve as a sense of protection. Typically, the insurance fees are 1-3% of the total operational costs. For our scope, the insurance fees are set to 1% of the costs [8].

17.4. Depreciation

The depreciation is necessary in identifying how our aircraft will lose its value over its lifespan. Specifically, the depreciation on the airframe and the engines was assessed. Although an accurate value would rely on complex depreciation formulas, a straight-line method can be used to get an understanding. Initially, the airframe cost alone was determined by negating the engine and avionics cost from the total purchasing price. The team hopes to obtain a resale value of at least 20% for a total operational life of 20 years. The airframe depreciation is then simply found by multiplying the airframe cost by the resale value and dividing that product by the operational years. The engine depreciation also follows this process, in which the engine price is divided by the total operational years, for a constant depreciation per year. Thus, the depreciation on our airframe and engine over the operational life of 20 years are $828,280 and $25000, respectively [8].

17.5 Total Operating Costs

It must be noted that the operational costs are initial estimate and based on various different assumptions. These values may vary greatly, but that amount cannot be determined unless the scope of this project is experienced. By summing up the factors affecting operational costs, we can get the total values. Our total operational costs for a specified crew size is shown below per flight and per year.

Table 49: Total operational costs

Cost Designation	Cost ($)
Total Operational Cost/Flight with 2-man Crew	3,402
Total Operational Cost/Flight with 3-man Crew	3,577
Total Operational Cost/Year with 2-man Crew	272,160

Total Operational Cost/Year with 3-man Crew	286,160
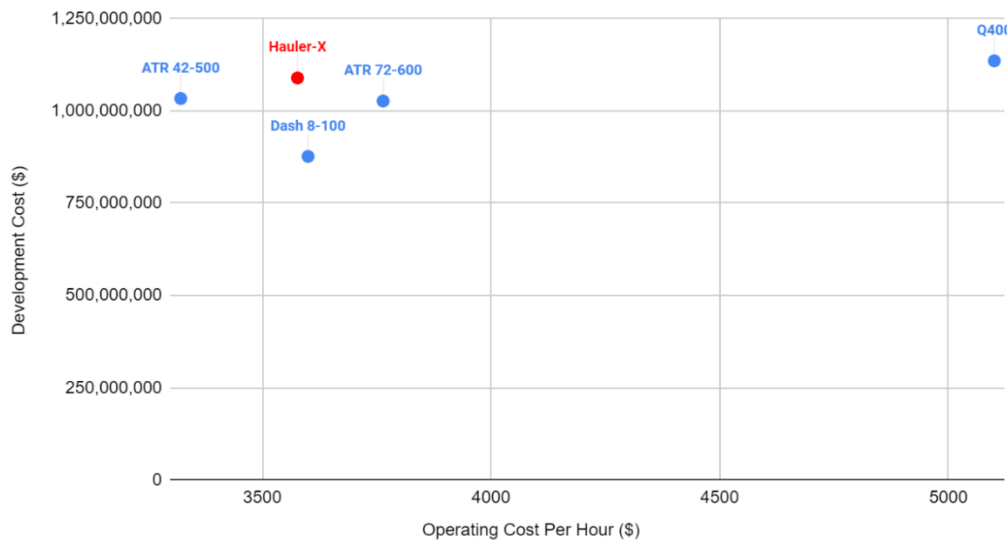
Figure 170: Operating cost analysis with respect to development cost

In order to determine the depth of our operating costs, a graph of operation costs versus development costs was made. Looking at the graph, it is evident that although we have a higher development cost than some competitors, our total operating costs in relation to that remain low. Our operating costs are lower than the ATR 72-500, Q400, and the Dash 8-100. The development cost of the ATR 72 and Dash 8-10 are lower, but their operating costs are higher. This shows that with initial estimates, we can be a viable option for buyers.

Overall, the operational costs were optimized in several different ways to reduce the cost and meet the project requirements. The maintenance was a crucial factor, as our engine choice allowed for much less maintenance required, to our already low flight time per year. Hence, why our maintenance man hours was lowered to a reasonable point. A more sustainable engine that is cheaper, requires less maintenance labour as well as materials and supplies. Another way the operational cost was lowered is by choosing a fuel with lower price per liter. Since oil cost is a percentage of the fuel cost, the oil costs also decrease.

18. Conclusion

Team Alpha's Hauler-X aircraft concept meets all mission requirements and objectives while proving to be a competitive design to be used in Bombardier Aerospace's fleet of aircrafts for the assembly process of the Global 7500. With a mission of delivering the cockpit and rear fuselage of the Global 7500 from Mirabel to Downsview, while keeping loading and unloading times under one hour, the Hauler-X was designed to optimize its weight, fuel efficiency, and operating costs. In summary, a twin-turboprop, fixed-wing aircraft was designed with a rear-loading cargo door, fuselage mounted landing gear, and a transitional fuselage.

The Hauler-X design has a length of 1258 *in* with a wingspan of 1347 *in*. The aircraft is capable of carrying the cockpit and rear fuselage of the Global 7500 from Mirabel to Downsview with a total crew of 4 people: a pilot, a first officer, and two crew members who will be loading and unloading the payload. The aircraft is powered by 2 PW127XT turboprop engines which allow the Hauler-X to complete the mission with 900 *lbs* of fuel for ground operations and loiter in the air, leaving an expendable fuel amount of 4100 *lbs*. The engine is currently certified for 50% SAF blends, with expectations of reaching 100% by 2025. With a maximum takeoff weight of 43496 *lbs*, the design boasts a power-specific fuel consumption of 0.45 *lb/hp·hr* (per engine), and an assume lift-to-drag ratio of 13. With a takeoff distance of 3868 *ft* and a landing distance of 3100 *ft*, the Hauler-X is operable at both Mirabel and Downsview.

In conclusion, Team Alpha was given a unique mission of designing an aircraft to transport a large payload over a relatively short distance. The Hauler-X meets all mission requirements while proving to be a competitive aircraft in terms of operation costs and sustainability for its weight class and function. The optimized fuselage sizing, use of smaller but more fuel-efficient engines, and custom jigs for loading and unloading the payload quickly, each contribute to the Hauler-X's potential to excel amongst Bombardier Aerospace's current fleet.

19.References

[1] [Online]. Available: https://www.antonov.com/en/airlines.

[2] [Online]. Available: https://aircraft.airbus.com/en/aircraft/freighters/belugaxl.

[3] [Online]. Available: https://aerocorner.com/aircraft/boeing-dreamlifter/.

[4] [Online]. Available: https://www.lockheedmartin.com/en-us/products/c130.html.

[5] [Online]. Available: https://simpleflying.com/33-years-of-the-atr-72/.

[6] [Online]. Available: https://www.aerospace-technology.com/projects/dash8/.

[7] [Online]. Available: https://skybrary.aero/aircraft/an26.

[8] D. P. Raymer, Aircraft Design - A Conceptual Approach, Playa del Rey: American Institute of Aeronautics and Astronautics, 2018.

[9] Z. Fawaz, "Quick Overview of Landing Gear Design Considerations," Toronto Metropolitan University , Toronto , 2022.

[10] D. G. H. L, "Pilot Compartment View Design Considerarions," U.S. Department of Transportation Federal Aviation Administration , 1993.

[11] "NASA Reynolds Number," NASA, [Online]. Available: [26] NASA. (n.d.). Reynolds number. NASA. Retrieved March 30, 2023, from https://www.grc.nasa.gov/www/k-12/airplane/reynolds.html#:~:text=The%20Reynolds%20number%20is%20a,used%20to%20model%20the%20flow. [Accessed 30 March 2023].

[12] R. D. P, Aircraft design: A conceptual approach (sixth Edition). American Institute of Aeronautics and Astronautics..

[13] L. D., "Incomplete Guide to Airfoil Usage," UIUC, 15 September 2010. [Online]. Available: https://m-selig.ae.illinois.edu/ads/aircraft.html. . [Accessed 30 March 2023].

[14] R. D, "Aerodynamics Design of Airbus High Lift Wings," [Online]. Available: physics.utoronto.ca. [Accessed 30 March 2023].

[15] L. D, "UIUC Airfoil Corodinate Database," UIUC airfoil data site, 2021 Septmeber 2021. [Online]. Available: mselig.ae.illinois.edu/ads/coord_database.html. [Accessed 30 March 2023].
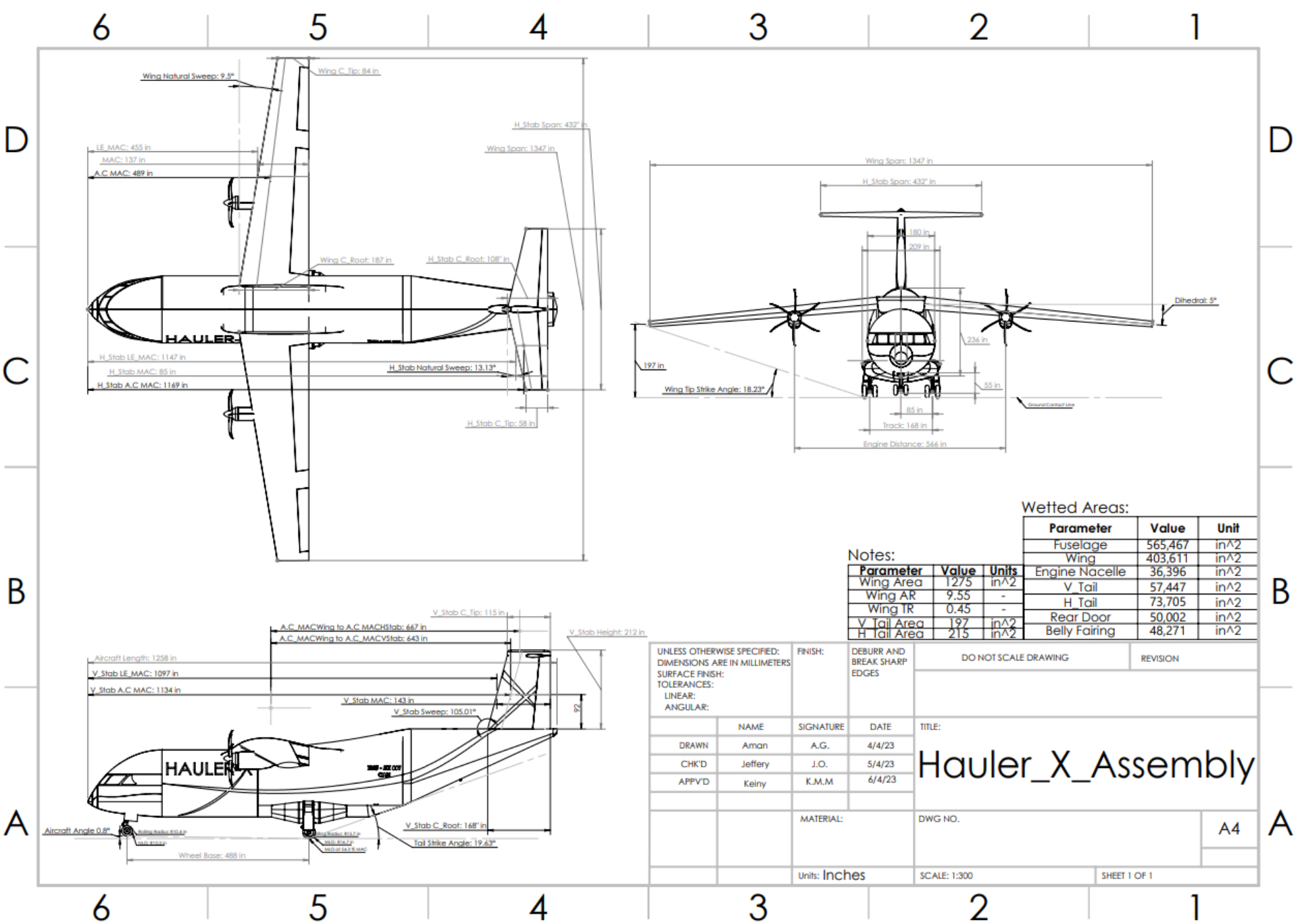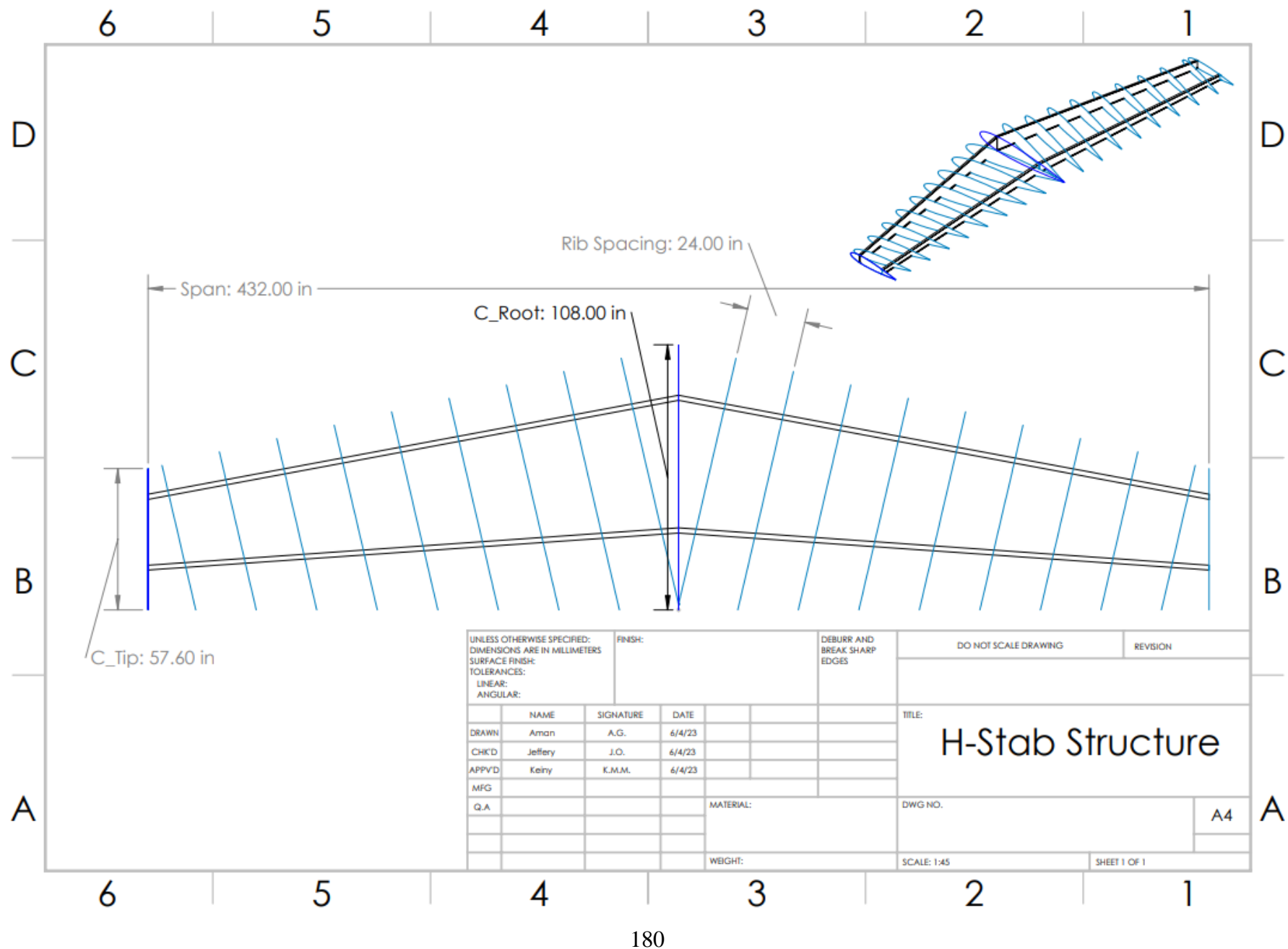
[16] "Aluminum 7075-T6; 7075-T651," ASM Aerospace Specification Metals INC., [Online]. Available: https://asm.matweb.com/search/SpecificMaterial.asp?bassnum=MA7075T6.

[17] "Aluminum 2024-T3," ASM Aerospace Specification Metals Inc., [Online]. Available: https://asm.matweb.com/search/SpecificMaterial.asp?bassnum=MA2024T3.

[18] "Titanium Ti-6Al-4V (Grade 5), Annealed," ASM Aerospace Specification Metals Inc., [Online]. Available: https://asm.matweb.com/search/SpecificMaterial.asp?bassnum=MTP641.

[19] "Deformation and damage mechanisms of laminated glass windows subjected to high velocity soft impact," International Journal of Solids and Structures, 2017. [Online]. Available: https://www.sciencedirect.com/science/article/pii/S0020768317300082.

[20] Z. Fawaz, "Structural Idealization Presentation," 2022. [Online].

[21] R. J, "Airplane Design III: Layout and Design of Cockpit, Fuselage Wing and Empennage," DARcorporation, 1995.

[22] Ambri and R. Kaur, "Spars and Stringers- Function and Designing," *International Journal of Aerospace and Mechanical Engineering,* vol. 1, no. 1, pp. 58-61, 2014.

[23] A. Abramowitz, T. G. Smith, D. T. Vu and J. Zvanya, "Vertical Drop Test of an ATR 42-300 Airplane," U.S. Department of Transportation Federal Aviation Administration, Springfield, 2006.

[24] "§ 25.571 Damage-tolerance and fatigue evaluation of structure," Code of Federal Regulations, [Online]. Available: https://www.ecfr.gov/current/title-14/chapter-I/subchapter-C/part-25/subpart-C/subject-group-ECFR7f2a560a8b50a3f/section-25.571.

[25] "PHYSICAL PROPERTIES OF GLASS," Saint-Gobain, [Online]. Available: https://www.saint-gobain-glass.co.uk/en-gb/architects/physical-properties.

[26] Delivery.Security.Liability, "Cargo History. DBL- The Longest Aircraft Loader in The World," DSL, [Online]. Available: https://dsl-ua.com/en/2020/05/15/ru-gruzovaya-istoriya-dbl-samyiy-dlinnyiy-aviatsionnyiy-pogruzchik-v-mire/.

[27] S. Gudmundsson, General Aviation Aircraft Design: Applied Methods and Procedures, Kidlington: Butterworth-Heinemann, 2014.
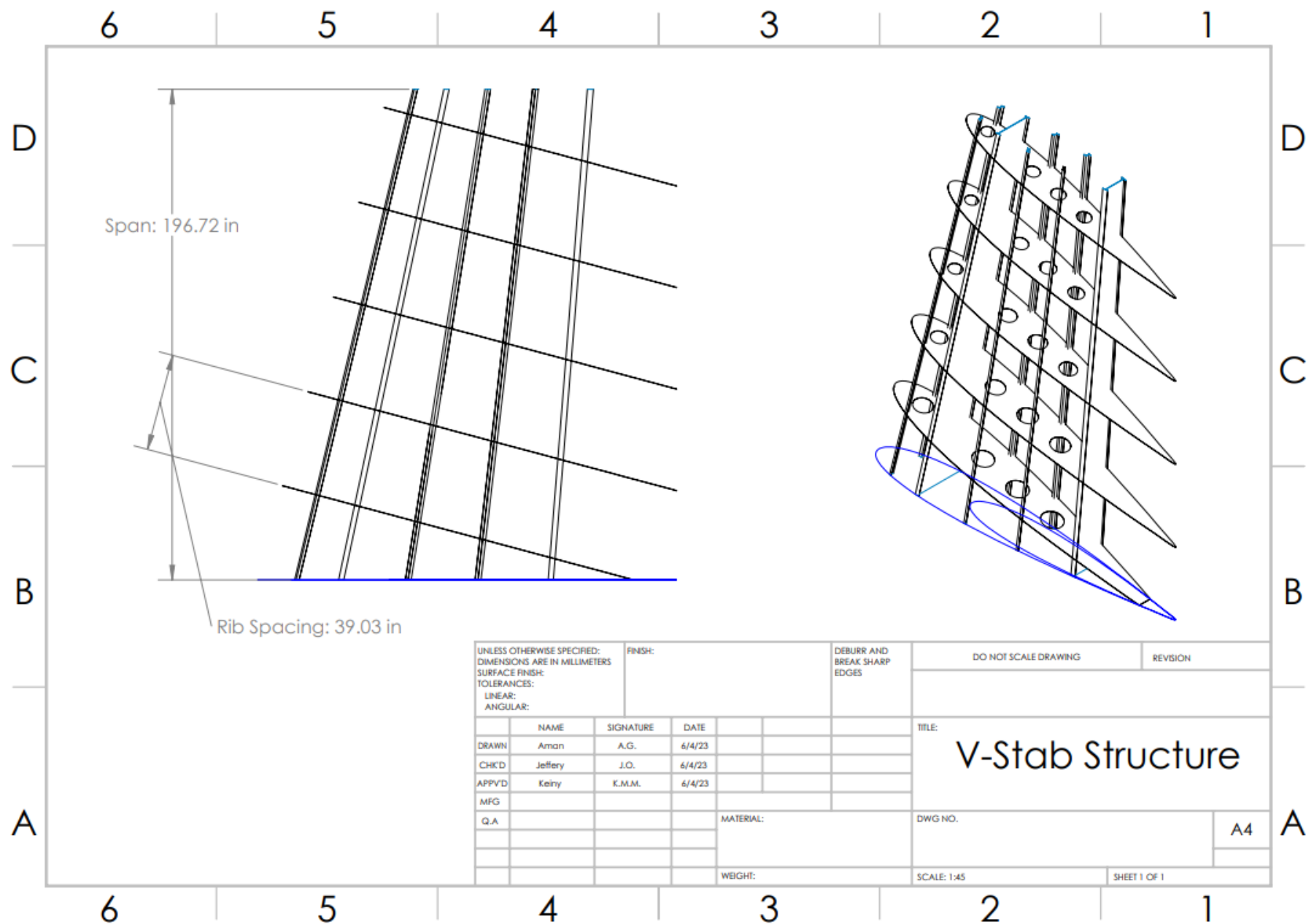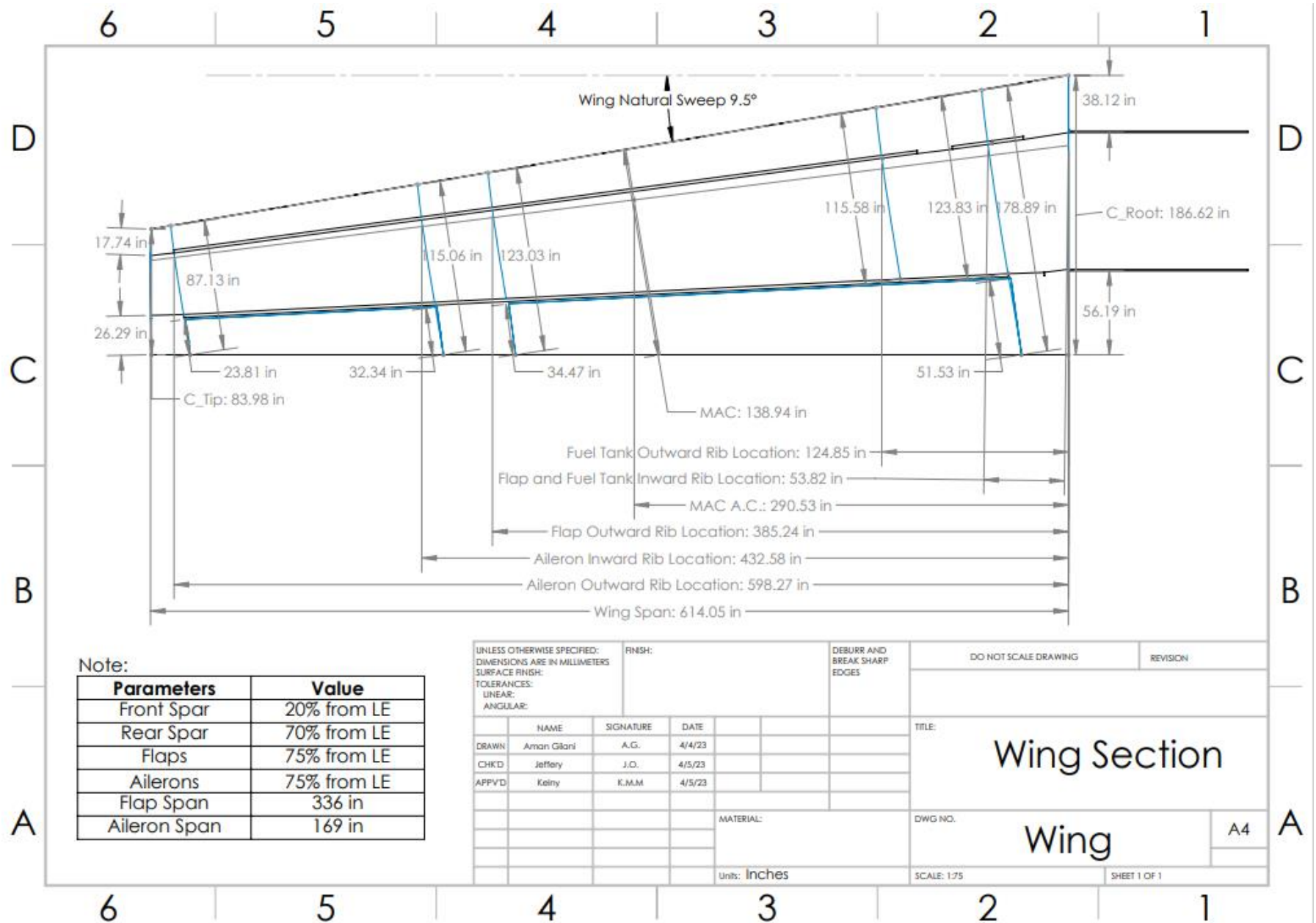
[28] A. Deperrois, "xflr5," Vic-Aéro, 14 January 2021. [Online]. Available: http://www.xflr5.tech/xflr5.htm. [Accessed 9 March 2023].

[29] ATR Aircraft, "ATR 72-600," 1 June 2022. [Online]. Available: https://www.atr-aircraft.com/wp-content/uploads/2022/06/ATR_Fiche72-600-3.pdf. [Accessed 2 March 2023].

[30] Aviation Regulators, "Part 25 - Airworthiness Standards: Transport Category Airplanes," Nimbus Dynamics, 2022.

[31] Airbus, "A350-900: Flight Deck and Systems Briefing for Pilots," SmartCockpit, September 2011. [Online]. Available: https://www.smartcockpit.com/docs/a350-900-flight-deck-and-systems-briefing-for-pilots.pdf . [Accessed 6th April 2023].

[32] Hursts, "Airbus Technical Notes," 12 November 2008. [Online]. Available: https://hursts.org.uk/airbus-technical/notes.pdf . [Accessed 6th April 2023].

[33] ATR, "Systems: ATR Training and Flight Operations Services," [Online]. Available: https://www.theairlinepilots.com/forumarchive/atr/atr-systems.pdf. [Accessed 6 April 2023].

[34] "Sustainability," Bombardier Aerospace, [Online]. Available: https://bombardier.com/en/sustainability. [Accessed 5 April 2023].

[35] [Online]. Available: https://www.portstoronto.com/airport/business-information/for-pilots/landing-fees.aspx.

[36] R. Kaur and Ambri, "Spars and Stringers- Function and Designing," *International Journal of Aerospace and Mechanical Engineering,* vol. 1, no. 1, pp. 1-4, 2014.

[37] Airbus, "A319/A320/A321 Flightdeck and systems briefing for pilots," September 1998. [Online]. Available: https://www.smartcockpit.com/docs/A320_Flight_Deck_and_Systems_Briefing_For_Pilots.pdf. [Accessed 6 April 2023].

[38] [Online]. Available: https://aircraft.airbus.com/en/aircraft/freighters/belugaxl.

[39] [Online]. Available: https://aircraft.airbus.com/en/aircraft/freighters/belugaxl.

Appendix A

Engineering drawing: Hauler_X_Assembly

Top view annotations:
- Wing Natural Sweep: 9.5°
- Wing C_Tip: 84 in
- H_Stab Span: 432 in
- Wing Span: 1347 in
- LE_MAC: 455 in
- MAC: 137 in
- A.C MAC: 489 in
- Wing C_Root: 187 in
- H_Stab C_Root: 108" in
- H_Stab LE_MAC: 1147 in
- H_Stab MAC: 85 in
- H_Stab A.C MAC: 1169 in
- H_Stab Natural Sweep: 13.13°
- H_Stab C_Tip: 58 in

Front view annotations:
- Wing Span: 1347 in
- H_Stab Span: 432 in
- 180 in
- 209 in
- 236 in
- Dihedral: 5°
- 197 in
- Wing Tip Strike Angle: 18.23°
- 55 in
- Ground Contact Line
- 85 in
- Track: 168 in
- Engine Distance: 566 in

Side view annotations:
- V_Stab C_Tip: 115 in
- V_Stab Height: 212 in
- A.C_MACWing to A.C MACHStab: 667 in
- A.C_MACWing to A.C_MACVStab: 643 in
- Aircraft Length: 1258 in
- V_Stab LE_MAC: 1097 in
- V_Stab A.C MAC: 1134 in
- V_Stab MAC: 143 in
- V_Stab Sweep: 105.01°
- 92
- HAULER X
- Aircraft Angle 0.8°
- Rolling Radius R10.4 in
- V_Stab C_Root: 168" in
- Tail Strike Angle: 19.63°
- Wheel Base: 488 in

Notes:

Parameter	Value	Units
Wing Area	1275	in^2
Wing AR	9.55	-
Wing TR	0.45	-
V Tail Area	197	in^2
H Tail Area	215	in^2

Wetted Areas:

Parameter	Value	Unit
Fuselage	565,467	in^2
Wing	403,611	in^2
Engine Nacelle	36,396	in^2
V_Tail	57,447	in^2
H_Tail	73,705	in^2
Rear Door	50,002	in^2
Belly Fairing	48,271	in^2

UNLESS OTHERWISE SPECIFIED:
DIMENSIONS ARE IN MILLIMETERS
SURFACE FINISH:
TOLERANCES:
  LINEAR:
  ANGULAR:

FINISH: | DEBURR AND BREAK SHARP EDGES

DO NOT SCALE DRAWING | REVISION

	NAME	SIGNATURE	DATE
DRAWN	Aman	A.G.	4/4/23
CHK'D	Jeffery	J.O.	5/4/23
APPV'D	Keiny	K.M.M	6/4/23

TITLE:

Hauler_X_Assembly

MATERIAL:

DWG NO.

A4

Units: Inches | SCALE: 1:300 | SHEET 1 OF 1

Span: 432.00 in

Rib Spacing: 24.00 in

C_Root: 108.00 in

C_Tip: 57.60 in

D D

C C

B B

A A

	NAME	SIGNATURE	DATE
DRAWN	Aman	A.G.	6/4/23
CHK'D	Jeffery	J.O.	6/4/23
APPV'D	Keiny	K.M.M.	6/4/23
MFG			
Q.A			

UNLESS OTHERWISE SPECIFIED:
DIMENSIONS ARE IN MILLIMETERS
SURFACE FINISH:
TOLERANCES:
  LINEAR:
  ANGULAR:

FINISH:

DEBURR AND
BREAK SHARP
EDGES

DO NOT SCALE DRAWING

REVISION

TITLE:

H-Stab Structure

MATERIAL:

DWG NO.

A4

WEIGHT:

SCALE: 1:45

SHEET 1 OF 1

180

Span: 196.72 in

Rib Spacing: 39.03 in

181

Wing Natural Sweep 9.5°

38.12 in

17.74 in

87.13 in

26.29 in

115.06 in   123.03 in

115.58 in   123.83 in   178.89 in   C_Root: 186.62 in

56.19 in

23.81 in   32.34 in   34.47 in   51.53 in

C_Tip: 83.98 in

MAC: 138.94 in

Fuel Tank Outward Rib Location: 124.85 in

Flap and Fuel Tank Inward Rib Location: 53.82 in

MAC A.C.: 290.53 in

Flap Outward Rib Location: 385.24 in

Aileron Inward Rib Location: 432.58 in

Aileron Outward Rib Location: 598.27 in

Wing Span: 614.05 in

Note:

Parameters	Value
Front Spar	20% from LE
Rear Spar	70% from LE
Flaps	75% from LE
Ailerons	75% from LE
Flap Span	336 in
Aileron Span	169 in

Stringer Spacing: 7.00 in

93.47

	NAME	SIGNATURE	DATE			TITLE:		
DRAWN	Aman	A.G.	6/4/23			**Wing Structure**		
CHK'D	Jeffery	J.O.	6/4/23					
APPV'D	Keiny	K.M.M.	6/4/23					
MFG								
Q.A				MATERIAL:		DWG NO.		A4
				WEIGHT:		SCALE: 1:50	SHEET 1 OF 1	

183

Cockpit Width: 180

Cockpit Length: 174

151

25

Frame Spacing: 19
Bulkhead and Frame Spacing: 9.83

Door Width: 32

Floor Height: 41

Door Height: 72

		UNLESS OTHERWISE SPECIFIED: DIMENSIONS ARE IN MILLIMETERS SURFACE FINISH: TOLERANCES: LINEAR: ANGULAR:	FINISH:	DEBURR AND BREAK SHARP EDGES	DO NOT SCALE DRAWING		REVISION
					TITLE:		
	NAME	SIGNATURE	DATE				
DRAWN	Keiny Mitchel Mugisha		04/04/2023		Cockpit Structures		
CHK'D	Keiny Mitchel Mugisha		04/04/2023				
		MATERIAL:		DWG NO.			A4
		UNITS:	INCHES	SCALE:1:100		SHEET 1 OF 1	

1347

1226

653

432

204

197

180

104°

25°

	NAME	SIGNATURE	DATE
DRAWN	Keiny Mitchel Mugisha		04/04/2023
CHK'D	Keiny Mitchel Mugisha		04/04/2023

UNLESS OTHERWISE SPECIFIED:
DIMENSIONS ARE IN MILLIMETERS
SURFACE FINISH:
TOLERANCES:
  LINEAR:
  ANGULAR:

FINISH:

DEBURR AND
BREAK SHARP
EDGES

DO NOT SCALE DRAWING

REVISION

TITLE:

Full Assembly Aircraft Structures

MATERIAL:

DWG NO.

A4

UNITS: INCHES

SCALE:1:300

SHEET 1 OF 1

| 39.4 | 24 |

| 48 | 45.4 |

110.94

Ø180

129

21.05

48

PROJECT					
Hauler-X					
TITLE					
Fuselage Forward Section					
APPROVED	Keiny M.	2023-04-07	SIZE	CODE	DWG NO	REV
CHECKED	Aman G.	2023-04-07	A			37
DRAWN	Jeffery O.	2023-04-07	SCALE 1:85	WEIGHT	SHEET 1/1

PROJECT
Hauler-X

TITLE
Fuselage Aft Section

APPROVED	Aman G.	2023-04-07	SIZE	CODE	DWG NO		REV
CHECKED	Keiny M.	2023-04-07	A				36
DRAWN	Jeffery O.	2023-04-07	SCALE 1:150	WEIGHT		SHEET 1/1	

17 | 7

18

188

98

108
60
111
Ø180
129
21
48

Appendix B

Table 50: Failure Mode Effects & Analysis

Failure Mode	Phase	Effects	Causes	Severity	Occurrence	Detection	RPN
Payload detachment	During flight	Cargo misplacement leading to weight imbalance	Improperly secured cargo locks, mechanical failure	9	3	10	270
APU or actuator malfunction	Pre-flight	Difficulty with un/loading process	Faulty wiring, component failure	9	2	10	180
Structural failure of jigs	During flight	Damage to payload components, leading to mission failure	Materials or design not adhering to calculations	9	3	9	243
Winch attaching failure	During flight	Linkage loss with the framing made for jig bases	Oversight of tightness of tie downs	5	5	5	125
Tail strike	During takeoff	Vibration of the assembled payload security system	Imperfect flying or DFM errors	6	2	9	108
Rear fuselage payload tail tip grazing the ceiling	Loading process	Damage to the corresponding payload	Errors in interior design or the jig height manufacturing	7	5	7	135

Material Selection

The following tables are mechanical and physical properties for various materials that will be used for the aircraft structures and components.

Table 51: Material properties of Al 7075-T6 [16]

Al 7075-T6	Parameters	Specifications
Mechanical Properties	Tensile Strength	83,000 psi
	Yield Strength	73,000 psi
	Elongation	11 %
	Hardness	Rockwell A 53.5, Rockwell B 87
	Modulus of Elasticity	10400 ksi
	Fatigue Strength	23,000 psi
	Shear Modulus	3900 ksi
	Shear Strength	48,000 psi
Physical Properties	Density	0.101 lb/in³
	Thermal Conductivity	167 W/m-K
	Thermal Expansion	11.8 μm/m-K
	Electrical Conductivity	41% IACS
	Specific Heat	0.23 Btu/lb-°F , 960 J/kg-K

Table 52: Material properties of Al 2024-T3 [17]

Al 2024-T3	Parameters	Specifications
Mechanical Properties	Tensile Strength	68,000 psi
	Yield Strength	47,000 psi
	Elongation	12 %
	Modulus of Elasticity	10600 ksi
	Shear Strength	42,000 psi
Physical Properties	Density	0.100 lb/in^3
	Thermal Conductivity	120 W/m-K
	Thermal Expansion	23.2 μm/m-K
	Electrical Conductivity	34% IACS
	Specific Heat	0.24 Btu/lb-°F , 897 J/kg-K

Table 53: Material properties of Ti-6AL-4V [18]

Ti-6AL-4V	Parameters	Specifications
Mechanical Properties	Tensile Strength	13,8000 psi
	Yield Strength	12, 8000 psi
	Elongation	14 %
	Hardness	Rockwell C 36
	Reduction of Area	36%
	Modulus of Elasticity	16,500 ksi

	Fatigue Strength	24,800 pisi - 74 000 psi
	Shear Modulus	6380 ksi
	Shear Strength	79 800 psi
Physical Properties	Density	0.16 lb/in^3
	Thermal Conductivity	11.5 W/m-K
	Thermal Expansion	8.6 μm/m-K
	Electrical Conductivity	6.0% IACS
	Specific Heat	0.12 Btu/lb-°F , 500 J/kg-K

Appendix C

Wingbox Structural Idealization MATLAB code

```matlab
clc;
clear;
% Wing Structure Data
% Setting the number of ribs and airfoil type for each rib
number_ribs = 29;
for i = 1:number_ribs
    airfoilList{i,1} = 'naca643418';
end
% Wing
% Defining the general parameters for the wing design
        % Setting the airfoil type for each rib
        R_Wing.airfoil    =  airfoilList;
        % Setting the wing span in ft
        R_Wing.span       =  113/2/3.281;
        % Setting the number of stations (ribs) along the wing
        R_Wing.numStations =  number_ribs;
        % Setting the leading edge sweep angle
        R_Wing.LEsweep    =  atand((15.57-7.007)/((113/2)));
        % Setting the wing dihedral angle (in degrees)
        R_Wing.wingHedral  =  -5;
% Root LE Origin
        % Setting the origin of the wing at the root leading edge
        R_Wing.x0 = 0;R_Wing.y0 = 0 ;R_Wing.z0 = 0;
% Geometric Washout
        % Setting the root and tip angle of attack to be zero
        R_Wing.rootAlfa = 0;R_Wing.tipAlfa = 0;
% Chord Distribution
        % Setting the root chord length in ft
        R_Wing.rootChord   =  15.57/3.281;
        % Setting the tip chord length in ft
        R_Wing.tipChord    =  7.007/3.281;
        % Setting the flat length of the wing to be zero
        R_Wing.flatLength  =  0;
% Generating the wing geometry using the defined parameters
% Loading the coordinates of each rib of the wing
R_Wing = loadWingCoordinates(R_Wing);
% Creating the left wing by mirroring the right wing
L_Wing = mirrorWing(R_Wing);
% Merging the left and right wings to obtain the full wing geometry
Full_Wing = mergeWings(L_Wing, R_Wing);
altitude_m = 20000 / 3.281; % ft -> m
```

```matlab
mach = 0.3;
[T_C, T_K, p_kPa, rho_kg_m3, soundSpeed_m_s, dynVisc_mu, kinVisv_v] =
atmosphereSI(altitude_m);
Altitude:                   6095.70 m
Static Pressure:            46.66 kPa
Temperature at Altitude:       -24.52 C | 248.63 K
Density of Air:                0.65 kg/m3
Speed of Sound:                315.52 m/s
Dynamic Viscosity:             0.000015920456 Pa.s
Kinematic Viscosity:           0.000024334620 m2/s
U_m_s = mach * soundSpeed_m_s;
q_Pa = 0.5 * U_m_s^2 * rho_kg_m3;
Bending Moment Calculations
%% Inputs
% Define the dimensions and taper ratio of the wing
r_c = 4.74; % Root chord length [ft]
t_c = 2.135; % Tip chord length [ft]
wingspan = 18; % Wingspan [ft]
taper_ratio = 0.45; % Taper ratio
sweep_angle = 5; % Wing sweep angles [degrees]
thickness = 3; % Airfoil thickness
n = 100; % Number of points along the wing span
rho = 0.1948; % Air Density
wing_area = 118.43; %ft^2
v = 160.5155235; % Airspeed
% Define the weight of the engine and fuel
engine_weight = 961.6158; % Engine weight [lbs]
fuel_weight = 1133.981; % Fuel weight [lbs]
% Define the lift distribution along the wing span
lift_distribution = @(y)(2*wingspan - 2*y)/(wingspan*r_c + wingspan*t_c); %
Elliptical lift distribution
%% Calculations
% Calculate the chord length at each wing station
y = linspace(0,wingspan,n); % Spanwise location [ft]
chord_length = r_c - (r_c-t_c)*(y/wingspan); % Chord length [ft]
% Calculate the lift force at each wing station
lift_force = lift_distribution(y).*(0.5*rho*v^2).*wing_area; % Lift force [lbs]
% Calculate the weight force at each wing station
wing_area = wingspan*(r_c+t_c)/2; % Wing area [ft^2]
engine_position = 0.3*wingspan; % Engine position [ft]
fuel_position = 0.15*wingspan; % Fuel position [ft]
g = 9.81; % Acceleration due to gravity [ft/s^2]
wing_mass = 2 * wing_area * thickness * (r_c + t_c) * 0.0023769; % Wing mass
[lbs]
```

194

```matlab
 weight_force = (engine_weight+fuel_weight+wing_mass)*g*ones(1,n); % Weight
force [lbs]
 weight_force(floor(engine_position/(wingspan/(n-1)))) =
weight_force(floor(engine_position/(wingspan/(n-1)))) - engine_weight*g;
 weight_force(floor(fuel_position/(wingspan/(n-1)))) =
weight_force(floor(fuel_position/(wingspan/(n-1)))) - fuel_weight*g;
 % Calculate the bending moment at each wing station
 moment_arm =
0.25*chord_length.*(1+taper_ratio)./(1+taper_ratio+taper_ratio^2)*(2/3)*wingspan
; % Moment arm [ft]
 bending_moment = lift_force.*moment_arm - weight_force.*(moment_arm-
0.25*wingspan); % Bending moment [lb.ft]
 % Plot the bending moment distribution along the wing span
 figure;
 hold on
    plot(y,bending_moment);
    grid on
    xlabel('Wing Span [ft]');
    ylabel('Bending Moment [lb.ft]');
    title('Bending Moment Distribution along Wing Span');
 hold off
 figure;
 hold on
    plot(y,weight_force);
    grid on
    xlabel('Wing Span [ft]');
    ylabel('Force [lb]');
    title('Force Distribution along Wing Span');
 hold off
 newStations = linspace(0, R_Wing.span, number_ribs)';
 M_x = spline(y, bending_moment.*1, newStations); %convert ib/ft to Nm
 M_z = zeros(number_ribs, 1);
 figure;
    hold on
        title('Moment Distribution Along Wing Span M_x N.m')
        subtitle(['Moment at Root = ' num2str(M_x(1,1)/1000, 4) ' kN.m' ])
        xlabel('Station Number')
        ylabel('Moment N.m')
        plot(R_Wing.stations, M_x)
    hold off
 figure;
    hold on
        title('Moment Distribution Along Wing Span M_z N.m')
        subtitle(['Moment at Root = ' num2str(M_z(1,1)/1000, 4) ' kN.m' ])
        xlabel('Station Number')
```

```
        ylabel('Moment N.m')
        plot(R_Wing.stations, M_z)
    hold off
 Wingbox Idealization
 % Material Selection: Al-7075-T6
 material.density_lb_in3    = 0.102;
 material.E_psi             = 10400000;
 material.G_psi             = 3900000;
 material.poisson           = 0.33;
 material.UltTenStr_psi     = 83000;
 material.TensYieldStr_psi  = 73000;
 material.shearStr_psi      = 48000;
 % Z Stiffener
 zeeS.name = 'Z Stiffener';
 zeeS.b1_mm    = 30;
 zeeS.t1_mm    = 2;
 zeeS.b2_mm    = 40;
 zeeS.t2_mm    = 2;
 zeeS.b3_mm    = 30;
 zeeS.t3_mm    = 2;
 zeeS.Area_mm2 = zeeS.b1_mm*zeeS.t1_mm + zeeS.b2_mm*zeeS.t2_mm +
zeeS.b3_mm*zeeS.t3_mm;
 zeeS.Area_in2 = zeeS.Area_mm2 / 645.16;
 stiffener_type = zeeS;
 stiffener_type.Material = material;
 forward_spar_location = 0.20;
 rear_spar_location = 0.70;
 rib_spacing = 2/3.218; %ft to m
 number_ribs = floor(R_Wing.span/(rib_spacing)) + 2
 number_ribs = 29
 numBooms = 14 % number of stiffeners in each rib on one surface
 numBooms = 14
 % Create empty cells to store rib and airfoil sections
 ribSections = cell(number_ribs,1);
 airfoilSections = cell(number_ribs,1);
 % Generate evenly spaced stations along the wing span
 stationNumbers = linspace(0, R_Wing.span, number_ribs)';
 % Extract the chord lengths, angles of attack, and leading edge coordinates of
each airfoil section
 chords = R_Wing.chords;
 alfas  = R_Wing.alfas;
 xLEs   = R_Wing.xLE;
 zLEs   = R_Wing.zLE;
 % Initialize empty arrays to store the locations of all booms and airfoil
coordinates
```

```matlab
 boomCloud = [];
 foilCloud = [];
 % Loop through each rib and generate the corresponding rib and airfoil sections
 for r = 1:number_ribs
    % Calculate the moments of inertia of the rib section and store them in the
rib section structure
    ribSections{r,1} = makeBox(airfoilList{r,1}, stationNumbers(r,1),
chords(r,1), alfas(r,1), xLEs(r,1), zLEs(r,1), forward_spar_location,
rear_spar_location, numBooms);
    ribSections{r,1}.I_xx_m4 = sum((ribSections{r,1}.allBooms_xyz(:,3) -
ribSections{r,1}.wingBox_Center(:,3)).^2*(stiffener_type.Area_mm2/1000000));
    ribSections{r,1}.I_zz_m4 = sum((ribSections{r,1}.allBooms_xyz(:,1) -
ribSections{r,1}.wingBox_Center(:,1)).^2*(stiffener_type.Area_mm2/1000000));
    ribSections{r,1}.I_xz_m4 = sum( ...
        (((ribSections{r,1}.allBooms_xyz(:,1) -
ribSections{r,1}.wingBox_Center(:,1)).*((ribSections{r,1}.allBooms_xyz(:,3) -
ribSections{r,1}.wingBox_Center(:,3))))...
        *(stiffener_type.Area_mm2/1000000)));
    boomCloud = [boomCloud; ribSections{r,1}.allBooms_xyz];
    foilCloud = [foilCloud; ribSections{r,1}.Coordinates];
 end
 figure;
 axis off
 axis equal
    hold on
        title('Structural Components of Wingbox: Spars & Stiffners')
        subtitle({ ...
            ['Root Chord = 15.57ft & Tip Chord = 7.007ft'].....
            ['Spar Locations:']...
            ['Root Spar Front = 3.114ft & Root Spar Rear = 10.899ft'],...
            ['Tip Spar Front = 1.401ft & Tip Spar Rear = 4.905ft'],...
            })
            plot(ribSections{1,1}.Upper_xyz(:,1),
ribSections{1,1}.Upper_xyz(:,3))
        plot(ribSections{1,1}.Lower_xyz(:,1), ribSections{1,1}.Lower_xyz(:,3))
        scatter(ribSections{1,1}.wingBox_Vertices(:,1),
ribSections{1,1}.wingBox_Vertices(:,2), 200, 'mpentagram', 'filled')
        plot(ribSections{1,1}.wingBox_Shape)
        xline(ribSections{1,1}.allBooms_xyz(1,1), '--k', '0.20c Front Spar',
'LabelHorizontalAlignment', 'center', 'LabelVerticalAlignment', 'middle',
'LabelOrientation','horizontal')
        xline(ribSections{1,1}.allBooms_xyz(numBooms,1), '--k', '0.70c Rear
Spar', 'LabelHorizontalAlignment', 'center', 'LabelVerticalAlignment', 'middle',
'LabelOrientation','horizontal')
        ylim([-1 1])
```

```matlab
        xlim([0 5])
    hold off
% Stress calculations
% Initialize a counter for stiffeners that fail the stress check
    failedStiffeners = 0;
    maxBoomForce_N = 0;
% Loop over each rib in the wing
for r = 1:number_ribs
    for b = 1:2*numBooms
        % Calculate the stress in the boom using bending moments and the boom's
geometry
        ribSections{r,1}.sigma_x_Pa(b,1) = ((M_z(r,1)*ribSections{r,1}.I_xx_m4 -
M_x(r,1)*ribSections{r,1}.I_xz_m4)/(ribSections{r,1}.I_xx_m4*ribSections{r,1}.I_
zz_m4 - ribSections{r,1}.I_xz_m4^2))*(ribSections{r,1}.allBooms_xyz(b,1) -
ribSections{r,1}.wingBox_Center(1,1)) ...
            + ((M_x(r,1)*ribSections{r,1}.I_zz_m4 -
M_z(r,1)*ribSections{r,1}.I_xz_m4)/(ribSections{r,1}.I_xx_m4*ribSections{r,1}.I_
zz_m4 - ribSections{r,1}.I_xz_m4^2))*(ribSections{r,1}.allBooms_xyz(b,3) -
ribSections{r,1}.wingBox_Center(1,3));
        % Calculate the force in the boom using the stress and the boom's cross-
sectional area
        ribSections{r,1}.boomForce_N(b,1) =
ribSections{r,1}.sigma_x_Pa(b,1)*(stiffener_type.Area_mm2/1000000);
        % Check if the stress is higher than the yield stress for the stiffener
material
        if ribSections{r,1}.sigma_x_Pa(b,1) <=
stiffener_type.Material.TensYieldStr_psi*6894.75729 %psi -> Pa
             % If the stress is below the yield stress, the check has passed
            ribSections{r,1}.checkStress{b,1} = 'Passed';
        else
            % If the stress is above the yield stress, the check has failed
            ribSections{r,1}.checkStress{b,1} = 'Failed';
            % Increment the counter for failed stiffeners
            failedStiffeners = failedStiffeners + 1;
        end

            % Check for Maximum Forces
        if ribSections{r,1}.boomForce_N(b,1) > maxBoomForce_N
            maxBoomForce_N = ribSections{r,1}.boomForce_N(b,1);
            mostStressedBoom = [r, b];
        end
    end
end
boomLabels = cell(2*numBooms, 1);
fprintf("%d Stiffeners Failed \n", failedStiffeners)
```

```matlab
 for r = 1:number_ribs
    fprintf("%s Rib Station %d", ribSections{r,1}.name, r)
        for b = 1:2*numBooms
            % Create labels for the booms based on their location in the wing
box
            boomLabels{b,1} = ['Station ' num2str(r) ' Boom ' num2str(b)];
        end
    % Create a stress table for the current rib station
    ribSections{r,1}.stressTable = table(ribSections{r,1}.allBooms_xyz(:,1)*
39.37, ribSections{r,1}.allBooms_xyz(:,2), ribSections{r,1}.allBooms_xyz(:,3) *
39.37, ones(2*numBooms,1).*stiffener_type.Area_mm2/645.2,
ribSections{r,1}.sigma_x_Pa/-6895);
    % Rename the columns of the stress table to be more informative
    ribSections{r,1}.stressTable.Properties.VariableNames = {'Boom Y Coordinate
[in]', 'Boom X Coordinate [in]', 'Boom Z Coordinate [in]', 'Boom Areas [in2]',
'Boom Normal Stress [psi]'};
    % Rename the rows of the stress table to match the boom labels
    ribSections{r,1}.stressTable.Properties.RowNames = boomLabels;
    % Display the stress table for the current rib station
    disp(ribSections{r,1}.stressTable)
 end
 figure;
 axis equal
    hold on
        % title(['Normal Stress (psi) ' num2str(mostStressedBoom(1)) ' Boom '
num2str(mostStressedBoom(2)) ])
        %subtitle(['Maximum Boom Normal Force = ' num2str(maxBoomForce_N/1000,
5) ' kN'], 'Color', [1 1 1])
        title('Normal Stress (psi)')
        pcshow(pointCloud(ribSections{mostStressedBoom(1,1),1}.Coordinates,
"Color", ones(length(ribSections{mostStressedBoom(1,1),1}.Coordinates),1).*[1 1
1]), "AxesVisibility","on")
        plot3(ribSections{mostStressedBoom(1,1),1}.wingBox_Vertices(:,1),
ones(length(ribSections{mostStressedBoom(1,1),1}.wingBox_Vertices(:,1)),1).*stat
ionNumbers(mostStressedBoom(1,1),1),
ribSections{mostStressedBoom(1,1),1}.wingBox_Vertices(:,2), 'Color', 'red')
        quiver3(ribSections{mostStressedBoom(1,1),1}.allBooms_xyz(:,1),
ribSections{mostStressedBoom(1,1),1}.allBooms_xyz(:,2),
ribSections{mostStressedBoom(1,1),1}.allBooms_xyz(:,3),...
                zeros(2*numBooms, 1),
ribSections{mostStressedBoom(1,1),1}.sigma_x_Pa, zeros(2*numBooms, 1), 'Color',
'red')
        xlabel x
        ylabel y
        zlabel z
```

```
        ylim([-1 1])
        xlim([0 5])
        zlim([-1 1])
  hold off
```

Flight Envelope Code

```
 clear all
clc
close all
 S = 1275 %ft^2


Cl_max = 1.9
Cl_cruise = 1.7


W = 43497; %weight in lbs
Vcruise = 331 %knots
Vstall = 128 %knots = sqrt((2*W*g)/(rho*S*Cl_max))

n_max = 2.5

n_neg = -1

n_ult = 3.97

n_neg_ult = n_neg*1.5


rho_sl = 0.002378 %slugs/ft^3 sea level density

Vd = Vcruise/0.8 %knots
Vdive = 355; %knots
rho_ratio = sqrt(rho_c/rho_sl)
rho_c = 0.001227 %slug/ft^3 cruise density at 21000ft
Mass = W/2.205 %mass of aircraft in kg

g = 32.2 %gravity in ft/s^2


%Positive Stall Curve
nlim = [n_neg_ult:0.01:n_ult]';
```

```matlab
for i = 1:length(nlim)

    V_pos = (rho_ratio*sqrt((2*abs(nlim)*Mass*g)/(rho_c*S*Cl_max))); % EAS
end


% %Negative Stall Curve
nneg = [0:0.01:abs(n_neg)]';
for j = 1:length(nneg)

     V_neg = rho_ratio*sqrt((2*nneg*Mass*g)/(rho_c*S*Cl_max)); % KEAS
end
for i = 1:length(nlim)
    if (nlim(i) == -1)
        Vneg1 = V_pos(i)
    end
end


[val,idx] = min(abs(nlim-n_max))
V_n_max = V_pos(idx)

% Stall index
[val1,idx1] = min(abs(V_pos-Vstall))

n_stall = nlim(idx1)


%Positive Stall Curve with Flaps
Cl_maxflaps = 2.0


nflaps = [0:0.01:2]';

for i = 1:length(nflaps)

    V_flaps = (rho_ratio*sqrt((2*abs(nflaps)*Mass*g)/(rho_c*S*Cl_maxflaps))); % m/s EAS
end

[val2,idx2] = min(abs(nlim-2))

V_flaps_max = V_pos(idx2)

b = 113; % ft
C_bar = S/b;
```

```matlab
AR = 9.552
a1 = 0.2; %2D lift curve slope from NACA 64(3)-418 Cl vs alpha graph

Ude_cruise = [-15.24 15.24] %knots at Vcruise
Ude_dive = [-7.62 7.62] %knots at Vdive


a = (a1*AR/(2+sqrt(4+AR^2)))*(180/pi) %3D lift curve slope % per rad



nu_g = (2*(Mass/S))/(rho_c*C_bar*a)

Kg = 0.88*nu_g/(5.33+nu_g)
n_gust_cruise = 1 + (0.5*rho_sl*a*Vcruise*Kg*Ude_cruise/(Mass*g/S))
n_gust_dive = 1 + (0.5*rho_sl*a*Kg*Vdive*Ude_dive/(Mass*g/S))

% for i = 1:length(n_gust_cruise)
%
%      V_gust_cruise = V
% end
figure(1)
% points
plot(Vcruise, n_max,'r*')
hold on
plot(Vdive, n_max,'b*')
plot(Vstall, -n_stall,'g*')
plot(V_flaps(end), 2,'black*')

% Gust Plot
plot([0 Vcruise], [1 n_gust_cruise(2)],'b--')
plot([0 Vdive], [1 n_gust_dive(2)],'m--')
plot([0 Vcruise], [1 n_gust_cruise(1)],'b--')
plot([0 Vdive], [1 n_gust_dive(1)],'m--')
plot([Vcruise Vdive], [n_gust_cruise(1) n_gust_dive(1)],'b--')
plot([Vcruise Vdive], [n_gust_cruise(2) n_gust_dive(2)],'b--')


plot (V_pos, nlim, 'r') % stall curve
plot([V_n_max Vdive], [n_max n_max], 'r') %upper

plot([Vneg1 Vcruise], [n_neg n_neg], 'r') %lower
plot([Vdive Vdive], [n_ult 0], 'r') %vertical
plot([Vdive Vcruise], [0 n_neg], 'r') %slanted

plot([V_pos(end) Vdive], [n_ult n_ult],'r') %positive ultimate load limit
plot([V_pos(1) Vcruise], [n_neg_ult n_neg_ult], 'r') %negative ultimate load limit
```

```matlab
plot([Vcruise Vdive], [n_neg_ult 0], 'r')




% Flaps deployed
plot(V_flaps, nflaps, 'r') % stall curve
plot([V_flaps(end) V_flaps_max],[2 2],'r')


legend('Cruise Speed','Dive Speed','Stall Speed','Flaps Deployed Maximum Speed','50 ft/s Gust
Line','25 ft/s Gust Line','Location','best')
xlabel('Equivalent Velocity (Knots)')
ylabel('Limit Load Factors (n)')
title('V-n Diagram for Manuvering Aircraft')
grid on
hold off
```

Elliptical Section Structural ideliasation code

```matlab
% Fuselage consists of 2 seperate ellipses (Upper and Lower) Both Centered
% around the floor level
floorLevel_ft = 0;

%%%%%%%%%% Define Upper Ellipse Properties %%%%%%%%%%%%%
upperEgg.h                            =                        0;
% Center X Coordinate
upperEgg.k                      =                   floorLevel_ft;
% Center Y Coordinate
upperEgg.a                          =                        7;
% Major Axis Coefficient
upperEgg.b                          =                       20;
% Minor Axis Coefficient
upperEgg.ellip1=15;
upperEgg.ellip2=10;
upperEgg.ellip3=10;
upperEgg.ellip4=15;

upperEgg.numBooms                                           =
upperEgg.ellip1+upperEgg.ellip2++upperEgg.ellip3++upperEgg.ellip4;        %
Number of Booms on Upper Surface
for                                        m=1:upperEgg.ellip1
% Fix to add last boom due to else statement
    if m==1
        upperEgg.yy(m) = upperEgg.a*cosd(0);
    else
        upperEgg.yy(m)=upperEgg.a*cosd(1*(45/upperEgg.ellip1)*(m-1));
    end
end

m=1;
while m<=upperEgg.ellip2
    if m==1
        upperEgg.yy(m+upperEgg.ellip1) = upperEgg.a*cosd(45);
    end
    upperEgg.yy(m+upperEgg.ellip1)                             =
upperEgg.a*cosd(45+1*(45/upperEgg.ellip2)*(m-1));
    m=m+1;
end

m=1;
while m<=upperEgg.ellip3
     if m==1
        upperEgg.yy(m+upperEgg.ellip2+upperEgg.ellip1) = upperEgg.a*cosd(90);
```

```matlab
    end
    upperEgg.yy(m+upperEgg.ellip1+upperEgg.ellip2)                                =
upperEgg.a*cosd(90+1*(45/upperEgg.ellip3)*m);
    m=m+1;
 end

 m=1;
 while m<=upperEgg.ellip4
    upperEgg.yy(m+upperEgg.ellip1+upperEgg.ellip2+upperEgg.ellip3)         =
upperEgg.a*cosd(135+1*(45/upperEgg.ellip4)*m);
    m=m+1;
 end

 upperEgg.yy=upperEgg.yy';
% Boom y Coordinates
 upperEgg.zz           =          sqrt((1          -          ((upperEgg.yy-
upperEgg.h).^2/(upperEgg.a^2)))*upperEgg.b^2 ) + upperEgg.k;          % Boom Z
Coordinates
 upperEgg.Circumference   =   pi*sqrt((upperEgg.a^2   +   upperEgg.b^2)   /   2);
% Upper Ellipse Circumference

 disp(upperEgg)
 % Define Lower Ellipse Properties
 lowerEgg.h                                    =                                    0;
% Center X Coordinate
 lowerEgg.k                          =                          floorLevel_ft;
% Center Y Coordinate
 lowerEgg.a                               =                               7;
% Major Axis Coefficient
 lowerEgg.b                               =                               7;
% Minor Axis Coefficient
 lowerEgg.numBooms                          =                          30;
% Number of Booms on Upper Surface
 lowerEgg.yy = lowerEgg.a*cosd( linspace(0,  180,  lowerEgg.numBooms+1)');
% Boom Y Coordinates
 lowerEgg.zz          =          -(sqrt((1          -          ((lowerEgg.yy-
lowerEgg.h).^2/(lowerEgg.a^2)))*lowerEgg.b^2 )) + lowerEgg.k;       % Boom Z
Coordinates
 lowerEgg.Circumference   =   pi*sqrt((lowerEgg.a^2   +   lowerEgg.b^2)   /   2);
% Upper Ellipse Circumference
 lowerEgg.boomSpacing_ft   =   lowerEgg.Circumference   /   lowerEgg.numBooms;
% Boom Spacing in feet (Approximation)
 lowerEgg.boomSpacing_in = lowerEgg.boomSpacing_ft * 12;
 disp(lowerEgg)
```

```matlab
%%%%%%%%% Merge Upper and Lower Ellipses to Form Full Egg %%%%%%%%%%
fullEgg.yy = [upperEgg.yy(1:end-1,1); flipud(lowerEgg.yy(2:end,1))];
fullEgg.zz = [upperEgg.zz(1:end-1,1); flipud(lowerEgg.zz(2:end,1))];
fullEgg.numBooms = lowerEgg.numBooms + upperEgg.numBooms-1;

%%%%%%%%% Find main 4 extremiite %%%%%%%%%%%%%%%%%%%%%
index.topzz= find(fullEgg.zz==max(fullEgg.zz),1,'first');
index.bottomzz= find(fullEgg.zz==min(fullEgg.zz));
index.minyy= find(fullEgg.yy==min(fullEgg.yy));
index.maxyy= find(fullEgg.yy==max(fullEgg.yy));

%%%%%%%%% Upper Egg Spacing calculation %%%%%%%%%%%%%%%%%%%%
syms z b y a

ellips_eq=(z^2)/(b^2)+(y^2)/(a^2)==1;
% Equation of Ellipse
ellips_eq2=z==sqrt((1-(y^2)/(a^2))*(b^2));
% Equation of Ellipse re-arange
b=18.6;                                                          a=7;
% Ellipise major and minor axis numbers

ellips_eq3=subs(ellips_eq2);
% Substitute b and a values into equation

derivative=diff(ellips_eq3,y);
% Actual derivative for sanity check
derivatice_eq=-(b^2*y)/(a^2*sqrt((1-(y^2)/(a^2))*(b^2)));
% Standard form of derivative
arclength_eq=sqrt(1+derivatice_eq.^2);
% Arclength equation

for m=1:index.minyy-1
    if m==1
        subspace(m)=(fullEgg.yy(m)-fullEgg.yy(m+1))/3;
% Divide spacing between
        length1=double(int(arclength_eq,6.99999,fullEgg.yy(m)-subspace(m)));
% Arc length of sector 1
        length.sec1(m)=abs(double(length1));
        length2=int(arclength_eq,fullEgg.yy(m)-subspace(m),fullEgg.yy(m)-
2*subspace(m));                % Arc length of sector 2
        length.sec2(m)=abs(double(length2));
        length3=int(arclength_eq,fullEgg.yy(m)-2*subspace(m),fullEgg.yy(m+1));
% Arc length of sector 3
        length.sec3(m)=abs(double(length3));
    elseif m==index.minyy-1
```

```matlab
            subspace(m)=(fullEgg.yy(m)-fullEgg.yy(m+1))/3;
% Divide spacing between
            length1=double(int(arclength_eq,fullEgg.yy(m),fullEgg.yy(m)-
subspace(m)));                                 % Arc length of sector 1
            length.sec1(m)=abs(double(length1));
            length2=int(arclength_eq,fullEgg.yy(m)-subspace(m),fullEgg.yy(m)-
2*subspace(m));               % Arc length of sector 2
            length.sec2(m)=abs(double(length2));
            length3=int(arclength_eq,fullEgg.yy(m)-2*subspace(m),-6.99999);
% Arc length of sector 3
            length.sec3(m)=abs(double(length3));
        else
            subspace(m)=(fullEgg.yy(m)-fullEgg.yy(m+1))/3;
% Divide spacing between
            length1=double(int(arclength_eq,fullEgg.yy(m),fullEgg.yy(m)-
subspace(m)));                           % Arc length of sector 1
            length.sec1(m)=abs(double(length1));
            length2=int(arclength_eq,fullEgg.yy(m)-subspace(m),fullEgg.yy(m)-
2*subspace(m));               % Arc length of sector 2
            length.sec2(m)=abs(double(length2));
            length3=int(arclength_eq,fullEgg.yy(m)-2*subspace(m),fullEgg.yy(m+1));
% Arc length of sector 3
            length.sec3(m)=abs(double(length3));
        end
        upperEgg.boomSpacing_ft(m)=length.sec1(m)+length.sec2(m)+length.sec3(m);
% Boom spacing (sum of sector 1,2,3)
        upperEgg.boomSpacing_in(m)=                   upperEgg.boomSpacing_ft(m)*12;
% Boom spacing in inches
  end

 %%%%%%%%% Plot Egg %%%%%%%%%%%%%%%%%%%
 figure;
     hold on
     axis equal
         title('Elliptical Cross-Sections')
         subtitle(['Number of Booms ' num2str(fullEgg.numBooms) ])
         ylabel('z \rightarrow (ft)')
         xlabel('y\rightarrow (ft)')
         scatter(fullEgg.yy, fullEgg.zz)
         %yline(floorLevel_ft, '--k', ['Floor Level = ' num2str(floorLevel_ft) '
ft'], 'LabelHorizontalAlignment', 'center', 'LabelVerticalAlignment','middle')
     hold off

 for i = 1:fullEgg.numBooms
     boomLabels{i,1} = ['Boom' num2str(i)];
```

207

```
end

x=zeros(fullEgg.numBooms,1); % Needed for soliworks coordinates
boomTable    =    table(fullEgg.yy,   fullEgg.zz,   x,'RowNames',   boomLabels,
'VariableNames', {'Boom Y Coordinate [ft]', 'Boom Z Coordinate [ft]','X'})
%writetable(boomTable, 'egg.txt'); % Text file to import into solidworks
```

Structural Input Parameters

```
%------- Parameters to update through out Project -----------------
% Weight.MTOW= 47029;    %lbs
% Weight.Empty=21323;    %lbs
% Weight.Crew=800;        %lbs
% Weight.Payload=10000; %lbs
% Weight.Fuel=7636;        %lbs
stringer.Area_mm2 = 117.4191;    %mm^2   *************** Update with change in
cross-section ****************
stringer.Area_in2 = stringer.Area_mm2 / 645.16;    %in^2
skinthickness=0.04; %in

bendingmoment.x=-559200;    %lbs.in
bendingmoment.y=500;    %lbs.in
shear.force=8470;          %lbs
shear.distance=(max(fullEgg.yy))*12;    %in
shear.area= (pi/2)*(lowerEgg.a*12)^2+((1/2)*pi*upperEgg.a*upperEgg.b);  %Area of
cross section in in^2
disp(bendingmoment)
```

Structural Idealization

```
%%%%%%%%% Upper Booms Stress %%%%%%%%%%%
for j = 1:upperEgg.numBooms-1
     if j==index.topzz||j==index.bottomzz

Boom.Area(j)=stringer.Area_in2+2*((skinthickness*upperEgg.boomSpacing_in(j))/6)*
(2+((fullEgg.zz(j+1))/((fullEgg.zz(j)))));
     elseif j==upperEgg.numBooms

Boom.Area(j)=stringer.Area_in2+((skinthickness*upperEgg.boomSpacing_in(j))/6)*(2
+((fullEgg.zz(index.minyy+1))/((fullEgg.zz(j)))))+...
            ((skinthickness*upperEgg.boomSpacing_in(j))/6)*(2+((fullEgg.zz(j-
1))/((fullEgg.zz(j)))));
     elseif j==index.maxyy||j==index.minyy
         Boom.Area(j)=stringer.Area_in2;
     else
```

```matlab
Boom.Area(j)=stringer.Area_in2+((skinthickness*upperEgg.boomSpacing_in(j))/6)*(2
+((fullEgg.zz(index.minyy+1))/((fullEgg.zz(j)))))+...
            ((skinthickness*upperEgg.boomSpacing_in(j))/6)*(2+((fullEgg.zz(j-
1))/((fullEgg.zz(j)))));
    end
    Iyy_in4.perboom(j)=Boom.Area(j)*(fullEgg.zz(j)*12)^2;
 end

 %%%%%%%%% Lower Booms Stress %%%%%%%%%%
 for j = upperEgg.numBooms-1:fullEgg.numBooms
    if j==index.topzz||j==index.bottomzz

Boom.Area(j)=stringer.Area_in2+2*((skinthickness*lowerEgg.boomSpacing_in)/6)*(2+
((fullEgg.zz(j+1))/((fullEgg.zz(j)))));
    elseif j==fullEgg.numBooms

Boom.Area(j)=stringer.Area_in2+((skinthickness*lowerEgg.boomSpacing_in)/6)*(2+((
fullEgg.zz(index.maxyy))/((fullEgg.zz(j)))))+...

((skinthickness*lowerEgg.boomSpacing_in)/6)*(2+((fullEgg.zz(fullEgg.numBooms-
1))/((fullEgg.zz(j)))));  % Note i is used to avoid dividing by 0
    elseif j==index.maxyy||j==index.minyy
        Boom.Area(j)=stringer.Area_in2;
    else

Boom.Area(j)=stringer.Area_in2+((skinthickness*lowerEgg.boomSpacing_in)/6)*(2+((
fullEgg.zz(j+1))/((fullEgg.zz(j)))))+...
            ((skinthickness*lowerEgg.boomSpacing_in)/6)*(2+((fullEgg.zz(j-
1))/((fullEgg.zz(j)))));
    end
    Iyy_in4.perboom(j)=Boom.Area(j)*(fullEgg.zz(j)*12)^2;
 end

 Iyy_in4.total=sum(Iyy_in4.perboom);

 Boom.Stress=((fullEgg.zz*12)).*(bendingmoment.x)/(Iyy_in4.total);    %Psi
 stressTable = table(fullEgg.yy, fullEgg.zz, Boom.Area', Boom.Stress,'RowNames',
boomLabels, 'VariableNames', {'Boom Y Coordinate [ft]', 'Boom Z Coordinate
[ft]','Boom Area (in^2)','Stress (Psi)'})

 figure;
    hold on
        pcshow(pointCloud([zeros(size(fullEgg.zz)) fullEgg.yy fullEgg.zz]))
        quiver3(zeros(size(fullEgg.zz)), fullEgg.yy, fullEgg.zz,...
```

209

```matlab
            -Boom.Stress, zeros(size(fullEgg.zz)), zeros(size(fullEgg.zz)) )

        ylim([min(fullEgg.yy) max(fullEgg.yy)])
        zlim([min(fullEgg.zz) max(fullEgg.zz)])
        view([0 0])
        xlabel ('x \rightarrow (ft)')
        zlabel ('Z \rightarrow (ft)')
        ylabel ('Y')
        title('Normal Stress (Psi)')
    hold off
```

Shear Flow

```matlab
q.bcoef=-shear.force/Iyy_in4.total;

for k=index.topzz:-1:index.maxyy
    if k==index.topzz
        Boom.Bryr(k)=(Boom.Area(k)/2).*(fullEgg.zz(k)*12);
        Boom.Bryrsum(k)= Boom.Bryr(k);
        q.b(k)=Boom.Bryr(k)*q.bcoef;
    else
        Boom.Bryr(k)=(Boom.Area(k)).*(fullEgg.zz(k)*12);
        Boom.Bryrsum(k)= Boom.Bryrsum(k+1)+Boom.Bryr(k);
        q.b(k)= Boom.Bryrsum(k)*q.bcoef;   % (K+1) because oder is backwards
instead of forwards
    end
end

for k=fullEgg.numBooms:-1:index.topzz+1
    if k== fullEgg.numBooms
        Boom.Bryr(k)=(Boom.Area(k)).*(fullEgg.zz(k)*12);
        Boom.Bryrsum(k)= Boom.Bryrsum(index.maxyy)+Boom.Bryr(k);
        q.b(k)= Boom.Bryrsum(k)*q.bcoef; % (index.maxyy index because of order
change
    else
        Boom.Bryr(k)=(Boom.Area(k)).*(fullEgg.zz(k)*12);
        Boom.Bryrsum(k)= Boom.Bryrsum(k+1)+Boom.Bryr(k);
        q.b(k)= Boom.Bryrsum(k)*q.bcoef; % (K+1) because order is backwards
instead of forwards
    end
end

q.so=-(shear.force*shear.distance)./(2*shear.area*ones(1,fullEgg.numBooms));
q.total=q.so+q.b;
shearflowTable = table(fullEgg.yy, fullEgg.zz, q.so', q.b', q.total','RowNames',
boomLabels,...
```

```
    'VariableNames', {'Boom Y Coordinate [ft]','Boom Z Coordinate [ft]','qso
(Psi)','qb (Psi)','Shear Flow (Psi)'})
 % Condition C was selected
 % a is the distance between frames = 20in
 % b is the distance between stringers wich is calculated earlier
 panel.ab=24/max(upperEgg.boomSpacing_in);
 panel.k=4; % Constant obtained from chart above
 panel.v=0.33; % Skin material poison ratio
 panel.E=10400000; % Skin material elastic modulus
 panel.critical=((panel.k*(pi^2)*panel.E)/(12*(1-
panel.v^2)))*(skinthickness/max(upperEgg.boomSpacing_in))^2
```

Circular Section Structural ideliasation code

```
 % Fuselage consists of 2 seperate ellipses (Upper and Lower) Both Centered
 % around the floor level
 floorLevel_ft = 0;

 % Define Upper Ellipse Properties
 upperEgg.h                           =                           0;
% Center X Coordinate
 upperEgg.k                      =                    floorLevel_ft;
% Center Y Coordinate
 upperEgg.a                           =                           7;
% Major Axis Coefficient
 upperEgg.b                           =                           7;
% Minor Axis Coefficient
 upperEgg.numBooms                       =                         28;
% Number of Booms on Upper Surface
 upperEgg.yy   =   upperEgg.a*cosd(  linspace(0,  180,  upperEgg.numBooms+1)');
% Boom Y Coordinates
 upperEgg.zz             =             sqrt((1           -          ((upperEgg.yy-
upperEgg.h).^2/(upperEgg.a^2)))*upperEgg.b^2 ) + upperEgg.k;         % Boom Z
Coordinates
 upperEgg.Circumference  =  pi*sqrt((upperEgg.a^2  +  upperEgg.b^2)  /  2);
% Upper Ellipse Circumference
 upperEgg.boomSpacing_ft   =   upperEgg.Circumference   /   upperEgg.numBooms;
% Boom Spacing in feet
 upperEgg.boomSpacing_in       =       upperEgg.boomSpacing_ft       *       12;
% Boom Spacing in inches
 disp(upperEgg)
 lowerEgg.h                           =                           0;
% Center X Coordinate
 lowerEgg.k                      =                    floorLevel_ft;
% Center Y Coordinate
```

```matlab
 lowerEgg.a                              =                              7;
% Major Axis Coefficient
 lowerEgg.b                              =                              7;
% Minor Axis Coefficient
 lowerEgg.numBooms                           =                          28;
% Number of Booms on Upper Surface
 lowerEgg.yy  =  lowerEgg.a*cosd(  linspace(0,  180,  lowerEgg.numBooms+1)');
% Boom Y Coordinates
 lowerEgg.zz         =         -(sqrt((1         -         ((lowerEgg.yy-
lowerEgg.h).^2/(lowerEgg.a^2)))*lowerEgg.b^2  ))  +  lowerEgg.k;      %  Boom  Z
Coordinates
 lowerEgg.Circumference   =   pi*sqrt((lowerEgg.a^2   +   lowerEgg.b^2)   /   2);
% Upper Ellipse Circumference
 lowerEgg.boomSpacing_ft    =    lowerEgg.Circumference    /    lowerEgg.numBooms;
% Boom Spacing in feet (Approximation)
 lowerEgg.boomSpacing_in = lowerEgg.boomSpacing_ft * 12;
 disp(lowerEgg)
 % Merge Upper and Lower Ellipses to Form Full Egg
 fullEgg.yy = [upperEgg.yy(1:end-1,1); flipud(lowerEgg.yy(2:end,1))];
 fullEgg.zz = [upperEgg.zz(1:end-1,1); flipud(lowerEgg.zz(2:end,1))];
 fullEgg.numBooms = lowerEgg.numBooms + upperEgg.numBooms;

 % Plot Egg
 figure;
    hold on
    axis equal
        title('Circular Cross-Sections')
        subtitle(['Number of Booms ' num2str(fullEgg.numBooms) ])
        ylabel('z \rightarrow')
        xlabel('y\rightarrow')
        scatter(fullEgg.yy, fullEgg.zz)
        %yline(floorLevel_ft, '--k', ['Floor Level = ' num2str(floorLevel_ft) '
ft'], 'LabelHorizontalAlignment', 'center', 'LabelVerticalAlignment','middle')

    hold off
 for i = 1:fullEgg.numBooms
    boomLabels{i,1} = ['Boom' num2str(i)];
 end

 index.topzz= find(fullEgg.zz==max(fullEgg.zz));
 index.bottomzz= find(fullEgg.zz==min(fullEgg.zz));
 index.minyy= find(fullEgg.yy==min(fullEgg.yy));
 index.maxyy= find(fullEgg.yy==max(fullEgg.yy));
```

```
boomTable    =    table(fullEgg.yy,    fullEgg.zz,    'RowNames',    boomLabels,
'VariableNames', {'Boom Y Coordinate [ft]', 'Boom Z Coordinate [ft]'})
% numFrames = 38;
% frameSpacing = 64/38;
% frames = linspace(0, frameSpacing*numFrames, numFrames)';
%
% catiaCoordinates = [];
%
% for frame = 1:numFrames
%     frameCoordinates(1:fullEgg.numBooms,1) = frames(frame,1);
%     frameCoordinates(:,2) = fullEgg.yy;
%     frameCoordinates(:,3) = fullEgg.zz;
%
%     catiaCoordinates = [catiaCoordinates; frameCoordinates];
% end
%
% figure;
%     hold on
%     axis equal
%                     scatter3(catiaCoordinates(:,1),  catiaCoordinates(:,2),
catiaCoordinates(:,3))
%         view(-30, 15)
%     hold off
% catiaCoordinates = catiaCoordinates.*304.8 %convert ft to mm for CATIA
coordinates
```

Structural Input Parameters

```
%------- Parameters to update through out Project ------------------
% Weight.MTOW= 47029;    %lbs
% Weight.Empty=21323;    %lbs
% Weight.Crew=800;       %lbs
% Weight.Payload=10000; %lbs
% Weight.Fuel=7636;      %lbs
stringer.Area_mm2 = 190;    %mm^2  ************** Update with change in cross-
section ****************
stringer.Area_in2 = stringer.Area_mm2 / 645.16;    %in^2
skinthickness=0.04; %in
bendingmoment.x=-559200;   %lbs.in
bendingmoment.y=500;    %lbs.in
shear.force=8470;          %lbs
shear.distance=(max(fullEgg.yy))*12;    %in
shear.area= pi*(upperEgg.a*12)^2;  %Area of cross section in in^2
disp(bendingmoment)
```

Structural Idealization

```matlab
 for j = 1:fullEgg.numBooms
     if j==index.topzz||j==index.bottomzz

Boom.Area(j)=stringer.Area_in2+2*((skinthickness*upperEgg.boomSpacing_in)/6)*(2+
((fullEgg.zz(j+1))/((fullEgg.zz(j)))));
     elseif j==fullEgg.numBooms

Boom.Area(j)=stringer.Area_in2+((skinthickness*upperEgg.boomSpacing_in)/6)*(2+((
fullEgg.zz(index.maxyy))/((fullEgg.zz(j)))))+...

((skinthickness*upperEgg.boomSpacing_in)/6)*(2+((fullEgg.zz(fullEgg.numBooms-
1))/((fullEgg.zz(j)))));  % Note i is used to avoid dividing by 0
     elseif j==index.maxyy||j==index.minyy
         Boom.Area(j)=stringer.Area_in2;
     else

Boom.Area(j)=stringer.Area_in2+((skinthickness*upperEgg.boomSpacing_in)/6)*(2+((
fullEgg.zz(j+1))/((fullEgg.zz(j)))))+...
             ((skinthickness*upperEgg.boomSpacing_in)/6)*(2+((fullEgg.zz(j-
1))/((fullEgg.zz(j)))));
     end
     Iyy_in4.perboom(j)=Boom.Area(j)*(fullEgg.zz(j)*12)^2;
 end
 Iyy_in4.total=sum(Iyy_in4.perboom);

 Boom.Stress=((fullEgg.zz*12)).*(bendingmoment.x)/(Iyy_in4.total);    %Psi
 stressTable = table(fullEgg.yy, fullEgg.zz, Boom.Area', Boom.Stress,'RowNames',
boomLabels, 'VariableNames', {'Boom Y Coordinate [ft]', 'Boom Z Coordinate
[ft]','Boom Area (in^2)','Stress (Psi)'})

 figure;
     hold on
         pcshow(pointCloud([zeros(size(fullEgg.zz)) fullEgg.yy fullEgg.zz]))
         quiver3(zeros(size(fullEgg.zz)), fullEgg.yy, fullEgg.zz,...
             -Boom.Stress, zeros(size(fullEgg.zz)), zeros(size(fullEgg.zz)) )

         ylim([min(fullEgg.yy) max(fullEgg.yy)])
         zlim([min(fullEgg.zz) max(fullEgg.zz)])
         view([0 0])
         xlabel ('x \rightarrow')
         zlabel ('Z \rightarrow')
         ylabel ('Y')
         title('Normal Stress (Psi)')
     hold off
```

Shear Flow

```matlab
q.bcoef=-shear.force/Iyy_in4.total;

for k=index.topzz:-1:index.maxyy
    if k==index.topzz
        Boom.Bryr(k)=(Boom.Area(k)/2).*(fullEgg.zz(k)*12);
        Boom.Bryrsum(k)= Boom.Bryr(k);
        q.b(k)=Boom.Bryr(k)*q.bcoef;
    else
        Boom.Bryr(k)=(Boom.Area(k)).*(fullEgg.zz(k)*12);
        Boom.Bryrsum(k)= Boom.Bryrsum(k+1)+Boom.Bryr(k);
        q.b(k)= Boom.Bryrsum(k)*q.bcoef;   % (K+1) because oder is backwards
instead of forwards
    end
end

for k=fullEgg.numBooms:-1:index.topzz+1
    if k== fullEgg.numBooms
        Boom.Bryr(k)=(Boom.Area(k)).*(fullEgg.zz(k)*12);
        Boom.Bryrsum(k)= Boom.Bryrsum(index.maxyy)+Boom.Bryr(k);
        q.b(k)= Boom.Bryrsum(k)*q.bcoef; % (index.maxyy index because of order
change
    else
        Boom.Bryr(k)=(Boom.Area(k)).*(fullEgg.zz(k)*12);
        Boom.Bryrsum(k)= Boom.Bryrsum(k+1)+Boom.Bryr(k);
        q.b(k)= Boom.Bryrsum(k)*q.bcoef; % (K+1) because order is backwards
instead of forwards
    end
end

q.so=-(shear.force*shear.distance)./(2*shear.area*ones(1,fullEgg.numBooms));
q.total=q.so+q.b;
shearflowTable = table(fullEgg.yy, fullEgg.zz, q.so', q.b', q.total','RowNames',
boomLabels,...
    'VariableNames', {'Boom Y Coordinate [ft]','Boom Z Coordinate [ft]','qso
(Psi)','qb (Psi)','Shear Flow (Psi)'})
```

Panel Buckling

```matlab
imshow(imread('panel critical.png'));
imshow(imread('panel graph.png'));
% Condition C was selected
% a is the distance between frames = 20in
% b is the distance between stringers wich is calculated earlier
panel.ab=20/upperEgg.boomSpacing_in;
panel.k=4; % Constant obtained from chart above
panel.v=0.33; % Skin material poison ratio
```

215

```matlab
panel.E=10400000; % Skin material elastic modulus
panel.critical=((panel.k*(pi^2)*panel.E)/(12*(1-
panel.v^2)))*(skinthickness/upperEgg.boomSpacing_in)^2
```

Stringer Buckling

```matlab
imshow(imread('z-stringer.png'));
imshow(imread('z-stringer guide.png'));
%---------- Stringer Dimensions/Parameters ------------
stringer.modulus=10400000;                                          %Psi
stringer.length=64*12;                                               %in
stringer.bsf=0.9;                                                    %in
stringer.th=0.1;                                                     %in
stringer.tsf=0.1;                                                    %in
stringer.ti=0.07;                                                    %in
stringer.bi=0.9;                                                     %in
stringer.hs=1.45;                                                    %in
stringer.height=stringer.ti+stringer.hs+stringer.tsf;
stringer.area=(stringer.tsf*stringer.bsf)+(stringer.th*stringer.hs)+...
    (stringer.ti*stringer.bi);                                      %in^2
imshow(imread('critical stress.png'));
imshow(imread('radius of gyration.png'));
imshow(imread('ybar.png'));
stringer.ys=((stringer.ti*stringer.bi*(stringer.tsf+stringer.hs+stringer.ti/2))
+...

(stringer.hs*stringer.th*(stringer.tsf+stringer.hs/2))+(stringer.bsf*stringer.ts
f*(stringer.tsf/2)))/stringer.area;

 stringer.ybar=(stringer.area*stringer.ys)/((upperEgg.boomSpacing_in*skinthickne
ss)+stringer.area);

 stringer.gyration=sqrt(((upperEgg.boomSpacing_in*skinthickness*stringer.ybar^2)
+2*stringer.bsf*stringer.ti*(stringer.height/2)^2+...
    (stringer.ti*((stringer.height^3)/12))+stringer.area*(stringer.ybar-
stringer.ys)^2)/stringer.area);

 stringer.crstress=(pi^2*stringer.modulus)/((stringer.length/stringer.gyration)^
2);
```

Takeoff Performance Main Code

```matlab
%% TAKEOFF PERFORMANCE
T_curve = [5978.786749, 0, 0];
Cd_curve = [0.03, 0.0312];
wind = 20;
```

```matlab
 [distRoll, timeRoll, spdRoll] =
TakeoffRoll(T_curve*2,43496.5,1275,127.7,1.2,Cd_curve,wind);

 [distTrans, timeTrans, spdTrans, initAlt] =
ClimbOut(T_curve*2,43496.5,1275,127.7,1.2,Cd_curve,5,wind);

 finalDist = 0;
 finalTime = 0;
 finalSpd = 0;
 for i = 1:length(initAlt)
     if initAlt(i) >= 50
         finalDist = distRoll(end)+distTrans(i);
         finalTime = timeRoll(end)+timeTrans(i);
         finalSpd = spdTrans(i);
         break
     end
 end

 figure(1); clf
 grid minor
 xlabel('Time (s)');
 yyaxis left
 plot([timeRoll, timeTrans+timeRoll(end)], [spdRoll, spdTrans], LineWidth=2);
 yyaxis right
 plot([timeRoll, timeTrans+timeRoll(end)], [distRoll, distTrans+distRoll(end)],
LineWidth=2);
 yyaxis left
 ylabel('Ground Speed (kts)');
 yyaxis right
 ylabel('Ground Distance (ft)');
 xline(timeRoll(end), Label='Rotate', LabelVerticalAlignment='bottom',
LabelHorizontalAlignment='left', Color='k');
 xline(finalTime, Label='50 ft AGL', LabelVerticalAlignment='bottom',
LabelHorizontalAlignment='left', Color='r');

 fprintf('\nFinal takeoff ground distance: %.2f ft.\n\tDuration: %.2f
s\n\tSpeed: %.2f kts\n', finalDist, finalTime, finalSpd);

 %% CLIMB PROFILE
 % Initial climb (leg 1)
 altHold = 10000;
 altCrz = 21000;
 timeHold = 2;

 height_1 = linspace(600,altHold);
```

```matlab
climbTime_1 = height_1*0;
climbDist_1 = height_1*0;
dh = height_1(2)-height_1(1);
V = 187.2;
i = 2;
for alt = height_1(1:end-1)
    dt = dh/MaxRoC(V,43496.5,1275,Cd_curve,2750*2,alt);
    dS = (V/60)*dt;
    climbTime_1(i) = climbTime_1(i-1)+dt;
    climbDist_1(i) = climbDist_1(i-1)+dS*cos(asin((dh/6076.115)/dS));
    i = i+1;
end

% Climb to cruise after 2 min loiter (leg 2)
height_2 = linspace(altHold,altCrz);
climbTime_2 = height_2*0;
climbDist_2 = height_1*0;
dh = height_2(2)-height_2(1);
V = 200;
i = 2;
for alt = height_2(1:end-1)
    dt = dh/MaxRoC(V,43496.5,1275,Cd_curve,2750*2,alt);
    dS = (V/60)*dt;
    climbTime_2(i) = climbTime_2(i-1)+dt;
    climbDist_2(i) = climbDist_2(i-1)+dS*cos(asin((dh/6076.115)/dS));
    i = i+1;
end
climbTime_2 = climbTime_2 + climbTime_1(end) + timeHold;
climbDist_2 = climbDist_2 + climbDist_1(end) + timeHold*V/60;

height = [height_1 height_2];
climbTime = [climbTime_1 climbTime_2];
climbDist = [climbDist_1 climbDist_2];
finalHeight = height(end);
finalClimbTime = climbTime(end);
finalClimbDist = climbDist(end);

figure(2); clf
grid minor
xlabel('Time (mins)');
yyaxis left
plot(climbTime,height,LineWidth=2);
yyaxis right
plot(climbTime,climbDist,LineWidth=2);
yyaxis left
```

```matlab
ylabel('Altitude (ft)');
yyaxis right
ylabel('Distance (nmi)');

fprintf('\nFinal cruise altitude: %d ft.\n\tDuration: %.2f mins\n\tDistance:
%.2f nmi\n', finalHeight, finalClimbTime, finalClimbDist);

%% DESCENT PROFILE
RoD_1 = ((250*1.687664)/13)*60;     %V_dec/(L/D)
RoD_2 = ((187.2*1.687664)/13)*60;   %V_land/(L/D)
altHold = 6000;
altCrz = 21000;
timeHold = 15;

% Initial descent (leg 1)
descendTime_1 = (20000-altHold)/RoD_1;
dS_1 = (250/60)*descendTime_1;
descendDist_1 = dS_1*cos(asin(((altCrz-altHold)/6076.115)/dS_1));

% Descent to ground level after 15 min loiter (leg 2)
descendTime_2 = (altHold-600)/RoD_2;
dS_2 = (187.2/60)*descendTime_2;
descendDist_2 = dS_2*cos(asin(((altHold-600)/6076.115)/dS_2));
descendTime_2 = descendTime_2 + descendTime_1 + timeHold;
descendDist_2 = descendDist_2 + descendDist_1 + timeHold*200/60;

descendTime = [0 descendTime_1 descendTime_1+timeHold descendTime_2];
descendDist = [0 descendDist_1 descendDist_1+timeHold*200/60 descendDist_2];
descend = [altCrz altHold altHold 600];

finalLand = descend(end);
finalDescTime = descendTime(end);
finalDescDist = descendDist(end);

figure(3); clf
grid minor
xlabel('Time (mins)');
yyaxis left
plot(descendTime,descend,LineWidth=2);
yyaxis right
plot(descendTime,descendDist,LineWidth=2);
yyaxis left
ylabel('Altitude (ft)');
yyaxis right
ylabel('Distance (nmi)');
```

```matlab
 fprintf('\nFinal descent altitude: %d ft.\n\tDuration: %.2f mins\n\tDistance:
%.2f nmi\n', finalLand, finalDescTime, finalDescDist);

 %% ENTIRE MISSION PROFILE

 cruiseDist = 350 - climbDist(end) - descendDist(end);
 cruiseTime = (cruiseDist/(0.5*sqrt(1.4*287*(273-25))*3600/1852))*60;
 missionAlt = [height descend];
 missionTime = [climbTime climbTime(end)+cruiseTime+descendTime];
 missionDist = [climbDist climbDist(end)+cruiseDist+descendDist];
 figure(4); clf
 grid minor
 xlabel('Time (mins)');
 yyaxis left
 plot(missionTime,missionAlt,LineWidth=2);
 yyaxis right
 plot(missionTime,missionDist,LineWidth=2);
 yyaxis left
 ylabel('Altitude (ft)');
 yyaxis right
 ylabel('Distance (nmi)');
 xline(climbTime(end), Label='Top of Climb', LabelVerticalAlignment='bottom',
LabelHorizontalAlignment='left', Color='k');
 xline(climbTime(end)+cruiseTime, Label='Top of Descent',
LabelVerticalAlignment='bottom', LabelHorizontalAlignment='left', Color='k');

 fprintf('\nFinal flight distance: %d nmi.\n\tDuration: %.2f mins\n',
missionDist(end), missionTime(end));



 MacRoC.m

 function [RoC, V_eas] = MaxRoC(V_tas, W, S, CD_curve, P_av, varargin)
 %
 % Compute the maximum attainable rate of climb using a range of velocity.
 %
 % [RoC, V_eas] = MAXROC(V, W, S, CD_curve, P_av)
 % Computes the maximum attainable rate of climb at sea level
 % INPUT ARGUMENTS
 %   V: Vector containing range of velocity (TAS)
 %   W: Weight of the aircraft (in lbs)
 %   S: Wing area (in ft^2)
 %   CDCurve: The equation of the aircraft's parabolic drag
```

```matlab
%          - Takes the form a + b*CL^2
%    P_av: Engine power available (in HP)
%
% [RoC, V_eas] = MAXROC(V, W, S, CD_curve, P_av, alt)
% Computes the maximum attainable rate of climb at altitude 'alt'
% INPUT ARGUMENTS (additional)
%    alt: Altitude at which to conduct the computation (in ft)
%
% [RoC, V_eas] = MAXROC(V, W, S, CD_curve, P_av, alt, eta, diam, rpm)
% Computes the maximum attainable rate of climb at altitude 'alt' with
% propeller efficiency polynomial curve 'eta'
% INPUT ARGUMENTS (additional)
%    eta: Polynomial function for the propeller efficiency vs advance ratio
%    diam: The diameter of the propeller (in inches)
%    rpm: The rated engine speed in RPM
%
% Created by:
% Jeffery Omorodion (500903166)

rho = 0.002377;
V_tas = V_tas*1.6878;     % Velocity conversion from knots to ft/s

if length(varargin) >= 1
    alt = varargin{1};
    correctionRatio = (1-0.0065*(alt/3.28)/288)^(9.81/(0.0065*287)-1);
    P_av = P_av*correctionRatio;
    rho = rho*correctionRatio;
end

CL = 2*W./(rho*V_tas.^2*S);
CD = CD_curve(1) + CD_curve(2)*CL.^2;

P_req = (CD*rho.*V_tas.^2*0.5*S).*V_tas;
P_av = ones(1, length(P_req))*P_av;

if length(varargin) == 4
    eta = varargin{2};
    diameter = varargin{3}/12;
    rev = varargin{4}/60;
    P_av = P_av.*polyval(eta, V_tas./(rev*diameter*0.5925));
end

V_eas = V_tas*(rho/0.002377)^0.5;
RoC = 60*(P_av*550-P_req)/W;
```

```
end


TakeoffRoll.m

function [gRoll,gTime,gVel] =
TakeoffRoll(T_curve,W,S,V_lof,CL,CD_curve,varargin)
%
% Compute the takeoff roll performance of a twin-jet aircraft at mean sea level
%
% [distance, time, speed] = TAKEOFFROLL(ThrCurve, Weight, WingArea, V_LOF,
CL_g, CDCcurve)
% Computes the ground roll distance (and takeoff time) from 0 kts to V_LOF
% INPUT ARGUMENTS
%   ThrCurve: The equation of thrust from a single engine (terms of ft/s)
%       - Takes the form a + b*V + c*V^2, where V is the velocity (ft/s)
%   W: Weight of the aircraft (in lbs)
%   S: Wing area (in ft^2)
%   V_LOF: Liftoff speed (in knots)
%   CL_g: Lift coefficient on the ground
%   CDCurve: The equation of the aircraft's parabolic drag
%       - Takes the form a + b*CL^2
%
% [distance, time, speed] = TAKEOFFROLL(ThrCurve, Weight, WingArea, V_LOF,
CL_g, CDCcurve, wind)
% Computes the ground roll distance (and takeoff time) with a headwind
% INPUT ARGUMENTS (additional)
%   wind: The velocity of the headwind (in knots)
%
% [distance, time, speed] = TAKEOFFROLL(ThrCurve, Weight, WingArea, V_LOF,
CL_g, CDCcurve, wind, engOut)
% Computes the ground roll distance (and takeoff time) with an engine INOP
% INPUT ARGUMENTS (additional)
%   engOut: The velocity at which the engine is made inoperable (in knots)
%
% Created by:
% Jeffery Omorodion (500903166)

g = 32.2;                    % Gravitational constant (ft/s^2)
mu_g = 0.025;                % Friction coefficient for a paved runway
rho = 0.002377;              % Standard density of air (slugs/ft^3)
w = 0;                       % Headwind in ft/s
engOutSpd = 1e6;             % Engine-out speed
gVel = (0:V_lof)*1.6878;     % Velocity conversion from knots to ft/s
```

```matlab
% Wind definition, if specified
if length(varargin) >= 1
    w = varargin{1}*1.6878;
end

% Engine out speed definition, if specified
if length(varargin) == 2
    engOutSpd = varargin{2}*1.6878;
end

% Thrust curve
T = T_curve(1) + T_curve(2)*(gVel-w) + T_curve(3)*(gVel-w).^2;

% Coefficient of Drag
CD = CD_curve(1)+CD_curve(2)*CL^2;

% Adjust for engine out if necessary
T = T-T.*(gVel >= engOutSpd)*0.5;
CD = CD+CD_curve(1).*(gVel >= engOutSpd)*0.1;

% Dynamic pressure and acceleration
q = 0.5*rho*(gVel-w).^2;
a = g*((T/W-mu_g) - (CD-mu_g*CL).*q*S/W);

% Time deltas required to accelerate 1 kt with an acceleration of 'a'
% (change in velocity / acceleration)
dT = 1.6878./a;

% Total times (to accelerate to V+1kt) via sum of required time deltas
gTime = zeros([1, length(dT)]);
for i = 1:length(dT)
    gTime(i) = sum(dT(1:i));
end

% Discard the last time (related to accelerating to V_LOF+1kt), begin at 0
gTime = [0, gTime(1:end-1)];

% Ground roll via numerical integration of v/a dv (NOT deltaV/a)
gRoll = cumtrapz(gVel, gVel./a);

% Convert velocity back to knots
gVel = gVel/1.6878;

end
```

ClimbOut.m

```matlab
function [gDist,aTime,aVel,alt] =
ClimbOut(T_curve,W,S,V_lof,CL,CD_curve,dGamma,varargin)

g = 32.2;                    % Gravitational constant (ft/s^2)
rho = 0.002377;              % Standard density of air (slugs/ft^3)
w = 0;                       % Headwind in ft/s
dt = 0.01;
dGamma = dGamma*pi/180;

if length(varargin) == 1
    w = varargin{1};
end

gDist = [0];
aVel = [V_lof*1.6878];
aTime = 0:dt:(15*pi/180)/dGamma;
alt = [0];

% Transition phase
% First entry isn't needed (gamma = 0)
for t = aTime(2:end)
    v = aVel(end);
    gamma = min(10*pi/180, dGamma*t);
    q = 0.5*rho*(v-w)^2;

    L = v*dGamma*(W/g) + W*cos(gamma);
    % CL = L/(q*S); <-- Not needed. Evaluate in ground effect.
    CD = CD_curve(1) + CD_curve(2)*CL^2;
    T = T_curve(1) + T_curve(2)*(v-w) + T_curve(3)*(v-w)^2;
    a = g*(T/W - CD*q*S/W - sin(gamma));

    dV = a*dt;
    dS = (v+dV)*dt + a*dt^2/2;

    aVel(end+1) = aVel(end)+dV;
    gDist(end+1) = gDist(end)+dS*cos(gamma);
    alt(end+1) = alt(end)+dS*sin(gamma);
end

aVel = aVel/1.6878;

end
```